FUSION ENERGY DIVISION ANNUAL PROGRESS REPORT

Period Ending December 31, 1977

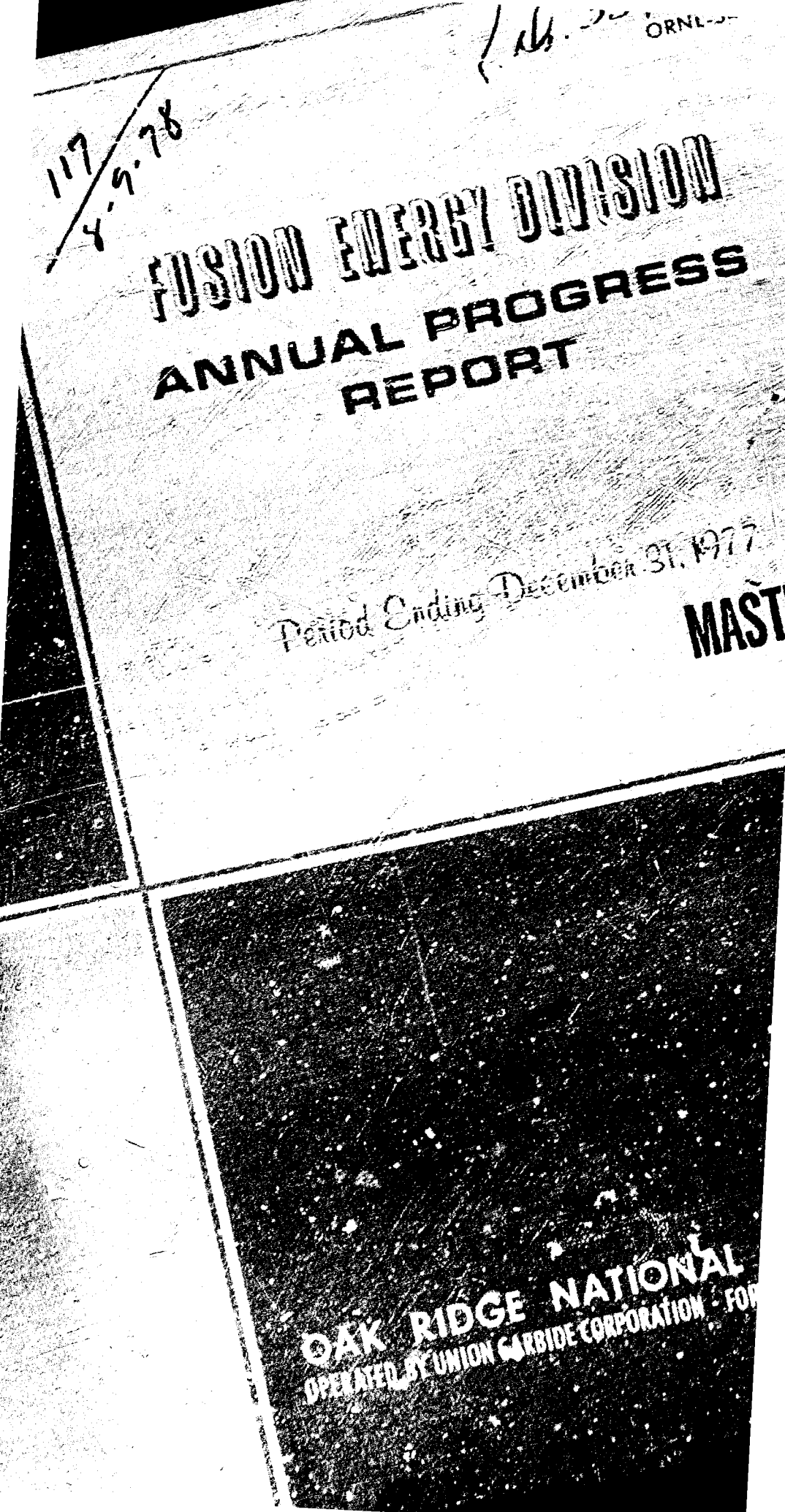

ORNL-5405
Dist. Category UC-20

Contract No. W-7405-eng-26

FUSION ENERGY DIVISION

ANNUAL PROGRESS REPORT

Period Ending December 31, 1977

AUGUST 1978

Prepared by the
OAK RIDGE NATIONAL LABORATORY
Oak Ridge, Tennessee 37830
operated by
UNION CARBIDE CORPORATION
for the
DEPARTMENT OF ENERGY

Reports previously issued in this series are as follow:

ORNL-2693	Period Ending January 30, 1959
ORNL-2802	Period Ending July 31, 1959
ORNL-2926	Period Ending January 31, 1960
ORNL-3011	Period Ending July 31, 1960
ORNL-3104	Period Ending January 31, 1961
ORNL-3239	Period Ending October 31, 1961
ORNL-3315	Period Ending April 30, 1962
ORNL-3392	Period Ending October 31, 1962
ORNL-3472	Period Ending April 30, 1963
ORNL-3564	Period Ending October 31, 1963
ORNL-3652	Period Ending April 30, 1964
ORNL-3760	Period Ending October 31, 1964
ORNL-3836	Period Ending April 30, 1965
ORNL-3908	Period Ending October 31, 1965
ORNL-3989	Period Ending April 30, 1966
ORNL-4063	Period Ending October 31, 1966
ORNL-4150	Period Ending April 30, 1967
ORNL-4238	Period Ending October 31, 1967
ORNL-4401	Period Ending December 31, 1968
ORNL-4545	Period Ending December 31, 1969
ORNL-4688	Period Ending December 31, 1970
ORNL-4793	Period Ending December 31, 1971
ORNL-4896	Period Ending December 31, 1972
ORNL-4982	Period Ending December 31, 1973
ORNL-5053	Period Ending December 31, 1974
ORNL-5154	Period Ending December 31, 1975
ORNL-5275	Period Ending December 31, 1976

CONTENTS

INTRODUCTION

In 1977 ORNL continued to be a major contributor to the international effort for the development of fusion energy into a useful power producer. This contribution remains broad, with major programs in plasma physics theory, plasma physics experiments, and technology development, and maintains a sufficient effort in each area to allow a high quality, in-depth effort. The examples in this introduction illustrate both the breadth and significance of the ORNL program.

The theoretical investigation of high beta tokamak configurations now uses a number of tools for investigating the stability of high beta equilibrium. Our analyses with initial value, semianalytic (BALOON), and energy principle (ERATO and PEST) computer codes have reinforced our previous conclusion that betas of 5-10% should be attainable. In addition, coupled transport and equilibrium codes are now investigating the evolution of tokamak equilibrium under the combined effects of heating and transport. Our understanding of resistive MHD phenomena continues to increase, and the predicted nonlinear properties of $m = 2$, $n = 1$ Mirnov oscillations agree quantitatively with experiments. It now appears also that nonlinear coupling between the $m = 3$, $n = 2$ and $m = 2$, $n = 1$ modes may be central to the major disruption process. In the continuing effort to understand the anomalous electron transport, it was found from both analytical and numerical calculations that the collisionless drift wave in a smoothly sheared magnetic field (the "universal instability") was stable. However, trapped particles do destabilize these waves. While the electrostatic effects of microinstabilities seem progressively less able to explain the observed electron losses, it now appears that the breakup of magnetic surfaces caused by such waves (the "magnetic flutter model") is a viable mechanism. The EBT theoretical effort, motivated by experiment, has been developing methods to self-consistently model the ambipolar electric field. This field strongly influences particle orbits and thus plasma transport. It appears that a completely classical model yields plasma parameters which are within a factor of about two of those which are measured. As the microscopic and macroscopic features of the models evolve, comparisons with experiment are becoming increasingly detailed. The ability to do computations such as the above and to deal with the large data flow from experiments was enhanced by the installation of a PDP KL-10. This computer has approximately twice the capacity of the KI-10 it replaced.

The principal thrust in the EBT program was an expanded effort to measure the radial profiles of key plasma parameters, including profiles of ion temperature, density, impurity ions, neutral hydrogen, and plasma potential. The effect of small field errors on plasma confinement was studied. Optimum confinement conditions were obtained when the global field errors were cancelled, and under these conditions the net toroidal current was very small. EBT-I was shut down at the end of the year for modifications which will allow higher microwave power levels and frequency (EBT-S). This increase in power is made possible by the superpower millimeter microwave tube development program at Varian Associates (Palo Alto, California) under an ORNL subcontract. Tubes with over 200 kW of power at 28 GHz and a dc-rf conversion efficiency of 35% were developed; a steady-state tube will be delivered in 1978. This 28-GHz development will be extended to 120 GHz for EBT-II, a proposed device which under neoclassical assumptions (consistent with EBT-I and which will be scaled on EBT-S) allows the possibility of $n\tau \sim 10^{13}$-10^{14} sec/cm^3, $T \sim 5$-10 keV, and $\tau = 0.1$-1 sec. The steady-state, high beta, and large aspect ratio properties of the EBT concept appear to lead to an attractive reactor concept.

The tokamak experimental effort was highlighted by the very successful run of ISX-A. Because of careful control of vacuum conditions, discharge cleaning, and titanium gettering, plasmas with $Z \sim 1$-3, $n = 5 \times 10^{12}$/cm^3 to 5×10^{13}/cm^3, and $\tau \leq 30$ msec were produced at a toroidal field of 15 kG. The confinement time was a factor of four higher than that observed in ORMAK under similar conditions. This difference apparently results from a reduction in the amount of power lost due to impurity radiation. The impurity flow reversal experiment, a joint effort with the General Atomic Company, was

BLANK PAGE

an attempt to reduce or reverse the movement of impurities from the plasma edge to the discharge core. Although not all aspects of the experiment were understood, an effect in the correct direction was seen and additional experiments on ISX-B (a noncircular, neutral beam heated modification to ISX-A) are planned. The fabrication for the ISX-A/ISX-B conversion progressed well, and experiments are expected to start in the summer as projected. The post-ISX tokamak program is based on a long pulse, superconducting device which investigates the physics and technology problems associated with producing and maintaining high beta plasma discharges for periods longer than 10-20 sec.

A major demonstration of pellet fueling was done on ISX-A using a 0.6-mm, 330-m/sec pellet injection system developed in the Plasma Technology Program. These pellets produced significant density increases, $\Delta n/n \sim 10$-50%, and penetrated the $1 \times 10^{13}/cm^3$ plasma about 10 cm, in agreement with model calculations. An intensive construction and development effort led to the delivery of four neutral beam lines to the Princeton Plasma Physics Laboratory for use on PLT. Each of these systems is capable of delivering 750 kW. The systems have very high atomic yields (~85%). The cryogenic, heat transfer, and ion source components can be improved and will form the basis for a new generation of beam lines.

The program to develop large toroidal superconducting magnets is now well established. The three coil contractors (General Dynamics, General Electric, and Westinghouse) are now in the detailed design and verification testing phase of their contracts. In addition, a contract for construction of the 10.7-m-diam, 11.3-m-high cylindrical vacuum vessel for the test facility has been let; actual construction is to begin in mid-1978. It is now expected that the three follow-on coils will be built outside of the United States as part of the IEA agreement which was signed by the Secretary of the Department of Energy in October 1977. Potential coil suppliers include Switzerland, Japan, and EURATOM. Full six-coil array tests are scheduled for 1982. The development of the conductor, instrumentation, and analytical tools required for this effort is now the principal activity of the Magnetics and Superconductivity Section, but in addition contributions have been made to the EBT-S, EBT-II, EBTR, ISX, and TNS programs.

The TNS effort has moved from a phase in which project definition and systems modeling were the most important activities to one of preconceptual design in which specific tasks are undertaken to reduce technology requirements, reduce costs, and/or increase the engineering feasibility of the device (e.g., analyzing the trade-offs between air and iron core devices and developing designs with fewer toroidal field coils). This program continues to play a strong role in defining and refining the plasma physics and technology programs at ORNL.

It should also be noted that a separation took place between the management functions of the Fusion Energy Division and the Fusion Program. Historically, programs within the Laboratory have cut across a number of discipline-oriented divisions and have been managed by a program director. This did not take place earlier in the fusion effort because most of the work centered in one division. The increased size of the program and the growing effort in other divisions motivated this change.

The year 1977 was an uncertain one for fusion development in the United States because priorities within the nation's advanced energy research and development program were under intensive study. However, the ORNL Fusion Program has made significant advances in establishing the physics and technology base which will be required for the future program. Progress is continuing to be made toward obtaining useful energy from the fusion process.

Lee A. Berry, Director
ORNL Fusion Program

O. B. Morgan, Jr., Director
Fusion Energy Division

HIGH BETA PLASMA

R. A. Dandl, Section Head

F. W. Baity
M. C. Becker[1]
F. M. Bieniosek[2]
F. J. Bresnock[3]
K. H. Carpenter[3]
J. A. Cobble
P. L. Colestock[4]
K. A. Connor[3]
H. O. Eason
J. C. Glowienka
G. R. Haste[5]
M. Hesse[6]
R. L. Hickok[2]
S. Hiroe[7]
H. Ikegami[7]
S. P. Kuo[3]
N. H. Lazar
R. L. Livesey
M. W. McGuffin
H. W. Moos[8]
B. H. Quon
J. W. Reynolds
R. K. Richards[8]
W. J. Schill
J. M. Tyson[8]
T. Uckan
T. L. White
R. E. Wintenberg[1]

Abstract. The main thrust of the experimental efforts in 1977 was directed toward the measurement of radial profiles of most key plasma parameters, mainly in the stable T-mode operation of EBT-I. Ion temperature and density profiles were measured by charge exchange neutral particle analysis, neutral hydrogen and impurity ion density profiles were measured spectroscopically, and plasma potential profiles were measured using the heavy ion beam probe technique for the first time. Work is continuing on the development of a new soft x-ray detector for measuring electron temperature profiles and a ruby laser scattering apparatus for measuring electron density profiles.

1. Instrumentation and Controls Division.
2. Consultant, Rensselaer Polytechnic Institute, Troy, New York.
3. Computer Sciences Division.
4. Consultant, Rensselaer Polytechnic Institute, Troy, New York, and Princeton Plasma Physics Laboratory, Princeton, New Jersey.
5. On leave to Centre d'Études Nucléaires de Grenoble, Grenoble, France.
6. On leave from Centre d'Études Nucléaires de Grenoble, Grenoble, France.
7. Consultant, Institute of Plasma Physics, Nagoya University, Nagoya, Japan.
8. Consultant, Johns Hopkins University, Baltimore, Maryland.

In addition to the efforts to obtain radial profile information, there were several other measurements which added significantly to our understanding of EBT. The effects of small magnetic field errors on plasma confinement were studied, and the dependence of other parameters, such as net toroidal current, on field errors was determined. Electron heating by microwaves was studied by soft x-ray analysis. Installation of a new neutral particle analyzer employing a cesium charge exchange cell increased our confidence in charge exchange measurements. The results of these measurements provided valuable guidance to the one-dimensional theory of EBT.

In November EBT-I was shut down for conversion to EBT-S, which is expected to be a crucial test of scaling for the EBT concept. Development was completed in 1977 for the 28-GHz, 200-kW (cw) gyrotron oscillator, waveguide distribution system, and power supply, which represent a 50% increase in microwave frequency and a threefold increase in total microwave power available.

Also in 1977 a design and engineering study was undertaken for the EBT-II device (to follow EBT-S). As currently conceived, EBT-II would achieve near breakeven conditions with auxiliary neutral beam heating for the ions if neoclassical scaling is valid. The EBT-II design calls for extension of the gyroklystron state of the art to 200-kW (cw) tubes operating at 120 GHz and for modest technology improvements in the areas of superconducting magnets and neutral beam

sources. The design also includes the innovative feature of aspect ratio enhancement coils, which reduces the size requirements for breakeven for an EBT device, possibly by a factor of three.

1.1 INTRODUCTION

Operation of the ELMO Bumpy Torus was concluded in 1977 as conversion of EBT-I to EBT-S began. Experimental efforts were concentrated on obtaining radial profile information, development of the 28-GHz gyroklystron for use on EBT-S was nearly completed, and a conceptual design study was undertaken of the next generation device, EBT-II.

The experimental program consisted of using new techniques as well as refining existing diagnostics. Section 1.2 discusses the results of soft x-ray analysis of electron heating. Section 1.3 describes the new charge exchange apparatus installed on EBT during 1977 and measurements of the ion radial profiles. The measurements of space potential profiles by the heavy ion beam probe are in Sect. 1.4. Section 1.5 details the results of our studies of toroidal current and magnetic field error compensation. Section 1.6 discusses the impurity distributions in the EBT plasma as measured by uv spectroscopy. Section 1.7 is a discussion of the visible light study of impurity spectral line shapes. Advances in microwave source development and preparations for EBT-S are described in Sect. 1.8. Finally, a summary of work on the EBT-II conceptual design study is given in Sect. 1.9.

1.2 STUDY OF ELECTRON HEATING BY SOFT X-RAY ANALYSIS

S. Hiroe F. J. Bresnock G. R. Haste

The recent progress of x-ray and other diagnostics on EBT has provided us with an understanding of the electron cyclotron resonance heated plasma. The calibration of the soft x-ray detector in the lower photon energy range is accomplished by operating EBT with magnetic field and microwave power applied to only a few cavities so that in the absence of a toroidal core plasma only the relativistic ring electrons illuminate the detector. Deviations at low energies from the known distribution of this energetic electron population may be used directly as a measure of detector efficiency. EBT may be operated in a mode to provide this calibration *in situ* to check the constancy of this calibration day to day.

1.2.1 Line Averaged Electron Temperature and Density with Only 18-GHz ECH

The behavior of the line averaged temperature, measured with the windowless soft x-ray detector, is shown in Fig. 1.1. In this figure, the ordinate is electron temperature and the abscissa is ambient pressure in the cavity containing the soft x-ray detector.

It is clear that the temperature changes steeply with pressure variations at low pressure and becomes almost constant at higher pressures. The temperatures obtained vary in the range of 300 eV-600 eV.

In Fig. 1.2, the dependence of line averaged density obtained from a 70-GHz interferometer and toroidal electron temperature on ambient pressure is shown. The EBT plasma consists of three different components: a surface plasma (s), a hot electron annulus (h), and a toroidal plasma (t). The measured nL is the sum of these components:

$$nL = n_s \ell_s + n_h \ell_h + n_t \ell_t .$$

Of these components, $n_h \ell_h$ is small and may be neglected compared to $n_t \ell_t$ and $n_s \ell_s$. It is evident that nL increases with ambient pressure but seems to saturate at high levels of microwave power.

The density obtained from the soft x-ray intensity is a measure of only the toroidal component. We can neglect the contribution of surface plasma because the electron temperature of the surface plasma is one order of magnitude

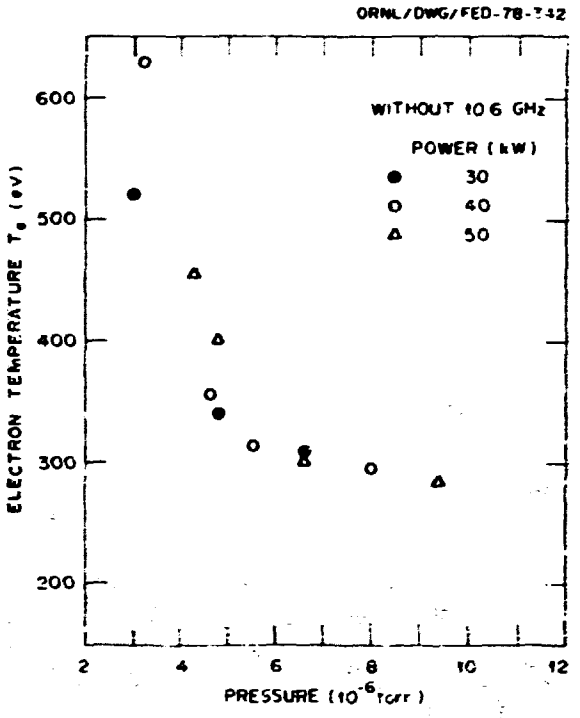

Fig. 1.1. Electron temperatures are shown vs feeding pressure. The operation condition varies from low pressure T-mode to high pressure T-mode.

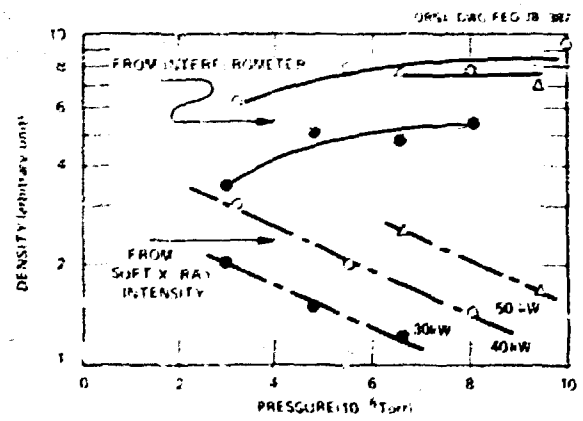

Fig. 1.2. Densities obtained from 70-GHz interferometer and soft x-ray intensity are shown vs feeding pressure.

smaller than that of the toroidal plasma and the measurements are taken from data above 0.7 keV. It is interesting that toroidal density decreases with increasing ambient pressure and increases with input power. From the interferometer measurements it appears that the density of surface plasma must then increase with ambient pressure. It is also clear that the energy contained in the toroidal plasma increases as the ambient pressure decreases toward the unstable M-mode.

From the above results, we can demonstrate the gross characteristics of the electron temperature and density in EBT. In Fig. 1.3 we show

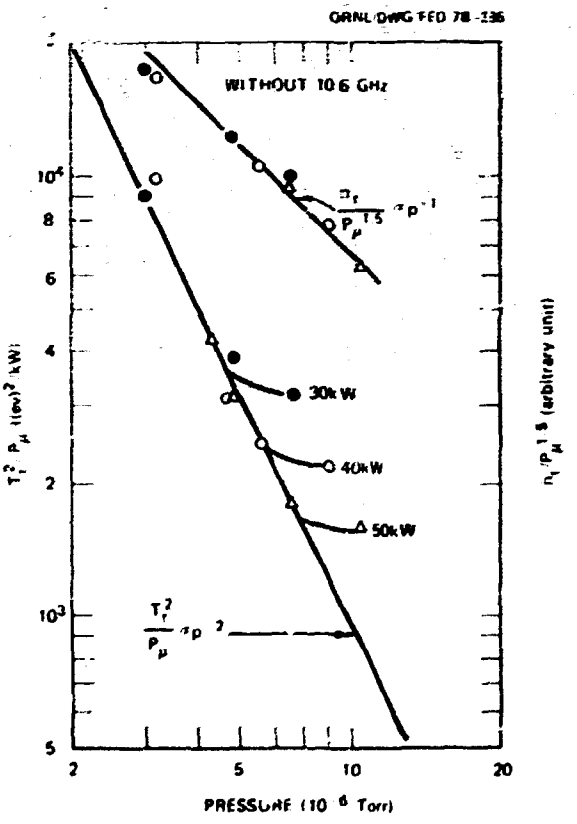

Fig. 1.3. Empirical scaling relation for 18-GHz ECH only.

the empirical relations between the toroidal temperature T_t, density n_t, input power P_μ, and ambient pressure p. The empirical relation between the toroidal density, microwave power, and ambient pressure can be written

$$n_t p \propto P_\mu^{1.5} . \qquad (1.2.1)$$

Except for operation at high pressure in the T-mode or in the C-T transition region, the relation between T_t and P_μ vs p is described by

$$T_t p \propto P_\mu^{0.5} . \qquad (1.2.2)$$

From Eqs. (1.2.1) and (1.2.2), we can eliminate p and write the relation

$$P_\mu \sim n_t/T_t . \qquad (1.2.3)$$

If we assume that the energy deposition in the toroidal plasma is proportional to $n_t T_t$, the deposited energy is

$$n_t T_t \propto (P_\mu/p)^2 . \qquad (1.2.4)$$

The energy deposition in the toroidal plasma increases with increasing microwave power and with decreasing ambient pressure. It is important to point out that these relations are applicable only for the T-mode.

As shown in Fig. 1.1, T_t appears to be nearly constant at high pressure in the T-mode. From Eq. (1.2.2), if T_t is constant, $p \propto P_\mu^{0.5}$. This relation is in good agreement with $p(\text{Torr}) = 10^{-6} P_\mu^{0.6}$ (kW), which is obtained at the C-T transition region, as reported earlier.[1]

1.2.2 Line Averaged Electron Temperature and Density with Both 10.6-GHz and 18-GHz ECH

In Fig. 1.4, the electron temperature with both 18-GHz and 10.6-GHz microwave power applied is shown as a function of ambient pressure. The different symbols represent different total microwave powers at 18 GHz and 10.6 GHz. The number by each experimental point is the power at 10.6 GHz.

When the results shown in Figs. 1.1 and 1.4 are compared, it is clear that the gross tendency is the same, except that T_e with additional 10.6-GHz power is smaller than with only 18-GHz power.

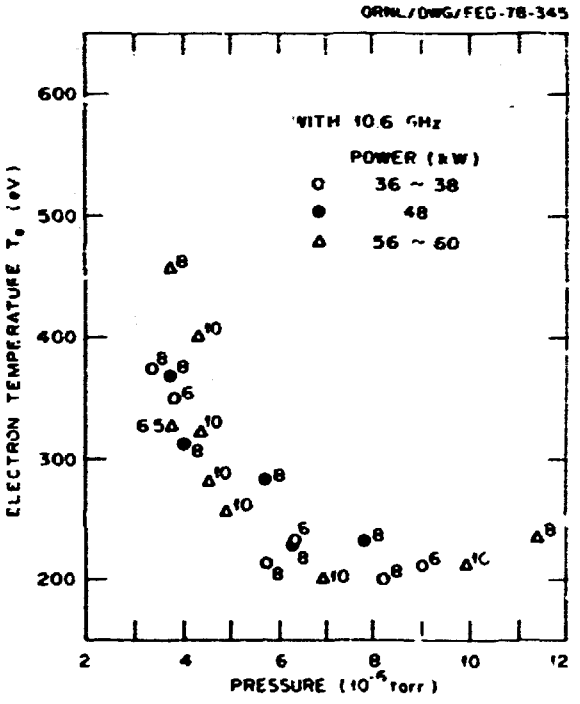

Fig. 1.4. Electron temperature with 10.6 GHz added.

In Fig. 1.5, the densities obtained from the 70-GHz interferometer and soft x-ray intensity are shown. In general, the total line-integrated density, nL, with 10.6 GHz is larger than that without 10.6 GHz; for example, compare the data for the powers of 30 + 8 (18-GHz and 10.6-GHz powers, in kW, respectively) and 40 + 0. As shown at the bottom of Fig. 1.5, with only 18-GHz power, $n_t \ell_t$ monotonically decreases with pressure, but $n_t \ell_t$ with additional 10.6-GHz ECH behaves in a more complicated way.

We have not measured the radial density profile yet, so it is not certain that i_t is constant for the many cases described. However, it should be pointed out that the cyclotron resonance region for 10.6 GHz lies very near the edge of toroidal plasma.

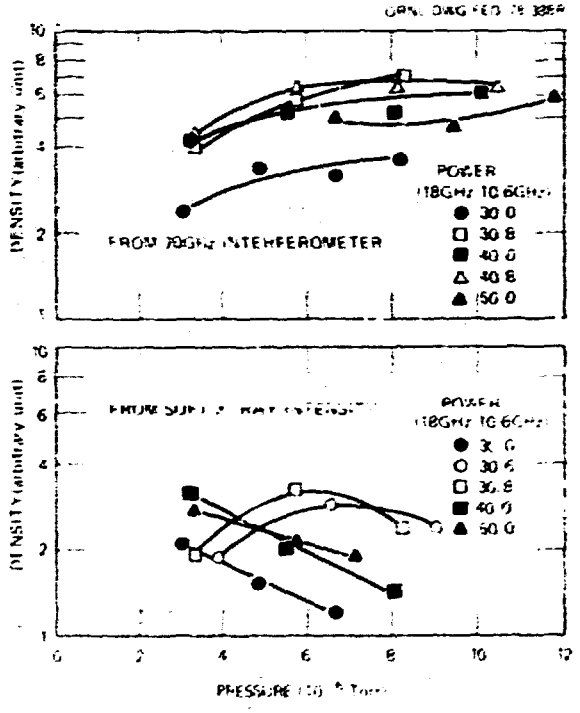

Fig. 1.5. Electron densities with and without 10.6 GHz.

In Fig. 1.6, the empirical scaling relation is shown when the 10.6-GHz microwave power is added to the 18-GHz power. The temperature scaling shows almost the same features as Fig. 1.3, except that the magnitude of the exponent of p is greater and the experimental data scatter is larger than those of Fig. 1.3. For this case, we have not yet determined the density scaling. The temperature scaling relation with 10.6-GHz power added is described by

$$T_t p^{1.5} = P_\mu^{1.5} , \qquad (1.2.5)$$

where P_μ is the total applied microwave power.

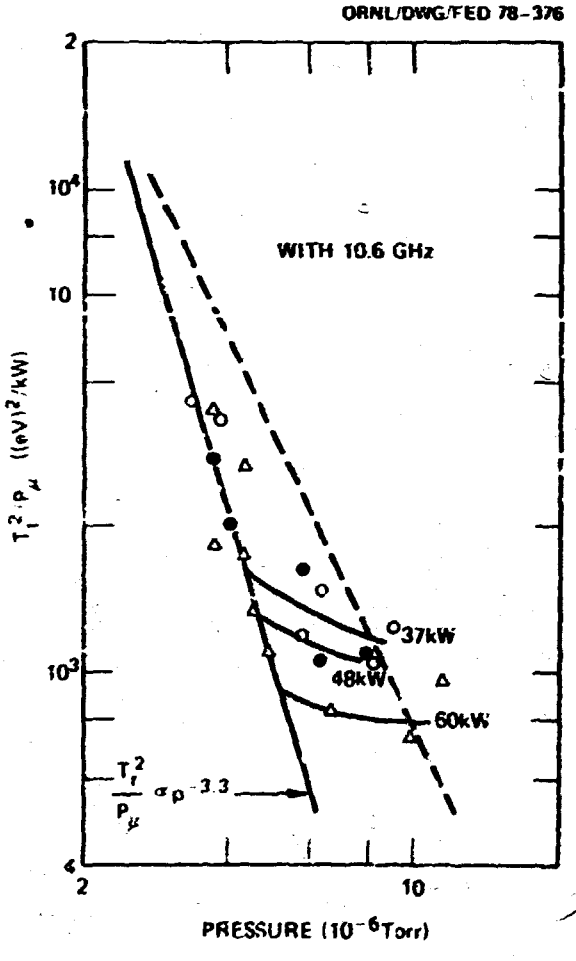

Fig. 1.6. Temperature scaling relation in the case with 10.6 GHz.

1.2.3 Electron Temperature Profiles from Heavy Ion Beam Probe Measurements

Relative electron temperature profiles were obtained by measuring the current ratios of the higher charge states of rubidium when employing the heavy ion beam potential probe. The signals Rb 2^+, 3^+, 4^+, and 5^+ are easily detectable, but data unfolding difficulties because of geometric factors and cross section uncertainties made an absolute T_e determination very difficult.[2]

1.3 ION CHARGE EXCHANGE MEASUREMENTS

F. W. Baity B. H. Quon

Two new neutral particle analyzers were installed on EBT-I. One is a four-chord analyzer which employs a conventional nitrogen stripping cell and which samples four parallel chords through the plasma for measurement of the ion radial profiles. The other is a single beam analyzer which employs a cesium charge exchange cell for converting the escaping fast neutrals to negative ions for energy analysis. Results from the two instruments are in good agreement with each other in the T-mode. The cesium spectrometer extends the sensitivity of temperature measurement to lower energies than is possible with a nitrogen stripping cell analyzer.

Central ion temperatures in the T-mode range from around 30 eV near the transition between C- and T-modes to 200 eV near the T-M transition for hydrogen. Near the T-M transition, the ion temperature is found to vary linearly with the plasma space potential well depth.

1.3.1 Ion Temperature Profile Measurements

A new neutral particle spectrometer was installed to detect energetic neutrals escaping along four parallel chords in the upper half of a cavity cross section. The instrument employs a conventional nitrogen stripping cell for converting the fast neutrals to positive ions. The data from this spectrometer can be analyzed by Abel inversion if plasma cylindrical symmetry is assumed.

Throughout the T-mode the ion temperature is seen to be practically constant in radius out to ~15 cm. Measurements of the ion-neutral density product ($n_i n_0$) radial profile are possible with this analyzer, but very thorough and careful calibrations are needed before much confidence is given to them. Direct measurement of the T_i profile confirmed what was suspected from the shape of spectra taken with a single chord analyzer. Distortion of the spectrum due to profile effects is seldom observed in EBT over a wide range of energy.

1.3.2 Cesium Charge Exchange Canal Spectrometer

In EBT-I charge exchange neutral measurements were hindered by low counting rates when using a conventional nitrogen stripping cell neutral particle analyzer since the plasma density was on the order of 2×10^{12} cm^{-3}, the ion temperature was typically ~100 eV, and the neutral hydrogen was significantly attenuated toward the center of the plasma. This low counting efficiency was an especially serious problem for energies approaching 100 eV, where good energy resolution is needed to measure radial profile effects on the ion temperature spectrum. An additional consequence of the low counting rate was that measurements of temporal changes in plasma density or temperature were precluded. Therefore, a new neutral particle analyzer which was much more efficient at low energies was needed. A vast improvement in counting efficiency was achieved at energies below 1 keV by using a cesium charge exchange cell to convert the escaping fast neutrals to negative ions. Cesium charge exchange canals have been built and studied in connection with negative ion beam development.[3,4]

Description of the cesium charge exchange canal

A cesium charge exchange cell similar to the design of Refs. 3 and 4 was constructed and combined with a converted energy analyzer to form a new charge exchange analyzer. The analyzer employs a 45° parallel plate electrostatic energy analyzer and a channel electron multiplier biased to analyze negatively charged particles. The electron multiplier is operated in the pulse counting mode. The cesium cell is shown schematically in Fig. 1.7. It is constructed

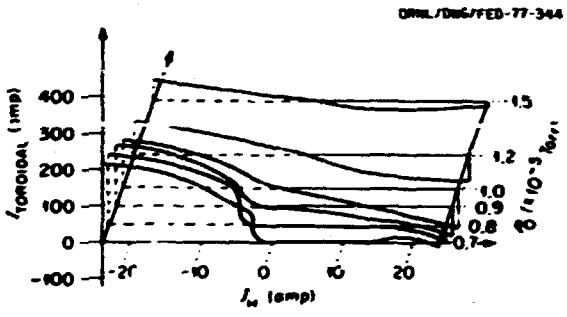

Fig. 1.7. (a) Cesium pipe schematic; (b) axial temperature distribution.

entirely of stainless steel. Two tubular 75-W heaters are located on either side of the cesium reservoir. The cell is designed for mounting between the end of the charge exchange port tube outside the lead wall and the analyzer housing box. The specifications of the cell are given in Table 1.1. The parallel plate electrostatic energy analyzer and housing were taken from an earlier neutral particle analyzer used on EBT. In order to detect negative particles, the channel electron multiplier has to be operated with the signal lead floating at 6 kV with respect to ground, necessitating the use of a blocking capacitor at the input to the preamp. The box housing the channel electron multiplier also must be floated, so a Teflon insulator was installed between it and the parallel plate analyzer.

Table 1.1. Cesium cell specifications

Material	304L stainless steel
Overall length	30.5 cm
Canal diameter	1.3-cm ID
Oven length	5.7 cm
Oven diameter	12.7 cm
Reservoir capacity	12 g
Heaters (2)	75 W
Wick	316 stainless steel mesh
Operating temperature	140 C
Cesium vapor pressure	7 mTorr
Lifetime (theoretical)	2700 hr
Lifetime (experimental)	~300 hr

The calibration curve obtained is shown in Fig. 1.8 with the nitrogen stripping cell result on the same graph. Note that the cesium cell

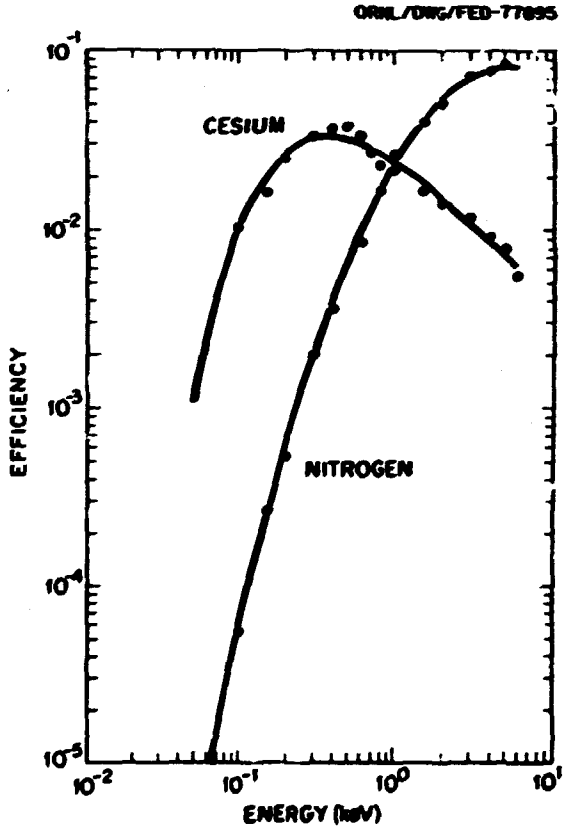

Fig. 1.8. Calibration curves for both the cesium and nitrogen spectrometers, showing the vast improvement in efficiency for the cesium spectrometer below 1 keV.

efficiency is higher for all energies below 1 keV, and that at 100 eV the improvement is over two orders of magnitude.

The limitation on the lifetime of the cell is the cesium loss rate out the ends of the pipe. Measurements of the exit flux give an estimate of 2700 hr for the lifetime of the cell with 12 g of cesium. The actual lifetime was found to be around 300 hr. This lifetime might be improved by modifying the operating temperature of the ends or by careful manufacture of the wick.

With the analyzer biased to accelerate negative ions, the electron multiplier also counts electrons entering it; therefore, precautions must be taken to prevent the emission of secondary electrons in the analyzer housing by the intense uv and x-ray flux from EBT. This is accomplished by shadowing all parts of the analyzer behind collimating apertures upstream as much as possible. When this is done the background counting rate is more than two orders of magnitude below the peak counting rate. Further reduction of the background may be possible.

The peak counting rate measured in EBT-I of about 5 x 10^4 counts/sec is well within the capability of the channel electron multiplier and its associated electronics.

Charge exchange measurements

Ion temperature measurements using the cesium cell analyzer were made over a wide range of operating conditions on EBT-I. The spectrum deviates from the Maxwellian for both high and low energies. At low energy the spectrum contains a sizable contribution from the cool surface plasma (measured spectroscopically to have an electron temperature of ~30 eV). At high energy the deviation may be due either to the background counting rate or to suprathermal ions sometimes observed in EBT-I with a nitrogen stripping cell neutral spectrometer. More effort is required to establish which explanation is correct. Neoclassical calculations predict – and direct measurements of ion radial profiles confirm – that the ion temperature profile in EBT-I is nearly flat out to the hot electron annulus, so that profile effects on the spectrum of fast neutrals escaping from the toroidal core plasma are small. Hence, there is good agreement between the observed spectrum and a single temperature Maxwellian distribution.

The relationship between ion temperature and background neutral pressure is shown in Fig. 1.9 for 48-kW total input power. In the C-mode the determination of ion temperature is difficult; however, regardless of background pressure there is always a significant population of energetic neutrals which appears to correspond to an ion temperature of 30-40 eV. In the T-mode, as the pressure is lowered, there is a smooth rise in ion temperature.

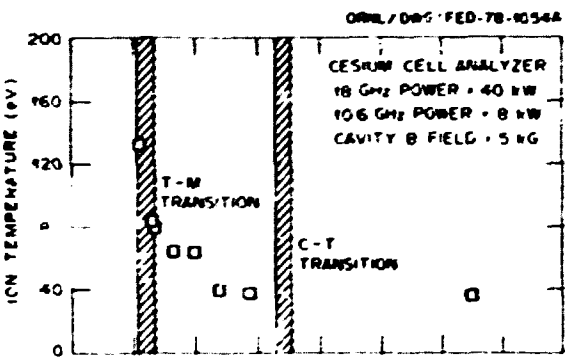

Fig. 1.9. Relationship between ion temperature and ambient pressure for typical operating conditions.

1.4 SPACE POTENTIAL PROFILE MEASUREMENT

S. P. Kuo P. L. Colestock

During the past year, significant advances were made in the measurement of the plasma space potential. The results indicate that under optimum confinement conditions the ambipolar electric field is nearly axisymmetric, points radially inward, and is of sufficient magnitude

to dominate the poloidal drifts. For T-mode operation the results are shown in Fig. 1.10. The maximum potential difference in this case is nearly 200 V. A series of radial scans along

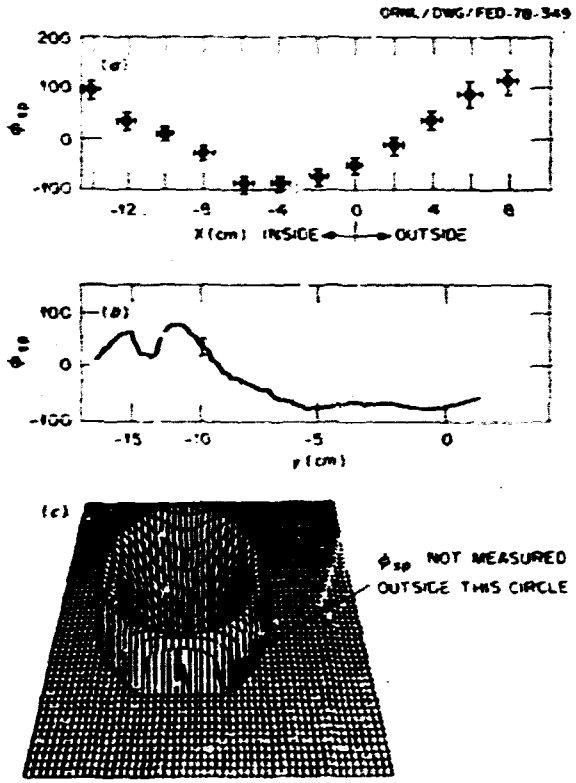

Fig. 1.10. T-mode space potential profile (a) along the vertical axis; (b) along the horizontal axis; and (c) two-dimensional profile

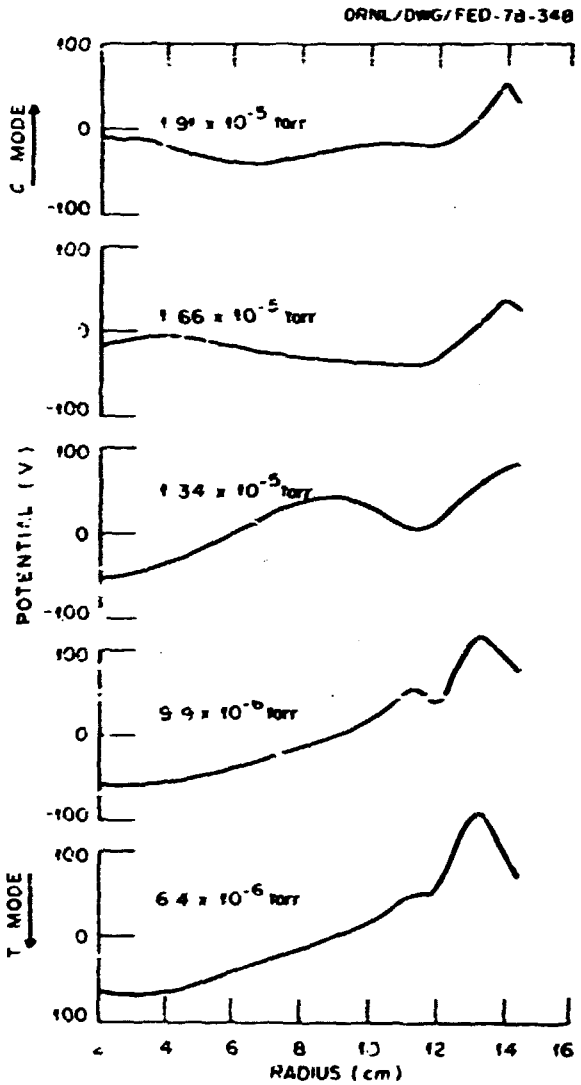

Fig. 1.11. Space potential profile along the vertical axis for several filling pressures.

the vertical line traversing the C-T transition is shown in Fig. 1.11 for several filling pressures. The change in plasma parameters which denotes the C-mode occurs rather abruptly at approximately p = 1.3 x 10^{-5} Torr.

Figure 1.12 shows that the space potential profile and hence the radial electric field are strongly affected by the profile resonance heating. The 10.6-GHz microwave seems to smooth the space potential profile and hence reduce the radial ambipolar field largely in the central region. This effect may result from the enhancement of the passing electron population by lower off-resonant heating from the profile heating source. A comparison between the space potential well depth and the plasma electron temperature is shown in Fig. 1.13, where the electron temperature is measured by the soft x-ray diagnostic.

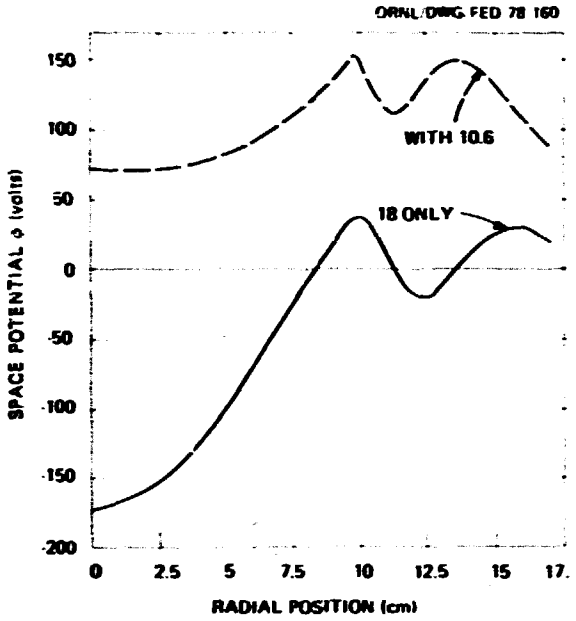

Fig. 1.12. Space potential profile in T-mode with and without 10.6-GHz prnfile resonant heating

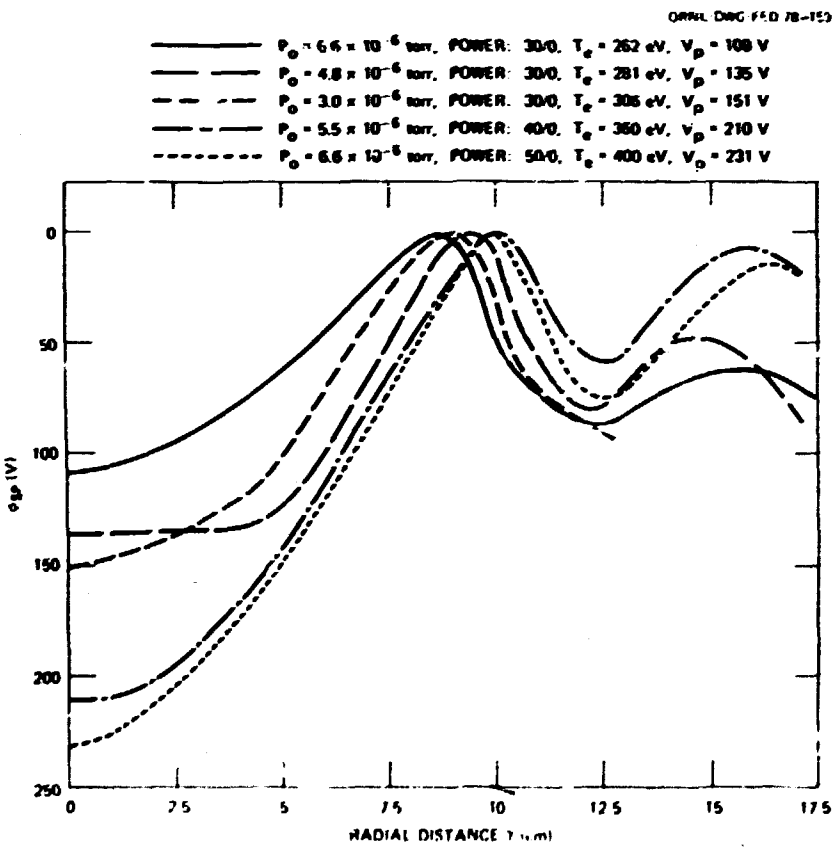

Fig. 1.13(a). Space potential profile under various operating conditions without 10.6-GHz resonant heating. All the curves have been shifted so that the peak potential is at zero volts.

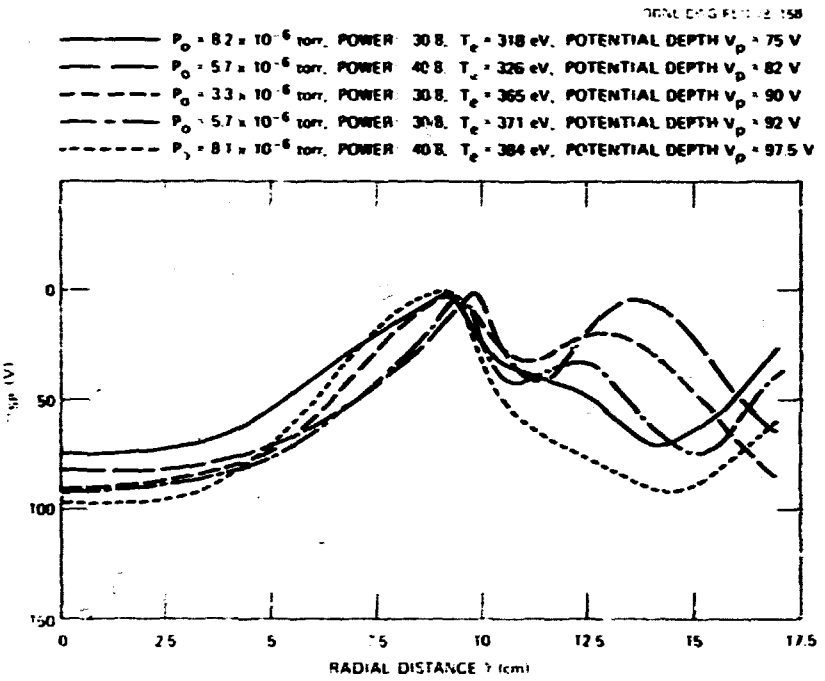

Fig. 1.13(b). Space potential profile under various operating conditions with 10.6-GHz resonant heating. All the curves have been shifted so that the peak potential is at zero volts.

1.5 TOROIDAL CURRENT AND GLOBAL FIELD COMPENSATION

B. H. Quon P. L. Colestock
H. Ikegami

The global error field compensation in EBT employs two pairs of current loops wound alongside the toroidally linked cavities, as schematically shown in Fig. 1.14. When current (I_H and I_V) is applied to these loops, a horizontal and a vertical field can be generated in an arbitrary plane perpendicular to the minor axis. These fields can be used to reduce or enhance the system global error field, thus permitting studies of plasma stability and confinement with field errors as a parameter. The net toroidal current is measured by integrating the electromotive force induced on two large pickup coils (Fig. 1.14). A 70-GHz microwave interferometer is used to obtain the average plasma density and density fluctuations. The two-dimensional plasma potential profile on the minor cross section is measured in the midplane of a single mirror using the heavy ion (rubidium) beam probe.

In order to show the relationship between the toroidal current and the global field errors, we have plotted the amplitude of the toroidal

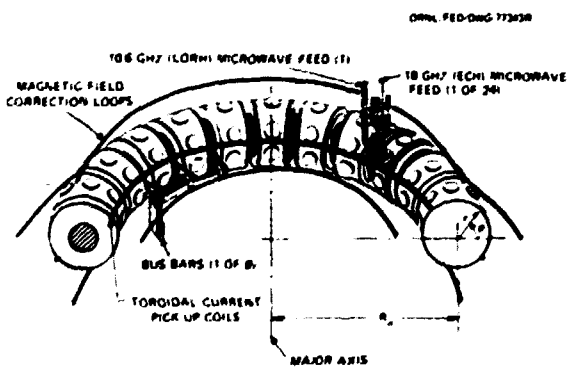

Fig. 1.14. Schematic diagram of the global field correction system on EBT. The correction loops are 50 cm from the minor axis. Each of these loops consists of a 20-turn coil capable of carrying a current up to 30 A. The major radius of the torus is 150 cm.

current as a function of the externally introduced horizontal field error for several gas filling pressures (see Fig. 1.15). In this range of pressure the EBT plasma is observed to change from C-mode (for $p_0 \geq 1 \times 10^{-5}$ Torr) to T-mode because of the stabilizing effect of the high β electron annulus.

In the high pressure C-mode the plasma is not stable against MHD instabilities, and the plasma transport is dominated by instabilities rather than by neoclassical diffusion. Our measurements on the plasma potential and other parameters show little change caused by field errors except the amplitude of the toroidal current, which increases almost linearly with the global field error, as shown by the top two curves in Fig. 1.15. In the low pressure T-mode, the plasma is stabilized by the high β (8-50%) electron annulus and is expected to behave neoclassically. This stability is manifested by the low level of plasma fluctuations and the relatively higher plasma temperature ($T_e \sim$ 200-500 eV, $T_i \sim$ 80-130 eV). We also observed the formation of a negative potential well in the plasma core. As shown in the lower three curves in Fig. 1.15, the measured toroidal current is significantly reduced for a range of the external field error. This change appears to relate to the formation of a negative potential well, as shown in Fig. 1.16.

The two-dimensional potential profiles shown in Fig. 1.16 were measured at a pressure $p_0 = 6 \times 10^{-6}$ Torr with an applied microwave heating power of ~50 kW. Figure 1.16(a) shows a radially symmetric potential well measured with global field error correction so that the toroidal current is minimized. The symmetry in the potential profile would seem to exclude the existence of convective cells and to indicate neoclassical ambipolar transport. This desirable potential profile symmetry is lost when the global error field correction is turned off. As shown in Fig. 1.16(b), the central plasma potential seems to be short-circuited to ground through the outer system wall.

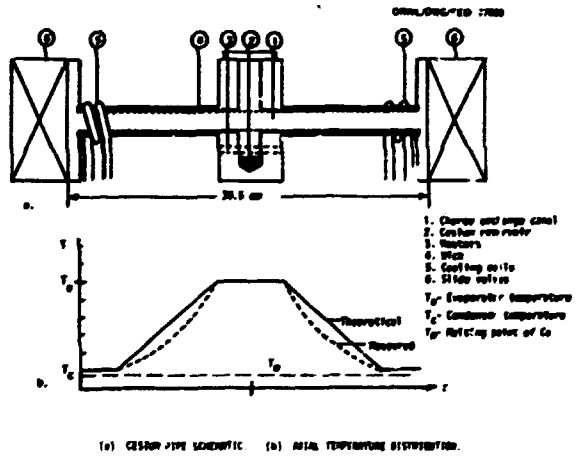

Fig. 1.15. Dependence of the net toroidal current on magnetic field errors introduced by the external loop current (I_H) for different gas filling pressures. I_v (≈20 A) is held fixed. The large current reduction for a range of field errors at low pressure suggests a change in the plasma potential profile.

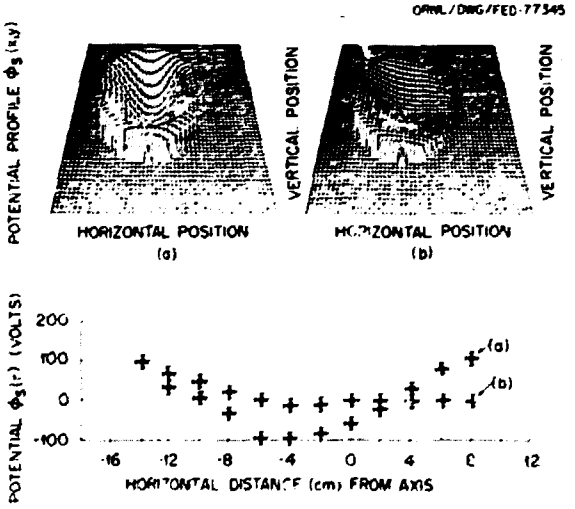

Fig. 1.16. The plasma potential profiles measured by using a rubidium ion beam probe (15 kV). Curve (a) is the horizontal scan across the minor axis; plot (a) is the two-dimensional profile generated using a spline fit to data obtained with a proper field correction on EBT. Curve (b) and plot (b) are measured without field corrections.

The effects of magnetic field errors on plasma stability and confinement in EBT are shown in Fig. 1.17. The net toroidal current, the average plasma density, the average density fluctuation amplitude, and the plasma potential measured at the center and near the annulus are plotted together with the horizontal field error as functions of the current I_H. This current is

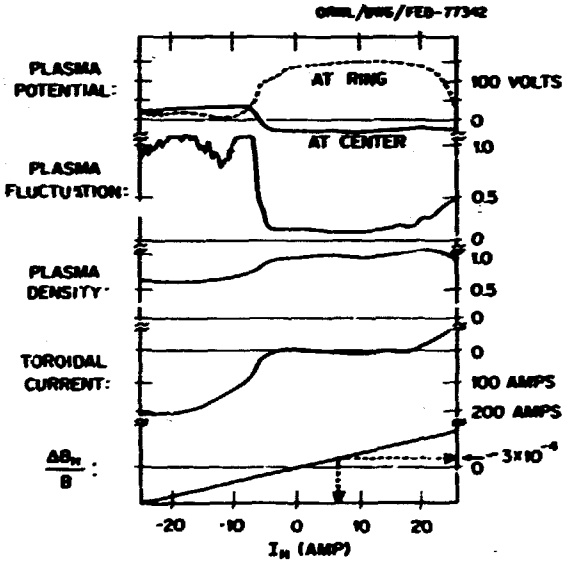

Fig. 1.17. Correlations of several parameters measured simultaneously as the horizontal field error scans in the range of $\pm 1\text{-}2 \times 10^{-3}$. The probable system global error is estimated to be 3×10^{-4}, as indicated by the arrowhead.

applied to the field correction coil and these curves show the correlation among all of these parameters, especially when the field error reaches a critical value. Taking the probable global field error as indicted by the arrow in the $\delta B_H/B$ curve, the critical field is estimated to be $(\delta B_H/B)_{cr} \cong 0.6 - 1 \times 10^{-3}$. We observe that below this field error:

(1) the plasma carries very small net toroidal current ($I_{toroidal} \leq 5$ A),
(2) the average plasma density is relatively higher (by ~30%),
(3) the plasma is free from fluctuations ($\overline{\delta n/n} \leq 2 \times 10^{-3}$, mainly at frequencies less than 20 kHz), and
(4) there is a large ambipolar field, which is consistent with the potential profile shown in Fig. 1.16(a).

Outside this range, there is a large toroidal current (up to 200 A), an enhanced fluctuation level, and a relatively small ambipolar field.

In this investigation, the use of externally generated global field errors on EBT has permitted a study of plasma sensitivity to such field error effects. Below a critical error field, the plasma behavior is predictable from a one-dimensional neoclassical theory. However, in the presence of large field errors, charged particles can leak along lines of force to the system wall. Inasmuch as the ambipolar field is self-consistently determined by particle diffusion, field errors can cause enhanced diffusion, resulting in the complete breakdown of the current-free equilibrium configuration. The observation of a large toroidal current and the simultaneous loss of the ambipolar potential might be evidence of such an effect. Enhanced plasma fluctuations can also cause anomalous particle and energy transport, thereby significantly altering steady-state plasma parameters. These results thus warrant further study in the next generation of EBT plasmas, especially where smaller collisionality is anticipated.

1.6 SPATIAL SCANS OF IMPURITY AND HYDROGEN LIGHT

N. H. Lazar H. W. Moos
K. H. Carpenter R. K. Richards
J. M. Tyson

The spectroscopic program in cooperation with Johns Hopkins University designed to determine the impurity ion distributions in EBT by spatial scanning of characteristic light emissions was continued and expanded by the addition of a second view into the plasma (Fig. 1.18). Analysis of the data was carried out using an iterative algebraic reconstruction

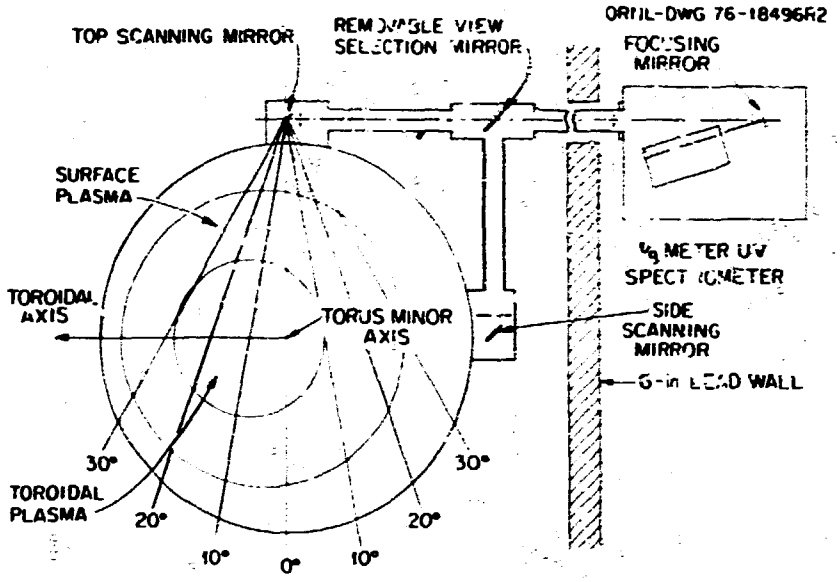

Fig. 1.18. Geometry for spatial scanning of light emissions from EBT showing the location of the two viewing directions.

technique similar to methods developed for medical tomography, which permits reconstruction of the light emission distribution even for asymmetric cases. Once again lines in the ultraviolet from H I, C II, C III, C IV, Al I, Al II, Al III, and now Al IV were observed. Using the reconstruction technique, it is now clear that some impurity ions are present in the toroidal plasma, although for all species the density is observed to be lower than that seen in the surface plasma. Further, repeated attempts to observe C V light were unsuccessful, and the best estimate of the ratio of carbon to electron density in the toroidal plasma, $n(C)/n_e < 5 \times 10^{-5}$, indicates that the surface plasma provides effective shielding against incoming impurities. The source of the impurities which are found in the toroidal plasma can be traced to the mirror throat regions, where open drift surfaces first strike the vacuum walls. The Al I distribution, viewed in the midplane between the coils, shows a near absence of neutral aluminum in the hot plasma core due to ionization by the surface plasma, but the aluminum ion species produce light which is clearly peaked in the toroidal core plasma (Fig. 1.19). Apparently, neutral aluminum produced in the mirror throats can penetrate the plasma core before being ionized, and the various aluminum ion charge states are then made visible in the midplane by electron collisional excitation. Nevertheless, the surface plasma is still an effective "divertor," apparently as a result of the combination of the moderate electron temperature and density, the short ion lifetimes previously reported, and the high positive plasma potential which must be crossed by inward diffusing impurity ions if they are to penetrate the toroidal core.

1.7 IMPURITY SPECTRAL PROFILES

J. A. Cobble

Spectral profiles of emission lines from low-Z impurity ions of the EBT plasma have been obtained using a Fabry-Perot interferometer (see Fig. 1.20). The line widths are due to the Doppler effect and for the observed ion species (He II, Al II, Al III) suggest a velocity at the half intensity points of 1.5×10^6 m/sec. Ascribing this velocity to the mass-independent $\vec{E} \times \vec{B}$ drift, one gets the relative values of fields at the source of the impurity light,

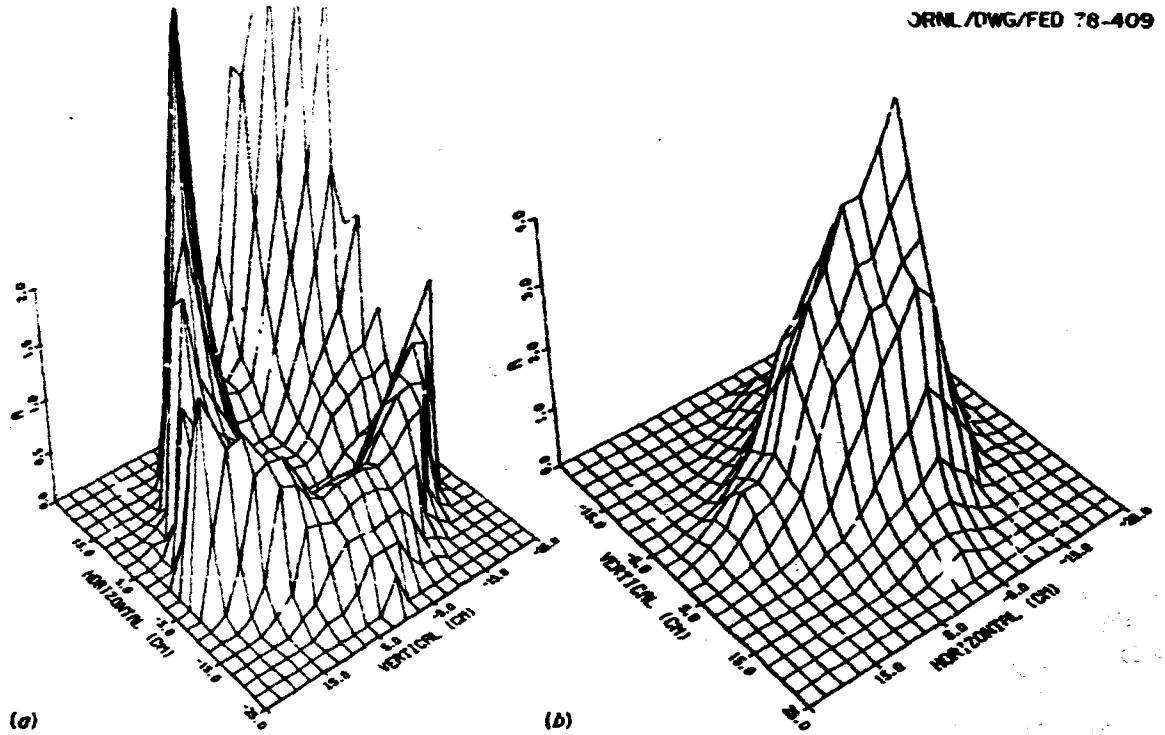

Fig. 1.19. Isometric view of reconstructed emissivity in EBT cavity midplane. Horizontal and vertical axes are indicated. Amplitude above plane A $\propto n_e n(Z_j)\langle\sigma v\rangle_{exc}$ is in arbitrary units. (a) Neutral aluminum light (λ 2151 Å); (b) singly ionized aluminum (λ 1651 Å).

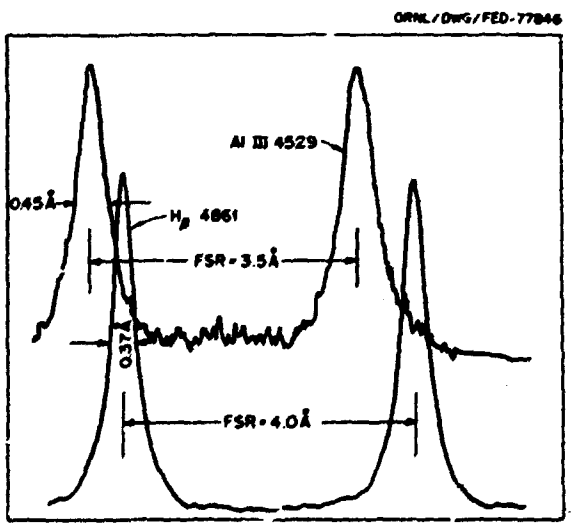

Fig. 1.20. Spectral profiles from EBT using a Fabry-Perot interferometer.

$v = E/B$. If the magnetic field is 0.2 T, then the electric field is 30 V/cm. This implies that light in the profile wings originates either in regions where the electric field exceeds 30 V/cm or, as is more likely, where the magnetic field is less than 0.2 T, i.e., on the edge of the plasma.

1.8 MICROWAVE DEVELOPMENT AND TECHNOLOGY

H. O. Eason — T. L. White
M. C. Becker — R. E. Wintenberg
M. W. McGuffin — T. Uckan

The development of super power millimeter wave sources was continued by Varian Associates, Palo Alto, California, under ORNL subcontract.

This effort has been directed toward the development of gyrotron oscillators and gyroklystron amplifiers, both of which are forms of the cyclotron resonant maser. The objective of the current phase of the program is the development of high efficiency devices having 200-kW (cw) capability at a frequency of 28 GHz. These devices are low frequency prototypes for later devices having similar power output capability at a frequency of 120 GHz.

Pulse testing was utilized through the initial phases of the device development program to simplify construction and permit separate consideration of the thermal design. The best test results have been obtained with the gyrotron oscillator, which has demonstrated peak power output of 248 kW at 28 GHz with dc-to-rf conversion efficiency of 35%. Operation at high duty cycle has yielded average power output of 20 kW with peak output >200 kW. High power, long pulse operation up to 1-msec pulse duration has been achieved. Continuous variation of 28-GHz power output over a range of 18 dB through adjustment of a single operating parameter has also been demonstrated. The first continuous wave, 28-GHz gyrotron has been constructed and initial testing is in progress.

Super power millimeter wave ECH systems development was continued with the objective of utilizing the first continuous wave, 28-GHz gyrotron in the primary ECH system for EBT-S. Specifications for the required 100-kV, dc, 10-A power supply system were developed, and this equipment was procured from an industrial source. Millimeter wave power distribution and plasma coupling structures were developed for EBT-S and installed on the facility. These structures, which also function as part of the vacuum pumping system, employ quasi-optical methods for millimeter wave power division and distribution from the single gyrotron to all of the 24 mirror confinement regions of the torus. All components for the high efficiency, multimode waveguide transmission system were developed and bench tested. These components, which include bends, directional couplers, terminations, mode filters, etc., employ a combination of waveguide and quasi-optic principles in their design. Their successful development resulted from application of both numerical and experimental methods. All other components and subsystems required for the EBT-S 200-kW (cw), 28-GHz ECH system have been developed concurrently with the gyrotron development. This system models a basic building block of much larger future systems which will utilize a number of 200-kW (cw), 120-GHz gyrotrons to achieve the multimegawatt ECH needs of large fusion devices.

1.9 EBT-II

J. C. Glowienka

An EBT reactor promises to be an extremely attractive device because of high beta, steady-state operation, good mechanical access, and modest technology requirements. Considerable impetus has been given to the program because the recently completed EBT-I experiments demonstrated proof of principle. Furthermore, EBT-S will shortly provide a more definitive test of transport scaling by the addition of 200 kW of electron cyclotron (microwave) heating at 28 GHz, made possible through straightforward technological development. During the past year, however, work was begun on a conceptual design study for the next and probably most critical step in the program sequence, EBT-II. The goal of the study was to define machine parameters that would allow experiments to fully test EBT scaling up to reactor conditions. The basic assumptions were two:

(1) electron and ion transport in EBT-II is neoclassical, and
(2) the requisite microwave and superconductor technology would become available provided sufficient lead time were allowed for development.

The resulting conceptual design for EBT-II represents a major scale-up in microwave frequency and power, magnetic field, and size, which (in terms of plasma parameters) presents

the possibility of demonstrating breakeven.

The EBT-II experiment, as proposed, will proceed in two steps. EBT-II Phase 1 will concentrate on examining the scaling made possible by the major scale-up in device parameters. For example, the higher magnetic field and microwave frequency should allow operation at higher density, and the larger aspect ratio should improve the confinement (which scales as A^2 neoclassically) by an order of magnitude over EBT-I and EBT-S. Furthermore, an additional feature built into the device in Phase 1 is the ability to increase flexibly the effective aspect ratio with supplementary toroidal aspect ratio enhancement (ARE) coils and thereby to push the test of neoclassical scaling further. The ARE coils increase A by modifying the field lines in such a way as to increase volumetric efficiency and passing particle confinement. Under optimum conditions Phase 1 may yield $\tau \sim 0.5$ sec, $T \sim 5$ keV, and $n\tau \sim 10^{13}$ sec/cm^3.

Phase 2 experiments center on the addition of 1.5 MW of neutral beam heating to heat ions as well as electrons directly and thus to provide control over the ambipolar potential. Presently, the injection geometry (i.e., number of beams, injection angle, etc.) has not been fully determined; however, with the added heat and particle sources, assuming 750 kW deposited in the plasma, one can predict neoclassically at least a factor of two increase in energy lifetime at increased plasma density. As a result, it is possible that Phase 2 could demonstrate breakeven conditions with $\tau \sim 1$ sec, $n \sim 10^{14}$, and $T \sim 5$-10 keV. Table 1.2 compares projected EBT-II parameters with those projected for EBT-S.

Table 1.2. EBT-II conceptual design study

EBT-S		EBT-II
7 kG, 14 kG	Magnetic field (midplane, mirror)	30 kG, 60 kG
12 MW	Magnetic field power	750 W (3.56 K)
1351 liters	Torus volume	2043 liters
150 cm	Major radius	480 cm
15 cm	Midplane minor radius	20 cm
8:1	Aspect ratio	21.6:1
	Continuous wave microwave power	
200 kW (cw), 28 GHz	Bulk heating	2000 kW (cw), 120 GHz
60 kW (cw), 18 GHz	Profile heating	200 kW (cw), 70-90 GHz
	Hot electron annulus – estimated parameters	
2-5 x 10^{11} cm^{-3}	n_e	1-6 x 10^{12} cm^{-3}
100-500 keV	T_e	500-2000 keV
0.1-0.4	F_A	0.1-0.5
	Toroidal plasma – estimated parameters	
		Phase 1 / Phase 2
2-6 x 10^{12} cm^{-3}	n_e	$\sim 5 \times 10^{13}$ / $\sim 10^{14}$
300 eV	T_e	3-9 keV / 5-10 keV
100 eV	T_i	3-8 keV / 5-10 keV
$\sim$0.5%	F_{max}	$\sim$1% / $\sim$10%
400 liters	Volume	1000 liters
10^{11}	$n\tau$	$\sim 10^{13}$ / $\sim 10^{14}$
	Refrigerator power	750 W @ 3.56 K

REFERENCES

1. R. A. Dandl et al., *Research Program for Plasma Confinement and Heating in ELMO Bumpy Torus Devices*, ORNL/TM-4947, p. A-12, Oak Ridge, Tennessee (June 1975).
2. F. J. Bresnock, P. L. Colestock and K. A. Connor, "Evaluation of T_e Measurement by Multiple Ionization of a Heavy Ion Beam," Bull. Am. Phys. Soc. 22(9), 1203 (1977).
3. M. Bacal, A. Truc, H. J. Doucet, F. Lemain, and M. Chrétien, Nucl. Instrum. Methods 114, 407-409 (1974).
4. M. bacal and W. Reichet, Rev. Sci. Instrum. 45, 769-772 (1974).
5. *Fusion Energy Division Annual Progress Report for Period Ending December 31, 1976*, ORNL-5275, p. 10, Oak Ridge, Tennessee (June 1977).

EXPERIMENTAL TOKAMAK

L. A. Berry, Section Head (Jan.-Nov.)
J. Sheffield, Section Head (Nov.-Dec.)
J. L. Dunlap, Assistant Section Head

T. Amano[1]
J. L. Anderson[1]
B. R. Appleton[3]
C. F. Barnett*
D. D. Bates[2]
S. C. Bates
N. A. Betz[2]
P. F. Brown
O. Burenko[6]
K. H. Burrell[7]
R. D. Burris[5]
C. E. Bush
J. D. Callen[1]
K. H. Carpenter[5]
J. Cecchi[2]
R. E. Clausing[3]
D. N. Clark
R. J. Colchin
A. Cooper[10]
V. Corso[2]
R. D. Cowan[11]
E. C. Crume, Jr.[1]
J. C. DeBoo[7]
S. M. DeCamp
N. W. Durfee[6]
G. R. Dyer
P. H. Edmonds
D. C. Eldridge*
L. C. Emerson[3]
A. C. England
E. S. Ensberg[7]
C. A. Foster[12]
R. H. Fowler[5]
J. E. Francis[1]
Y. Gomei[7]
A. D. Guttery
L. Heatherly[9]
K. W. Hill
H. C. Howe[1]
D. P. Hutchinson[4]
R. C. Isler
G. L. Jahns[7]
T. C. Jernigan
A. R. Kemp[6]
H. C. Ketterer
H. J. Kim[12]
P. W. King
R. A. Langley
C. M. Loring
D. C. Lousteau[6]
J. F. Lyon
L. A. Massengill
H. C. McCurdy
R. W. McGaffey[5]
D. H. McNeill
V. J. Meece
J. T. Mihalczo
S. L. Milora[12]
P. Minduszewski[13]
E. C. Moore
M. Murakami
W. Namkung[14]
A. Navarro[15]
R. V. Neidigh
G. H. Neilson
D. R. Overbey[1]
V. K. Paré[7]
J. W. Pearce
C. C. Queen[6]
J. A. Ray[4]
T. F. Raybourn
W. J. Redmond
J. A. Rome[1]
M. J. Saltmarsh
H. C. Sanderson
D. E. Schechter[12]
R. R. Schmidt[6]
R. J. Sentell[16]
D. J. Sigmar[1]
J. E. Simpkins
D. L. Slagle[17]
T. E. Smith[6]
P. A. Staats[4]
W. L. Stirling[12]
D. W. Swain
B. F. Thomas[18]
K. L. Vander Sluis[4]
W. T. van Rij[5]
C. C. Weaver
C. W. White[3]
R. M. Wieland[5]
J. B. Wilgen
W. R. Wing
S. P. Withrow[3]
S. K. Wong
R. E. Worsham
O. C. Yonts[1]
R. A. Zuhr[3]
B. Zurro[15]
S. J. Zweben[19]

---

*Part-time.

1. Plasma Theory Section, Fusion Energy Division.
2. Instrumentation and Controls Division.
3. Solid State Division.
4. Physics Division.
5. Computer Sciences Division.
6. UCC-ND Engineering.
7. General Atomic Company.
8. Princeton Plasma Physics Laboratory.
9. Metals and Ceramics Division.
10. University of Michigan, Ann Arbor, Michigan.
11. University of California, Los Alamos Scientific Laboratory.
12. Plasma Technology Section, Fusion Energy Division.
13. Visiting Scientist, Institut für Plasmaphysik, K.F.A., Jülich, F.R.G.
14. Postdoctoral Staff, University of Tennessee, Knoxville, Tennessee.
15. Visiting Scientist, Spanish Nuclear Energy Commission.
16. Tennecomp Systems Incorporated, Oak Ridge, Tennessee.
17. Fusion Program, Advanced Energy Systems.
18. Health and Safety Research Division.
19. UCLA, Los Angeles, California.

Abstract. The papers which comprise the first part of this section analyze neutral beam-heated plasmas produced late in 1976 in ORMAK. The scaling of average electron temperature with total power input to electrons was found to be approximately the same with or without injection. Impurity radiation during concurrent neutral beam injection and gas puffing is shown to be strongly dependent on changes in the electron temperature profile.

Tungsten radiation has been identified in the wavelength range of 40-60 Å. Concentrations are estimated to be of the order of 10^{-3} n_e.

Further studies include internal MHD mode structure, distortion in the wings of the H_α line profile, wall power loss measurements, and neutron time behavior for deuterium neutral beam injection.

The basic impurity study experiment, ISX, was completed. ISX-A began operation in the latter half of 1977 and continued into early 1978. ISX-A is a tokamak with circular cross section and relatively low toroidal field (B_T < 15 kG). Gross energy confinement times (τ_E ~ 30 msec) and toroidal betas (β_T ~ 2.2%, peak) obtained are significantly larger than those observed in other tokamaks at low B_T, and the good confinement in this device is believed to be primarily due to the absence of high-Z impurities, coupled with good feedback control of plasma position and possibly the large gap (4-6 cm) between the plasma and the wall. Inferred from conductivity, Z_{eff} steadily decreased from 3.5 to 1.7 over a two-month period of operation without gettering and approached unity with titanium gettering. In the impurity flow reversal experiment, a poloidally asymmetric source of protons substantially altered the transport of an injected neon impurity, and the changes observed are consistent with expectations based on simple neoclassical transport models.

ISX-A is to close down at the beginning of March 1978 and be replaced by ISX-B, which has a new torus and poloidal coil system which will permit a range of noncircular plasmas to be produced with ellipticity up to two.

The neutral beam injection systems originally intended for ORMAK upgrade will become the injectors for ISX-B. In addition, ISX-B will have a versatile PF system which will allow the generation and control of circular, elliptical, or D-shaped plasmas, and provision will be made for bundle divertor, ripple injection, and ECRH experiments. A new mass-energy neutral particle analyzer and a soft x-ray energy spectrometer for ISX-B are described.

Design parameters are described for the LPTT.

2.1 INTRODUCTION

During the past year, significant advances were made in our understanding of tokamak-produced plasmas. In this section we further analyze the plasma produced by the ORMAK machine in the 1976 period, then describe the basic ISX machine with an initial analysis of the ISX-A experiments, and finally look at ISX-B and the next step, LPTT.

Our presentation of plasma analyses is in seven general categories of interest: (1) enhanced confinement and extension of basic plasma parameters in ORMAK, Sect. 2.1.3; (2) plasma behavior as depicted by MHD mode studies, toroidal rotation, and neutron flux. Sects. 2.1.4, 2.1.5, 2.1.7, 2.2.9; (3) description, operation, and plasma properties of ISX-A, Sects. 2.2.1, 2.2.2; (4) increased understanding of the role of plasma impurities, Sects. 2.1.1, 2.1.2, 2.1.6, 2.2.3; (5) wall surface and limiter material effects, Sect. 2.2.5; (6) plasma impurity flow, Sect. 2.2.4; and (7) refinement of data collection techniques, Sects. 2.1.5, 2.2.6, 2.2.7, 2.2.8, 2.2.10.

2.1.1 Impurity Behavior During Concurrent Neutral Beam Injection and Gas Puffing

R. C. Isler H. C. Howe
E. C. Crume, Jr. M. Murakami

In an attempt to achieve maximum electron concentrations during neutral beam injection, hydrogen was puffed into a 175-kA, 26-kG plasma

while the injectors were operating. Radiation from the impurity lines exhibited rather distinctive behavior during the influx of the hydrogen, and extensive efforts were made to interpret these results.

The evolution of the radiation from several spectral lines is shown in Figs. 2.1 and 2.2. The low ionization stages of oxygen exhibit little or no apparent change when the injectors are turned on. Although the O VII, O VIII, and the Fe XVI do demonstrate an increase beginning near the time of injection, the same features are also present in the noninjection experiments and seem not to result from the action of the beams. However, the addition of the gas puff produces rather dramatic changes in the signals. Several lines from the low stages of ionization rapidly increase until the puff is turned off and then begin to relax back into a steady state in which the emission is much greater than it was before the gas puff. For lines which demonstrate this behavior it is obvious that the lower the ionization stage the larger is the relative rise in amplitude, in contrast to the results from gas puff experiments on the Pulsator device.[1] Therefore, we do not conclude that recombination which would proceed successively from the higher to the lower stages of ionization plays a significant role here.

Results similar to those for the 1032-Å line of O VI are often interpreted as indicating an influx of impurities. However, if changes of radiation are construed as arising only from changes of the impurity influx, then all the lines of a given ionization stage should behave in exactly the same manner. But it is clear from Fig. 2.1 that although the 1032-Å line of O VI rises by a factor of four during the gas puff, the O VI line at 150 Å appears to remain almost constant; thus, factors other than impurity concentrations must be considered.

Again in contrast to the strong lines of the low ionization stages, the resonance transitions of O VII and O VIII appear to decrease

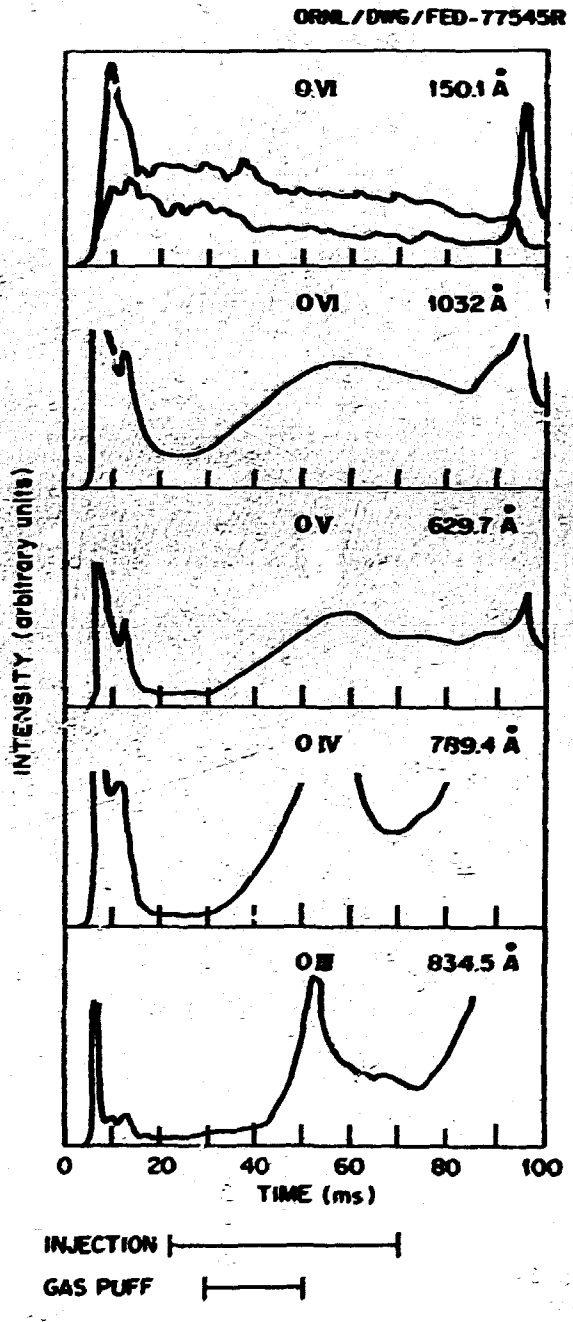

Fig. 2.1. Spectral emissions from low ionization stages of oxygen during 350-kW neutral beam injection into a 175-kA plasma when accompanied by a hydrogen gas puff. The lower trace in the 150.1-Å data is nearby background; actual line intensity is the difference of the two signals. Traces begin 4 msec before breakdown.

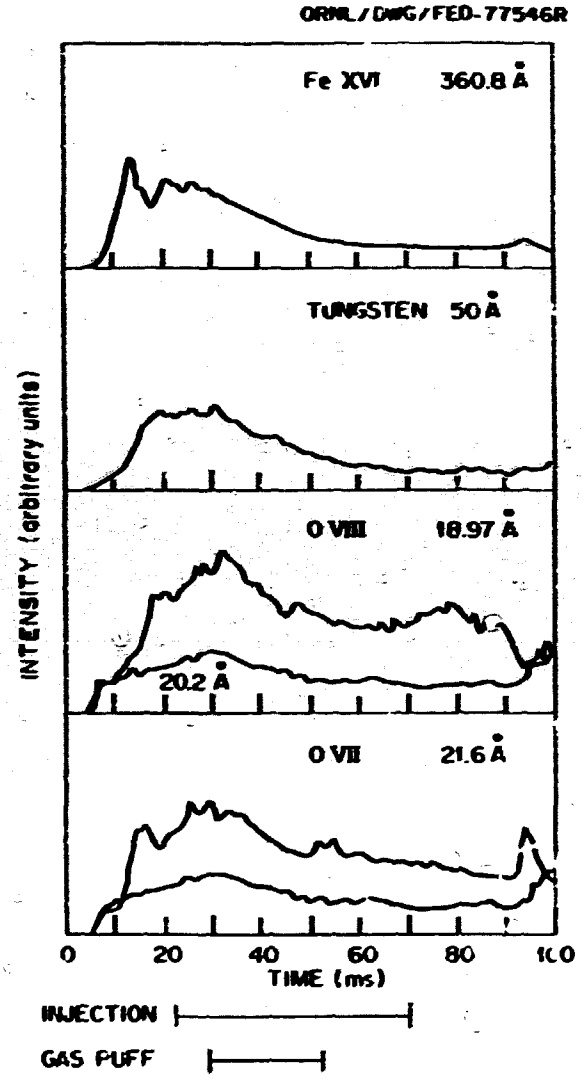

Fig. 2.2. Spectral emissions from O VII, O VIII, tungsten, and iron during 350-kW neutral beam injection into a 175-kA plasma when accompanied by a hydrogen gas puff. The lower traces in the O VII and O VIII data are nearby background. Traces begin 4 msec before breakdown.

due to the addition of hydrogen. In order to reconcile these observations with the idea that the low ionization stages indicate an increased influx of oxygen, it would be necessary to conclude that such an influx did not reach the interior of the plasma but recirculated only within the periphery. Such conclusions appear unwarranted to us for explaining the present data without first investigating the effects caused by variations of the electron temperature and concentration profiles during injection and gas puffing. Profiles of the electron temperatures and concentrations are shown in Figs. 2.3 and 2.4 for times immediately before, during, and immediately after the gas puff. As expected, the electron concentration increases at all locations within the plasma due to the added hydrogen. The temperature profile appears to remain about the same at the intermediate radii but increases at the center so that the slightly "hollow" profile becomes peaked. It is, however, most significant for the interpretation of the spectroscopic data to notice that the temperature gradients at outer radii appear to decrease as a result of the gas puff.

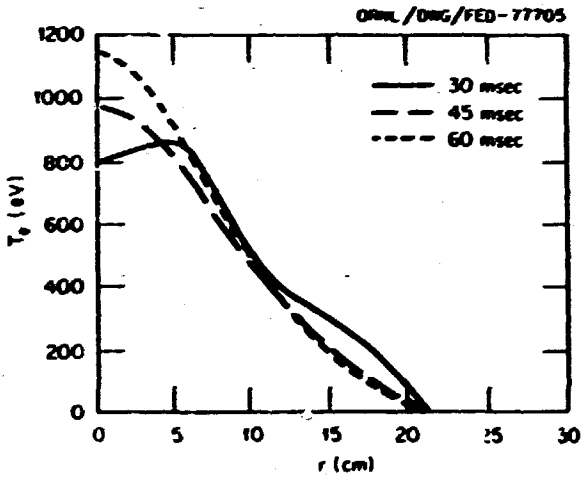

Fig. 2.3. Electron temperature profiles when neutral beam injection is accompanied by a hydrogen gas puff between 30 and 55 msec.

In order to assess whether profile effects alone could be responsible for the behavior of the oxygen lines, we have solved the coupled rate equations (which include transport as well as ionization and recombination for the ions). These equations can be written as:

$$\left.\begin{aligned}
\frac{dn_0}{dt} &= -S_0 n_0 n_e + \alpha_1 n_1 n_e - \frac{1}{r}\frac{d(rn_0 v_0)}{dr} , \\
\frac{dn_1}{dt} &= S_0 n_0 n_e - S_1 n_1 n_e - \alpha_1 n_1 n_e \\
&\quad + \alpha_2 n_2 n_e - \frac{1}{r}\frac{d(rn_1 v_1)}{dr} , \\
&\vdots \\
\frac{dn_{z'}}{dt} &= S_{z'-1} n_{z'-1} n_e - \alpha_{z'} n_{z'} n_e \\
&\quad - \frac{1}{r}\frac{d(rn_{z'} v_{z'})}{dr} .
\end{aligned}\right\} \quad (2.1.1)$$

The concentration of an ion in a given charge state is denoted by n_z, and z' is the charge of a fully stripped ion; S and α are ionization and recombination coefficients; and the transport terms are written simply as the radial gradients of the fluxes, $n_z v_z$, for each ion species.

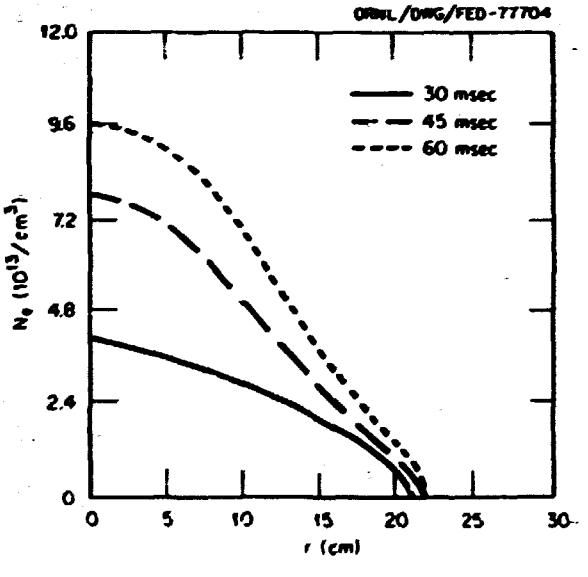

Fig. 2.4. Electron concentration profiles when neutral beam injection is accompanied by a hydrogen gas puff between 30 and 55 msec.

In general the transport velocity, v_z, is a function of r and an additional set of equations is necessary in order to determine the n's and v's. If the ion diffusion can be described by the Pfirsch-Schlüter regime, then $v_z(r)$ depends on the gradients of concentrations of all ions present at the position r, and the solution of a large number of coupled equations is required to obtain the ion concentrations. Such a procedure is obviously quite complex and has only recently been accomplished.

Because our present goal is to obtain a fast numerical code which will provide semi-quantitative insight into the impurity behavior, we have not attempted to compute the transport velocities from first principles. Instead we find steady-state numerical solutions for oxygen by specifying inward radial velocities for neutral particles from the wall and inward ion velocities consistent with neoclassical transport theory for v_1 at the edge of the plasma. The particles are then assumed to diffuse inward, to turn around at some point near the center of the plasma, and to recycle completely back to the edge. By keeping the magnitudes of rnv equal at all points (for both the influx and efflux) and specifying the distribution of the total oxygen content, the v's are determined at all radii in the plasma. Distributions of oxygen which are independent of r or which are proportional to n_e have been investigated. Most of the calculations have employed ionization coefficients equal to one-half the values obtained by Lotz[2] for O I-O VI and equal to the full values specified by him for O VII and O VIII. Recombination rates as tabulated by Mattioli[3] are used.

Analytic expressions for the electron temperatures and concentrations are assumed for the computations

$$T_e = T_{e1}\left[1 - \left(\frac{r^2}{a^2}\right)^m\right]^n + T_{e2} , \quad (2.1.2)$$

$$n_e = n_{e1}\left[1-\left(\frac{r^2}{a^2}\right)^m\right]^n + n_{e2}\ , \qquad (2.1.3)$$

where T_{e1} and n_{e2} are the values of the electron temperature and density at the limiter radius, a; $T_{e1} + T_{e2}$ and $n_{e1} + n_{e2}$ are the values at $r = 0$; and the quantities m and n are integers chosen to allow us to investigate the effects of various temperature profiles on the relative intensities of the oxygen lines.

Although Eqs. (2.1.1) have been solved for a wide variety of profiles, neutral particle velocities, ion velocities, rate coefficients, etc., it is not useful to present all of these results. Instead, we limit ourselves to a discussion of those parameters which appear to be most important for analyzing the experimental results discussed here. The effects of changing electron concentrations and temperature profiles.

We compare the intensities of several lines for a fixed temperature profile and two different electron concentrations. The original concentrations are taken as $n_e(0) = 3 \times 10^{13}/cm^3$ and $n_e(a) = 3 \times 10^{12}/cm^3$; these values are then doubled, and the relative line intensities are computed as shown in Table 2.1. As expected, changes in the line intensities may occur from operations which add electrons to the plasma even though the flux of a particular impurity species remains constant. However, these changes should not be linear with n_e.

Of even greater significance than the electron density in affecting the intensity of lines from low ionization stages is the temperature profile near the edges of the plasma. The results of changing the temperature profiles while holding all other parameters constant are illustrated in Figs. 2.5 and 2.6 for two values of the ion transport velocity at the edge of the plasma, 10^2 and 10^3 cm/sec. The intensities for (m, n) parameters of (1, 2) and (1, 4) are compared to those calculated for parameters of (1, 1). The higher the value of n, the smaller are the temperatures and the gradients toward the edge of the plasma. It is shown that the intensities of the lower stages of oxygen are very strongly dependent on the temperature profiles on the outside, and any alteration of these profiles by injection or gas puffing can cause significant changes of radiated intensities even though the total oxygen flux and density are not altered. Such changes tend to be more pronounced at low transport velocities. The lines from the higher ionization stages, O VII and O VIII, are much less influenced by profile changes than are the lines from the lower stages.

Table 2.1. Calculated increase of multiplet emission rates, I'/I, if $n_e(0)$ and $n_e(a)$ are changed from $3 \times 10^{13}/cm^3$ and $0.3 \times 10^{13}/cm^3$ to $6 \times 10^{13}/cm^3$ and $0.6 \times 10^{13}/cm^3$. Other plasma parameters are $T_e(0) = 1000$ eV, $T_e(a) = 10$ eV, (m, n) = (1, 2), $v_t(a) = 10^2$cm/sec, $v_0 = 55$ cm/sec, n(oxygen) = $1.9 \times 10^{11}/cm^3$

Species	Mean wavelength (A)	I'/I
O II	833.8	1.65
O III	834.5	2.03
O IV	789.4	1.94
O V	629.7	1.73
O VI	1033.8	1.72
O VI	150.1	1.41
O VII	21.6	1.39
O VIII	19.0	1.55

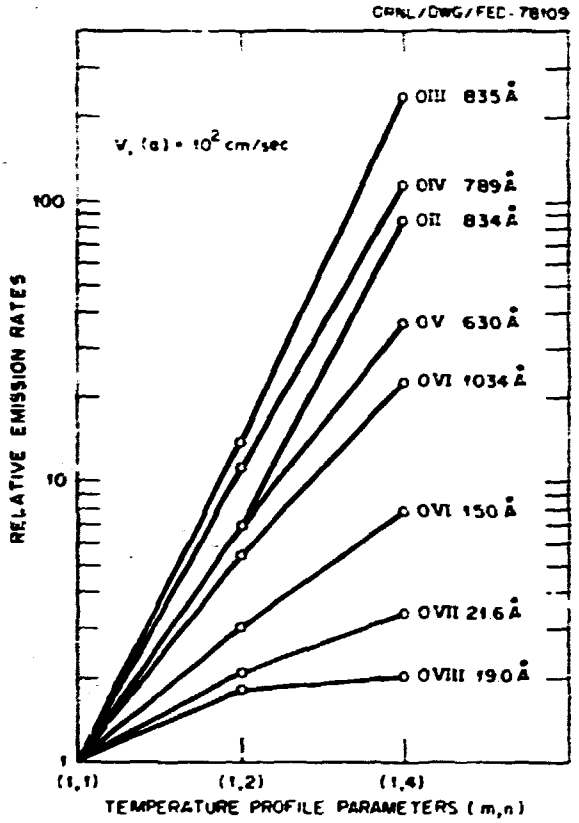

Fig. 2.5. Relative emission rates for oxygen lines as a function of electron temperature profiles. Velocity of neutral oxygen is 55 x 10^3 cm/sec; inward velocity of ions at wall, $v_i(a)$, is 10^2 cm/sec.

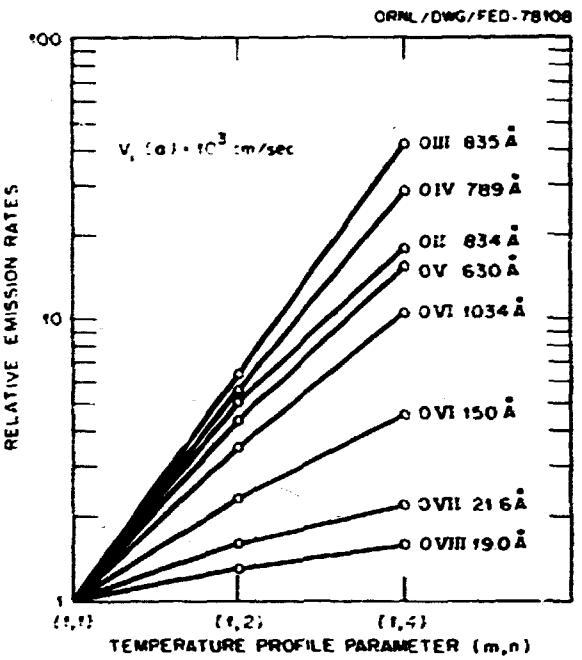

Fig. 2.6. Relative emission rates for oxygen lines as a function of electron temperature profiles. Velocity of neutral oxygen is 55 x 10^3 cm/sec; inward velocity of ions at wall, $v_i(a)$, is 10^3 cm/sec.

We believe that the spectroscopic results are readily understood by considering Table 2.1 and Figs. 2.5 and 2.6 together with the variations of T_e and n_e shown in Figs. 2.3 and 2.4. Although the laser-produced results for T_e and n_e are less reliable in the outer regions of the plasma than they are in the interior, there is a clear indication that the gas puff reduces the magnitude of the temperature gradient near the limiter. In view of the results illustrated by Figs. 2.5 and 2.6, we should expect that the evolution of the temperature profile alone would generate larger changes of radiation from the lower stages of ionization. In addition, the observation that the intensity of the 1032 Å of O VI increases much more than the intensity of the 150-Å line is consistent with the calculations.

The narrowing of the temperature profile and the rise of the electron concentration should result in higher intensities from all the lines of oxygen after the addition of the gas puff if the oxygen distribution is unchanged. The fact that the signals from the O VII and O VIII lines actually decrease is indicative of a smaller concentration of oxygen after the gas puff despite the fact that the peripheral ions radiate more strongly. The change of temperature is relatively minor at radii less than 13 cm (where the O VII and O VIII radiation is most intense), so variations of the lines are controlled more strongly by variations of the electron and ion concentrations than by other factors. Between 30 and 60 msec the profile of the electron concentration increases almost uniformly by a factor of 2.5, so we estimate from Table 2.1 that the oxygen concentration has fallen by a factor of 0.3 to 0.4. This conclusion is supported by analyses which show that $\langle Z_{eff} \rangle$ (as measured from the resistivity)

changes from 6.3 to 2.5 in this period. Such an analysis implies that the oxygen concentration is 0.7 of its initial value after taking the dilution into account. In view of the experimental uncertainties and the *ad hoc* nature of the theoretical calculations, better agreement between the two results cannot be expected. It is obvious from the present analysis that inferring the transport of light ions solely from radiation of the lower ionization stages can be very uncertain.

The tungsten emission around 50 Å is only weakly dependent upon T_e, and it arises from ions which should have relatively large dielectronic recombination rates. This radiation most strongly reflects the actual concentration of ions in the plasma and should be little influenced by transport effects. Therefore, Fig. 2.2 indicates that the tungsten concentration is also significantly lowered by the introduction of the gas puff, perhaps by as much as a factor of 7 or 8. Similar conclusions can be drawn for iron, but with the realization that radiation from this element is often highly variable as a function of the type of discharge and of time into the discharge, so that some caution must be exercised in relating its behavior to the influence of the gas puff.

2.1.2 Tungsten Radiation from Tokamak-Produced Plasmas

R. C. Isler R. V. Neidigh
R. D. Cowan

Recent theoretical calculations using an average ion model indicate that radiative losses due to high-Z impurities in tokamaks may be more severe than previously believed.[4] These computations imply that a concentration of tungsten as small as 5×10^{-4} of the electron concentration can prevent the achievement of break-even conditions. It is important, therefore, to the concepts of large machines now being designed (such as TFTR) to determine the fraction of heavy elements which actually get into the plasmas produced by presently operating machines and to assess independently the validity of the calculations which have employed the average ion model. Until now it has not been possible to perform such evaluations for heavy elements because just establishing the presence of the ionized stages has been hindered by a basic lack of knowledge of their spectra.

Tungsten radiation from ORMAK has been identified by comparing experimental results (Fig. 2.7) with calculated spectra (Fig. 2.8) for ions having open 4d subshells.[5] The concentrations of tungsten are estimated from computed oscillator strengths to be of the order of $10^{-3}\ n_e$.

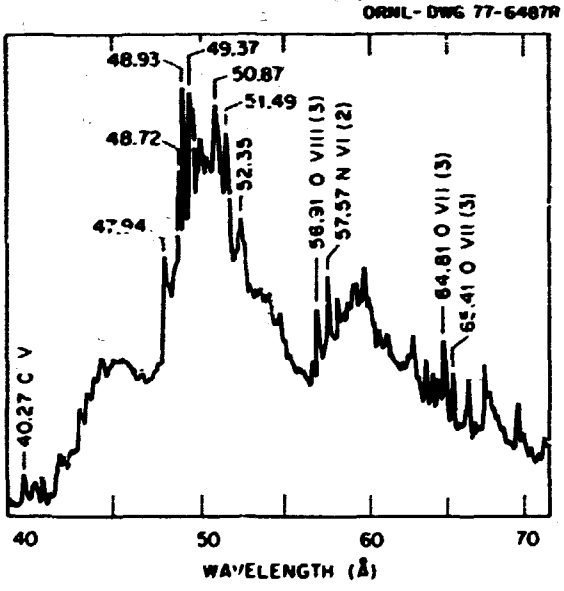

Fig. 2.7. Typical ORMAK-produced spectrum between 40 and 70 Å. Numbers in parentheses denote spectral order.

2.1.3 Electron Heating by Neutral Beam Injection in the Oak Ridge Tokamak[6]

L. A. Berry R. C. Isler
C. E. Bush P. W. King
J. L. Dunlap J. F. Lyon
G. R. Dyer D. H. McNeill
P. H. Edmonds M. Murakami

Substantial electron heating by energetic neutral beam injection has been observed in ORMAK plasmas. Impurity radiation is enhanced

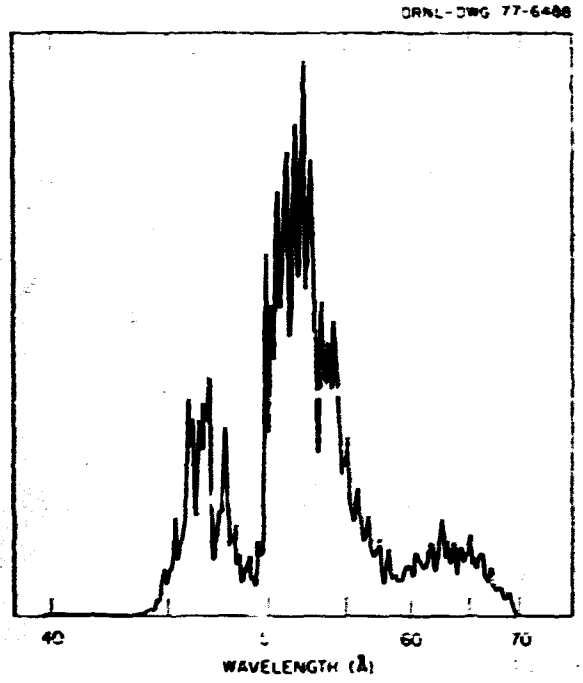

Fig. 2.8. Calculated spectrum for $\Delta n = 0$ transitions of W XXXI-W XXXV relative concentrations of 0.1, 0.2, 0.4, 0.2, 0.1. Each line is represented by a Gaussian curve with full width at half maximum of 0.15 eV and area proportional to the weighted oscillator strength gf. The computer spectrum of W XXXII alone is qualitatively similar.

by injection but only to the degree expected for ohmically heated discharges with the same total power input to electrons, and the electron heat conduction loss is comparable with that in ohmically heated plasmas. The scaling of average electron temperature with total power input to electrons is approximately the same with or without injection.

2.1.4 Internal Mode Structures in ORMAK

R. D. Burris J. L. Dunlap
V. K. Paré

Introduction

We have continued to study MHD modes in ORMAK, using the detector and analysis systems described earlier.[7] Briefly, we use:

(1) 12 $\tilde{B}_\theta$ loops in a poloidal array (to determine the poloidal mode number m of current perturbations $\tilde{I}$),
(2) 8 $\tilde{B}_\theta$ loops in a toroidal array (to determine the toroidal mode number n of $\tilde{I}$),
(3) 13 soft x-ray detectors in 2 arrays (to determine the m number of the x-ray perturbations $\tilde{X}$),
(4) analog recording of signals on magnetic tape, and
(5) digitization followed by Fourier transform analysis in 4-msec time blocks.

Uncoupled modes

The typical behavior of ohmically heated discharges in ORMAK is that modes with different m values are coupled with identical perturbation frequencies observed by all detectors and with the outward-going radius a line of phase reinforcement for the different modes.[7] Here we describe the one discharge recognized as an exception to this behavior. It was 70 msec in duration with $I_p = 119$ kA, $B_T = 13.4$ kG, $q(a) = 5$, and $n_e(0) \approx 1 \times 10^{13}$ cm^{-3}. It was obtained near the end of ORMAK's operation, after prolonged hydrogen discharge cleaning that yielded $Z_{eff} \approx 3$-4 (significantly lower than the typical values of 6-10). This discharge was not profiled with the Thomson scattering diagnostic, so the possibility cannot be excluded that it may have been hollow.

Figure 2.9 indicates the unique feature of the discharge. The sweep expansion captures an interval in which the $\tilde{B}_\theta$ signal is dominated by a higher frequency than that of $\tilde{X}$. Figure 2.10 gives the time history of the two frequency branches. Where there is only one branch indicated, the $\tilde{B}_\theta$ and x-ray systems detect the same dominant frequency.

The $\tilde{I}$ modes from 8 msec on were all $n = 1$, including both branches during the two-frequency interval. The m number progression prior to the two-frequency interval was 5, 4, 3; after the two-frequency interval, $m = 2$. During the interval, the Fourier transform analysis system

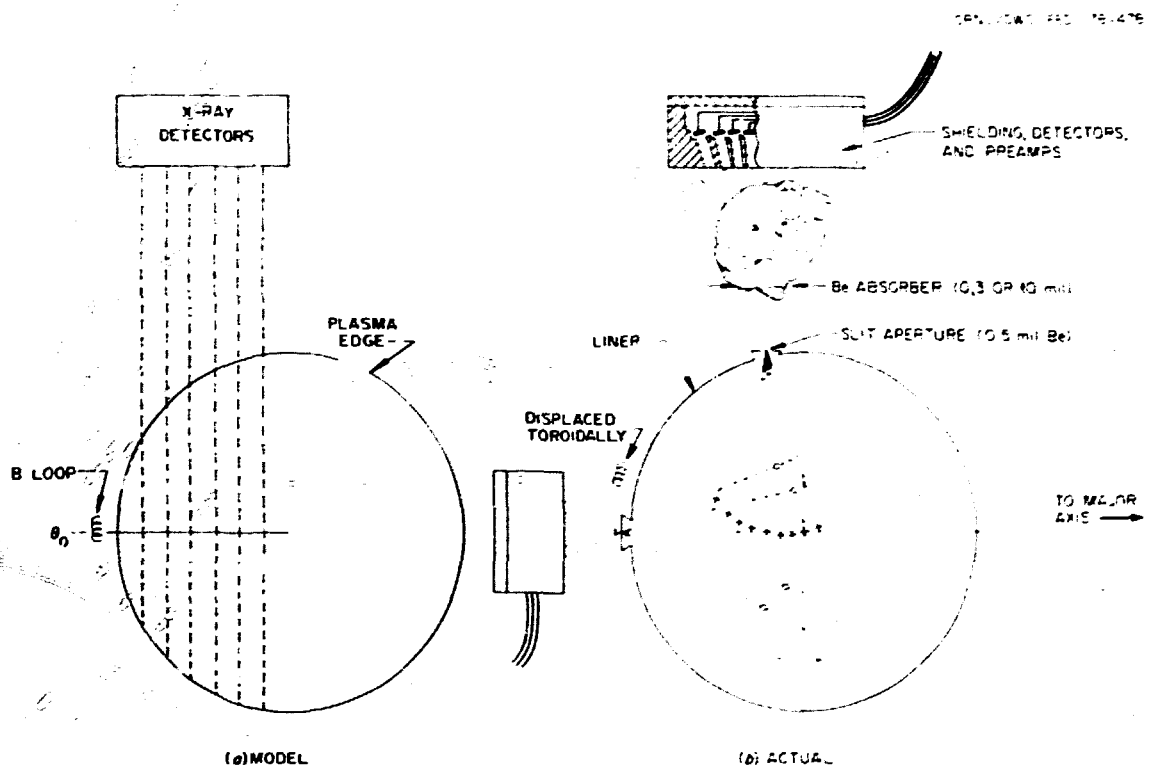

Fig. 2.12. X-ray detector systems.

r/a = 0.25, 0.35, and 0.43. At 54 and 66 msec, an m = 2 was defined at each of these locations; at 78 msec it was m = 2 at r/a = 0.25 but indeterminate at the others.

In ORMAK the question of the m = 2 mode structure outside the critical surface could be addressed only during rundown, since during the constant I_p interval the singular surface was near the limit of the plasma region monitored by the diode arrays. In PLT the detector arrays examine a more extensive region, and there the phase line changes with radius in a similar fashion during the normal portion of the discharge.[8]

Analysis of distorted magnetic perturbation structures

In ORMAK, ohmically heated discharges with $q(a) \lesssim 4$ at densities near the upper limit yielded high amplitude distorted waveforms for the $\tilde{B}_\theta$ and $\tilde{X}$ signals. The associated mode is of particular interest because severe distortion of this nature characterizes one approach of the plasma toward disruption.[3] That the basic structure is an m = 2 was recognized early, but a detailed description that included the distortions was lacking. With multichannel analog tape recording followed by digital Fourier analysis, we have been able to obtain the information required to develop some details of the mode structure in time and space. As described below, the $\tilde{B}_\theta$ distortion patterns ir lve second harmonic content with significantly asymmetric poloidal and toroidal phase progressions.

Figure 2.14 shows oscilloscope photos of the signals from magnetic loops and soft x-ray detecto. for one of a series of virtually identical shots which we have analyzed. These were at 120 kA with 12.8 kG, yielding q(a) = 3.5. The waveforms are distorted throughout most of

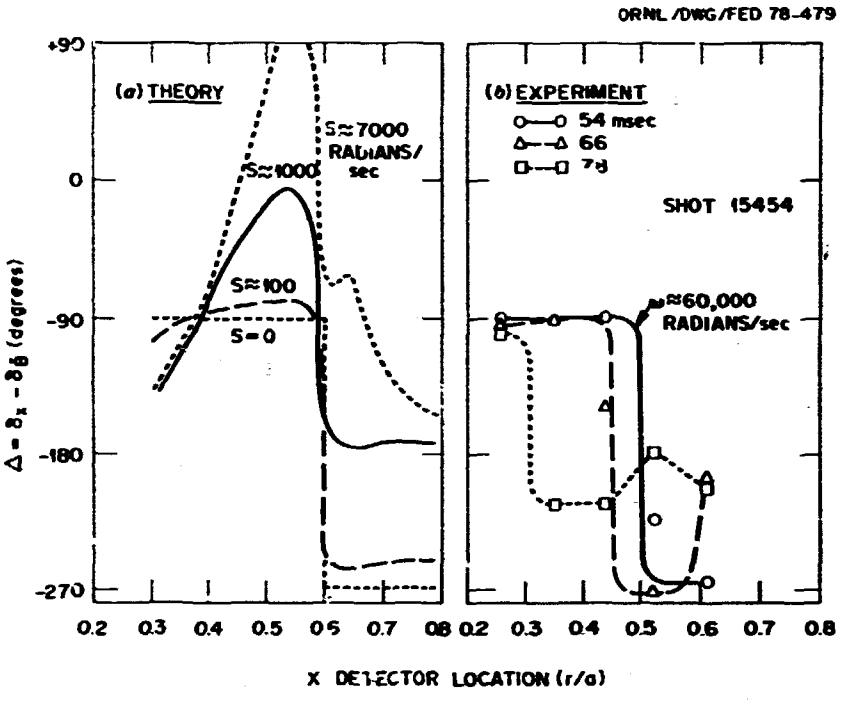

Fig. 2.3. Signal phase differences – theory and experiment.

the period of strong MHD activity. For the period 28-32 msec, Figs. 2.15 and 2.16 show the phases of the fundamental and second harmonic components of the magnetic loop signals as functions of poloidal and toroidal angle. The fundamental is clearly m = 2, n = 1 with relatively smooth phase variation except near θ = 0 (at the inside of the torus). The second harmonic phase is much less smooth; it is clearly m = 4, but if its phase follows the dashed line on Fig. 2.16, it is n = 1 and its overall helicity – as well as its local helicity – differs from that of the fundamental.

The second harmonic phase characteristic shown in Fig. 2.16 persisted through most (20-36 msec) of the period of strong MHD activity. In the two time segments at the end of the strong activity it made a transition to a nearly linear n = 2 characteristic. The amplitude of the second harmonic was very small in the region of the phase anomaly (φ = 45-90°); thus the phase plotted at φ = 45° in Fig. 2.16 may not be valid. It is in fact inconsistent with phases measured in the poloidal array nearby, at φ = 58°. It is possible, therefore, that the phase line actually falls an additional 360° between φ = 100° and φ = 0, yielding n = 2 with severe toroidal asymmetry.

No explanation has been found for the toroidal asymmetry of the second harmonic. The principal structural sources of asymmetry in ORMAK were the limiter and the outside vertical core leg, both of which were located at φ = 334°, some distance from the phase anomaly.

2.1.5 Hot Ion Distribution in ORMAK

R. V. Neidigh D. J. Sigmar

A distortion of the Maxwellian ion-energy distribution function in tokamak-produced plasmas may be revealed in the spectral line radiation. We have reported[10] experimental evidence that (1) a change in the value of Z_{eff}, (2) delayed gas injection, (3) neutral beam injection, and (4) liner cleaning procedures alter the profile

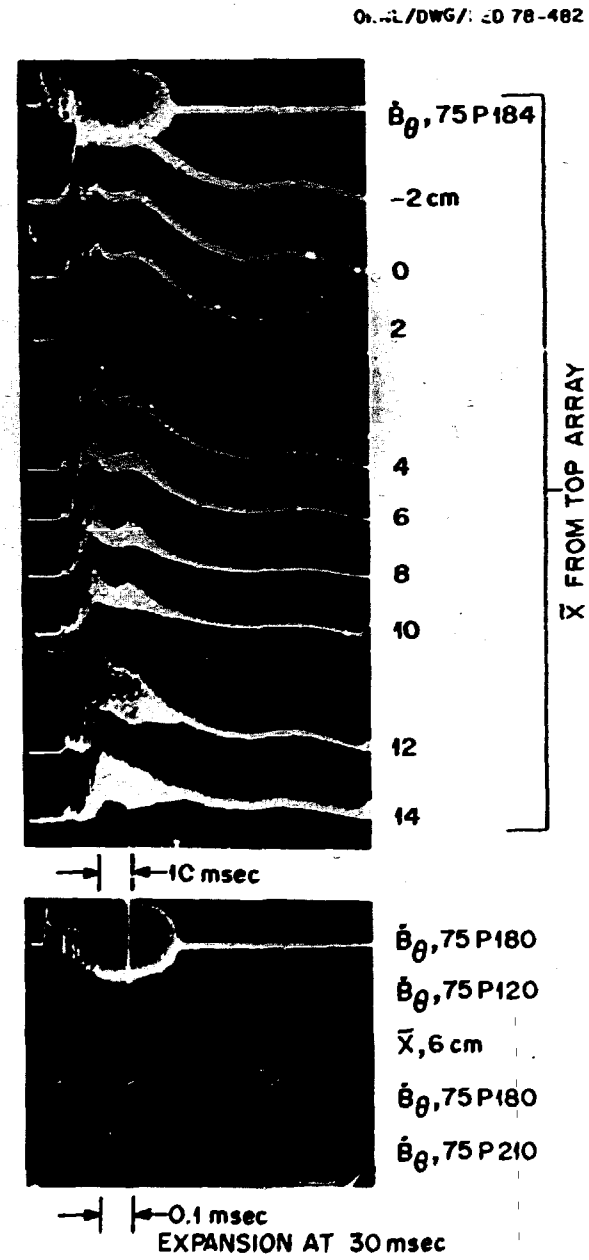

Fig. 2.14. Oscilloscope traces of soft x-ray and magnetic loop signals with high amplitude distorted waveforms, shot 15801.

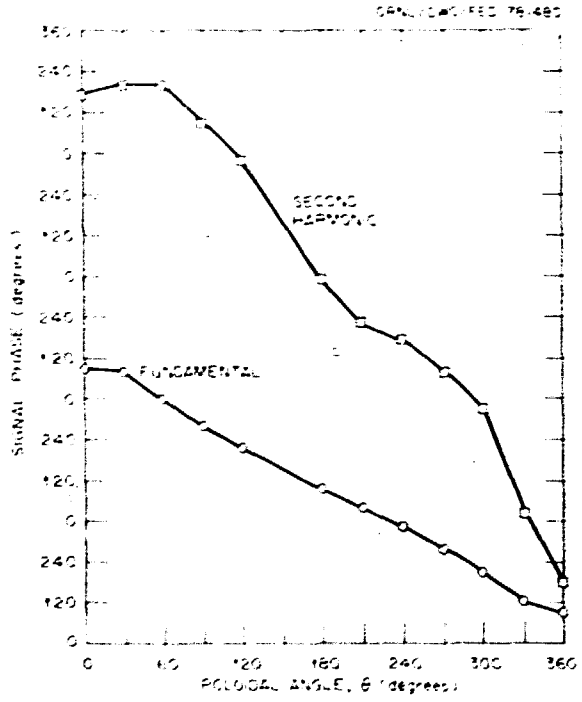

Fig. 2.15. Electrical phase vs mechanical angle for the poloidal magnctic loop array.

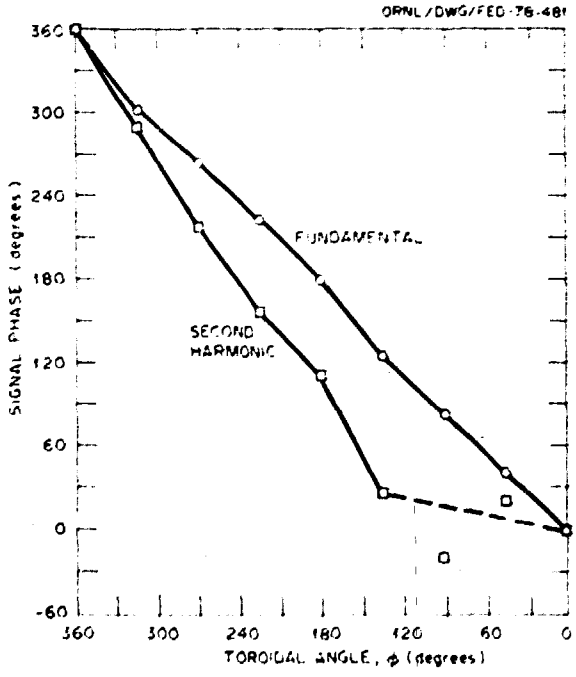

Fig. 2.16. Electrical phase vs mechanical angle for the toroidal magnetic loop array.

of the Balmer-α (6563-Å) line of hydrogen. The distortion is analyzed in terms of an effective toroidal drift velocity, ion-temperature relation.

It has been observed that tokamak plasmas execute poloidal rotation early and late and toroidal rotation during the constant current portion of the ohmic heating cycle.[10,11] Early theories of poloidal rotation were given by Stringer[12] and toroidal rotation by Rosenbluth et al.[13] The theories were later reviewed by Hinton and Hazeltine.[14] Recently, Hirshman[15] has determined the poloidal and toroidal ion flow velocities in all collisionality regimes from a fluid theory point of view. The observed toroidal rotational velocity of the plasma was theoretically shown by Sigmar[10] et al. to be related to the existence of trapped particles.

A discussion of the effective toroidal drift velocity ($v_{\parallel i}$), ion-temperature (T_i) relation, and the plasma parameters which affect $dv_{\parallel i}/dT_i$ is to be published[16] and is summarized in this report. We conclude that: (1) there is sufficient charge exchange neutral hydrogen radiation (through the energy range up to ten times thermal) from the ORMAK-produced plasma to measurably raise the intensity in the wings of the H_α line profile above the noise; (2) drift velocities up to 10^7 cm sec^{-1} show a consistent relationship to Z_{eff}, neutral injection, and ion temperature; (3) in an experiment with reduced ohmic heating power so that it was exceeded by injection power, toroidal rotation appears to be largely that induced by the neutral beams (see Fig. 2.17); and (4) the spatial distribution of toroidal velocity from $v_{\parallel i}(T_i)$ and $T_i(r)$ indicates a steep velocity gradient at the plasma boundary (see Fig. 2.17) due to ripple viscosity or some presently unknown factor.

2.1.6 Wall Power Measurements of Impurity Radiation in ORMAK[17]

C. E. Bush J. F. Lyon

Time- and space-resolved measurements of the power loss to the liner of ORMAK indicate that a large fraction (~60%) of the electron power input is lost to the wall rather than to the limiter. This fraction is relatively constant over a wide range of input powers (ohmic heating plus neutral beam injection) and plasma conditions and for most of the discharge duration. Most of this energy loss is due to impurity radiation from an emission profile having a mean radius about a third that of the limiter radius and is time-correlated with gross plasma fluctuations, internal disruptions, and

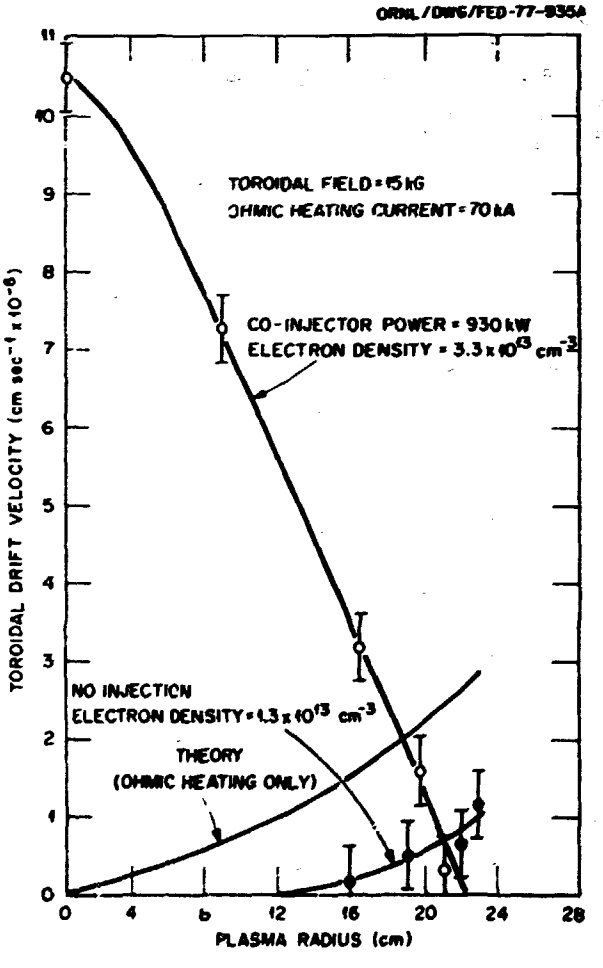

Fig. 2.17. $V_{\parallel i}(r)$ from $T_i(r)$ and $V_{\parallel i}(T_i)$. Error bars indicate scatter in drift velocity measurements for cases of no-injection and injection power > OH power. The charge exchange data are best fit by the ion-temperature profiles: $T_i(r) = 180\ [1 - (r/a)^2]^{0.6}$ for the no-injection shots, and $T_i(r) = 513\ [1 - (r/a)^2]^{1.16}$ eV for the injection shots.

related spectroscopic impurity signals. In gas puffing experiments resulting in higher densities, the ratio of radiative power to the electron density continually falls as density increases during the course of the discharge.

See Table 2.2 for comparison of ISX-A with ORMAK.

Table 2.2. Comparisons of ORMAK with ISX-A

	ORMAK	ISX-A
Minor radius	23 cm	26 cm
Limiter material	Tungsten	Stainless steel
Longest τ_E with OH alone	10 msec	30 msec
Radiation loss normalized to OH power		
Radiometer	50-80%	25-40%
Spectroscopy	38.7%	11.8%
Hydrogen		3.6%
Carbon	0.2%	2.3%
Oxygen	16.8%	5.5%
Iron	0.3%	0.5%
Tungsten	21.4%	

2.1.7 Neutron Time Behavior for Deuterium Neutral Beam Injection into a Hydrogen Plasma in ORMAK[18]

A. C. England J. T. Milhalczo
H. C. Howe R. H. Fowler

Neutrons were produced by D-D interactions when a 28-keV deuterium beam was coinjected into a hydrogen plasma in ORMAK. Fokker-Planck calculations, which correctly predict the time behavior of the neutron rate after beam turnon, show that the majority of the neutrons are from injected particles interacting with previously injected deuterons that have scattered to pitch angles of ~60-90° while slowing down.

2.2 ISX-A MACHINE AND EXPERIMENTS

2.2.1 ISX-A Introduction and Summary

ISX was designed to be a flexible research tokamak with good experimental access. The capability to be rapidly changed to meet varying experimental configurations was a prime design goal. The success of this design philosophy has been demonstrated, both with the rapidity with which significant results have been obtained and the ease with which major modifications are being made as the physics goals of ISX change. The initial goals of ISX were to study the evolution, transport, and control of impurities in thermonuclear-relevant plasmas. The results from ISX demonstrate the dramatic improvements in plasma quality brought about by impurity control. The impurity flow reversal experiment, an attempt to reverse the expected inward neoclassical flow of impurities, has produced results consistent with the theory. Successful tests of hydrogen pellet fueling have also been demonstrated on ISX.

During 1977, the primary goals of ISX were redirected from impurities to high beta tokamak experiments. Modification to ISX will begin early in 1978 to produce noncircular, high beta, neutral beam injected plasmas. All of these areas will be discussed in detail in subsequent sections.

Machine description

ISX is a moderate-size, shell-less tokamak with an iron core. There are eighteen TF coils which are demountable as in Doublet II so that the vacuum vessel and poloidal coil system can be replaced. In the initial configuration, the major radius is 92 cm, the minor radius is 26 cm, and the toroidal field on axis is 18.7 kG. The initial vacuum vessel is all welded stainless

steel with bellows sections to provide a net resistance of 7 mΩ. Movable carbon and molybdenum are also used. The vacuum vessel averages ~6 cm larger than the limiter radius.

Machine operation

Initial construction of ISX-A was completed in February 1977 and the first demonstration plasma was obtained on February 26, 1977. Regular discharge cleaning began on August 1, 1977, and safety clearance for full tokamak operation was given by ERDA on August 16, 1977, when shakedown operations were initiated. The first tokamak shot with plasma of short duration (cap bank only) occurred on August 26, 1977 (shot #106). During this period and up to the first week in October all fields were demand-driven (i.e., no feedback). This phase of operation was used to establish operating parameters and bring diagnostics on-line. Stress analysis of the various coil systems and an analysis of the effect of an iron core on the torus fields were also performed during this time to aid engineering support personnel in future design. During early October the vertical field and radial field feedback systems were brought on-line, followed by a week of downtime when stronger support chocks were installed on the TF coil system. By early November (~700 shots), the machine was operating reliably and serious plasma physics experiments were begun.

In cooperation with General Atomic Company, impurity flow reversal apparatus (limiters, gas puff valves, and titanium ball gettering systems) were installed during the second week of November. From then until March 5, 1978, approximately 5000 plasma shots were taken. The distribution of operating time among the major studies was: confinement ~30%, impurity flow reversal ~50%, surface physics ~10%. Aside from a few minor vacuum accidents there were only two incidents that caused unscheduled downtimes: a 110-v extension chord with a metal outlet box was left too close to the machine and was pulled into the TF coil system causing arcover, and spontaneous flashover occurred on a back-bias winding due to faulty insulation.

Plasma properties of ISX

With its relatively low toroidal field, ISX has produced exceptional plasma parameters. The toroidal magnetic field has varied from 8 to 15 kG. Plasma current has ranged from 60 to 160 kA. With discharge cleaning alone Z_{eff} was brought below 2. With the addition of titanium gettering in the vacuum vessel, Z_{eff} was reduced to 1. Line average densities varied from 5×10^{12} to 7×10^{13} cm^{-3}. Energy confinement times reached 30 msec, far above previously used scaling factors. Beta at the center of the discharge reached 2.2% – a value reached by only two other tokamaks, the noncircular Doublet II at General Atomic Company and the neutral beam-heated ORMAK at ORNL.

2.2.2 Confinement Studies in ISX-A

D. D. Bates, S. C. Bates, K. H. Burrell, C. E. Bush, R. J. Colchin, J. C. DeBoo, S. M. DeCamp, J. L. Dunlap, G. R. Dyer, P. H. Edmonds, A. C. England, E. S. Ensberg, K. W. Hill, R. C. Isler, T. C. Jernigan, H. E. Ketterer, P. W. King, R. A. Langley, J. F. Lyon, J. T. Mihalczo, D. H. McNeill, M. Murakami, W. Namkung, A. Navarro, R. V. Neidigh, G. H. Neilson, D. R. Overbey, V. K. Paré, J. W. Pearce, T. F. Rayburn, W. J. Redmond, J. E. Simpkins, R. M. Wieland, J. B. Wilgen, W. R. Wing, B. Zurro

Introduction

The confinement studies in ISX-A confirmed the damaging role of high-Z impurities[19] in the plasma. The initial machine configuration presented only stainless steel to the plasma edge, so heavy metals (tungsten and molybdenum) were excluded. The first stage of the studies developed optimum confinement parameters for these conditions without gettering, and the studies were then extended to include titanium gettering. Finally, the plasma was deliberately contaminated with heavy metal so that its effect could be observed.

This section gives a preliminary description of the confinement studies in ISX-A. After noting characteristics of typical discharges, we describe scalings of energy confinement times (τ_E) and toroidal betas (β_T), which are significantly higher than those obtained in other tokamaks of similar scale in size and field. We then discuss the results of deliberately introducing tungsten into the discharge and conclude that the good confinement in ISX-A is primarily due to the absence of heavy metal impurities.

Characteristics of typical discharges

Time histories of the plasma current (I), loop voltage (U), and line-average electron density ($\bar{n}_e$) for a typical discharge in ISX-A are shown in Fig. 2.18(a). Results of various diagnostic measurements in the same discharge are shown in the subsequent figures; evolutions of central ion temperature from charge exchange analysis [Fig. 2.18(b)], Mirnov oscillations and a PIN diode signal along a central chord [Fig. 2.18(c)], a pyroelectric detector signal (see Sect. 2.2.3, Fig. 2.24), and electron temperature [$T_e(r)$] and density [$n_e(r)$] profiles from Thomson scattering at 140 msec into the discharge (Fig. 2.19). Table 2.3 lists plasma parameters at 140 msec for this discharge (column 4) along with those for other discharges as well as maximum (or minimum) parameters attained during the entire ISX-A operational period.

The line-average electron density decreased with a time constant of 10 to 20 msec in the absence of gas puffing during the discharge due to the small recycling rate inherent to clean walls. Titanium gettering, required for the impurity flow reversal experiment, further reduced the recycling rate. Therefore, gas puffing was essential in the ISX-A discharges.

There was a clear correlation between density behavior and MHD fluctuations. Higher densities resulted from puffing into discharges with low level Mirnov oscillations and clear internal disruptions [such as shown in Fig. 2.18(c)], as opposed to discharges with high level oscillations and no (or very weak) internal disruptions.

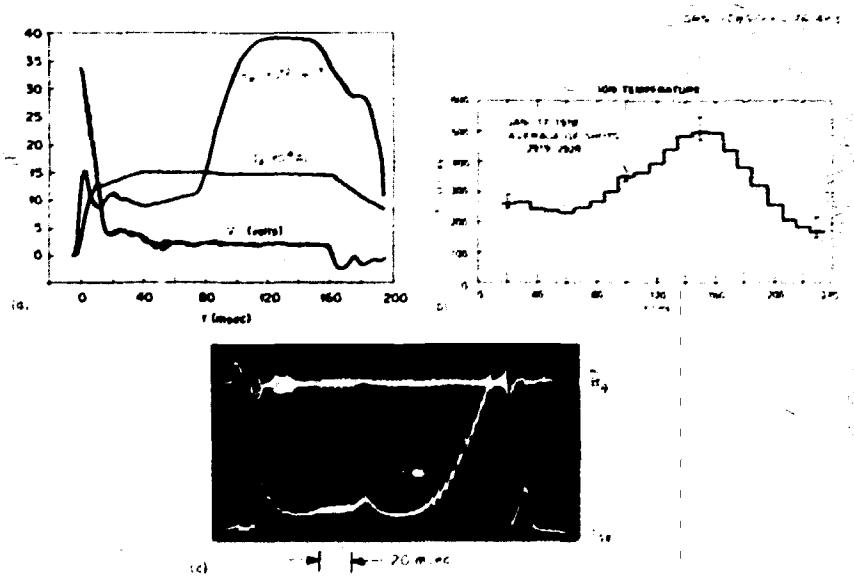

Fig. 2.18. Time histories of plasma parameters in a typical ISX-A discharge: (a) plasma current, I, loop voltage, U, and line-average electron density, $\bar{n}_e$; (b) central ion temperature, $T_i(0)$, from charge exchange analysis; (c) Mirnov oscillations, $\tilde{B}_\theta$, and a PIN diode signal along a central chord.

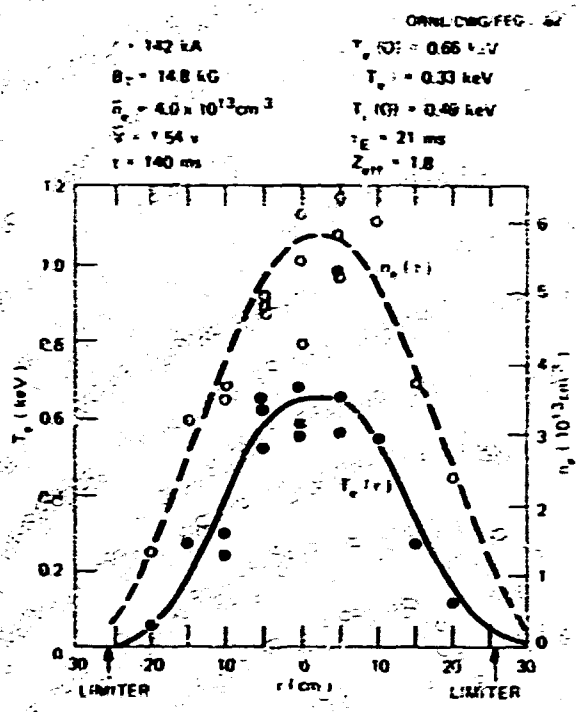

Fig. 2.19. Radial distributions of electron temperature and density from Thomson scattering at 140 msec into the discharge shown in Fig. 2.18.

Furthermore, a moderate gas puffing frequently converted the MHD signature to that favorable for strong gas puffing. Such a technique was used to obtain higher densities, as shown in Fig. 2.18(e). The maximum line-average density allowed without disruption was 7 x 10^{13} cm^{-3} at 13 kG, which is about 4.5 times higher than that resulting from the B_T/R_0 scaling.[20]

Scalings of confinement parameters

Parametric dependences of plasma parameters have been studied by systematically changing discharge conditions, and confinement parameters (τ_E, β_T, etc.) obtained are compared with various empirical scaling laws.

In view of the strong dependence of τ_E on $\bar{n}_e$ observed in ORMAK and other tokamaks, scalings of plasma parameters with density ("$\bar{n}_e$ scan") have been studied in greater detail. Figure 2.20(a,b) shows results of the "$\bar{n}_e$ scan" with deuterium plasmas. An important feature of this scan is the fact that the Z_{eff} value is constant

Table 2.3. Plasma parameters of typical discharges and maximum (or minimum) parameters obtained during the entire period of ISX-A operation

Case	1	2	3	4	Max (min)
B_T, kG	8.1	12.3	12.8	14.8	14.8
I_p, kA	92	131	120	142	175
$q(a_s)$	3.2	3.5	4	3.8	2.5 (min)
$\bar{n}_e$, 10^{13} cm^{-3}	2.4	3.9	3.3	3.7	7
$n_e(0)$, 10^{13} cm^{-3}	3.7	6.1	6.5	5.8	9
$\langle n_e \rangle$, 10^{13} cm^{-3}	1.7	2.8	2.1	2.8	4.5
V, V	1.4	1.7	1.1	1.5	0.9 (min)
$T_e(0)$, keV	0.49	0.94	0.64	0.66	1.5
$\langle T_e \rangle$, keV	0.33	0.46	0.38	0.33	0.5
$T_i(0)$, keV	0.31[a]	0.48[b]	0.38[a]	0.49[a]	0.55[a]
$\langle \beta_p \rangle$	0.61	0.62	0.55	0.56	0.76
$\langle \beta_T \rangle$, %	0.53	0.52	0.28	0.35	0.52
$\beta_T(0)$, %	1.7	2.2	1.6	1.2	2.2
τ_E, msec	13	22	27	21	27
Z_{eff}	3.5	3.2	1.6	1.8	1 (min)
Gas	H_2	H_2	D_2	H_2	H_2, D_2

[a] From charge exchange analysis, uncorrected.

[b] Estimated from the Artsimovich scaling.

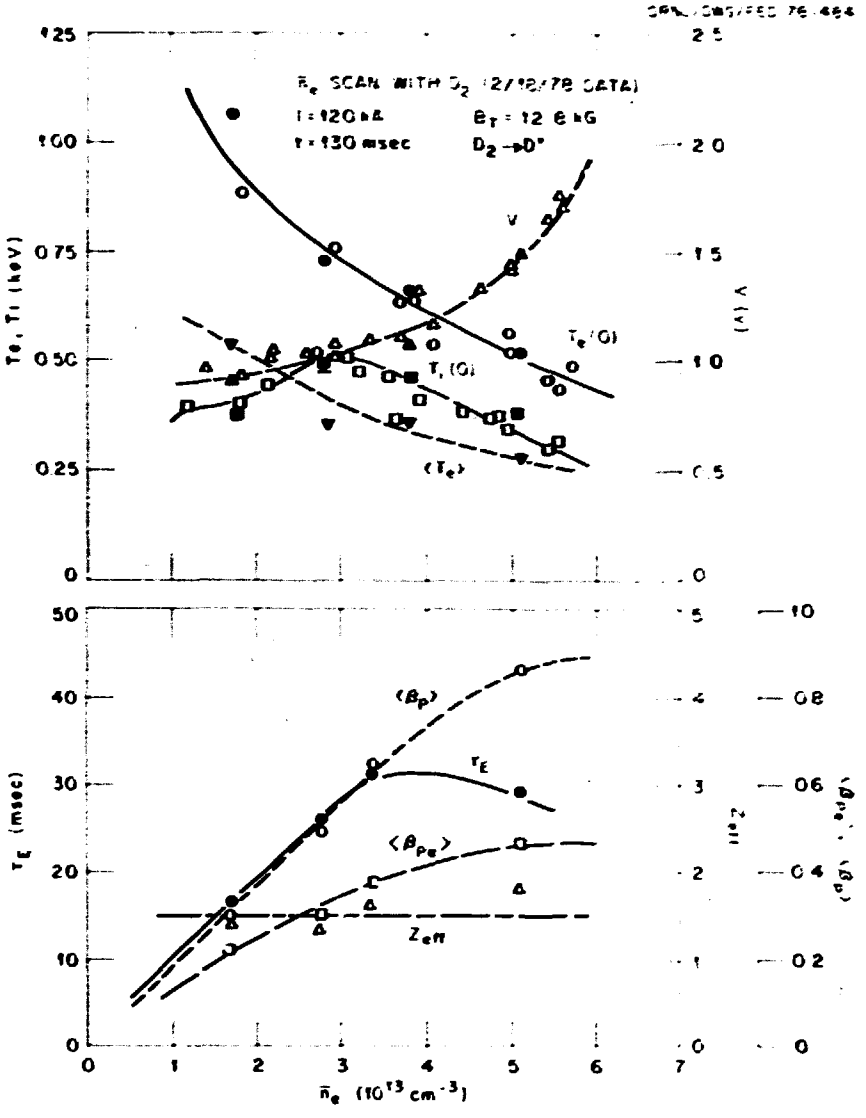

Fig. 2.20. Results of the "$\bar{n}_e$ scan" with deuterium plasmas: (a) scalings of loop voltage, the central and particle-average electron temperatures, and central ion temperatures (from charge exchange and neutron analyses) with the line-average density; (b) variations of volume-average total ($\langle \beta_p \rangle$) and electron ($\langle \beta_{pe} \rangle$) poloidal betas, gross energy confinement time (τ_E) and effective charge (Z_{eff}).

and low (≈1.5) over the density range studied. This behavior sharply contrasts with the normally observed reduction of Z_{eff} with $\bar{n}_e$. Both $T_e(0)$ and $\langle T_e \rangle$ fall with rising $\bar{n}_e$, resulting in an increase in loop voltage with $\bar{n}_e$, as expected from the constant Z_{eff}. The central ion temperature (both from charge exchange analysis and absolute neutron flux measurements) increases with $\bar{n}_e$ at low densities, as expected from the Artsimovich scaling. However, it tends to decline in the high density range. Therefore, both electron and total energy contents (or equivalently $\langle \beta_{pe} \rangle$ and $\langle \beta_p \rangle$) tend to saturate in the high density range. As a result, τ_E increases approximately linearly

with $\bar{n}_e$ at low densities, but the increase tends to saturate at higher densities. Transport calculations (done by H. C. Howe, Plasma Theory Section) suggest that this may be explained in terms of increased electron-ion coupling and neoclassical ion heat conduction at high densities. Empirical confinement scaling ($\tau_E \propto \bar{n}_e a^2$) is therefore limited by neoclassical ion heat losses (for which $\tau_E \propto \bar{n}_e^{-1}$), and this limit is encountered at low density (relative to Alcator, for example) due to the low fields and currents (resulting in relatively poor ion confinement) of ISX-A. The trend of τ_E with $\bar{n}_e$ is confirmed by larger numbers of data points for both hydrogen and deuterium discharges, as shown in Fig. 2.21, which also shows that τ_E values for D_2 are higher than those for H_2.

Values of τ_E obtained in ISX-A compare favorably with various empirical scaling laws. Values of τ_E are higher by a factor of 1.5 (average) than those predicted by the Alcator scaling ($\tau_E = 3.2 \times 10^{-16} \bar{n}_e a^2 \sqrt{q_a}$; sec, cm^{-3}, cm) (Ref. 21), and higher by a factor of 3.5 (average) than the Hugill-Sheffield scaling ($\tau_E = 2.7 \langle n_e \rangle^{0.41} a_L^{1.57} B_T^{0.66} A_I^{0.65}$; msec, 10^{13} cm^{-3}, m, kG) (Ref. 22), indicating that confinement is significantly better than in some tokamaks operated at low B_T.

The good confinement at low B_T has led to β_T values which are among the highest achieved in ohmically heated tokamak plasmas. The highest $\beta_T(0)$ value obtained in ISX-A (2.2% at 12 kG) is comparable with the highest published value (Doublet II, 2.1% at 8 kG; Ref. 23). Values of β_T were observed to increase with both current (as shown in Fig. 2.22) and density, indicating that β_T rises with ohmic heating power.

Impurities and their effects

As demonstrated above, ISX-A has achieved unusually large values of τ_E and β_T for tokamaks operated at low B_T. The good confinement appears to result from an unusually low level of high-Z contaminants.

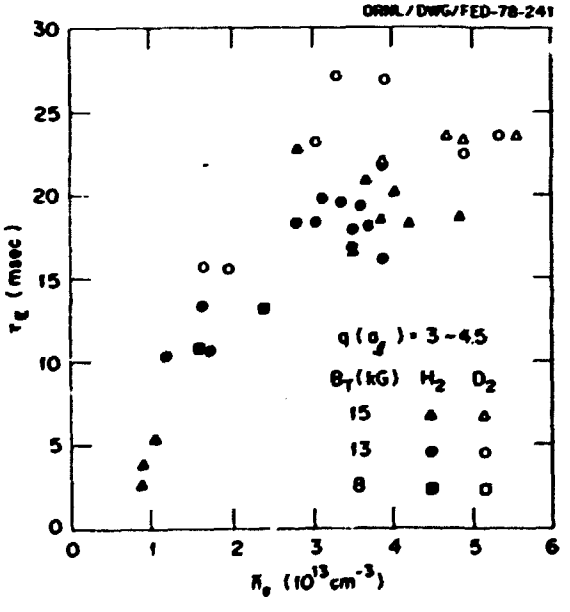

Fig. 2.21. Gross energy confinement time (τ_E) as a function of line-average electron density for various hydrogen (open points) and deuterium (closed points) discharges.

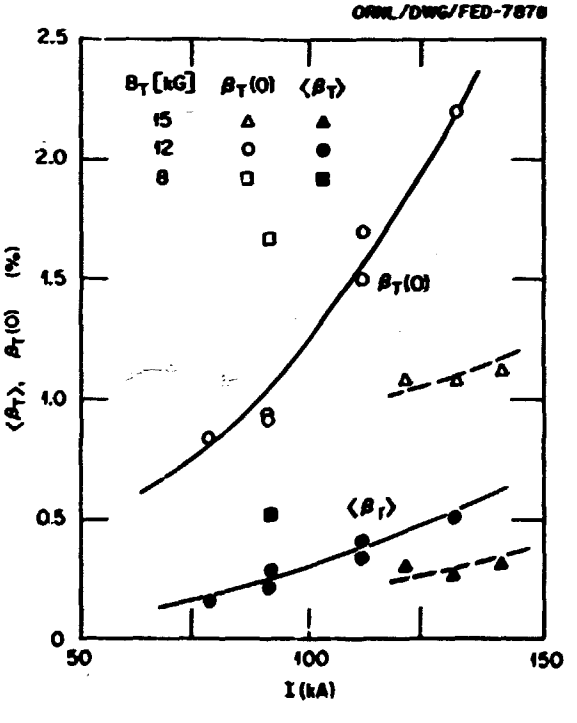

Fig. 2.22. Variations of toroidal betas with discharge current for three different values of toroidal field. The central betas [$\beta_T(0)$] are shown by open points and the volume-average betas ($\langle\beta_T\rangle$) by closed points.

Inferred from conductivity, Z_{eff} steadily decreased from 3.5 to 1.7 over a two-month period of operation without gettering and approached unity with titanium gettering. The trend of Z_{eff} correlated well with the residual gas analysis and the surface physics analysis of samples exposed to tokamak discharges (as discussed in Sect. 2.2.5). Spectroscopic measurements in the vuv range show that carbon, oxygen, and nitrogen accounted almost totally for the Z_{eff} values. Radiation from iron (off limiters and walls) was low (<1% of the OH power). Approximately one-third of the OH power was transported to the wall, as discussed in Sect. 2.2.3. This fraction is about half that observed in ORMAK, where a tungsten limiter was used.

Effects of heavy metal impurities in plasmas were simulated by injecting a short (<0.2-msec) burst (<0.1% of the total number of electrons) of tungsten into an established discharge using Q-switched laser irradiation on a thin film.[24] Figure 2.23(a) shows time histories of I, V, and $\bar{n}_e$ with and without tungsten injection. The injection produced an increase (≈15%) in loop voltage and a small density rise, and led to disruptive instability. Figure 2.23(b) illustrates the evolution of a wall power signal and the central electron temperature with and without injection. The energy flux to the wall increased by a factor of two, and the increase mainly originated from the central core (as discussed in Sect. 2.2.3). At the same time $T_e(0)$ decreased by ≈40%, resulting in a hollow T_e profile as shown in Fig. 2.23(c). The decrease in τ_E was 20-30%. No such gross effects were observed with aluminum injection used in conjunction with the impurity flow reversal experiment.

These were the only hollow profiles ever observed in ISX-A, other than mild, transient ones upon strong gas puffing. Had a heavy metal limiter been used instead of stainless steel, the hollow profiles would likely have been more common, as suggested by results from ORMAK, PLT, and DITE operating with heavy metal limiters.

The above observations suggest that the good confinement observed in ISX-A results from a low level of radiation loss. In this context the most important feature of the experiment was the use of stainless steel limiters rather than tungsten or molybdenum. Good feedback control of plasma position and possibly the large gap (6-cm average) between plasma and wall also contributed.

2.2.3 Measurements of Energy Flux to the Walls in ISX-A

C. E. Bush H. C. Sanderson

Time- and space-resolved measurements of the energy flux to the walls of ISX-A were made using pyroelectric detectors similar to those used on ORMAK. Two uncollimated detectors were used to monitor the total power loss to the walls and to obtain most of the energy flux data on ISX-A. A limited amount of spatially resolved energy flux data was obtained using an array of six detectors. This array consisted of well collimated detectors, each viewing the plasma along chords at different radii of the minor cross section. All detectors including the array were located in two adjacent torus sectors, both at least 160° from the limiter section.

The radiometer monitors indicated that <20 to 50%, and in general ~30%, of the input ohmic heating power was lost to the walls. The losses were probably detected by the radiometers as a combination of photons due to impurity radiation and as fast neutral particles resulting from charge exchange. The observed fractional power loss to the ISX-A wall was half the ~60% (ranging from 40 to ~80%) observed on ORMAK. On ORMAK there was extremely close time correlation between the radiometer signals and the intensities (from vuv spectroscopy) of impurity radiation in the 20- to 100-A portion of the radiated spectra. This was felt to be due to contamination of the ORMAK plasma mainly by tungsten from the tungsten limiter, but with additional contributions due to oxygen and gold. In ISX-A, where high-Z impurities were excluded, little correlation between individual vuv impurity line intensities and radiometer signals was observed and none persisted throughout the discharge. The best correlation

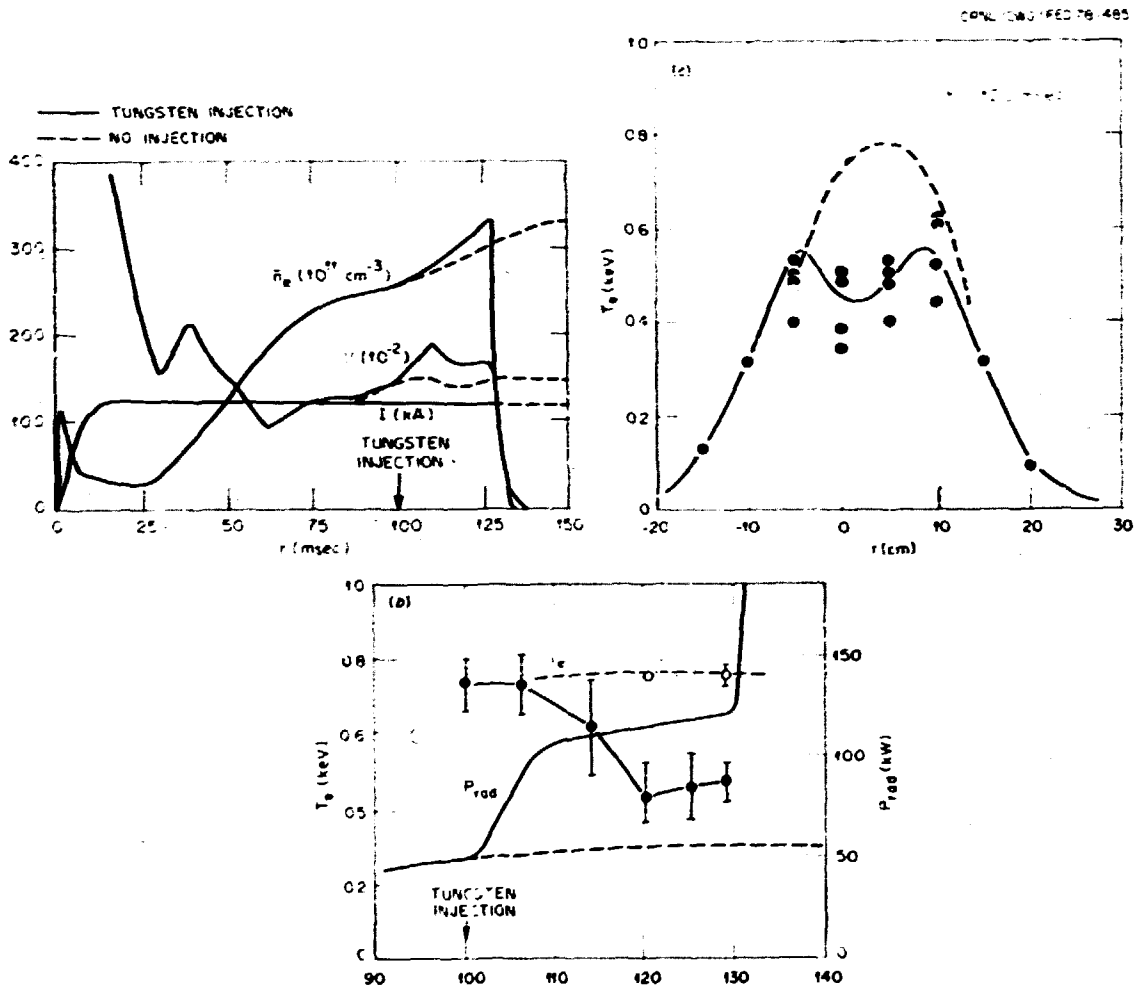

Fig. 2.23. Comparisons between discharge characteristics with and without tungsten injection. Continuous curves and closed points correspond to the discharge with tungsten injection, broken curves and open points to the discharge without it: (a) time histories of I, V, and $\bar{n}_e$; (b) evolutions of wall-energy flux from a pyroelectric radiometer and the central electron temperature; and (c) radial distributions of the electron temperature with and without tungsten injection.

for many discharges (but not necessarily the majority) was with the H_α monitor, which viewed along a chord through the outer half of the plasma column; in this case there was one-to-one relative correspondence throughout the discharge. On the other hand, for another large group of discharges there were correlations between radiometer signals and several impurity lines and charge exchange flux data, but during different time segments. The implication for those discharges was that the losses to the walls resulted from a combination of radiation from various low-Z impurities and charge exchange losses, each having varying degrees of importance at different times during the discharge.

The radiometer signal for a discharge in which a double gas puff was used to obtain a relatively high density is shown in Fig. 2.24 along with other discharge parameters. In general, with gas puffing the signal increased with increasing density during the discharge but not as rapidly as the density during the early

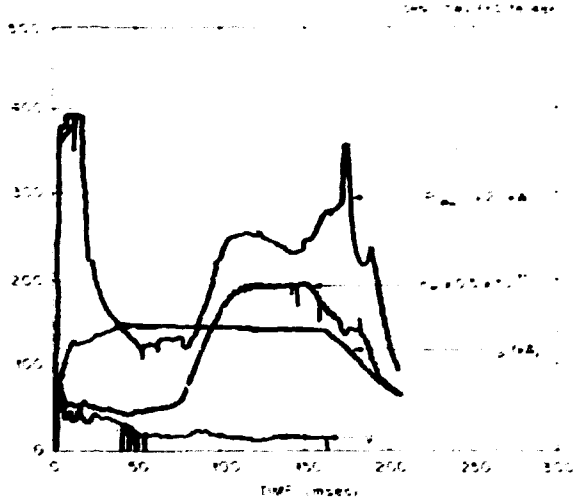

Fig. 2.24. Comparison of radiometer signal (P_{wall}) with density as a function of time during a discharge. The relatively high density is obtained using neutral gas puffing (I_p = 145 kA).

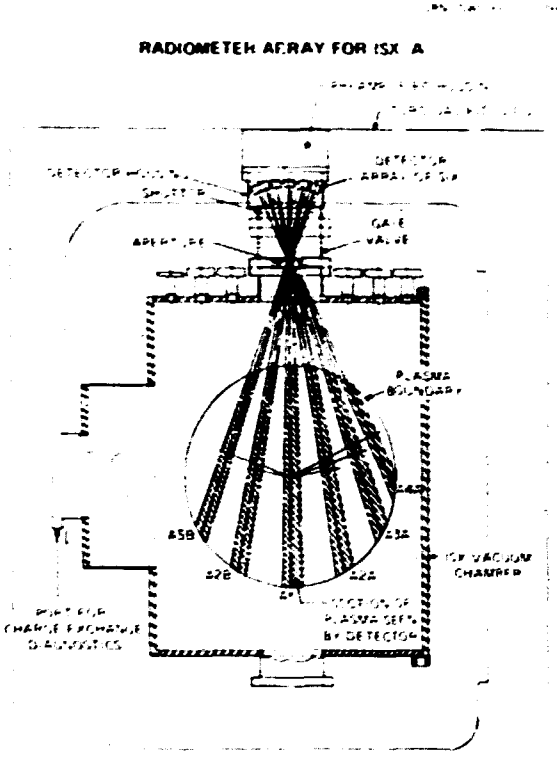

Fig. 2.25. Schematic diagram of the six-detector radiometer array for ISX-A. Cross-hatched areas are the chords viewed by the detectors. A1 is the detector which views the center; A2A, A3A, and A4A indicate the detectors viewing along chords in the inner half of the plasma at 9, 17, and 22 cm radii respectively. A2B and A3B view chords at 9 and 17 cm in the outer half.

phases of the neutral gas influx. The result in this case was that even though the density, $\bar{n}_e$, increased by a factor of four, the radiometer signal only doubled. In density scaling experiments in which the plateau value of $\bar{n}_e$ was varied from 1.5 to ≥5 x 10^{13}, while I_p, B_T (~120 kA and 12.8 kG, respectively), and other parameters were held constant, the radiometer signal (and P_{OH}) increased with $\bar{n}_e$ resulting in a relatively constant fractional loss (P_{wall}/P_{OH} ~ 30%). However, P_{wall}/P_{OH} vs $\bar{n}_e$ data did show a shallow minimum at $\bar{n}_e$ ~ 3.3 x 10^{13}, corresponding to the knee of the τ_E vs $\bar{n}_e$ data shown in Fig. 2.20 of Sect. 2.2.2. The fractional loss was also relatively constant for plasma current between 30 and 138 kA for a given B_T.

A schematic drawing of the six-detector array is shown in Fig. 2.25. Detector A1 viewed along a chord through the center of the plasma; detectors A2A, A3A, and A4A viewed chords at radii of 9, 17, and 22 cm, respectively, in the inner half of the cross section; and A2B and A3B viewed chords at 9 and 17 cm of the outer half. A common rectangular slot served as the final collimating aperture for all detectors and resulted in spatial resolution of 3 cm or better at the center of each chord. A set of baffles was placed in front of each detector to reduce errors due to reflected stray light.

Signals for five of the array detectors along with those for the two uncollimated monitors for a single discharge are shown in Fig. 2.26. Unfortunately, detector A4A which viewed the outer portions of the plasma, was damaged soon after installation. These data are for the tungsten blowoff experiment in which a laser pulse was used to vaporize a small amount of tungsten, thus propelling it into the plasma beginning at ~100 msec into the discharge. The signals for detectors viewing the outer layers of

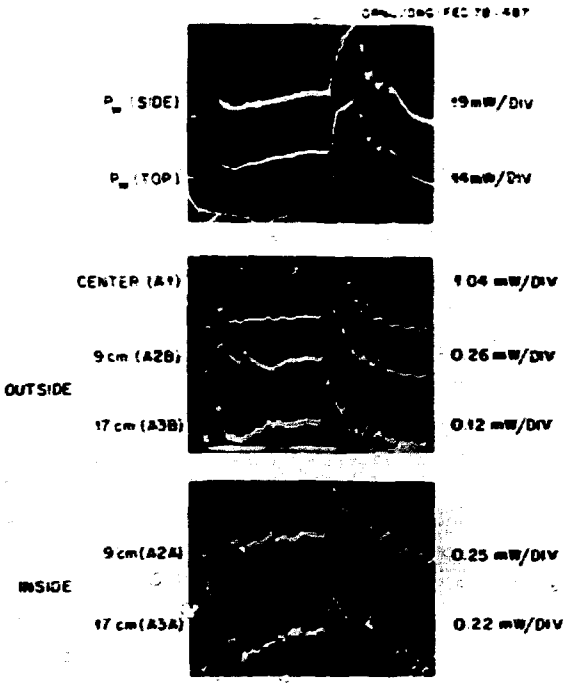

Fig. 2.26. Oscillograms of radiometer signals for the tungsten blow-off experiment. The sudden increase in signal halfway through the discharge is due to the influx of tungsten: (a) signals from the two uncollimated monitors; (b) signals for detectors viewing the center and outer half of the plasma column; (c) signals from two of the detectors viewing the inner half (shot 5476).

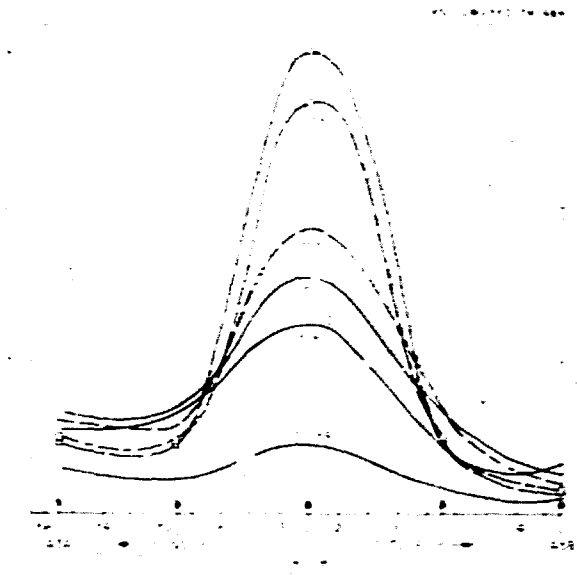

Fig. 2.27. Time evolution of the distribution of energy flux intensity; data taken from oscillograms of Fig. 2.26.

the plasma increase and peak much sooner than those viewing nearer the center. The middle three traces [Fig. 2.26(b)] show distinct time delays, which may imply an inward rate of transport of the tungsten. Detector A3B (at 17 cm outside) peaks 5 or 6 msec before A2B (at 9 cm) and 13 msec before A1, the central detector. This time behavior may provide information about the transport of tungsten and other high-Z materials in high temperature plasmas.

In order to obtain a clearer picture of the time evolution of the radial distribution of emission, the data of Fig. 2.26 are plotted as emission intensity vs radius in Fig. 2.27 for several times into the discharge. Without tungsten injection the signals remain fairly constant over the duration of the discharge. The emission over the duration of the discharge. The emission intensity profile at t = 123 msec differs very little from that at t = 94 msec in the absence of tungsten injection. With tungsten the signal from the central detector, A1, increases by a factor of six; the outer (17-cm) detector signals only increase by a factor of three and decrease again while the signal from A1 continues to increase. Volume emission data are normally obtained by inverting intensity data such as that in Fig. 2.27; however, with only five data points and due to the lack of data for the outer edges (R = 18-24 cm) Abel inversion was not applicable. A modeling approach is now in progress, and the distribution so determined is to be checked using gross energy flux data provided by the uncollimated monitors.

Although the six-detector array of ISX-A provided a considerable quantity of spatial information, the need for a more extensive array was clearly indicated. Such an array is planned for ISX-B, for which a 12 x 12 detector arrangement is being designed for application to noncircular plasma cross sections.

2.2.4 Experimental Observation of the Impurity Flow Reversal Effect in the ISX Tokamak

K. H. Burrell, P. H. Edmonds, J. C. DeBoo, K. W. Hill, E. S. Ensberg, R. C. Isler, S. K. Wong, T. C. Jernigan, C. E. Bush, M. Murakami, R. J. Colchin, G. H. Neilson

The inward transport of impurity ions in tokamak plasmas, which is predicted by neoclassical theory and which was clearly seen in the ATC tokamak,[29] poses a major problem. Impurities, especially high-Z impurities, can be quite deleterious for fusion reactor plasmas. Accordingly, it is of interest to study impurity transport with a view towards methods of impurity control.

Neoclassical theory[16-23] also predicts that poloidally asymmetric source of protons or heat of sufficient strength can reduce or reverse the inward transport of impurities, thus providing a method of impurity control. The impurity flow reversal experiment was designed to test neoclassical theory, especially the predictions concerning these asymmetric source terms.

In experiments performed on ISX,[24] we have found a substantial alteration of the transport of an injected neon impurity when poloidally localized injection of hydrogen gas is used to produce the asymmetric sources. The observed changes are qualitatively consistent with expectations based on simple theoretical models. More quantitative comparisons will be reported later. If these preliminary indications are confirmed by subsequent experiments, this technique could be the basis for a simple, compact impurity control technique for tokamak plasmas.

In order to explain the experiment, a short review of the theory is necessary. The fundamental physics that must be added to go from classical to neoclassical transport theory is the effect of guiding center motion on plasma transport.[16] In the collisional regime, the important guiding center motion is the vertical particle drift due to the inhomogeneous curved toroidal field. The drift, coupled with the radial pressure gradient, creates a small poloidal variation in the pressure of each species which, in turn, drives a return flow of particles along the magnetic field. It is the frictional force due to these parallel flows that drives neoclassical transport.[16]

The essence of the flow reversal effect is the use of poloidally localized sources to alter the parallel proton flows. This modifies the proton-impurity friction, thus reducing or perhaps reversing the inward impurity transport. Theoretical calculations have shown that in the presence of asymmetric sources, the radial flux of an impurity Γ_I of charge Z_I is given by[17]

$$\Gamma_I = \frac{2q^2 n_i}{Z_I^2 eB_\zeta^2 \omega_{ci}^2 \tau_{iI}} \left[\Delta_1 \left(\frac{1}{n_i} \frac{\partial p_i}{\partial r} - \frac{1}{n_I Z_I} \frac{\partial p_I}{\partial r} \right) - \frac{5}{2} \Delta_2 \frac{\partial T_i}{\partial r} - \frac{1}{2} eB_\zeta R \left(\Delta_1 \frac{a_{iI}}{n_i} - \Delta_2 \frac{a_{TI}}{p_i} \right) \right], \tag{2.2.1}$$

where the subscript i(I) denotes protons (impurities), q is the safety factor, τ_{iI} is the proton-impurity collision time, ω_{ci} is the proton cyclotron frequency, B_ζ is the toroidal field, R is the major radius, r is the minor radius, and e is the magnitude of the electron charge. The quantities Δ_1 and Δ_2 are numerical factors of order unity which depend on the precise collision model used.[17]

Equation (2.2.1) illustrates that radial transport is driven by gradients in the density and temperature, but that the sin Fourier components of the proton source a_{iI} and the heat source a_{TI} can also affect the flux. Neutral transport calculations have been done to see how large an H_2 injection rate must be used to make the source terms comparable to the other terms in Eq. (2.2.1). For model profiles similar to those in ISX, on the order of 10^{21} particles per second are required, a rate close to the natural particle loss rate from the ISX plasma. However, since gas is used as the source, the source terms are large only in the outer 1-2 cm of the plasma. Thus, the flow reversal effect can alter impurity transport only in the plasma edge.

The poloidally asymmetric sources due to injection of H_2 into the bottom of the plasma were somewhat enhanced by depositing a layer of titanium gettering over the top half of the vacuum chamber every few shots, thus reducing hydrogen recycling there. (In addition, the titanium reduced effective Z in the plasma from values around two to a value close to one.) Due to the nine-fold symmetry of the ISX vacuum chamber, nine getter sources and nine feedback-controlled gas injectors[31] were used.

The effect of the source terms has been investigated by observing the spectral lines produced by short bursts of neon and aluminum introduced into the plasma after the H_2 injection has been established. As shown in Fig. 2.28, the 1-msec neon pulse was produced by a fast gas valve; the 200-μsec aluminum burst was generated by a 0.5-J, 20-nsec laser pulse hitting an aluminum-coated glass slide. (This latter technique is similar to one used on ATC.[32])

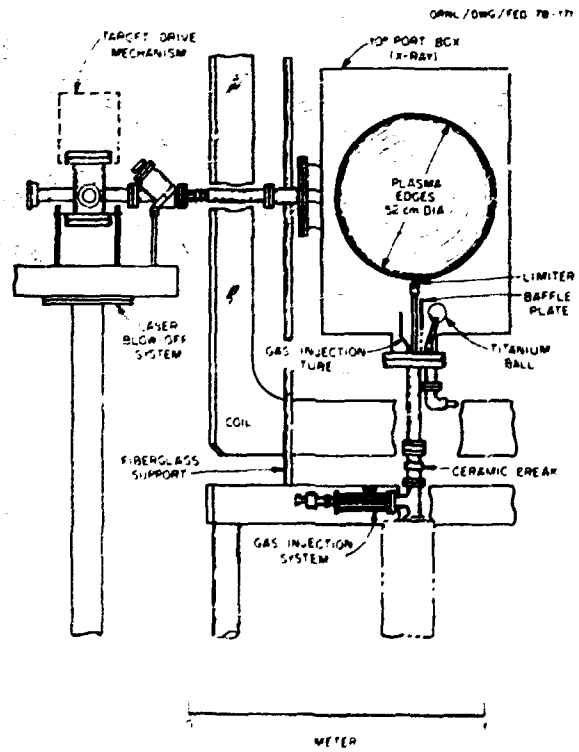

Fig. 2.28. Illustration showing equipment attached to the machine.

According to Eq. (2.2.1), reversing the sign of B_ϕ reverses the sign of the contribution that the source terms make to Γ_I. [With the source configuration used in ISX, a clockwise (CW) toroidal field causes the sources to enhance the inward impurity transport, while for a counterclockwise (CCW) field it reduces or reverses inward transport.] If similar plasmas can be obtained with both polarities of the toroidal field, this dependence on B_ϕ can be used to separate the effect of the source terms from that of other plasma parameters.

In Figs. 2.29 and 2.30, we summarize a series of measurements that were made on CW and CCW discharges to verify that the plasmas were

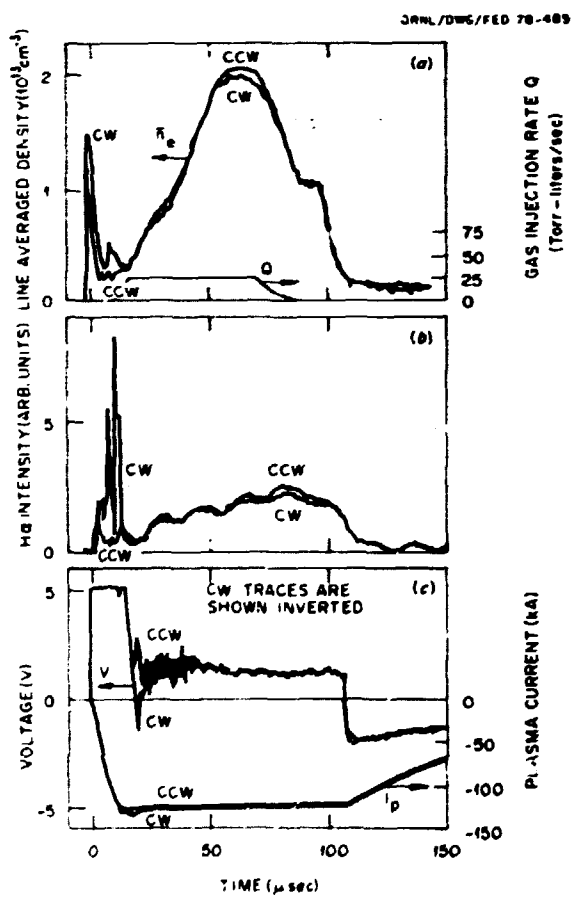

Fig. 2.29. (a) $n_e(t)$ for CW and CCW, $H_\alpha(t)$ for CW and CCW; (b) V(t) for CW and CCW (CW inverted), I(t) for CW and CCW (CCW inverted).

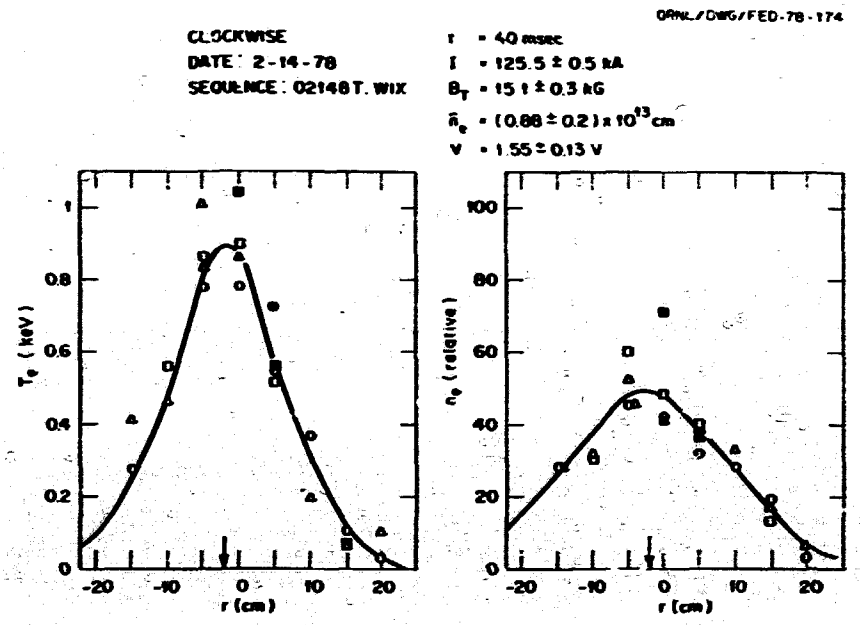

Fig. 2.30(a). $n_e(r)$ and Te(r) for CW.

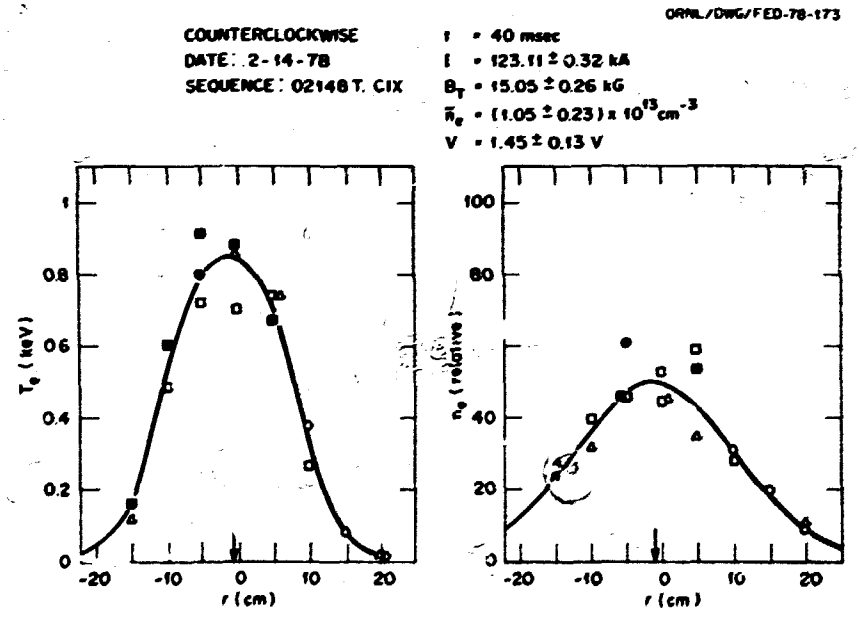

Fig. 2.30(b). $n_e(r)$ and Te(r) for CCW.

the same. (To minimize problems with error fields, the plasma current was reversed whenever the toroidal field was.) While there are some differences during the breakdown phase prior to 20 msec, the plasmas are very similar during the main discharge phase when the H_2 injection takes place and when the neon and aluminum transports are investigated. Both the gross discharge parameters in Fig. 2.29 (voltage, current, and line-average density) and the edge processes producing the H_α radiation are quite similar for both polarities of the toroidal field. In addition, the time behavior of the charge exchange neutral flux is identical, indicating a great similarity in proton parameters. Finally, the radial profiles in Fig. 2.30 agree to within the error in the data. The spectrometer and the radiometer do exhibit some dissimilarities between the two directions. For example, the radiometer signal for CW plasmas is always greater than or equal to that for CCW plasmas. We will return to this point later.

In Fig. 2.31, we present a sample of the experimental spectroscopic data. It is clear from these data (and those in Fig. 2.32) that the signal amplitude is definitely higher in the CW discharges, in agreement with the predictions of Eq. (2.2.1).

Calculations have shown that, if the background plasma does not change, the following ratio of amplitudes should vary linearly with the gas injection rate

$$\Delta = \frac{S_{CW} - S_{CCW}}{S_{CW} + S_{CCW}} . \qquad (2.2.2)$$

This linearity is manifested in the high gas injection rate points in Fig. 2.32. Since Eq. (2.2.1) predicts that transport rates depend on the $n_i(r)$ and $T_i(r)$ profiles, and since a large decrease in injection rate probably alters these profiles, it is not too surprising that the result departs from linearity at low injection rates. More detailed calculations are in progress to verify that the numerical values of the points shown in Fig. 2.32 are consistent with Eq. (2.2.1) using the measured plasma parameters.

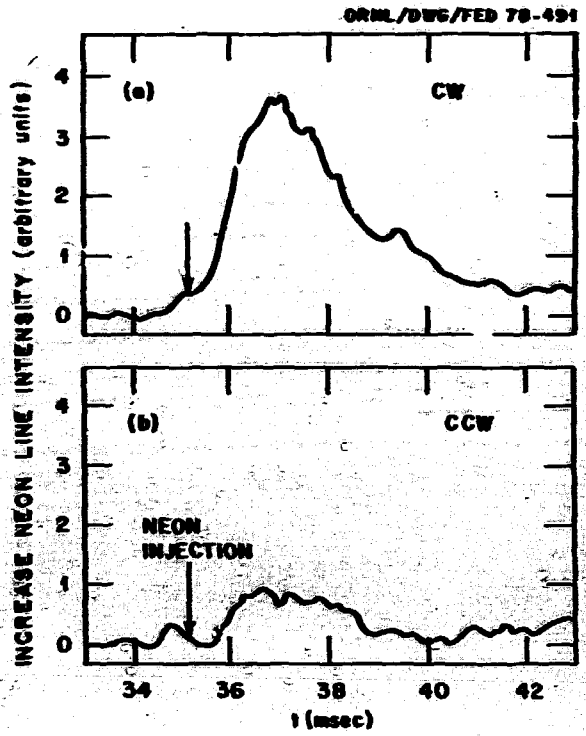

Fig. 2.31. Neon signal for CW and CCW.

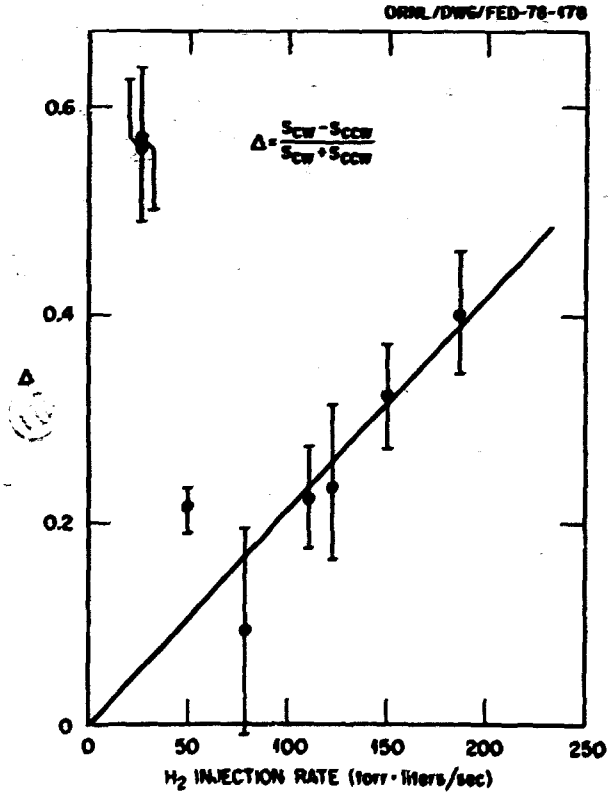

Fig. 2.32. Plot of Δ vs Γ. Error is one standard deviation.

Data in Fig. 2.32 were all taken for nearly the same value of line-average plasma density, $\bar{n}_e \cong 10^{13}$ cm^{-3}. By varying the trigger time for the neon pulse, we could study the change of the effect with plasma density at a constant gas injection rate. In general, as density rose, Δ decreased. This is consistent with Eq. (2.2.1), since the sources appear there normalized by the local density. As part of the sequence, neon was injected into the plasma before the H_2 gas injection was established. A value of $\Delta = 0.0 \pm 0.28$ was found, i.e., essentially zero.

Aluminum was injected simultaneously with neon for several sets of discharges. In spite of an appreciable difference in the neon signal for the CW and CCW discharges in each set, no consistent variation in the aluminum signals was seen. Any changes were smaller than the 30% shot-to-shot variation in the amplitude of the spectroscopic signal. This may be due to the superior ability of the fast aluminum atoms to penetrate the edge of the plasma, where the flow reversal layer exists. The aluminum injection system[24,25] produces atoms with energy of 1.5-2.5 eV, while the neon is at room temperature. The lack of change in the aluminum signal can be used as an additional piece of evidence that the bulk plasma is the same for CW and CCW discharges.

We also studied the effect of H_2 injection on the naturally occurring impurities. This study is complicated by the dissimilarity of the breakdown phase of the CW and CCW discharges, since this is the time when a large fraction of these impurities first enters the plasma. The radiometer data suggest that, just as with neon, more intense impurity radiation should be seen from the CW discharges. However, no clear-cut directional dependencies were seen in the O III, O IV, and O VI lines, while the CCW signals were larger for Ar VIII, Ti XI, and Ti XII. An understanding of the behavior of the intrinsic impurities will be necessary to fully assess the effectiveness of the flow reversal technique.

In conclusion, it appears that we have produced a significant change in the transport of neon ions in the plasma. That change is connected with the H_2 injection, since it does not exist without the gas injection and it varies as that injection rate changes. The sign of the change and its qualitative behavior are consistent with the results of neoclassical theory. Because theory predicts that it will increase with B_ϕ and R [see Eq. (2.2.1)], the impurity flow reversal effect should be easier to see in the larger, higher field machines of the future.

We would like to thank J. L. Dunlap, P. W. King, D. H. McNeill, and J. B. Wilgen for their diagnostics and H. E. Ketterer, W. J. Redmond, and T. F. Rayburn for machine operation.

2.2.5 Wall Impurities in ISX-A

B. R. Appleton — L. Heatherly
R. E. Clausing — R. A. Langley
R. J. Colchin — P. Mioduszewski
L. C. Emerson — S. P. Withrow
R. A. Zuhr

Introduction

Plasma-wall interaction studies, begun in ORMAK, have been greatly expanded in ISX-A. This expansion has been made possible by the implementation of a vacuum transfer and Auger analysis system to ISX-A, as well as a CAMAC-controlled residual gas analyzer. In addition, ion backscattering has been used to characterize silicon samples exposed to ISX-A discharges. Laboratory studies of hydrogen recycle phenomena have been confirmed and extended. With the exception of the backscattering studies, results of ISX-A wall impurities studies are contained in papers published as *Proceedings of the Third International Conference on Plasma-Surface Interactions in Controlled Fusion Devices.*

Plasma Wall Impurity Experiments in ISX-A.[32]
R. J. Colchin, C. E. Bush, P. H. Edmonds, A. C. England, K. W. Hill, R. C. Isler, T. C. Jernigan, P. W. King, R. A. Langley, D. M. McNeill, M. Murakami, G. H. Neilson, J. E. Simpkins, and J. B. Wilgen.

The ISX-A was a tokamak designed for studying plasma-wall interactions and plasma impurities. It fulfilled this role quite well, producing reliable and reproducible plasmas which had currents up to 175 kA and energy containment times up to 30 msec. With discharge precleaning, Z_{eff} was as low as 1.6, with titanium evaporation, Z_{eff} approached 1.0. Values of $Z_{eff} \geq 2.0$ were found to be proportional to residual impurity gases in the vacuum system immediately following a discharge. However, there was no clear dependence of Z_{eff} on base pressure. Stainless steel limiters were used in most of the ISX-A experiments. Upon introducing carbon limiters into the vacuum system, Z_{eff} increased to 5.6. After 12 days of cleanup with tokamak discharges, the carbon limiters tended to give slightly higher values of Z_{eff} than stainless steel limiters. Injection of $\leq 10^{16}$ atoms of tungsten into discharges caused the power incident on the wall to double and the electron temperature profile to become hollow.

Surface Impurities Studies During the Startup and Early Operations of ISX Using a Surface Analysis Station with Sample Transfer.[32]
L. C. Emerson, R. E. Clausing, and L. Heatherly.

ISX is a clean tokamak built to study plasma-wall interactions and the role of impurities in tokamak plasmas. The vacuum vessel is of all welded 304L stainless steel construction suitable for ultra-high vacuum operation. A surface analysis station was installed before startup and has since provided data on typical wall material and a variety of other materials exposed at positions between the surface of the first wall and the limiter inner radius. Samples are introduced, from air, into the ultra-high vacuum transport system without disturbing the vacuum in ISX or the analysis system. The samples may then be specially prepared (by outgassing, sputter cleaning, evaporation, etc.), analyzed before exposure to the plasma, exposed to the plasma, and subsequently reanalyzed (by AES, thermal desorption, electron-induced desorption, or SIMS), to determine what changes have occurred. The analysis station and a residual gas analyzer and plasma diagnostics have provided information on the initial "cleanup," changing wall conditions, and hydrogen loading during the startup period as well as the subsequent routine operations of ISX-A. During the startup period substantial sulfur contamination was evident, but this has been greatly reduced as hydrogen discharge cleaning has proceeded. Samples of oxidized stainless steel were not cleaned to an oxygen-free status, but the surface was apparently reduced to a thin substoichiometric oxide. Carbon was significantly removed but not eliminated entirely. Routine tokamak operations are monitored by means of a special composite sample which makes possible estimates of both the state of cleanliness of the system and its rate of cleanup.

The surface analysis station has also played a key role in several impurities studies. Pertinent results of experiments involving purposeful addition of oxygen to the system, the transport of stainless steel and other metals, hydrogen recycle, and the use of titanium in ISX-A are presented.

Sputtering and Chemical Attack of 304 Stainless Steel, Aluminum, and Gold by Hydrogen Ions of 100-eV Energy.[32] R. E. Clausing, L. C. Emerson, and L. Heatherly.

Samples of polished and oxidized 304 stainless steel, aluminum, and gold have been subjected to bombardment by hydrogen ions in order to simulate effects expected in tokamak fusion devices. This paper reports on the sputtering and chemical effects of bombardment with 100- and 200-eV ions with fluence levels of 2×10^{21} ions/cm^2 and 4×10^{21} ions/cm^2, respectively. Under these conditions gold is badly blistered and eroded, aluminum is slightly blistered at 100 eV and substantially eroded at 200 eV, but few changes are seen in the case of polished stainless steel. The oxide film (produced in a 30-min

exposure to air at 500°C) on the polished stainless steel sample was, however, removed and only a very thin layer of substoichiometric oxide remained on the surface after exposure to either 100- or 200-eV hydrogen plasmas. Sample temperatures during bombardment were about 50°C for the 100-eV ions and 65°C for the 200-eV ions.

Only the major characteristics of the apparatus will be described here. The plasma is a low temperature, partially ionized plasma supported by electron emission from a hot cathode. The plasma discharge is inside a 3.2-cm-diam stainless steel tube and extends approximately 10 in. from the cathode to the main anode. Hydrogen ions are drawn from the plasma and accelerated through the sheath between the plasma and the wall to provide a high flux of hydrogen ions (1 mA/cm^2). An external power supply can be used to bias the plasma with respect to the wall and thereby provide ion bombardment at any energy between 30 and several hundred volts. The discharges normally operate at a pressure near 10^{-2} Torr of hydrogen. For many experiments the sample surface includes the entire tube wall. However, small samples of wall material can be moved under ultra-high vacuum conditions from the discharge chamber to a separate chamber for surface analysis. The entire system is of ultra-high vacuum construction and is free of organic materials. Ion species accelerated from the plasma into the wall are estimated to be about 80% molecular ions and 20% atomic hydrogen ions.

Aluminum, gold, and stainless steel samples were exposed to 100-eV ions at 50°C for an integrated dose of 2 x 10^{21} ions/cm^2. The conditions of this exposure did not reduce the aluminum oxide surface layer, but evidence of the blistering and tearing was found. The irradiated area on the gold sample shows evidence of both erosion and blistering. The stainless steel oxide was reduced in the irradiated area leaving a roughened surface but with no blisters or sharply defined features. Unoxidized polished stainless steel samples had no easily recognizable erosion- or bombardment-created features, although macroscopic optical reflectivity changes made it easy to identify the irradiated area. The topography was developed by 200-eV hydrogen ions incident on aluminum, gold, and stainless steel at 65°C with a total dose of 4 x 10^{21} ions/cm^2. The aluminum topography is shown to be mostly an erosion pattern. The gold sample also shows erosion and no blisters. The behavior of both the oxidized and unoxidized stainless steel samples was similar to that observed in the 100-eV irradiation.

Auger analyses of the samples were made after each exposure. These analyses revealed the following points.

(1) The oxide on the stainless steel is partially reduced with relative atomic concentrations being given by Fe = 1.0, Cr = 0.6, Ni = 0.3, and O = 1.2.

(2) The aluminum oxide surface layer was not significantly reduced in the 100-eV exposure (as indicated by the aluminum Auger line shape).

(3) The gold sample exposed to 100-eV ions had approximately 20 at. % of metal atoms from the stainless steel wall on its surface after the exposure. This can be used to estimate that the sputtering rate under these conditions is about 10^{-6} atoms per incident ion, assuming that all sputtering is due to atomic hydrogen ions and none is due to plasma impurities or molecular hydrogen ions. The irregular topography of this sample probably introduces considerable error in the estimate, however.

(4) The sample of gold exposed to 200-eV ions was so completely covered with sputter products that the Auger spectra showed no gold.

Conclusions are as follows.

(1) The plasma-wall interaction simulator produces a useful measure of the ability of materials to resist attack by low energy hydrogen ions.

(2) Hydrogen ions of 100 eV and above produce significant surface damage in gold and aluminum under the conditions of this experiment but do little apparent microscopic damage to 304 stainless steel.

(3) Hydrogen plasmas of the type used in this experiment can reduce the oxides on stainless steel to a thin substoichiometric layer of atomic dimensions. (Other experiments in ISX-A have shown that higher purity plasmas can partially reduce Al_2O_3 and reduce the oxygen level on stainless steel to <1 at. %.)

Studies of Hydrogen Recycle from the Walls in Tokamaks Using a Plasma-Wall Interaction Simulator.[32] R. E. Clausing, L. C. Emerson, and L. Heatherly.

The recycle of hydrogen from walls and limiters plays a fundamental role in the operation of tokamaks for several reasons: (1) the average proton confinement time in the plasma is short with respect to plasma pulse length, and therefore each proton is, on the average, recycled several times to and from the walls; and (2) the walls may elastically or inelastically reflect the hydrogen but, according to our measurements, at least half or more of the hydrogen incident on the walls may be buried in the wall and thermalized, and most will return to the plasma volume on a time scale which is on the order of 10^{-1} sec.

We have studied details of the hydrogen recycle phenomena from 304L stainless steel using a plasma-wall interaction simulator. Low energy (30 to 200 eV) atomic and molecular hydrogen ions are used. The evolution rate from surfaces bombarded with a flux of 6×10^{15} ions/sec/cm^2 has been measured for several conditions and appears to be controlled by complex diffusion phenomena and perhaps, in some cases, by surface recombination rates. The evolution rate reveals effects due to diffusion from the highly supercharged, near surface region. We interpret the prompt desorption process in terms of damage to the crystal structure in the near surface region. The measurements were made in the simulator but were found to correlate well with observations made in ISX-A.

2.2.6 Charge Exchange Measurements on ISX-A

G. H. Neilson J. T. Mihalczo
J. B. Wilgen

Ion behavior in ISX-A was inferred from measurements of the energetic (0.3 keV < E < 4 keV) charge exchange neutral atoms escaping from the plasma. For this purpose, a mass-energy neutral analyzer (described later in this section) viewing along a fixed midplane chord 6° from perpendicular was used. (This orientation avoids difficulties resulting from particles trapped in field ripples.) In a typical shot, neutral fluxes at seven energies spanning a range of 10.6:1 were measured simultaneously with a basic time resolution of 2 msec. In this report, we discuss the interpretation of these data in terms of ISX-A plasma parameters, namely:

(1) ion temperatures and neutral atom densities in pure (H^+ or D^+) plasmas,
(2) relative H^0 and D^0 emission from mixed plasmas, and
(3) directional similarity in IFR experiments.

T_i and n_o in pure plasmas

The determination of ion temperatures (T_i) and neutral atom densities (n_o) from measured charge exchange flux has been described previously[33] in connection with ORMAK data. The methods used have been adapted for analysis of ISX-A data, for which the most notable difficulties are the "thickness" of the plasma to neutrals due to the high value of $\bar{n}_e a$ ($\leq 2 \times 10^{15}$ cm^{-2}), and the lack of profile information due to the inability to view different chords through the plasma. The method is basically one in which a charge exchange spectrum calculated from a plasma profile model is fitted to the measured data. In the ohmically heated plasmas under consideration, T_i is determined by the shape of the spectrum and $n_o(0)n_i(0)$ by the amplitude. Because T_i profile shapes cannot be measured, they

are assumed for modeling purposes, and the calculated values of T_i and $n_0 n_i$ are then consistent with the assumption. Error analysis is done by varying the profile assumptions within extreme but realistic limits.

Figure 2.33 shows the variation of central T_i with line-average electron density in D^+ plasmas for which I_p and B_T were fixed and the external gas puff rate was varied. The open circles represent values calculated from the slope of the neutral spectrum, with approximate attenuation and profile corrections applied. The solid dots and error bars are determined by the profile modeling procedure. The dots are consistent with a parabolic T_i profile, and the error bars with profiles respectively broader and more peaked than parabolic. Relative corrections introduced by this method are greatest at high densities, reflecting the progressively increasing severity of plasma thickness effects with density.

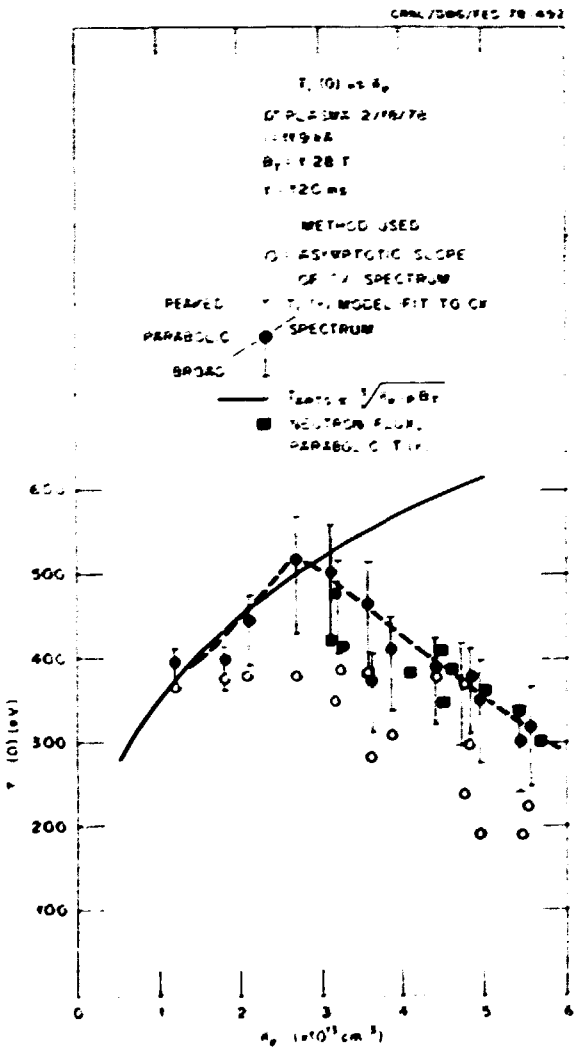

Fig. 2.33. Variation of T_i with line-average density in deuterium plasmas.

At low densities, the ion temperature is observed to be consistent with Artsimovich's scaling,[34] in which power delivered to ions is assumed to be lost by heat conduction in accordance with neoclassical "plateau" scaling. The decreasing trend at high densities is a significant observation. Neoclassical transport simulations of this experiment (by H. C. Howe, Plasma Theory Section) suggest that ion losses dominate the power balance at the high densities due to increased ion heat conduction and to enhanced electron-ion coupling. It is noted that the electron temperature is also observed to decrease with density (see Sect. 2.2.2 of this report), although it remains somewhat higher than the ion temperature. Furthermore, the charge exchange data are in agreement with temperatures inferred from measurements of the absolute flux of D-D neutrons (see Sect. 2.2.9).

In Fig. 2.34, central neutral densities, $n_0(0)$, are plotted against density for both H^+ and D^+ plasmas. This quantity is calculated from values of $n_0(0)n_i(0)$ obtained in the profile modeling analysis procedure. The D^+ data correspond to the points in Fig. 2.33; the H^+ data were obtained in a similar experiment, performed at slightly higher toroidal field. Both curves indicate that $n_0(0)$ falls approximately exponentially with plasma density in otherwise similar plasmas. The low values of $n_0(0)$ obtained, especially at high densities, imply a very low rate of local plasma production by ionization. This supports the conclusion that plasma must be produced at the edge and transported to the center by some convective mechanism, as has been suggested.[35]

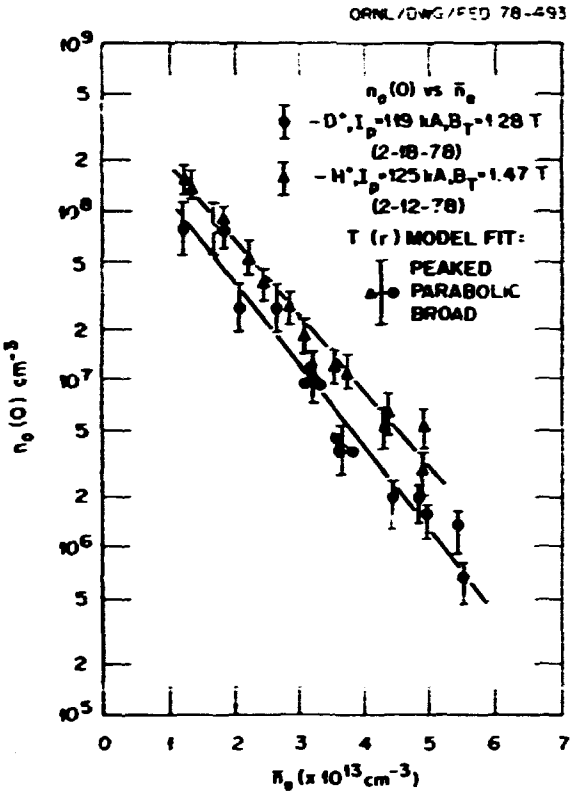

Fig. 2.34. Variation of n_o inferred from charge exchange with density in H^+ and D^+ plasmas.

Mixed species plasmas

The mass analysis capability of the neutral analyzer is useful in the study of mixed H^+-D^+ plasmas. In order to study confinement and heating of particles introduced by gas puffing, some experiments were done in which a tenuous H^+ plasma was initiated using a hydrogen gas feed which was then turned off and replaced by a substantial deuterium gas feed. The time evolution of both H^0 and D^0 charge exchange neutral flux was monitored at several different energies. The observed behavior is plotted in Fig. 2.35. Deuterium replaces hydrogen on a time scale of ~20 msec; after this, transient H^0 accounts for about 20% of the measured flux at all energies for the remainder of the discharge. This is in spite of the fact that during this time there is no external hydrogen feed, while the density is still rising dramatically due to the deuterium feed. Full interpretation of these data will require a model for neutral transport in mixed plasmas. This is now being developed.

IFR experiments

An important requirement for the IFR experiments done on ISX was plasma similarity with respect to CW and CCW operation (see Sect. 2.2.4 of this report). Charge exchange neutral data are one index of such similarity inasmuch as they reflect the behavior of ions and neutrals in the plasma. In Fig. 2.36 we present the time evolution of absolute neutral flux at a typical energy and the time-evolved ion temperature obtained from complete spectra for CW and CCW discharges. Based on these measurements, as well as numerous other indexes these conditions were sufficiently similar for IFR studies

Mass-energy neutral particle analyzer for ISX

G. H. Neilson J. F. Lyon
C. F. Barnett L. A. Massengill
J. A. Ray

A seven-channel neutral particle analyzer incorporating mass and energy resolution has been constructed, tested, calibrated, and implemented on ISX-A. As Fig. 2.37 shows, it consists of a gas stripping cell followed by a seven-slit, 180° magnetic momentum analyzer. Each slit defines a momentum beamlet which is effectively mass-analyzed by means of an electrostatic energy filter and detected by a channel electron multiplier.

The analyzer has been calibrated for incident H^0 in the range 0.5 keV < E < 10 keV using H_2 gas at ≈8 x 10^{-3} Torr in the gas cell. The apparatus and procedure are identical to those used in previous calibrations of electrostatic

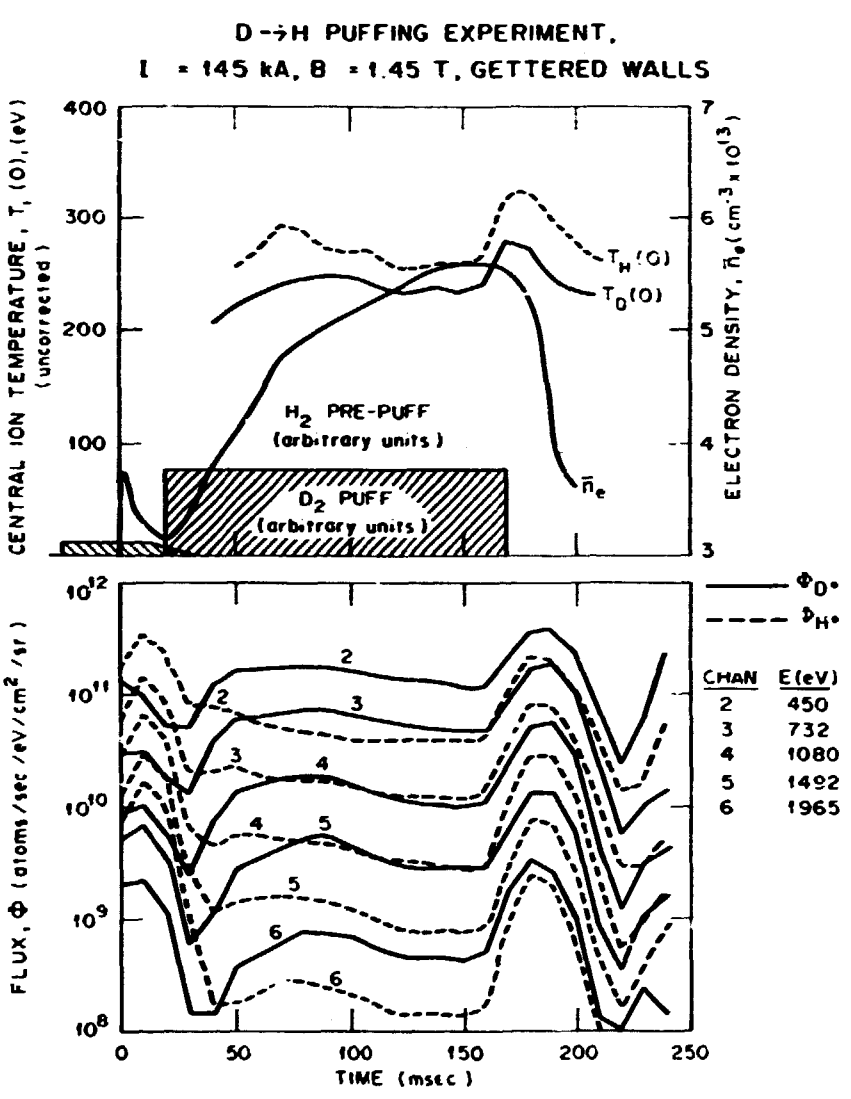

Fig. 2.35. D → H puffing experiment: (a) time evolution of gas feeds and electron density (T_i calculated from asymptotic slope of CX spectrum); (b) mass-energy analyzer permits separate measurement of H^0 and D^0 charge exchange spectra.

analyzers for ORMAK.[36] The mass-energy characteristics of the present analyzer were determined experimentally and found to be in good agreement with those calculated from the geometry, slit widths, and field settings. The net detection efficiency was measured for each channel; results for a typical channel are presented in Fig. 2.38, and deviation over all channels was within 10% of the average.

This instrument was used on ISX-A to measure central ion temperatures and central neutral atom densities in both H^+ and D^+ plasmas; the mass resolution feature was also employed in mixed species particle confinement experiments. Results of these measurements are described in this section. The analyzer will be used in injection experiments on ISX-B to resolve, by means of mass identification, the fast ion and thermal ion

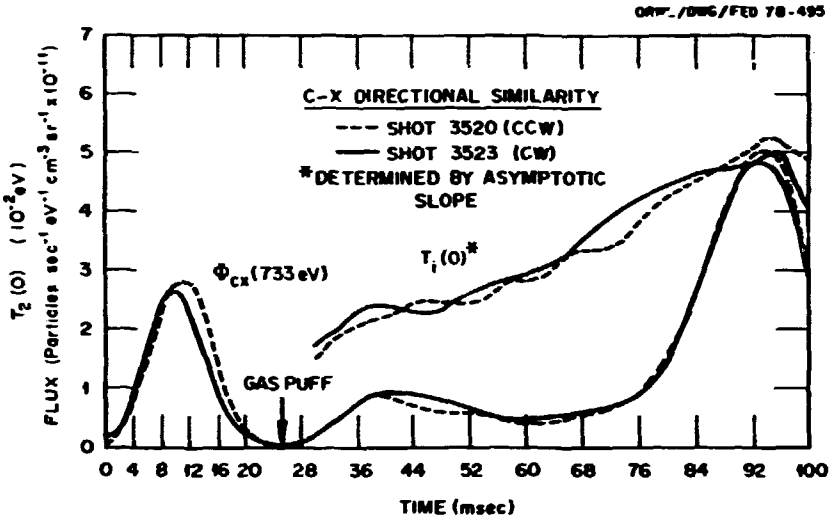

Fig. 2.36. Charge exchange data show acceptable directional similarity for IFR experiments.

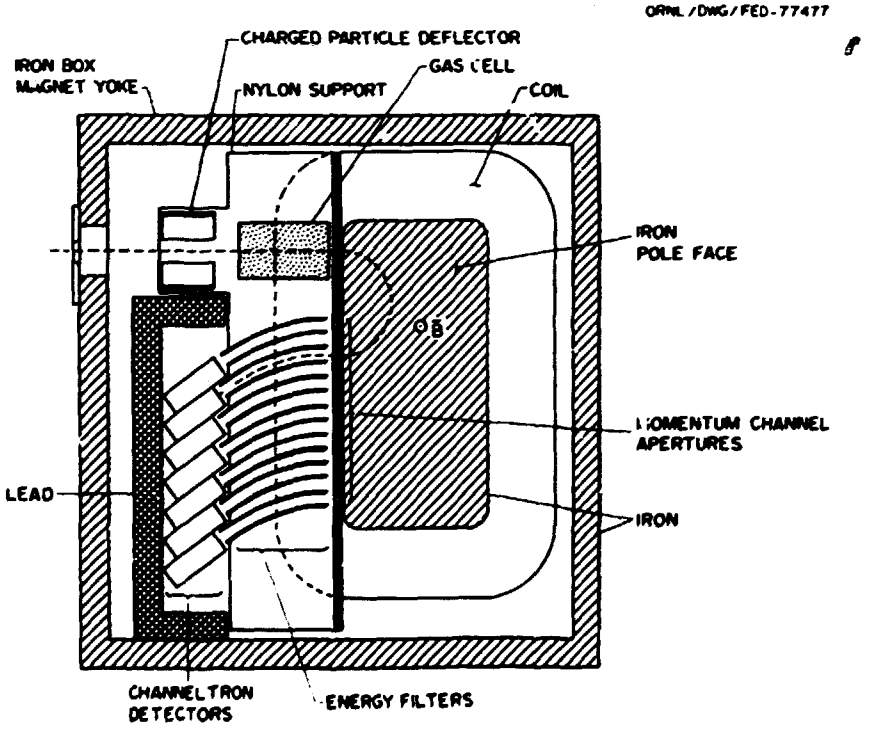

Fig. 2.37. Diagram of mass-energy neutral analyzer showing major components.

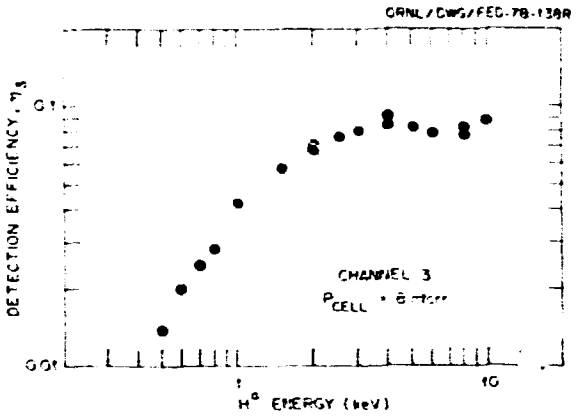

Fig. 2.38. Measured net detection efficiency for channel 3 of analyzer.

distributions. Further testing and calibration are necessary for this application, and these will be done while ISX modifications are in progress.

2.2.7 Some Surface Plasma Studies in ISX-A

A. C. England W. Namkung
J. L. Dunlap R. V. Neidigh

Four diagnostics have been used in monitoring the plasma near the limiters in ISX-A. Correlation has been observed between low frequency signals from (1) an MHD loop, (2) double Langmuir probe current, (3) current between the outside limiter and the vacuum tank, and (4) light from singly charged iron impurity atoms (Fe II). Characteristic frequencies are in the range of 6-9 kHz. A necessary condition for observation of signals on the double probe current, the limiter current, and the Fe II light is for the MHD loop to show oscillations. Large, nonoscillatory signals in the Fe II light are also observed when instabilities cause large currents to the limiter.

Double Langmuir probe measurements in the shadow of the limiter have shown that the electron temperature is ~20 eV and the ion density is ~2.5-3 x 10^{12} cm^{-3} with modest gas puffing. If these values are typical for the plasma in contact with the limiter, then the floating potential of the limiter can exceed 50 V. The limiter-to-liner current measurement has shown that currents >10 A can flow through a small external resistance; these currents are consistent with this observation.

These various observations suggest that conditions are propitious for the formation of unipolar arcs. However, there is no evidence to suggest that any of the observations is evidence of a unipolar arc.

Double Langmuir probe

W. Namkung A. C. England

The double Langmuir probe was used to study the temporal behavior of the ion density and electron temperature of the scrape-off plasmas at three different locations relative to the limiter. In these experiments the limiter was moved and the Langmuir probe was fixed. During gas puffing modes of operation, the outer positions (1.4 and 3.2 cm from the limiter edge) show a sudden drop of the ion saturation current (proportional to $n_i T_e^{1/2}$) while $\langle n_e \rangle$ is increasing in the main plasma column. Analysis shows that this transition is due mainly to a density change of more than a factor of five with little change of T_e ($\lesssim$10 eV). At the innermost position (0.64 cm), both the density and temperature change by less than a factor of 1.5-2 with moderate gas puffing. On the other hand, the same behavior has been observed with massive gas puffing, namely, $\langle n_e \rangle \geq 5 \times 10^{13}$ cm^{-3}. In order to explain this phenomenon, it is suggested that there may be two distinct layers in the scrape-off plasmas and that the boundary is moving inward toward the limiter. The existence of the boundary has been confirmed indirectly by a sudden shift of the plasma column during the feedback control experiments.

2.2.8 Time-Resolved Electron Temperature of a Tokamak Plasma by Soft X-ray Energy Spectrometry

G. R. Dyer P. H. Edmonds

X-ray-derived electron temperatures have been obtained on ORMAK and ISX-A using a soft x-ray energy spectrometer with a cryogenic Si(Li) detector. Electronics especially designed for high counting rates allows pulse-height analysis of a signal pulse in 1 μsec, the duration of the linear amplifier pulse above the baseline. Count rates are limited by pileup to ~10^5/sec. If 10^3 counts are considered adequate for a single spectrum, then one spectrum per 10 msec may be acquired by this spectrometer.

Energy resolution is compromised by both short pulse shaping time and intrinsic resolution of the present multichannel analyzer; basic resolution is 500 eV, adequate for the temperature measurements desired (if measurements are made on the high energy tail of a spectrum).

The apparatus collects x rays along a central chord of the plasma, with no provision for spatial scanning or off-axis sampling. Because the chordal measurement samples all regions of the plasma, from coldest to hottest, profile effects must be accounted for in temperature calculations. Figure 2.39 shows a profile of electron density, N_e, and temperature, T_e, as a function of radius, R, for several ORMAK-produced discharges.

Note that T_e is not maximum at center. The calculated x-ray intensity along a chord through this profile is obtained from the equation:

$$I(E) = C \sum_R \frac{N_e^2(R)}{T_e^{1/2}(R)} e^{-E/T_e(R)} .$$

The plot of Ln I(E) vs E is shown in Fig. 2.40. Departure from a linear relation is negligible, and the temperature derived from the plot is 280 eV, very close to the peak profile temperature of 290 eV.

ORNL/DWG/FED 78-496

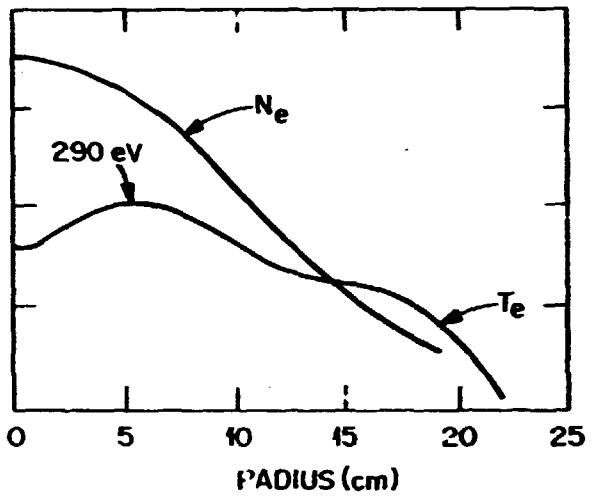

Fig. 2.39. Laser profiles at 35 msec.

ORNL/DWG/FED 78-497

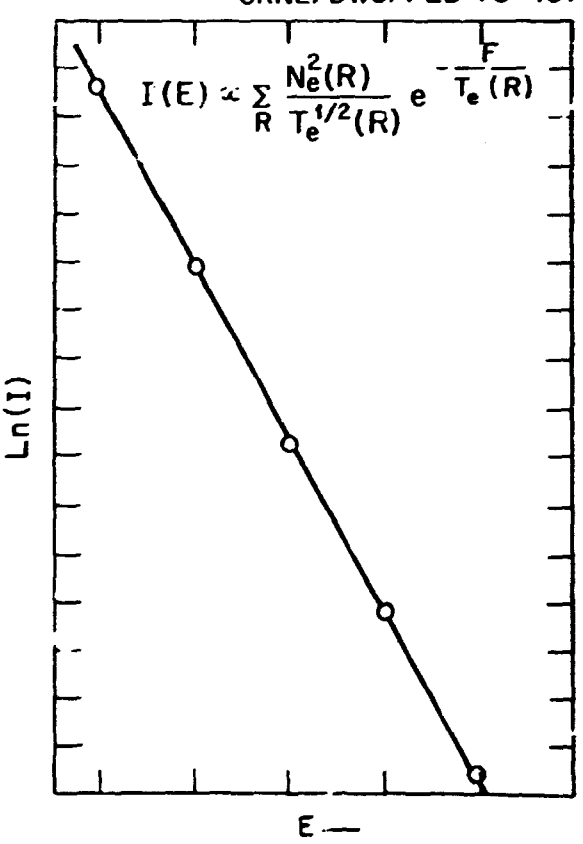

Fig. 2.40. Calculated Ln(I) vs energy, E.

Results of several calculations of this type lead us to believe that maximum plasma electron temperature may be approximated adequately by the simple equation

$$I(E) = \frac{Cn_e^2}{T_{e_{max}}^{1/2}} e^{E/T_{e_{max}}},$$

where

$$T_{e_{max}} = \frac{\Delta E}{\Delta \text{ Ln } I(E)},$$

and that profile effects may by neglected.

Temperatures are calculated by a straight-line, least-squares fit computer program using the above equation. Figure 2.41 shows a comparison of x-ray- and laser-derived temperatures for an electron heating study done on ORMAK. In general the agreement is good.

The present system has several disadvantages. In spite of its high counting rate acceptance, it has a limited dynamic range in the sense of plasma parameters n_e and T_e, because x-ray intensity depends on n_e^2 and on e^{-E/T_e}. Intensity at the detector must be adjusted by movable apertures to be $\sim 10^5$/sec maximum and must be monitored to ensure that it remains in an acceptable range.

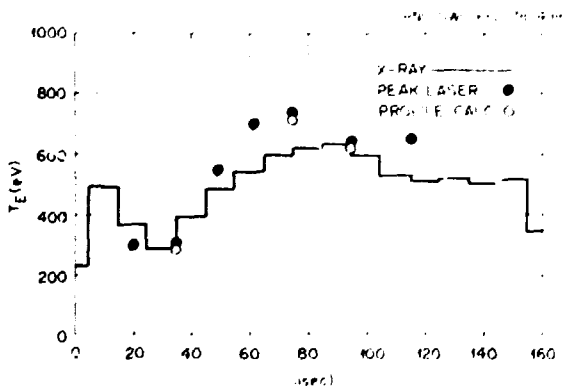

Fig. 2.41. A 35-shot average of electron temperature vs time.

Even with 10^3 counts included, a single spectrum is subject to fairly large statistical variations because the exponential nature of the spectral distribution rapidly diminishes the number of counts in higher channels. This makes the least-squares fit uncertain.

The single-channel system in the present arrangement can only measure along a fixed central chord, so data for profile calculations, density, etc., must be obtained from other diagnostics. The T_e calculation assumes a Maxwellian electron velocity distribution, negligible profile and absorption effects, and counting rates which are relatively well behaved. It is difficult to check some of these assumptions with the present system.

On the other hand, the system is relatively simple. It collects data routinely and rapidly once it has been adjusted and provided constant plasma parameters are maintained. It uses no absorbing foil except for the beryllium entrance window and thus can measure over a greater T_e range than can a fixed-foil system. It provides T_e measurements within two minutes of a discharge, with moderate time resolution and generally in good agreement with other diagnostics.

2.2.9 Neutron Measurements on ISX-A

J. T. Mihalczo A. C. England

Measurement of the neutron counting rate in ^{3}He proportional counters placed around ISX-A and absolute calibration of these detectors with a ^{252}Cf neutron source located in the center or at nine port boxes on the plasma axis allowed the determination of the ion temperature. For these low temperature plasmas (central ion temperature of 300-500 eV), the neutron yield is very sensitive to temperature (a factor of ten in yield corresponds to ~100-eV change in temperature). Ion temperatures obtained from neutron reaction rates will be compared with those from charge exchange fluxes. Neutron reaction rate measurements were also used to study the effects

of gas puffing (both $H_2 \rightarrow D^+$ and $D_2 \rightarrow H^+$) and the effects of injecting hydrogen pellets into a deuterium plasma.

2.2.10 Diamagnetic Measurements

A. C. England G. R. Dyer
J. T. Mihalczo J. W. Pearce

Preliminary diamagnetic measurements have been made on ISX-A, and two different coil systems have been tried. The first had the diamagnetic coil wound on one of the MHD (Mirnov) loop support frames which was positioned over a bellows. The bucking loop was mounted on the same frame but was sensitive only to the TF variation. This coil system proved to be unsatisfactory, apparently because of the shaking of the coil supports. It was found to be impossible to buck out the variations on the diamagnetic loop from the loop sensing the toroidal field only.

The second system had the diamagnetic loop wound directly on one of the stainless boxes making up the vacuum tank. The bucking loop consisted of four thin coils mounted directly over the coil on all four sides of the vacuum tank. The coils were fitted between the vacuum tank and the fiberglass torque cylinders on the inside and outside; on the top and bottom they were fitted between the box and the flanges on the ports.

The coil on the bellows would have been more desirable because it would have been sensitive to rapid diamagnetic signals. The L/R time of the bellows is ~70 μsec, and diamagnetic fluctuations with a characteristic period longer than this could have been seen.

The coil on the box could only observe diamagnetic fluctuations with periods of ≤4 msec due to the decay of the eddy currents in the thick (0.5-in.) walls.

Diamagnetic measurements on ISX are extremely difficult because of the TF supply in use. The SCR-controlled, 12-phase supply gives a magnetic field ripple on the flat top of ~0.15% at 720 Hz. In addition, there are strong modulations at 30 and 120 Hz and a small ripple at 60 Hz.

Special high performance notch filters at 30, 60, and 120 Hz were built to eliminate these components, and low pass filters with 3-dB points at 100 and 500 Hz eliminated the 720 Hz signal and its higher harmonics.

Rogowski loops on the OH, vertical field, and radial field buses were used to subtract direct pickup. However, only ~1% pickup has been observed and is easily subtracted.

To date, signals have been obtained which appear to be true diamagnetic signals. However, the data has not been correlated with calculations based on Thomson scattering and charge exchange measurements of temperature and interferometer measurements of density.

2.3 ISX-B

2.3.1 Introduction

ISX-B is a new research tokamak which is to replace the present ISX. The device is designed with a rectangular cross-section vacuum chamber and a versatile PF system will allow the creation and control of circular, elliptical, or D-shaped plasmas, with vertical elongation of up to 1.8:1. In addition, two neutral beam injectors will be installed to inject up to 1.8 MW of neutral beam heating power into the tokamak. The combination of plasma shaping and high power heating will allow the study of the equilibrium and stability limits of noncircular, high beta plasmas.

2.3.2 Design Description

The tokamak, illustrated in Fig. 2.42, consists of a stainless steel, rectangular cross-section torus with a major radius of 93 cm and plasma dimensions up to 54 x 100 cm (determined by the limiters). The vacuum vessel has been designed for good experimental access, with 164 diagnostic and pumping ports. The two

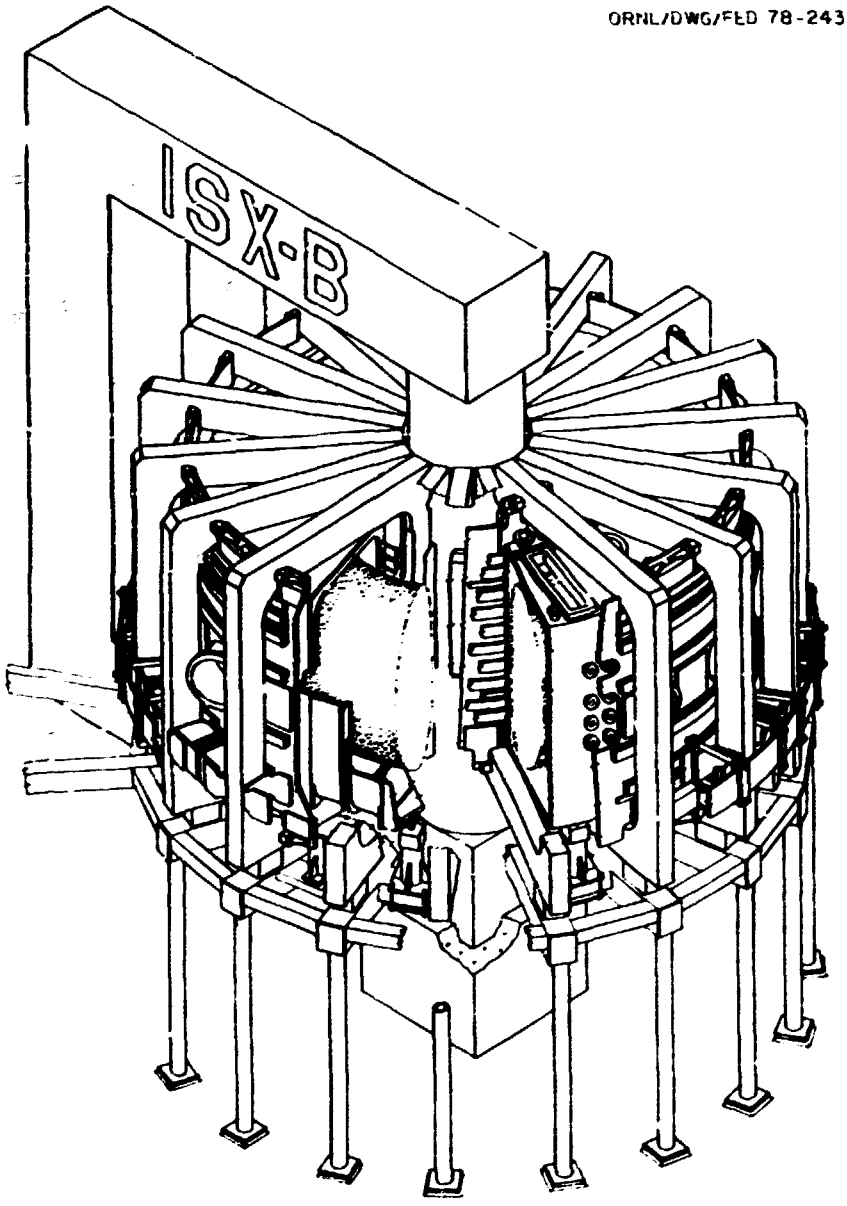

Fig. 2.42. ISX-B tokamak.

neutral beams will be injected tangentially (both in the same direction) through two 28-cm-diam injection ports. A more complete design description of the vacuum vessel is given in Ref. 37.

The new poloidal coil system will be mounted on two fiberglass cylinders which are concentric with the vacuum vessel, similar to the present ISX coil system. The fiberglass cylinders also serve as the torque restraint system for the TF coils.

ISX-B will use the same iron core, TF coils, and power supply and support stand as the present ISX. Most of the poloidal coil supplies will be the same.

2.3.3 Progress in 1977 and 1976 Schedule

The ISX-B project was approved by DMFE in August 1977. Designs of the vacuum vessel, poloidal coils, and torque cylinders were completed, and fabrication of these components was started. Engineering design for most of the electrical modifications and for the neutral beam installation was completed. The neutral beams are being fabricated by the ORMAK Upgrade program and are now in the final assembly phase.

The schedule calls for shutting the present ISX machine down at the end of February 1978. The transition period will last until the end of August, at which time the tokamak, neutral beam systems, and associated power supplies should be installed and ready for testing.

2.3.4 Experimental Program

The primary goal of the ISX-B program is to study the stability and transport of noncircular, high beta plasmas. Table 2.4 lists the expected plasma properties with ohmic heating only, and with 1.8 and 3 MW of injection power, assuming that no large MHD instabilities occur. The neutral beams will initially inject about 1.8 MW into the plasma, but can be upgraded to 3 MW in the future. In addition, the machine has special provision for apparatus which will allow several unique experiments on ISX-B.

High beta stability and transport experiments

Measurements of basic plasma properties (density and temperature profiles, energy confinement times, impurity levels, etc.) are presently being carried out on ISX. This capability will be carried over to ISX-B, utilizing much of the same equipment. New diagnostics for the measurement of the two-dimensional properties of the elongated plasma are under construction. Some problems to be investigated are:

(1) How does plasma confinement depend on plasma shape and beta?

Table 2.4. Plasma parameters expected for ISX-B for three values of neutral beam injection power

	$P_{inj} = 0^a$	$P_{inj} = 1.8$ MW^b	$P_{inj} = 3$ MW^b
$\bar{T}_t$, T	1.2	1.2	1.2
$\sigma = b/a$	1	1.5	1.5
I, kA	130	200	200
$q_{limiter}$	3.5	3.8	3.8
$\bar{n}_e$, cm^{-3}	4×10^{13}	$4\text{-}8 \times 10^{13}$	$\geq 15 \times 10^{13}$
$\bar{T}_e$, eV	450	$\sim$1500	$\sim$1500
$\bar{T}_i$, eV	300	$\sim$1500	$\sim$1500
Z_{eff}	<2	$\leq$2	$\leq$2
τ_E, msec	30^c	28-56	$\sim$60
$\bar{\beta}$, %	0.5	3-6	$\geq$10

[a] These numbers have been achieved on ISX-A. For ISX-B we assume that $\tau_B = \tau_A f(n_B/\tau_A) 2\sigma^2/1 + \sigma^2$, where $f(n_B/n_A) = (n_B/n_A)^\alpha$ with $\alpha = 0.5\text{-}1$. n_B and n_A are the line densities in the respective tokamaks. We assume that both density and temperature profiles are parabolic, and the temperatures quoted are volume averages.

[b] Scaling laws for a noncircular plasma with $P_{inj} > P_{OH}$ have not been experimentally investigated. Consequently, the numbers for $P_{inj} = 1.8$ and 3 MW are estimates based on extrapolations of present knowledge.

[c] $\tau_E = 21$ msec was achieved in hydrogen (ISX-A).
$\tau_E = 30$ msec was achieved in deuterium (ISX-A).

(2) What are the maximum beta stability limits for a plasma subjected to massive heating, and how do these limits change as a function of plasma elongation and triangularity?
(3) How do tokamak plasmas behave when the injected power is 5-10 times the ohmic heating power?

Ripple injection experiment

A diagnostic neutral beam injector (40 kV, 3 A) which will direct the beam vertically upward through the center of the plasma is to be installed. Two coils, located under the machine and adjacent to the diagnostic injector, will be able to cause a ripple in the toroidal magnetic field, with the field perturbation being larger at the bottom of the machine than at the top. This field will allow an experiment to test the concept of ripple injection, which, if successful, would allow the heating of reactor-size tokamaks with neutral beams of much lower energy than would be required for direct injection.[38] These experiments are to be carried out in collaboration with PPPL.

ECRH experiment

Seven ports have been designed on the vacuum vessel to allow the injection of microwave energy from the inside of the torus. The frequency of this radiation will be at the electron cyclotron frequency at some location in the plasma and will allow the study of electron cyclotron resonant heating in a hot tokamak plasma. This work, to start in 1979 provided funds are available, will use a 200-kW source at 28 or 35 GHz. The experiments are designed to study the effects of ECRH alone, both for bulk heating and for preionization, and to use ECRH in conjunction with neutral beam heating to modify the plasma profile and to study the effects on high beta stability.[39]

Bundle divertor

Design studies have been completed for the use of a bundle divertor on ISX-B, and provision has been made in the vacuum vessel and poloidal coil design for its installation. This experiment is designed to help in the reduction of impurities in the plasma and to study the effects of such a device on a high beta, noncircular tokamak plasma. Results from DITE[3] indicate that plasma refueling must be done in conjunction with a bundle divertor experiment. To that end, plans exist for injecting solid hydrogen pellets of submillimeter diameter into the machine.[41]

2.3.5 Charge Exchange Diagnostic System for ISX-B

J. T. Mihalczo J. F. Lyon
G. H. Neilson R. E. Worsham

The neutral particle diagnostic system for spatially resolved ion measurements on ISX-B employs a diagnostic neutral beam charge exchange analyzer combination (both a tangential analyzer and a perpendicular analyzer array view the diagnostic beam). Among the uses of this system are location temperature measurements in single (H or D, or mixed (H and D) plasmas, measurement of ripple-enhanced trapping of the diagnostic beam, and measurement of beam attenuation. The tangential analyzer has been tested on ISX-A and is described in Sect. 2.2.6. The perpendicular array and diagnostic beam configuration are shown in Fig. 2.43.

Some features of the diagnostic beam are horizontal translation to provide radial profile capability and variable energy up to 40 keV.

Some features of the perpendicular array are simultaneous mass-energy analysis (H and D) up to 50 keV by use of a velocity filter, electrostatic analyzer combination; energy spectral determination within 10 msec by synchronously varying the electric fields in the

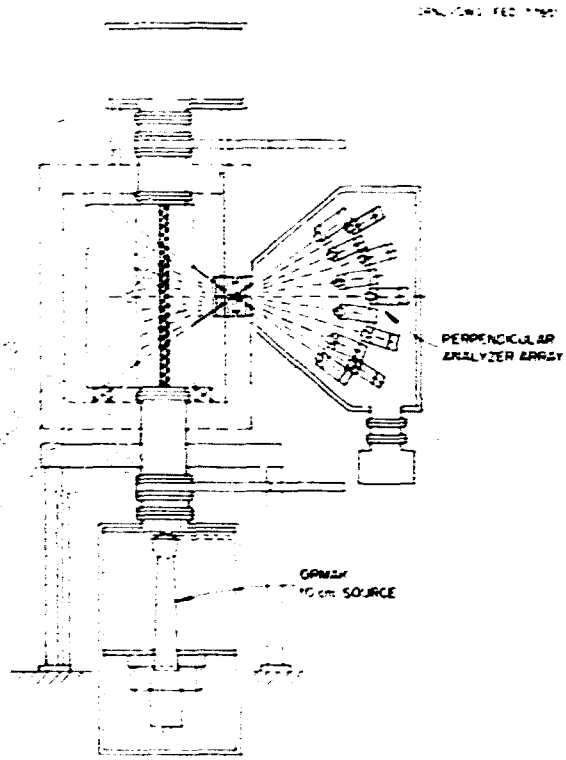

Fig. 2.43. Perpendicular analyzer, diagnostic beam configuration on ISX-B.

velocity filter and electrostatic energy analyzer; multipoint capability by simultaneously viewing the diagnostic beam with several analyzer modules; and variation of the analyzer viewing angle from -7° to +14° from perpendicular. A photograph of a single perpendicular analyzer module with four detection channels is shown in Fig. 2.44. This module will view the plasma center, and other modules will have two channels each and will view the off-center position.

2.4 ORMAK UPGRADE (NEUTRAL BEAM SYSTEMS FOR ISX-B)

L. A. Berry
J. D. Callen
A. R. Kemp
C. M. Loring
H. C. McCurdy
C. C. Queen
W. L. Stirling

The original purpose of the ORMAK Upgrade program was to design and construct a new research tokamak designed specifically for neutral beam heating experiments and intended to replace ORMAK as the principal tokamak physics device in the ORNL program. Because of budget constraints and changes in fusion program priorities, work on the tokamak part of ORMAK Upgrade was stopped in February 1977, and the available resources were concentrated towards completing the vertical field power supply and the neutral beam systems for use in high beta experiments with ISX-B (Sect. 2.3). A later reevaluation of tokamak research needs led us to conclude that the principal objectives of ORMAK Upgrade will be effectively met by the combination of planned high beta experiments in ISX-B and the proposed LPTT (Sect. 2.5). Consequently, there are no plans to complete the ORMAK Upgrade tokamak.

Two neutral beam systems consisting of beam lines, electrical supplies, and related instrumentation will be completed for use with ISX-B. The new accel power supplies being purchased will not be ready for ISX-B initial operation; for an interim period ISX-B will time-share modules of the existing 150-kV power supply system.

2.4.1 Neutral Beam System Design

The beam lines for ISX-B are basically the same design as previously provided for PLT, with minor modifications to simplify certain features and to facilitate a future increase of pumping in the drift tube region. The two neutral beam systems initially will have a target capability of 1.8 MW of neutral beam power injected into the ISX-B plasma. The injection capability can be increased to 3 MW by proposed modification of the beam lines and replacement of the 60-A, PLT-type ion sources with the 100-A sources being developed under the neutral beam program; the electrical systems initially installed, with the possible exception of the decel supplies, are designed to be adequate for driving the 100-A sources.

Physical characteristics and performance goals of the neutral beam systems are given in Table 2.5.

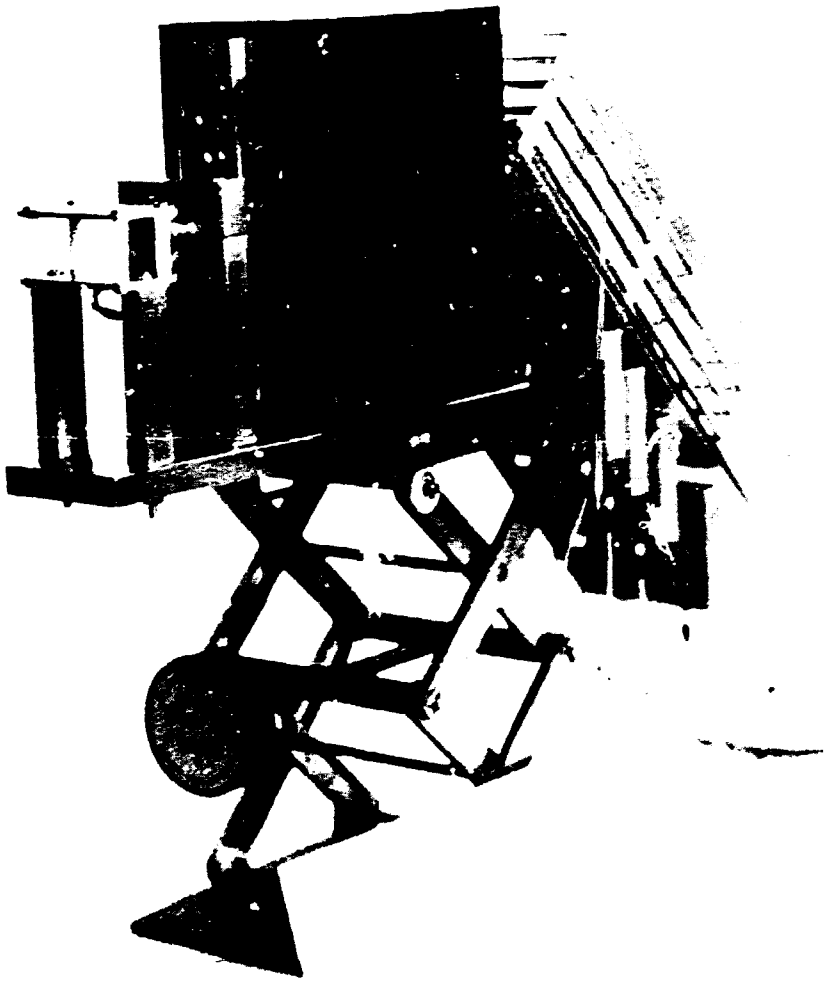

Fig. 2.44. The single perpendicular analyzer module with four detection channels.

2.4.2 Progress in 1977

The principal activities were detailed design of the neutral beam systems (which was about 70% completed), purchase and fabrication of system components, and assembly of beam lines and electrical systems as components were received.

Tokamak systems

The 5-MW, 1000-2000-V power supply planned for the ORMAK Upgrade vertical field system will be used instead to drive the ISX-B outer coils. The supply was delivered by Robicon Corporation in October 1977 and installed in the enclosure that houses the 72-MW TF power supply. Electrical and instrumentation installation will be completed during the conversion of ISX-A to ISX-B.

Neutral beam systems

Procurement and fabrication of beam line mechanical components were about 80 completed; assembly of beam lines was started and about 25 completed. Since the cryocondensing pumps appear to be a critical schedule item, parallel

Table 2.5 ISX-B neutral beam systems baseline reference design

Physical characteristics

Neutral beam injectors

Injector design	PLT-type
	10-cm-diam grid
	40-kV accel
	65-A drain
Number of injection lines	2
Number of injectors total	2

Injector power supplies

Accel supplies	New supplies
Number	2
Rated output	60 kV
	65-A pulses @ 10% duty
	130-A pulses @ 3% duty
Insulation	132 kV
Decel supplies	Modify existing ORMAK
Number	2
Rating	5 kV at 6 A
	3 kV at 10 A

Performance goals

Neutral beam injectors

Injection energy	40 keV
Injected power	1.8 MW
Design base pressure	2 x 10^{-7} Torr
Gas loading to torus per shot	1 Torr-liter

procurement efforts were initiated with two potential suppliers: Arnold Engineering Development Center (Air Force) and United Technologies Research Center.

A purchase order for two accel power supplies with capability for driving 100-A sources was placed with Universal Voltronics Corporation at a purchase price of $738 K and vendor-estimated delivery of 44 weeks (July 1978). The source and modulator tables were redesigned to be adequate for 100-A sources, and major components were purchased and received. Assembly of the modulator tables was about 90% completed, and the source tables were about 50% completed. An existing ORMAK decel supply was modified, and tests indicated that it would be suitable for ISX-B neutral beams. Modification of two additional ORMAK supplies was initiated. The neutral beam systems will be completed in 1978.

2.5 LONG PULSE TECHNOLOGY TOKAMAK

John Sheffield

The LPTT program is proposed to support and speed up the realization of a PEPR-TNS by providing extensive systems integration and prototypical component tests in collaboration with various industries. LPTT will have superconducting coils in a modular assembly allowing very good access, which will permit tests of: a variety of high beta poloidal systems; a variety of plasma cleaning techniques, including a new style of bundle divertor which has great potential for use in a reactor; and a variety of heating methods, initially including neutral injection at a level sufficient to give reactor level thermal power densities. Operation is proposed with pulse lengths of at least 20 sec

and with the possibility of a high duty cycle. LPTT systems will be designed for ease of maintenance and in the limit for remote handling. It is considered that while the ultimate test of remote handling is in the hostile radioactive environment, this is not necessarily the best environment to iron out problems and establish optimum designs.

Studies have been made to identify the region of minimum size for LPTT which would satisfy the conceived goals of the program and the constraints set by physics and technology. This work has benefited from the previous design studies at ORNL of ORMAK-II and TFTR. A tokamak design which is representative of the minimum size region has the following parameters.

Pulse length	≥20 sec
Major radius	230 cm
Minor radius	65 cm
Maximum plasma noncircularity	1.6
Number of toroidal coils	16

	Stage 1 (low field)	Stage 2 (high field)	
		Basic	Extended
Toroidal field	10-15 kG	35 KG	50 kG
Plasma current	0.3-0.5 MA	1 MA	1.5 MA
Heating power	~5 MW	12-24 MW	~24 MW

REFERENCES

1. D. Meisel et al., *Proc. 6th Int. Conf. on Plasma Physics and Controlled Nuclear Fusion Research*, Vol. I, p. 259 (1977).
2. W. Lotz, Garching Plasma Physics Institute Report IPP 1/62, Garching, F.R.G. (1967).
3. C. Breton, C. de Michelis, and M. Mattioli, Nucl. Fusion 16, 891 (1976).
4. R. Jensen, D. Post, B. Tarter, W. Grasberger, and W. Lokke, PPPL Report 1334, Princeton, New Jersey (1977).
5. R. C. Isler, R. V. Neidigh, and R. D. Cowan, Phys. Lett. 63A, 295 (1977).
6. M. Murakami et al., Phys. Rev. Lett. 39, 615 (1977).
7. *Fusion Energy Division Annual Progress Report for Period Ending December 31, 1976*, ORNL-5275, Sect. 2.1.10, p. 49, Oak Ridge, Tennessee (June 1977).
8. N. R. Sauthoff, S. von Goeler, and W. Stodiek, *A Study of Disruptive Instabilities in the PLT Tokamak Using x-ray Techniques*, PPPL-1373, Princeton, New Jersey (January 1978).
9. *Thermonuclear Division Annual Progress Report for Period Ending December 31, 1975*, ORNL-5154, Sect. 2.1.4, pp. 29-31, Oak Ridge, Tennessee (June 1976).
10. D. J. Sigmar, J. F. Clarke, R. V. Neidigh, and K. L. Vander Sluis, Phys. Rev. Lett. 33, 1376 (1974).
11. M. G. Bell, *Proc. 8th European Conf. on Controlled Fusion and Plasma Physics*, Vol. I, p. 11 (1977).
12. T. E. Stringer, Phys. Fluids 13, 810 (1970).
13. M. N. Rosenbluth, P. H. Rutherford, J. B. Taylor, E. A. Frieman, and L. M. Kovrizhnikh, *Proc. 4th Int. Conf. on Plasma Physics and Controlled Nuclear Fusion Research*, Vol. I, p. 495 (1971).

14. F. L. Hinton and R. D. Hazeltine, Rev. Mod. Phys. 48, 239 (1976).

15. S. P. Hirshman, Phys. Fluids 21, 224 (1978).

16. R. J. Weldon and D. J. Sigmar, ORNL/TM-6198, Oak Ridge, Tennessee (March 1977); also submitted for publication in Plasma Phys.

17. C. E. Bush and J. F. Lyon, ORNL/TM-6148, Oak Ridge, Tennessee (December 1977); to be published in Nucl. Fusion.

18. A. C. England, H. C. Howe, J. T. Mihalczo, and R. H. Fowler, ORNL/TM-6035, Oak Ridge, Tennessee (October 1977); submitted to Nucl. Fusion.

19. *Fusion Energy Division Annual Progress Report for Period Ending December 31, 1976*, ORNL-5275, Sect. 2.1.3, pp. 25-32, Oak Ridge, Tennessee (June 1977).

20. M. Murakami, J. D. Callen, and L. A. Berry, Nucl. Fusion 16, 347 (1976).

21. D. L. Jassby, D. R. Cohn, and R. R. Parker, Nucl. Fusion 16, 1045 (1976).

22. J. Hugill and J. Sheffield, Nucl. Fusion 18, 15 (1978).

23. T. H. Jensen et al., Phys. Rev. Lett. 34, 257 (1975).

24. E. S. Marmar, J. L. Cecchi, and S. A. Cohen, Rev. Sci. Instrum. 46, 1149 (1975).

25. S. A. Cohen, J. L. Cecchi, and E. S. Marmar, Phys. Rev. Lett. 35, 1507 (1975).

26. T. Ohkawa, Kaku Yugo Kenkyu 32, 67 (1974).

27. K. H. Burrell, Phys. Fluids 19, 401 (1976) and 20, 342 (1977).

28. M. S. Chu and J. M. Rawls, Phys. Fluids 20, 1787 (1977).

29. S. K. Wong, Phys. Fluids 21, 299 (1978).

30. R. J. Colchin and T. C. Jernigan, J. Nucl. Mater. 63, 83 (1976).

31. K. H. Burrell, General Atomic Co. Report GA-14804, San Diego, California (September 1977); also submitted to Rev. Sci. Instrum.

32. Abstract of paper presented at the 3rd Int. Conf. on Plasma Surface Interactions in Controlled Fusion Devices, Culham, England, April 3-7, 1978; proceedings to be published in J. Nucl Mater.

33. *Fusion Energy Division Annual Progress Report for Period Ending December 31, 1976*, ORNL-5275, pp. 62-63, Oak Ridge, Tennessee (June 1977).

34. L. A. Artsimovich, Nucl. Fusion 12, 215-252 (1972).

35. *Fusion Energy Division Annual Progress Report for Period Ending December 31, 1976*, ORNL-5275, p. 68, Oak Ridge, Tennessee (June 1977).

36. C. F. Barnett and J. A. Ray, "A Calibrated Neutral Atom Spectrometer for Measuring Plasma Ion Temperatures in the 0.165 to 10 keV Energy Region," Nucl. Fusion 12, 65 (1972).

37. D. W. Swain, T. E. Smith, D. J. Sigmar, and M Murakami, ORNL/TM-5985, Oak Ridge, Tennessee (September 1977).

38. R. J. Goldston, D. L. Jassby, H. . Towner, R. H. Fowler, J. F. Lyon, J. A. Rome, and T. Brown, PPPL Report No. 1398 (October 1977); also published in *Proc. 7th Symp. on Engineering Problems of Fusion Research*, Vol. II, p. 1333 (1977).

39. A. C. England, C. M. Loring, O. C. Eldridge, W. Namkung, H. C. Howe, G. L. Campen, H. L. Mitchell, and D. B. Ratchelor, ORNL/TM-6011, Oak Ridge, Tennessee (October 1977).

40. J. W. M. Paul et al., Culham Laboratory Report No. CLM-D-502, Culham, England (October 1977).

41. S. L. Milora and C. A. Foster, *ORNL Neutral Gas Shielding Model for Pellet-Plasma Interaction*, ORNL/TM-5776, Oak Ridge, Tennessee (May 1977).

DIAGNOSTIC DEVELOPMENT

C. F. Barnett[1]
D. A. Brisson[2]
S. E. Greco[3]
D. P. Hutchinson[1]
C. H. Ma[4]
R. V. Neidigh
J. A. Ray[1]
P. A. Staats[1]
D. M. Thomas[5]
K. L. Vander Sluis[1]

Abstract. During the past year the far-infrared or submillimeter diagnostic research program resulted in three major developments: (1) an optically pumped 0.385-μm D_2O-laser oscillator-amplifier system was operated at a power level of 1 MW with a line width of less than 50 MHz; (2) a conical Pyrex submillimeter laser beam dump with a retention efficiency greater than 10^4 was developed for the ion temperature Thomson scattering experiment; and (3) a new diagnostic technique was developed that makes use of the Faraday rotation of a modulated submillimeter laser beam to determine plasma current profile. Measurements of the asymmetric distortion of the H_α (6563 Å) spectral line profile show that the effective toroidal drift velocity, $dv_{\parallel i}/dT_i$, may be used as an indicator of plasma quality and as a complement to other ion temperature diagnostics.

3.1 HIGH POWER SUBMILLIMETER LASERS FOR THOMSON SCATTERING

During the past year research continued on the development of a 1-MW submillimeter laser to be used to measure the ion temperature of plasmas in the next generation of tokamaks. For such tokamaks, with plasma densities of 10^{14}, the requirements of the laser system are: (1) 1 MW of output power; (2) a pulse length of at least 200 nsec; (3) laser and viewing dumps with a rejection ratio of better than 10^{-4}; and (5) spectral purity (peak-to-valley ratio of pulse amplitude) of no less than 10^4.

Early in the year a decision was made to concentrate on D_2O (0.385 μm) as the lasing gas because of its high efficiency of converting optical pump power to submillimeter power. Briefly, the optical system is composed of a continuous wave, tuned CO_2 laser whose output forces a 150-J, pulsed CO_2 laser to oscillate near the absorption pump line of D_2O. The output from the CO_2 pump is split, with part of the beam pumping an unstable resonator-oscillator and the other part pumping a beam-expanding optics amplifier. Since most submillimeter lasers tend to operate in a superradiant mode, precautions must be taken with the amplifier to establish single mode amplification. Thus, the amplifier is 1 m long, and the beam-expanding optics makes use of a large volume of D_2O gas to provide the required power. We have operated the system successfully at low power levels. The frequency spectrum was determined using a Schottky diode as a detector; the time profile of the spectrum was obtained by a Tektronix fast transit digital analyzer. Fourier analysis of the time profile gave the frequency spectrum of the output pulse. For the CO_2 pump laser, the full width at half maximum (FWHM) of the time profile and frequency was 100 nsec and 5 MHz, respectively. The characteristics of the oscillator output were 320 nsec and approximately 2 MHz. Figure 3.1(a) and 3.1(b) shows output characteristics of the complete system. The time profile in Fig. 3.1(a) has an FWHM of

1. Physics Division.
2. Graduate student, North Carolina State University, Raleigh, North Carolina.
3. Summer student, LaSalle College, Philadelphia, Pennsylvania.
4. On sabbatical leave from the University of Mississippi, University, Mississippi.
5. Summer student, University of Texas at Austin, Texas.

BLANK PAGE

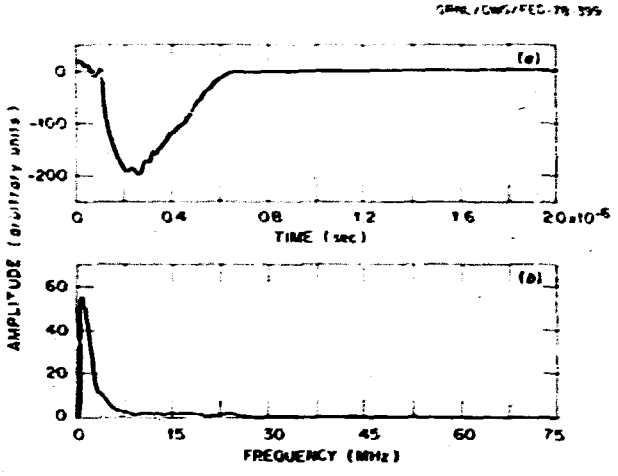

Fig. 3.1. (a) Time profile of 0.385-μm D_2O laser oscillator-amplifier system operating at 200-kW output power; (b) Fourier transform of the time profile of Fig. 3.1(a). Frequency at FWHM is approximately 4 MHz.

150 nsec, and the frequency profile has an FWHM of 4 MHz. At frequencies exceeding 50 MHz, no signal was observable.

With the system operating in this configuration, the maximum power obtainable was 200 kW, being limited by the coupling of the CO_2 pump power to the D_2O pump line in the amplifier. This limitation is determined by an offset of 325-MHz difference in the tuned CO_2 pump line and the D_2O line. This decreased coupling was overcome by placing a 5-m-long, 15-cm-diam extension at the exit end of the amplifier. With full pump power, 1 MW of D_2O power has been obtained with an FWHM pulse width of 100 nsec and an FWHM frequency of 5 MHz. The frequency spectrum of the complete system is shown in Fig. 3.2. There is some evidence of low level narrow-band superradiance for this configuration. The system appears to be operating as a pure Raman, two-photon laser at low pressure (1 Torr) and as a mixture of a Raman and a normal transition laser at higher pressures (5 Torr). Studies are under way to further improve the power output and reproducibility of the high power pulses with the use of a small, atmospheric pressure CO_2 laser containing an intercavity Fabry-Perot interferometer to injection tune the 150-J CO_2 pump laser. The expected tuning range is ±1.5 GHz, which will permit operation of the pump CO_2 laser at the D_2O pump line and eliminate the need for the 5-m extension of the amplifier system.

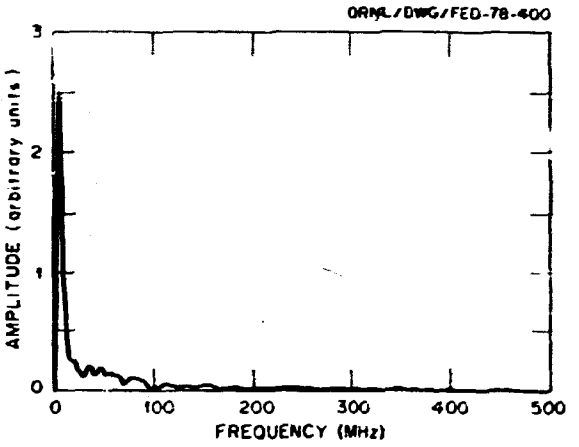

Fig. 3.2. Frequency profile of D_2O submillimeter laser operating at 1-MW power level with 5-m-long, 15-cm-diam extension to the D_2O laser amplifier.

3.2 LASER BEAM DUMPS FOR SUBMILLIMETER WAVELENGTHS

One of the many problems encountered in the measurement of plasma ion temperature by Thomson scattering is the extreme smallness of scattered signal compared with input power. For most plasmas of interest this ratio is 10^{-14}. Thus, highly efficient laser beam and viewing dumps are essential to prevent the desired signal from being greatly exceeded by the reflected primary beam. Vacuum requirements and the long wavelengths preclude the use of many of the conventional beam dump techniques.

A large hemiellipsoid mirror was constructed for measuring the retention efficiency of various beam dump designs. In the tests the dump was placed at one focus of the mirror, and a detector

was positioned at the other focus. Submillimeter radiation, generated by a pulsed, superradiant D_2O laser, was focused through an aperture (1-cm-diam) in the back of the elliptical mirror onto the dump. A gold mirror with a reflectivity greater than 98% was placed at the same position as the dump and used as a reference. Because it is easily constructed, a pyramid cone configuration was used to evaluate several materials, including Lucite, flint glass, carbon spheres (250-300-μm-diam) epoxyed to an aluminum surface, and a circular cone of Pyrex. The reflection coefficients of the Lucite, flint glass, and Pyrex were measured to be less than 10^{-4}. Studies indicated that to provide reflection coefficients of 10^{-4} the ratio of the length of the dump to its entrance diameter should be at least 10. Further refinements are being made to the drawn Pyrex cone design for the ISX-B experiment.

3.3 FARADAY ROTATION FOR MEASURING PLASMA CURRENT DENSITY PROFILES

When tokamak plasmas are studied experimentally, it is important to be able to measure the poloidal magnetic field and the toroidal plasma current, as these parameters confine and heat the plasma and are responsible for MHD stability. Theoretical analyses have shown that in some cases the poloidal magnetic field, and thereby the plasma current, can be determined by directing a linearly polarized electromagnetic wave through the plasma and measuring the Faraday rotation of the polarization. Since the rotation angle is proportional to the square of the wavelength, the longer the wavelength, the easier it becomes to measure the rotation angle. However, it is desirable to use shorter wavelengths to improve the spatial resolution and wave transmission. As a result, even at far-infrared (FIR) wavelengths, techniques are required to measure rotation angles which, for present-day tokamak experiments, may be only a fraction of a degree. During the past year we experimentally investigated the possible use of polarization modulation techniques in a submillimeter wave polarimeter to measure such small rotation angles with accurate time resolution.

The experimental configuration is shown schematically in Fig. 3.3. The source of the system was a 393-μm (cw) HCOOH laser, pumped with a CO_2 laser. The FIR laser beam passed

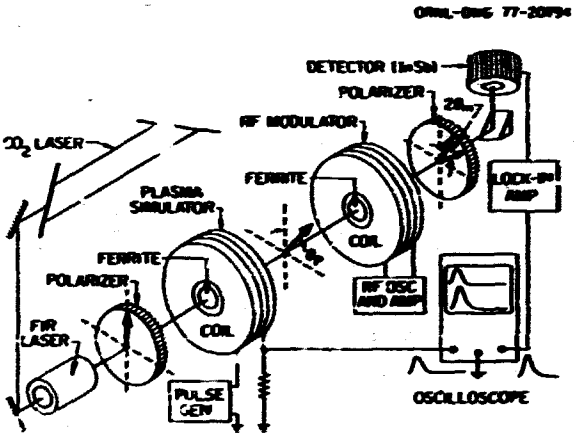

Fig. 3.3. Experimental configuration for the submillimeter wave polarimeter.

through two wire grid polarizers, a plasma simulator, and a polarization modulator that was driven by rf current. The polarizers were mounted in crossed orientation. For small modulation, the amplitude of the output signal at the modulation frequency was directly proportional to $\theta_m \sin(2\theta_p)$, where θ_m is the amplitude of the modulation angle and θ_p is the angle of the simulated plasma rotation. In preliminary bench tests, ferrite polarization rotators were used as the plasma simulator and the rf modulator. A liquid helium cooled InSb detector and lock-in amplifier were employed to measure the low level laser signal. The simulated plasma rotation and the output of the lock-in amplifier are shown in Fig. 3.4. In Fig. 3.5, both theoretical and experimental results for simulated plasma are summarized, with the modulation angle given as a parameter. A polarization sensitivity of 26 mV/milliradian

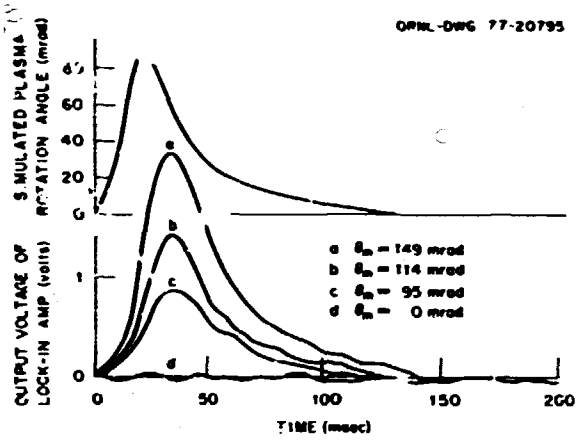

Fig. 3.4. Simulated and measured rotation angles at a modulation frequency of 9.1 kHz.

was achieved at a modulation angle of 149 milliradians with a FIR laser power of 4 mW. The system was installed at ISX-A for preliminary tests, but because of large losses of submillimeter power in transmission, low sensitivity of the available detector, and extremely high x-ray fluxes, the signal at the modulation frequency was indistinguishable from the noise.

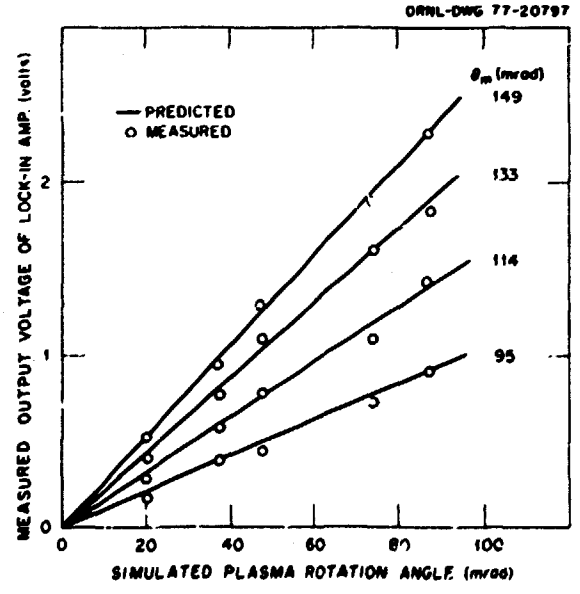

Fig. 3.5. Predicted and measured rotation angles at a modulation frequency of 9.1 kHz.

3.4 A PLASMA QUALITY INDICATOR FOR TOKAMAKS

R. V. Neidigh

The asymmetric distortion of the H_α (6563 Å) spectral line profile radiating from the ORMAK-produced plasma bears the signature of its proton velocity distribution.[1,2] The relation of the effective toroidal drift velocity to the ion temperature, $dv_{\parallel i}/dT_i$, may be used as a shot-to-shot plasma quality indicator since $dv_{\parallel i}/dT_i$ appears to be sensitive to injected hydrogen gas (gas puffing) and neutral injection which, in turn, alter Z_{eff} (see Fig. 3.6).

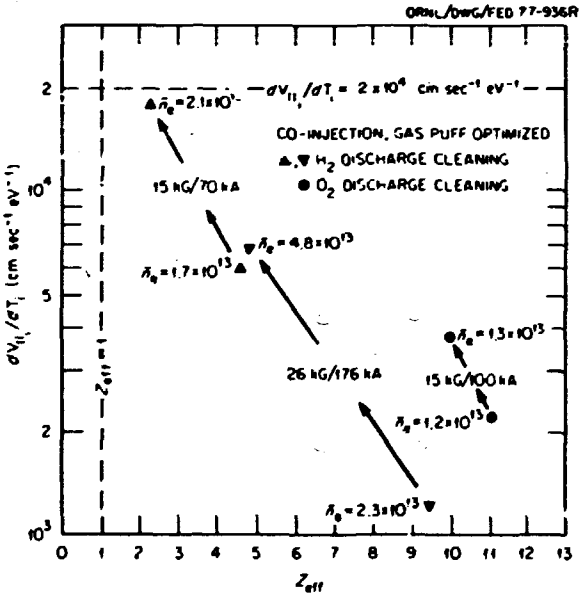

Fig. 3.6. Gas puff optimization. Neutral beam injection and maximum ohmic heating raise the impurity level (Z_{eff}). The optimized hydrogen gas puff raises the density and also the toroidal drift velocity, indicative of a lower Z_{eff}. The effect is noticeably less if the liner has been discharge cleaned with oxygen. The dashed horizontal line was the average $dv_{\parallel i}/dT_i$ found in ORMAK I with a single-channel rapid-scan spectrometer (Ref. 1).

Although the source of H_α radiation is predominantly the cold edge of the plasma, the intensity of radiation in the wings of the line

profile is sufficiently above the noise level to permit analysis of dv_i/dT_i in the energy range up to ten times thermal, as shown in Fig. 3.7. This is a worthwhile complement to the ion temperature determined from charge exchange analysis of the high energy tail of the distribution function.

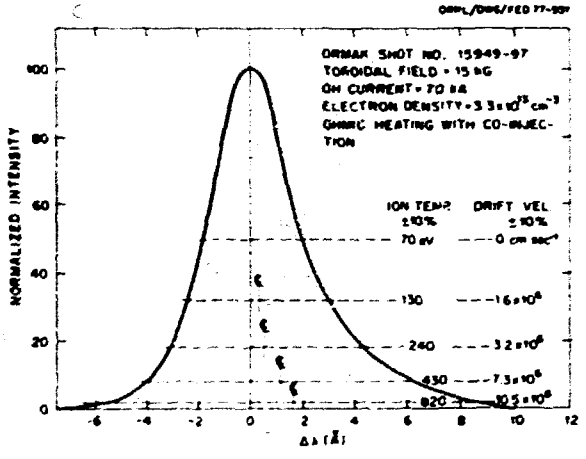

Fig. 3.7. Spectral line profile of H_α (6563 Å). The line width and displacement of its center of gravity are measured at intensity levels of 2, 8, 18, 32, and 50% of maximum and are related to ion-temperature and toroidal drift velocity, respectively.

REFERENCES

1. D. J. Sigmar, J. F. Clarke, R. V. Neidigh, and K. L. Vander Sluis, Phys. Rev. Lett. 33, 1376 (1974).
2. R. V. Neidigh and D. J. Sigmar, "Hot-Ion Distribution Function in ORMAK, the Oak Ridge Tokamak," to be published in Plasma Phys. and as ORNL/TM-6198.

PLASMA THEORY

J. D. Callen, Section Head

R. A. Dory, Assistant Section Head

T. Amano[1]	J. Benavit[2]	A. H. Kritz[2]	G. J. Sigmar[3]
C. H. An[2]	G. C. Eldridge[2]	G. K. Lee[3]	D. Smith[2,3]
D. E. Arnurius[2]	G. A. Emmert[11]	S. J. Lynch[3]	M. Soler[6]
[illegible]	[illegible]	D. G. McAfee[12]	D. A. Spong
B. Batchelor	J. E. Francis, Jr.	J. E. McCune[13]	W. M. Stacey, Jr.[3]
R. G. Bateman, Jr.	P. W. Gaffney[3]	J. R. McNally, Jr.	C. R. Stewart, Jr.[3]
C. O. Beasley, Jr.[3]	R. C. Goldfinger[3]	H. K. Meier	K. A. Stewart[20]
S. K. Borowski[4]	R. K. Gryder[12]	A. T. Mense	D. J. Strickler[3]
I. Burnett, III	C. E. Hammons	J. P. Moore[16]	J. S. Tolliver[3]
R. D. Burris[3]	E. S. Harris[15]	J. K. Munro, Jr.[3]	K. T. Tsang
B. Carreras[6]	C. L. Hedrick, Jr.	W. Namkung[17]	T. C. Tucker[3]
N. F. Carver[5]	H. R. Hicks[3]	D. B. Nelson	N. A. Uckan
P. J. Catto[7]	J. T. Hogan	D. R. Overbey	T. Uckan[21]
L. A. Charlton[3]	J. A. Holmes[3]	L. W. Owen[3]	G. Vahala[22]
D. N. Clark[3]	W. A. Houlberg	C. E. Parker	W. I. van Rij[3]
W. A. Cooper[6]	H. C. Howe	Y-K. M. Peng	B. V. Waddell
E. C. Crume, Jr.[3]	M. A. Iskra[3]	J. W. Reynolds[18]	H. Weitzner[23]
J. N. Davidson[4]	E. F. Jaeger	J. A. Rome	J. C. Whitson[3]
L. E. Deleanu[3]	C. O. Kemper[3]	K. E. Rothe[3]	R. M. Wieland[3]
	O. C. Yonts	M. A. Zuniga[24]	

1. Permanent address: Osaka University, Osaka, Japan.
2. Student, University of Tennessee, Knoxville, Tennessee.
3. UCC-ND Computer Sciences Division.
4. On leave of absence to Max Planck Institut für Plasma Physik, Garching, Federal Republic of Germany.
5. Student, University of Michigan, Ann Arbor, Michigan.
6. Visitor from Spanish Nuclear Energy Commission, Madrid, Spain.
7. Consultant, University of Rochester, Rochester, New York.
8. Consultant, Georgia Institute of Technology, Atlanta, Georgia.
9. Northwestern University, Evanston, Illinois.
10. Consultant, University of Tennessee, Knoxville, Tennessee.
11. University of Wisconsin, Madison, Wisconsin.
12. On leave of absence to IAEA, Vienna, Austria.
13. Hunter College, New York, New York.
14. Consultant, Exxon Nuclear Co., Inc., Richland, Washington.
15. Consultant, Massachusetts Institute of Technology, Cambridge, Massachusetts.
16. UCC-ND Engineering Division.
17. Postdoctoral Staff, University of Tennessee, Knoxville, Tennessee.
18. Instrumentation and Controls Division.
19. On leave of absence from Massachusetts Institute of Technology, Cambridge, Massachusetts.
20. On leave of absence to University of Tennessee, Knoxville, Tennessee.
21. Now with High Beta Plasma Section, Fusion Energy Division.
22. ORAU Faculty Research Participant, College of William and Mary, Williamsburg, Virginia.
23. New York University, New York, New York.
24. Student, Massachusetts Institute of Technology, Cambridge, Massachusetts.

BLANK PAGE

Abstract. While plasma theory has been evolving toward more realistic models of magnetically confined plasmas for more than two decades now, very significant advances were made at ORNL in the past year. Theoretical techniques were developed for reliably modeling the finite beta, noncircular, resistive, finite collisionality plasmas confined in tokamaks and in the ELMO Bumpy Torus. An important indication of the realism of these theoretical models is the fact that many of them are bei , compared in very detailed ways with present experimental results. The intensive interplay between theory and experiment has led to improvements in both and also to a significant deepening of our understanding of plasma confinement.

In EBT theory the primary emphasis has been on developing methods for calculating the self-consistent ambipolar potential because it dominates plasma transport. Stimulated by experimental measurement of this important element of plasma confinement, one-dimensional kinetic and fluid transport codes have been developed to take into account the numerous and highly nonlinear effects of the ambipolar potential on transport. A very encouraging result of this work is that the plasma parameters, including temperatures, densities, and ambipolar potential, can be predicted within a factor of about two using a totally neoclassical model, i.e., with no need to introduce anomalous transport processes. Other EBT theory studies this past year include consideration of macroscopic and microscopic instabilities and microwave heating processes.

The MHD theory group has continued its pioneering work in developing the concept of high beta tokamaks. This work includes consideration of the dynamic evolution of injection heated plasmas to high beta; the PF systems (including in detail the iron core effects in ISX-A and -B) required to position, control, and shape these plasmas; and the stability of these plasmas against ballooning modes. The ballooning mode stability question has been examined with initial value, semi-analytic (BALOON), and energy principle (ERATO and PEST) computer codes. The answer from these studies is that volume-average betas in the range of 5-10% should be achievable. Another major MHD theory development is the very successful correlation of the resistive MHD studies with the observed macroscopic modes in tokamaks. As reported last year, the m = 1/n = 1 resistive modes have been shown to instigate internal disruptions in tokamaks. This past year it was shown that the theoretical nonlinear saturation level of the 2/1 resistive modes agrees in detail and also in scaling with the 2/1 Mirnov oscillations observed in ORMAK. Further, it was shown that an unstable coupling between the 3/2 and 2/1 modes causes a drastic rearrangement of the current profile in the very short growth time of the 2/1 mode; this has been proposed as the mechanism causing the disruptive instability. The 2/1 theoretical growth period is consistent with the disruptive instability time in tokamaks from LT-3 to PLT — about three orders of magnitude in time scale.

The most startling new development in kinetic theory this past year was the demonstration from both numerical and analytic investigations that, contrary to most drift wave literature, the collisionless drift wave is *not* unstable in a smoothly sheared magnetic field. The region near the rational surface where the wave phase velocity exceeds the electron thermal speed (and which has been neglected previously) introduces just enough damping to overcome the growth from other spatial regions so that the overall mode is damped. Even though the collisionless drift wave is damped, the trapped particle modes are still unstable. Another major development in the kinetic theory of tokamaks was the introduction of the "magnetic flutter" model, in which microinstabilities break up the flux surfaces into microscopic islands and thereby provide a new and more plausible mechanism for explaining the anomalous radial electron heat transport in a tokamak. The remaining kinetic theory activities were directed toward an increasing degree of realism

code [illegible] including [illegible] noncircular cross sections, [illegible] toroidal field ripple effects on transport and charged particle heating of alpha particle driven instabilities. In the computational Collisional Plasma Model techniques were developed for calculating self-consistent electric fields and these tools are beginning to be used to investigate drift waves in a cylindrical plasma.

The major new thrust in the transport simulation group was the development of 1-1/2-D transport codes. In these codes the cross-section shape of the tokamak plasma is allowed to evolve as the plasma parameters are changed (e.g., by heating or compression), but the plasma is still assumed to be one-dimensional. Thus, transport within the flux surfaces is averaged out, but between surfaces is taken into account by an appropriate metric relating the flux surfaces to an effective radial cylindrical coordinate. One important aspect of this development is the ability to calculate ideal and resistive MHD instability criteria as plasmas evolve to high beta through intense heating. Other developments this past year include improved computational tools for calculating impurity ionization, recombination, and transport; a multispecies neutral model; and pellet fueling studies in collaboration with experiments performed on ISX-A.

A number of new developments emerged from the plasma engineering group. From pellet fueling studies it was found that less pellet penetration is required than previously thought necessary and that the relatively flat density profiles induced should lead to longer energy containment times, at least to the extent that drift-dissipative trapped particle modes govern transport. A new microwave-assisted startup scenario has been proposed which has the potential of helping to burn rapidly through the early ionization stage in a tokamak and thereby significantly reduce the voltage required during the breakdown phase. Neutral beam heating scenarios have been proposed in which medium energy (≤150-keV) injection into a low density plasma is followed by density buildup and subsequent alpha heating of the central plasma when the beams cannot be used to heat the plasma. A four-factor formula for the charged particle energy or thermal multiplication in a tokamak has been developed in analogy with the fission particle or "neutron chain reacting" in a fission reactor. It has been used to calculate the increases in confinement achieved in the fusion program by allowing it to achieve ignition in D-T and advanced fuels. Finally, the extent to which the concept could be developed by ASDEX was examined, and the conclusion was that it could tolerate about [illegible] increase in confinement over that predicted by present transport laws and still achieve ignition conditions.

A major development in the computing service area was the upgrading of the User Service CDC 7600 processor to a roughly three times faster 6-10 cpu. In addition, the USC has been hardware-interfaced to the PDP 11/45 data handling controller for the ISX-A. The data handling system from ORMAK was very successfully converted to and utilized on the ISX-A experiment. Further improvements were also made in the neutral beam, superconducting magnet, and PDP data handling and control systems.

INTRODUCTION

The principal goals of the Plasma Theory Section are to: (1) develop the theory of plasma equilibrium, stability (macroscopic and microscopic), transport, and heating to the level where it can be meaningfully applied to relevant fusion plasma experiments; and (2) apply this theory to understanding and improving present and future fusion experiments and devices. In addition, the computer support services provided within the Fusion Energy Division are administered by the Plasma Theory Section.

The progress during the past year, which is reported below, is organized by group efforts and divided into six major areas. The basic tokamak areas and the sections in which their

work is summarized are: MHD theory (4.2), kinetic theory (4.3), and transport simulation (4.4). The EBT theory work (4.1) has its own research projects on MHD theory, kinetic theory, and transport simulation. In the plasma engineering area (4.5), relevant research work is further developed and synthesized into models that are used in the design of advanced fusion systems – TNS, Demo, EBTR, etc. Finally, the computer support activities during the past year are summarized in Sect. 4.6.

4.1 EBT THEORY

D. B. Batchelor
R. C. Goldfinger
C. L. Hedrick, Jr.*
L. W. Owen
A. H. Kritz
T. C. Tucker
L. E. Deleanu
E. G. Harris
D. B. Nelson
E. F. Jaeger
D. A. Spong
J. C. Tolliver
H. Weitzner

Neoclassical transport calculations presently provide the focus for theory associated with EBT. In the past year there has been a rapid evolution in neoclassical transport theory. The most recent results of radially resolved transport calculations (Sect. 4.1.1) are in reasonable agreement with experimental observation. In particular, the sign of the self-consistent ambipolar electric field is negative, in agreement with experimental observation. Earlier calculations with the radially resolved transport code (Sect. 4.1.2) yielded positive electric fields; the key is the proper choice of initial conditions. Valuable insights into the choice of initial conditions were provided by work associated with kinetic model calculations (Sect. 4.1.3) and in the refinement of expressions for the transport coefficients (Sect. 4.1.4). Thus the present radially resolved neoclassical transport calculations with self-consistent electric fields are a significant advance over the initial transport modeling which included self-consistent electric fields (Sect. 4.1.5). Still further increases in realism should be forthcoming in the next year.

Studies of microwave heating (Sect. 4.1.8) and stability (Sects. 4.1.6, 4.1.7) are also important facets of the theoretical description of EBT. For example, the stability boundaries for the dissipative modes studied (Sect. 4.1.7) are quite similar to those obtained from MHD (Sect. 4.1.6). Pressure profiles which are stable to the modes are compatible with the requirements of neoclassical transport and do not now appear to pose a significant limit on the plasma beta.

Calculations of magnetic equilibria and particle orbits are presently less visible. These calculations undergird most of the other theoretical work and now are playing an important part in design studies for future EBT devices.

Related work on electron cyclotron heating as specifically related to tokamaks has also been performed (Sect. 4.1.9).

4.1.1 Neoclassical Transport in EBT[1]

E. F. Jaeger D. A. Spong
C. L. Hedrick, Jr.

In EBT, neoclassical transport coefficients depend critically on the ambipolar electric field. These coefficients, calculated for arbitrary radial electric fields, are applied in a one-dimensional radial transport calculation which, for the first time, treats the electric field self-consistently. This purely classical model predicts many features of experimental operation, including steady-state solutions with radially inward pointing ambipolar fields.

4.1.2 A Numerical Model for Radial Transport in EBT[2]

E. F. Jaeger C. L. Hedrick, Jr.

Neutral and charged particle densities and temperatures are calculated as functions of radius for the toroidal plasma in the EBT

*Group Leader

experiment. Energy-dependent ionization and charge exchange rates, ambipolar diffusion, and self-consistent radial electric field profiles are included. Variation in magnetic field due to finite plasma pressure, effects of energetic electron rings, and transport due to drift waves and magnetic field errors are neglected. Diffusion is assumed to be neoclassical with enhanced losses at low collisionalities. The model reproduces many of the observed features of EBT operation in the quiescent toroidal (T) mode. The self-consistently calculated electric field is everywhere positive (not as in experiments) unless enhanced electron collisionality is included. Solutions for advanced EBT's are obtained and confinement parameters predicted.

4.1.3 A Kinetic Transport Model EBT[3]

E. F. Jaeger C. L. Hedrick, Jr.
J. S. Tolliver

A bounce-averaged drift kinetic equation is solved for the toroidal plasma in EBT. The distribution function is assumed isotropic in pitch angle and is calculated as a function of radius and speed using finite differences on a 2-D grid. A Fokker-Planck representation of the collision operator includes Coulomb, microwave, ionizing, and charge exchange collisions. Ion and electron fluxes, computed as integrals of the distribution function, are of comparable magnitude for ambipolar potentials which are approximately self-consistent. Initial results assume an unperturbed distribution function which is Maxwellian; however, this is not a necessary assumption in the model. Careful accounting of loss regions where electric and magnetic poloidal drifts cancel (superbanana particle orbits) leads to ion loss rates which are in some cases two orders of magnitude greater than electron rates. In these cases, radially inward pointing, self-consistent electric fields occur with potentials on the order of a few times the ion temperature. These negative field results are in approximate agreement with experiment and appear to be stable to the electric field runaway encountered in positive field cases.

4.1.4 Kinetic Transport Properties of a Bumpy Torus with Finite Radial Ambipolar Field[4]

D. A. Spong E. G. Harris
C. L. Hedrick, Jr.

Bumpy torus neoclassical transport coefficients, including finite values of the radial ambipolar field, have been calculated. These are obtained by solving a bounce-averaged drift kinetic equation in a local approximation for perturbations in the distribution function (away from a stationary Maxwellian) caused by toroidicity and radial gradients in plasma density, temperature, and potential. Particle and energy fluxes, along with the associated transport coefficients, are then calculated by taking appropriate moments of the distribution function. Particle orbits are treated by breaking them up into a vertical drift component (due to toroidicity) and a θ precessional drift (as a result of $\vec{E} \times \vec{B}$ and drift due to the bumpy toroidal field). The kinetic equation has been solved using both a functional expansion method and ADI finite difference techniques. The resulting transport coefficients exhibit a strong dependence on the ambipolar electric field and plasma collisionality. In the large electric field limit, our results are in close agreement with the earlier work of Kovrizhnykh.

4.1.5 A Simple Neoclassical Point Model for Transport and Scaling in EBT[5]

C. L. Hedrick, Jr. E. F. Jaeger
D. A. Spong G. E. Guest*
N. A. Krall† J. B. McBride†
G. W. Stuart†

A simple neoclassical point model is presented for the EBT experiment. Solutions for steady state are derived. Comparison with experimental observations is made, and reasonable agreement is obtained.

4.1.6 Macroscopic Stability and β Limits in EBT[6]

D. B. Nelson C. L. Hedrick, Jr.

MHD stability limits are determined for EBT. The relativistic hot electron annuli are considered to be rigid, modifying the magnetic field but not interacting with the instability. A modified energy principle is used, and the stability problem is reduced to determination of the eigenvalues of an ordinary differential equation along each field line. A threshold hot electron current is required for stability; its value agrees with experimental measurements. The calculations show that stable, high beta equilibria are easily generated.

4.1.7 A Preliminary Investigation of Trapped Particle Instabilities in EBT[7]

D. B. Batchelor C. L. Hedrick, Jr.

An investigation is presented of the role which trapped particles might play in the drift wave stability of EBT. The model adopted consists of a bounce-averaged, drift kinetic equation with a Krook collision operator. Care has been taken to model, at least in an elementary way, the features which distinguish the physics of EBT from that of tokamaks — namely the large magnitude and velocity space dependence of the poloidal drift frequency ω_*, the relatively small collisionality ν/ω_*, the enhancement of ν_{eff} for passing particles, and the closed nature of the field lines. Instabilities which have a somewhat dissipative character are found; however, the precessional drift is a significant stabilizing influence. In most cases the modes are completely stabilized when $\omega_*/\omega \lesssim 1$ for normal gradients. For reversed gradients ($\omega_*/\omega < 0$), stability is greatly enhanced.

4.1.8 Status of the Theoretical Study of Microwave Heating in EBT[8]

D. B. Batchelor

The basic strategy of the theoretical study of microwave heating in EBT is outlined, and the current status of the various aspects of the study is described. There are four broad areas which are being investigated: (1) heating and wave damping mechanisms, (2) the geometrical optics of microwave propagation in EBT, (3) reflection and mode conversion effects at regions such as cutoff and resonances where the geometrical optics approximation breaks down, and (4) nonlinear effects such as ponderomotive effects and parametric decay. Details are given of the geometrical optics code which has been developed to do ray tracing in arbitrary 3-D plasma equilibria. Examples are given for plasma parameters characteristic of EBT-I and EBT-II. Details are also given of the stochastic heating model currently in use with the 1-D transport code and of the linear wave damping model used in the ray tracing code. The most pressing problems of physics yet to be addressed and the directions for future work are indicated.

---

*General Atomic Company
†Science Applications, Inc.

4.1.9 Electron Cyclotron Heating in Tokamaks*

O. C. Eldridge W. Namkung
A. C. England*

Tokamaks may be efficiently heated at electron cyclotron resonance by launching of the extraordinary wave from the inside of the torus with a simple waveguide aperture. For typical tokamak parameters, 90% of the incident energy is absorbed in one traversal of the resonant surface. There is an effective maximum density for linear heating at the point where the plasma frequency is equal to the cyclotron frequency. The bulk of the plasma electrons is heated, increasing the perpendicular energy with no tendency to accelerate a high energy tail of the velocity distribution. The ordinary wave may be launched from outside the torus with somewhat smaller heating efficiency. Heating rates and velocity diffusion coefficients are presented.

4.2 MHD THEORY

C. H. An J. A. Holmes
G. Bateman J. H. Munro, Jr.
B. Carreras D. B. Nelson‡
L. A. Charlton Y-K. M. Peng
R. A. Dory† D. J. Strickler
H. R. Hicks G. Vahala
B. V. Waddell

The purpose of the MHD group is to formulate and apply fluid models of plasma behavior. Such models, because of their relative simplicity, allow much greater understanding of configurational space effects than do the kinetic models which underlie them. Of course, velocity space effects are less well treated by fluid models. In this past year considerable progress was made in understanding the resistive instabilities which dominate present tokamak behavior. The major and minor disruptive instabilities and the Mirnov oscillations appear to be quantitatively understandable in terms of resistive instability theory and calculations (Sects. 4.2.1-4.2.8). Methods for detecting island rotation in a resistive plasma have also been developed (Sect. 4.2.21). Looking ahead, many of the limits on operating tokamaks at higher beta have been elucidated (Sects. 4.2.9-4.2.13, 4.2.15, 4.2.16). By proper plasma shaping using well chosen poloidal field design, equilibria with beta of 5-10% can be maintained which are stable to ideal MHD modes (Sects. 4.2.14, 4.2.18, 4.2.19, 4.2.20). The ISX-B and PDX experiments are designed to test these predictions, and they will provide valuable comparison between theory and experiment during the next few years.

4.2.1 Nonlinear Numerical Algorithms for Studying Tearing Modes[15]

B. V. Waddell M. N. Rosenbluth*
D. A. Monticello† R. B. White+
B. Carreras

This lecture consists of a summary of the numerical methods that have recently been developed to study the nonlinear evolution of tearing modes in tokamaks. The essential features of tearing modes can be described by the resistive MHD equations. The numerical algorithms described here are based on a reduced set of 2-D MHD equations that are numerically tractable.

Two distinct types of numerical methods are described in detail. In the first method, referred to as the MASSLESS algorithm, the inertia is neglected. On the other hand, in the second method, referred to as the MASS algorithm, the inertia is retained and consequently the scheme is capable of handling a larger variety of problems. Codes based on these two algorithms give similar results for the nonlinear evolution of the m = 2 tearing mode.

---

*Tokamak Experimental Section
†Group Leader
‡Section 4.2 Coordinator

*Institute for Advanced Study
+Princeton Plasma Physics Laboratory

4.2.2 Interpretation of Tokamak Sawtooth Oscillations[11]

B. V. Waddell G. L. Jahns*
J. D. Callen H. R. Hicks

Sawtooth oscillations appear to be the result of a cyclic process in which the plasma core is resistively heated until the safety factor drops below unity, causing the m = 1 tearing mode to become unstable and ultimately to flatten the electron temperature and safety factor profiles. A systematic model based on this hypothesis is shown to provide a consistent interpretation of ORMAK experimental data, including for the first time an explanation of the accelerating growth rate of the m = 1 precursor oscillations and the repetition time of the sawteeth.

4.2.3 Internal Disruptions in Tokamaks[12]

G. L. Jahns* M. Soler
B. V. Waddell J. D. Callen
H. R. Hicks

We study the hypothesis that sawtooth oscillations or internal disruptions are the result of a cyclic process in which the plasma core is resistively heated until the safety factor drops below unity, causing the m = 1 tearing mode to become unstable, to grow with an accelerating growth rate, and ultimately to flatten the electron temperature and safety factor profiles. A model based on this hypothesis compares favorably with experimental data from ORMAK in explaining (1) the rate at which a sawtooth rises, (2) the radial dependence of the precursor and main sawtooth oscillation amplitudes, (3) the accelerating growth of the m = 1 precursor oscillations, and (4) the repetition time of the sawteeth. The heat lost from the central region during the internal disruption is found to transport diffusively through the exterior plasma with a conduction coefficient that agrees within a factor of two with the value inferred from the observed electron power balance.

4.2.4 Comment on "Simulation of Large Magnetic Islands: A Possible Mechanism for a Major Tokamak Disruption"

B. Carreras B. V. Waddell
H. R. Hicks S. J. Lynch

In Phys. Rev. Lett. 39, 1618 (1977), it was reported by White, Monticello, and Rosenbluth that for S = 10^4, the m = 2/n = 1 magnetic island grows exponentially for a certain safety factor profile until it saturates at a width of 0.7 a, where a is the minor radius. Here, m and n are the poloidal and toroidal mode numbers, respectively, and S is the ratio of the skin time and poloidal MHD time. It has been found that these results were severely affected by the numerical error due to the coarse poloidal grid. Specifically, if a fine poloidal grid is employed, rather than exponentiating the island grows algebraically. It attains a maximum width of 0.48 a, relaxes, and eventually saturates at 0.33 a. (This comment will appear in the July 1978 issue of Phys. Rev. A.)

4.2.5 Interaction of Tearing Modes of Different Pitch in Cylindrical Geometry[13]

H. R. Hicks B. Carreras
J. A. Holmes B. V. Waddell

In cylindrical geometry, we have conducted a preliminary analysis of the hypothesis that the major disruption in tokamaks is due to the interaction of tearing modes of different pitch. For a flat safety factor profile having a value of 1.4 at the plasma center, we find that the m = 3/n = 2 tearing mode, which is linearly unstable, is strongly destabilized nonlinearly by the m = 2/n = 1 mode. Other modes are nonlinearly destabilized, particularly the m = 1/n = 1 and m = 5/n = 3 modes. Due to the development of islands of many different pitches,

*General Atomic Company

the toroidal current density is severely deformed. The corresponding region of island activity can extend essentially from the plasma center to the limiter. Presumably, this deformation of the field lines can lead to rapid transport of heat and particles from the plasma center to the limiter. The destabilization of the m = 3/n = 2 mode is significant because it may correspond to the observed vertical asymmetry of some of the major disruptions in PLT.

4.2.6 Analytic Model for the Nonlinear Interaction of Tearing Modes of Different Pitch in Cylindrical Geometry[14]

B. Carreras B. V. Waddell
H. R. Hicks

An analytic model has been developed for describing the nonlinear interaction of tearing modes of different pitch in cylindrical geometry for equilibria characterized by flat safety factor profiles. The analysis shows that the m = 2/n = 1 tearing mode can destabilize odd m modes, particularly the 3/2 mode. The model compares well with our 3-D code with respect to the time evolution of the 0/0, 1/1, 2/1, 3/2, and 5/3 modes. Scaling rules are obtained for the position and location in time of the maximum or peak in the 3/2 growth rate. The characteristic time of destabilization of the odd m modes predicted by the model correlates well with the observed time scale for the major disruption in tokamaks.

4.2.7 Disruptions in Tokamaks[15]

B. V. Waddell

Both minor (or internal) and major (or external) disruptions will be discussed. First, the following model will be analyzed. Sawtooth oscillations (or internal disruptions) are the result of a cyclic process in which the plasma core is resistively heated until the safety factor q at the plasma center drops below unity, causing the m = 1 tearing mode to become unstable, to grow with an accelerating growth rate, and ultimately to flatten the electron temperature and safety factor profiles as magnetic reconnection occurs. In order to explain the experimental data, the modification of the m = 1 tearing mode growth rate due to diamagnetic drifts must be taken into account. This model compares favorably with experimental data[16] in explaining (1) the rate at which a sawtooth rises, (2) the radial dependence of the precursor and main sawtooth oscillation amplitudes, (3) the accelerating growth of the m = 1 precursor oscillation, and (4) the repetition time of the sawteeth. This favorable comparison with experiment indicates that magnetic reconnection is probably an important phenomenon in laboratory plasmas.

Secondly, the hypothesis that the major disruption is due to the interaction of low mode number tearing modes of different helicity will be discussed. The experimental evidence indicates that probably the most important interactions are those between the m = 3/n = 2 and m = 2/n = 1 modes and between the m = 1/n = 1 and m = 2/n = 1 modes; here m and n are respectively the poloidal and toroidal mode numbers. Numerical results from RS3 (a 3-D version of the MASS code[17]) will be presented. For example, the results indicate that for current profiles that are flat in the plasma interior, the m = 3/n = 2 tearing mode can be nonlinearly destabilized by the presence of the m = 2/n = 1 mode. In fact, nonlinearly the width of the magnetic island corresponding to the m = 3/n = 2 mode can become larger than that corresponding to the m = 2/n = 1 mode.

4.2.8 Theoretical Explanation of the Poloidal Magnetic Field Fluctuations in Tokamaks

B. Carreras B. V. Waddell
H. R. Hicks

By applying elementary nonlinear tearing mode theory in 2-D cylindrical geometry, the amplitude of the oscillations in the m = 2 poloidal magnetic field (Mirnov oscillations) at

the limiter as a function of the safety factor at the limiter can be predicted quite reliably; here m is the poloidal mode number. The input required is the radial electron temperature profile, from which the safety factor profile can be calculated in standard fashion. The saturation amplitude of the m = 2 tearing mode is calculated from the safety factor profile using the nonlinear Δ' analysis which requires that the mode saturate at the magnetic island width where Δ' is the discontinuity in the flux eigenfunction across the associated magnetic island. This gives an absolute result (no arbitrary factors) for the amplitude of the perturbation in the poloidal magnetic field everywhere and, in particular, at the limiter. A detailed analysis of ORMAK and T-4 profiles gives results that are in surprisingly good agreement with the experimental data.

4.2.9 MHD Stability of Flux Conserving Tokamak Equilibria[18]

R. G. Bateman Y-K. M. Peng

Large-scale MHD instabilities of flux conserving tokamak equilibria are studied computationally. Stable equilibria are found with average beta up to 5%. As beta is increased, the observed instabilities take on a strong ballooning character, concentrating near the outer edge of the torus with a mix of poloidal harmonics.

4.2.10 Theory of Ballooning Modes in Tokamaks with Finite Shear[19]

D. Dobrott* H. H. Glasser†
D. B. Nelson M. S. Chance†
J. M. Greene† E. A. Frieman†

We studied ballooning instabilities in tokamaks of arbitrary cross section and finite shear. These azimuthally localized, ideal MHD modes have large toroidal mode numbers but finite variation along the field and across the flux surfaces. Stability is determined by solving a second order ordinary differential equation on each flux surface, subject to the proper boundary conditions. Qualitative agreement is achieved with the Princeton PEST stability code.

4.2.11 High Pressure Tokamaks[20]

R. G. Bateman

The successful development of the neutral beam injection method of heating tokamaks has opened up a new range of theoretically predicted phenomena to be explored. This article, intended for the nonspecialist, reviews the existing experimental observations and theoretical understanding of tokamak equilibrium and large-scale stability. Then a survey is presented of the new phenomena, such as flux conserving sequences of equilibria and pressure-driven ballooning modes, that are expected to accompany the significantly enhanced plasma pressure to be produced in tokamaks now under construction.

4.2.12 High Beta Tokamak Instabilities[21]

R. G. Bateman

Theoretical predictions using the ideal MHD model indicate that large-scale ballooning modes should appear when the average beta is raised above 1-2% in present-day tokamak geometries or 5-10% in more optimized geometries. The onset of instability is predicted to be sudden and the behavior of ballooning modes to be strikingly different from the sawtooth and Mirnov oscillations experimentally observed at low beta. Conditions close to the predicted onset were achieved in ORMAK with no noticeable change in plasma behavior. Experiments are planned for ISX to test the beta limit.

---

*General Atomic Company
†Princeton Plasma Physics Laboratory

4.2.13 Stability of Tokamaks with Elongated Cross Section

C. H. An R. G. Bateman

Fixed boundary MHD instabilities are studied computationally as a function of diamagnetism and current profile in highly elongated toroidal equilibria. It is found that paramagnetic plasmas with either peaked or broad current profile as well as mildly diamagnetic plasmas with peaked current profile are stable to large-scale instabilities whenever the q-value at the magnetic axis is greater than or of order unity. However, even slightly diamagnetic plasmas with broad current profile and highly elongated cross section are subject to a ballooning instability for q-values well above unity at the magnetic axis.

4.2.14 Tokamak Ideal MHD Instability Analysis Code ERATO

R. A. Dory Y-K. M. Peng
L. A. Charlton D. J. Sigmar

The ERATO code of Centre de Recherches en Physiques des Plasmas, École Polytechnique Fédérale de Lausanne, was made available by Prof. F. Troyon and Drs. R. Gruber, D. Berger, and C. Bernard. The code uses a finite element technique to evaluate the energy principle for tokamak equilibria. Seminminor revisions were made to run on the National MFE Computer Center system, to allow increased resolution, and to accept input equilibria from the ORNL equilibrium codes. The ERATO code has been used to analyze high beta and FCT tokamak equilibria for stability within the ideal MHD model. Results to date suggest that flattened current profiles stabilize ballooning or internal modes. However, flattening the current profiles makes kink or external modes more unstable unless a conducting shell is provided near the plasma surface. If the ratio of shell distance to plasma minor radius is 10-20%, then equilibria stable to both types of modes have been found with average beta values as high as 8%.

4.2.15 Intense Neutral Beam Heating in the Adiabatic Approximation[21]

D. B. Nelson

A simple method is exhibited for accurately following the dynamic evolution of a toroidal, arbitrary beta plasma under neutral beam heating. While the method used is also being applied to more general transport calculations, for these calculations it is assumed that the heating is rapid compared with resistive diffusion or cross-field heat conductivity. Thus the plasma evolves adiabatically, i.e., according to the ideal MHD equations. It is found that high beta states can be attained with a wide variety of initial conditions and heating profiles. The final profiles and plasma stability vary greatly, depending upon the deposition profile chosen. Skin currents can be avoided by programming the PF coil system to control plasma size and shape during the evolution. It is not necessary to program the TF coil currents.

4.2.16 Inductive Effects in Flux Conserving Tokamaks[22]

R. G. Bateman

Scenarios are worked out in straight circular cylindrical geometry for the evolution of flux conserving sequences of equilibria as the plasma is heated or compressed. It is shown that force-free currents are induced when the low pressure region at the edge of the plasma is compressed against a flux conserving wall. A force-free surface current is induced if there is a vacuum region between the expanding plasma and the wall. These edge currents run opposite to the direction of the current in the main body of the plasma. The force-free currents can be avoided or reversed at the edge of a plasma with diffuse resistivity profile by programming the total longitudinal current as the plasma is heated or compressed.

4.2.17 The Ripple Bundle Divertor for Tokamaks

J. Sheffield* R. A. Dory

The bundle divertor, designed for density and impurity control, has been successfully applied on the DITE tokamak. In this application it is subject to high stresses and is restricted to short pulses and low toroidal fields. A new version is made possible by fitting the vacuum vessel close to the toroidal coils, which allows the plasma to exist in the outer regions of higher TF ripple. This ripple bundle divertor should operate at lower stresses and for longer pulses at higher magnetic fields.

4.2.18 Plasma Magnetics for D-shaped, Air Core Tokamaks

Y-K. M. Peng R. A. Dory
J. A. Holmes D. J. Strickler

The location of the EF coils, whether they are interior or exterior to the TF coils, is expected to have a large impact on the design of tokamak reactors. A closely related plasma magnetics problem is how far can the coils recede from the plasma and still maintain the D-shaped equilibrium over a wide range of $\bar{\beta}$ values. Free boundary MHD equilibrium calculations have been carried out to answer the latter question. It is found that properly placed EF coils exterior to the TF coils will work but will require an order of magnitude increase in currents. The interior and the exterior coil arrangements are shown in Fig. 4.1, with the corresponding MHD equilibria shown in Figs. 4.2 and 4.3, respectively. A comparative study is made of the power supplies required by interior and exterior coils. It is shown that the interior coils need power supplies

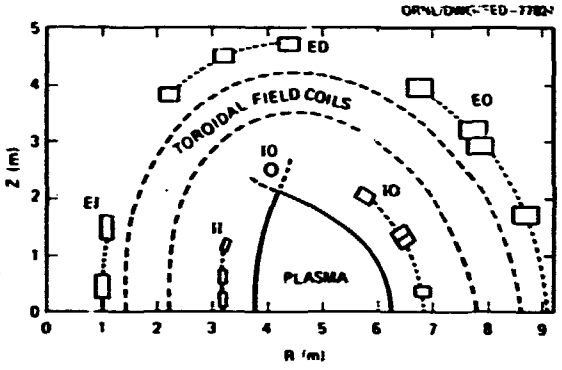

Fig. 4.1. Generic EF coils that are interior (II, ID, IO) and exterior (EI, ED, EO) to the TF coils. Either the interior or exterior coils can be used alone to maintain high beta, D-shaped equilibria. The dotted lines indicate a group of coils connected in series and using a single power supply.

that [illegible] an order of magnitude below those re[illegible] the exterior coils, while the latter are [illegible]ess difficult to build than the former. A hybrid EF coil concept is proposed that combines the interior and the exterior coils to retain their advantages in avoiding large interior coils while lowering the power supplied to the exterior coils by an order of magnitude. The MHD equilibria maintained by the hybrid coils are shown in Fig. 4.4.

4.2.19 Noncircular MHD Equilibria and Shell-like Poloidal Field System in ISX-B

Y-K. M. Peng R. A. Dory
D. J. Strickler D. W. Swain*

ISX-B will have neutral beams up to 3 MW to explore plasma beta limits in a tokamak. One of the limits is expected to come from ideal MHD ballooning instabilities. To ensure adequate flexibility in achieving high beta and to permit

*Tokamak Experimental Section

*Tokamak Experimental Section

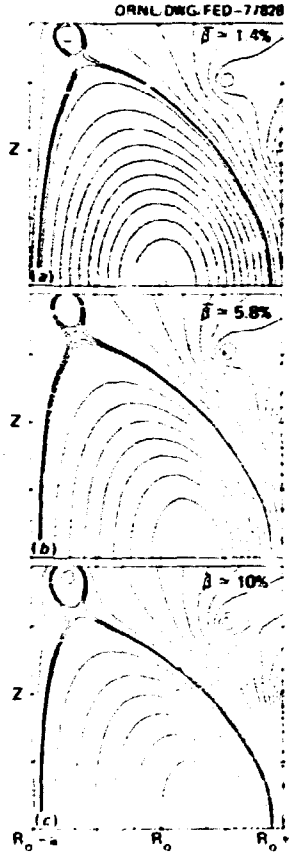

Fig. 4.2. FCT equilibrium flux plots with various β values for TNS, using only the interior coils shown in Fig. 4.1. The plasma edge is represented by the inserted and closely spaced flux contours passing near but within the separatrix.

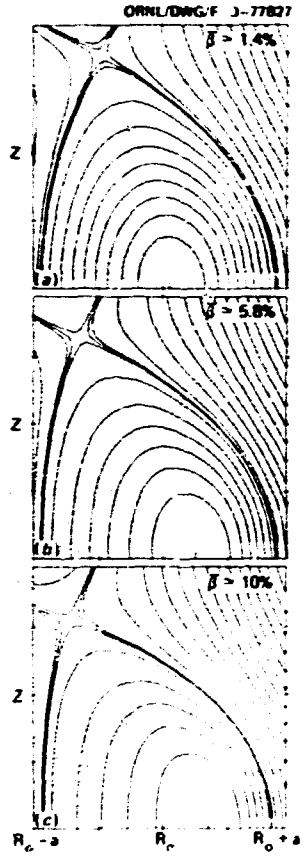

Fig. 4.3. FCT equilibrium flux plots with various β values for TNS, using only the exterior coils shown in Fig. 4.1. The plasma edge is represented by the inserted and closely spaced flux contours passing near but within the separatrix.

large access for beams and diagnostics, a "shell-like" PF system was designed for ISX-B. The system contains an inside and an outside set of coils that carry currents opposite to the plasma current to drive the plasma current and produce the vertical field that centers the plasma column radially. Shaping coils with interchangeable connections are added roughly above and below the plasma chamber to produce shaping fields (Fig. 4.5). Free-boundary MHD equilibrium calculations show that cross sections of D shapes, inverted D shapes, and ellipses can be obtained with vertical elongations up to two, averaged betas up to 9%, and large safety factors (Fig. 4.6).

4.2.20 Poloidal Field Modeling for the Iron Core ISX

Y-K. M. Peng — R. A. Dory
T. C. Tucker — W. D. Cain*
D. H. McNeill+ — W. R. Wing+

The ISX tokamak uses an iron transformer core with a single return leg and a vacuum vessel with a magnetic flux diffusion time of a few msec. During each plasma discharge, the

*Magnetics and Superconductivity Section
+Tokamak Experimental Section

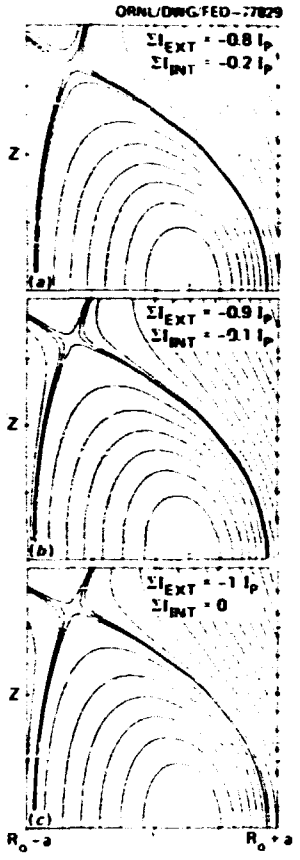

Fig. 4.4. Flux contours for equilibria ($\bar{\beta}$ = 5.3%) maintained by a hybrid EF coil system with various distributions of currents between the exterior and interior sets.

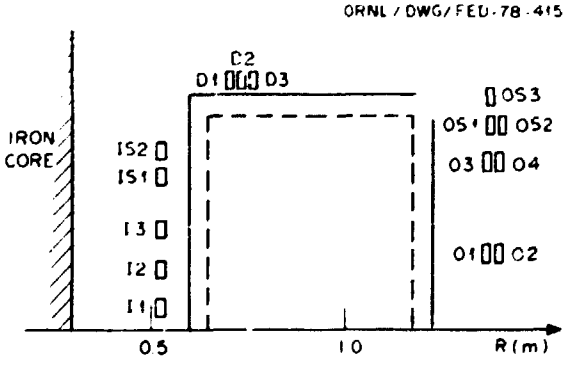

Fig. 4.5. The shell-like EF coils consist of an outside group (O1-O4), an inside group (I1-I3), and a shaping group (IS1, IS2; D1-D3; OS1-OS3). Alternative connections are also built in to increase the flexibility of plasma shaping.

image field from the iron core has a strong effect on the plasma equilibrium position and cross section. To model the magnetic field, we employ a 2-D axisymmetric analytic model (Fig. 4.7) and a 3-D tetrahedral iron element model GFUN3D[23] (Fig. 4.8). In the plasma chamber, the 2-D and 3-D results are found to agree within a few percent when the iron is not saturated. The variation of the field strength in the toroidal direction is also found to be within a few percent. The calculations agree with the measurements within the experimental error (Fig. 4.9). These results justify the use of the 2-D model in MHD equilibrium calculations. However, the results by the 2-D and 3-D models agree with the measurements only to within 20% along the horizontal leg of the TF coils (Fig. 4.10).

4.2.21 Perturbed Magnetic Field Phase Slip for Tokamaks[24]

G. Vahala L. Vahala*
J. H. Harris† R. G. Bateman
B. V. Waddell

Given a set of rotating helical current filaments within a cylindrical plasma and a set of fixed magnetic field detectors at the edge of the plasma, a mathematical model is used to investigate the observable effect of rotation or longitudinal motion in the intervening plasma. If the soft x-ray signals from magnetic islands indicate the instantaneous position of the helical current filaments within the plasma, then the phase difference between the x-ray signal and the magnetic fluctuations should provide a diagnostic of tokamak plasma rotation. The relative motion between the islands and the surrounding plasma is measured by the "slip" $S(r) = \omega - kv_z(r) - m_{v_\theta}(r)/r$, where ω is the rotation frequency of the islands and v is the plasma velocity.

*College of William and Mary
†University of Wisconsin

ORNL/DWG/FED 78-416

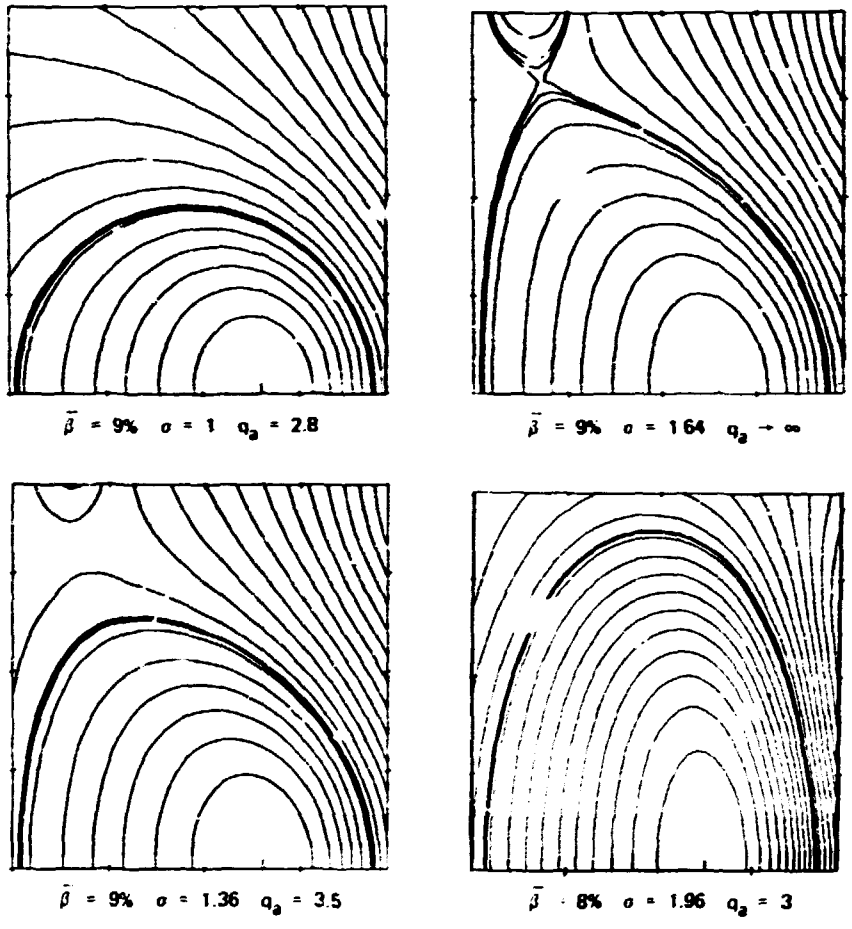

Fig. 4.6. Some examples of MHD equilibria computed for ISX-B using the coil system shown in Fig. 4 1.

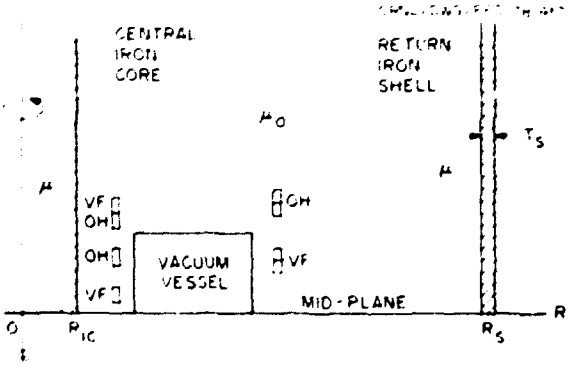

Fig. 4.7. Two-dimensional iron model and the PF coil arrangement in ISX.

The plasma velocity is added to Rosenbluth's reduced equations to compute the phase difference between the island position and the perturbed magnetic field at the edge of the plasma as a function of the slip for a variety of resistivity profiles. The current profile within the islands is taken from the nonlinear computer results of White, Monticello, Rosenbluth, and Waddell. For peaked conductivity profiles, the phase difference is observed to saturate and the n to decrease at large values of the slip.

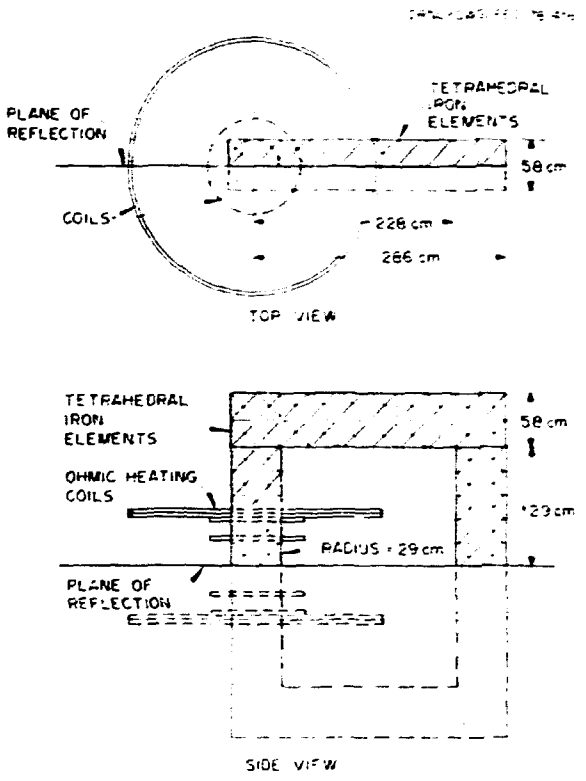

Fig. 4.8. Three-dimensional tetrahedral iron element model (GFUN3D).

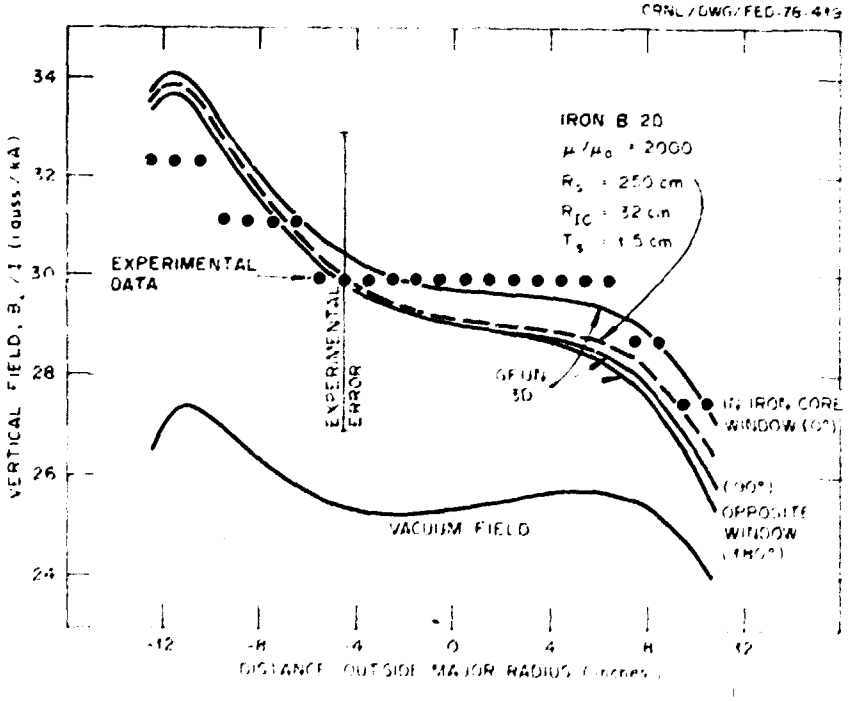

Fig. 4.9. Vertical fields (B_z) on the midplane produced by the VF coils in ISX, as calculated by the 2-D and 3-D models in comparison with the experimental measurements.

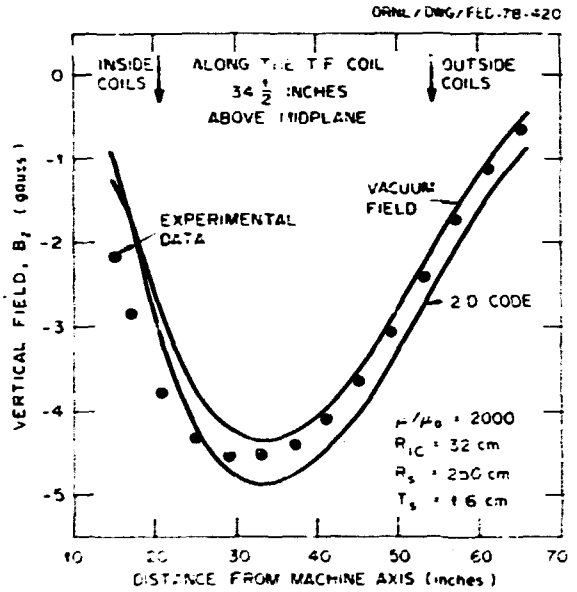

Fig. 4.10. Vertical fields (B_z) along the horizontal leg of the TF coils produced by 450 A in the VF coils.

4.3 KINETIC THEORY

C. O. Beasley, Jr.
J. D. Callen
P. J. Catto
E. C. Crume, Jr.
J. Denavit
R. H. Fowler
P. W. Gaffney
J. E. McCune
H. K. Meier
Y-K. M. Peng
J. A. Rome
K. E. Rothe
D. J. Sigmar*
J. Smith
M. Soler
W. M. Stacey, Jr.
K. T. Tsang
W. I. van Rij
J. C. Whitson

Research in this area will be broken down into the subgroups 4.3.1, Analytic High Beta Equilibrium Studies and Neoclassical Transport; 4.3.2, Anomalous Transport; 4.3.3, Energetic Particle Orbits; and 4.3.4, Numerical Transport Studies Using the Collisional Plasma Model. After pointing out selected highlights, a systematic account of published papers and reports will serve to describe last year's progress.

1977 was a particularly eventful year. Highlights in Sect. 4.3.1 include the analytic existence and accessibility proof of flux conserving, high beta tokamak equilibria and an exact unified theory of the neoclassical multispecies transport coefficients for arbitrary MHD equilibria in the banana-plateau regime.

Our work in anomalous transport theory, Sect. 4.3.2, led to several surprises. A careful analytic-numerical investigation of the radial eigenmode structure of the universal instability showed completely unexpected stability — in the electrostatic approximation as well as in a finite beta treatment. A quantitative quasilinear calculation of the velocity space instabilities due to alpha particles in a tokamak fusion plasma revealed the possibility for substantial anomalous alpha losses.

The flutter model of anomalous electron transport due to magnetic islands caused by high mode number drift instabilities has provided a new and more viable mechanism for explaining the anomalous radial electron heat transport in a tokamak.

By improving previous work on electron heat pulse propagation, it was shown that the observed cross-field electron heat loss rate in present-day tokamaks can be consistently interpreted as a purely diffusive process.

Concerning energetic particle orbits, Sect. 4.3.3, the concept of ripple injection (which may be necessary for beam penetration in large devices) progressed substantially. A cooperative effort between ORNL and PPPL resulted in a magnetic design for ripple injection into ISX-B and TFTR.

The CPM is discussed in Sect. 4.3.4 in terms of its basic content, application to neoclassical equilibria, and nonlinear evolution of drift modes.

4.3.1 Analytic High Beta Equilibrium Studies and Neoclassical Transport

Until recently, the bulk of neoclassical theory papers focused on the calculation of transport coefficients at the expense of a careful treatment of the underlying MHD equilibrium. The advent of powerful neutral beam

*Group Leader

heating and the economic necessity for high beta reactors now necessitate an analytic formulation of circular and noncircular finite beta equilibria (first 5 topics in Sect. 4.3.1). Realistic geometry is the motivation also for investigation of banana drift diffusion due to field ripples (topic 6), while a fresh look at the impurity problem for near equal mass-species led to the discovery of an impurity screening effect in the Pfirsch-Schlüter regime (topic 7).

High Pressure Flux Conserving Tokamak Equilibria[25]

J. F. Clarke* D. J. Sigmar

An analytic theory is developed to calculate poloidal beta β_I and the diamagnetic parameter μ_I for axisymmetric toroidal MHD equilibria confining high pressure plasma [$\beta \sim O(a/R)$] under the constraint of flux conservation. To satisfy the equilibrium equations, the plasma current increases with pressure as $p^{1/3}$. Previously calculated equilibrium limits on poloidal beta are avoided.

Analytic, High Beta, Flux Conserving Equilibria for Cylindrical Tokamaks[26]

D. J. Sigmar G. Vahala

Using Grad's theory of generalized differential equations, the temporal evolution from low to high beta due to adiabatic and nonadiabatic (i.e., neutral beam injection) heating of a cylindrical tokamak plasma with circular cross section and peaked current profiles is calculated analytically. The influence of shaping the initial safety factor profile and the beam deposition profile and the effect of minor radius compression on the equilibrium is analyzed.

*OFE/DOE

Fundamental Time Scales for Flux Conserving Tokamak Heating and Certain Global FCT Equilibrium Properties[21]

D. J. Sigmar

Because the existence of high beta flux conserving equilibria has been established, it becomes important to analyze the accessibility of these equilibria via auxiliary heating, to discuss the resistive decay of the safety factor profile, and to extend the virial theory to noncircular plasma cross sections.

Neoclassical Transport of a Multispecies Toroidal Plasma in Various Collisionality Regimes[27]

S. P. Hirshman* D. J. Sigmar

Continuously valid expressions for the neoclassical transport coefficients are analytically calculated for a multispecies plasma in the low to intermediate collision frequency regimes. The modification of the transport problem which results when a single heavy impurity ion species is in the collisional regime is presented. Consistent with the detailed balancing principle, a qualitative change in the magnitude of the long mean-free-path particle flux is shown to arise whenever there is more than a single collisionless species. A novel calculation of the bootstrap current permits the computation of a complete set of transport coefficients throughout the various collisionality regimes.

Neoclassical Transport in an Elliptic Tokamak[28]

K. T. Tsang

Neoclassical transport for an elliptic tokamak in all collisional regimes is investigated by the technique of partitioning the

*Princeton Plasma Physics Laboratory (now with FED Theory Section as an ORNL Wigner Fellow)

velocity space. It is found that in a tokamak of moderate elongation, particle and ion heat confinement times are increased by a factor of σ^2, where σ is the ratio of the vertical minor radius to the horizontal minor radius. Ripple diffusion in an elliptic tokamak is also studied. Ion heat conductivity due to ripples is reduced by a factor of approximately σ^2.

Banana Drift Diffusion in a Tokamak Magnetic Field with Ripples[29]

K. T. Tsang

The drift motions of trapped particles in a tokamak field with ripples lead to a new transport process in large tokamaks in addition to the diffusion process due to particles trapped in the ripples. This problem is studied by solving the bounce-averaged, drift kinetic equation with a model collision operator. It is shown that the "banana drift diffusion" is proportional to the collision frequency when the poloidal banana drift frequency is smaller than the effective collision frequency. This result is contrary to earlier predictions, but in a reactor regime, this loss mechanism is shown to be unimportant.

Temperature Screening Effect in Two-Ion-Species Pfirsch-Schlüter Transport[30]

K. T. Tsang E. C. Crume

The particle and heat flux problems in the collisional or Pfirsch-Schlüter regime for a two-ion-species tokamak plasma are solved by using a kinetic approach with exact Fokker-Planck collision operators. These solutions are appropriate for analyzing the behavior of impurities in the low temperature plasma edge region, where impurities first enter the plasma from the outside. We find that low charge states of low mass impurities can be screened effectively from further penetration of the plasma.

4.3.2 Anomalous Transport

In this area, part of the effort was directed at advancing fundamental techniques, such as deriving a gyrokinetic equation (a method to retain fully the two-dimensional eigenmode structure of trapped particle instabilities) and developing the "flutter model." Part of the effort went into calculating specific transport problems.

For example, we scrutinize the often made assumption that fusion-born alpha particles will be contained classically during their slowing down period (see topic 1).

In the collisionless limit of the parameter space, the collisionless drift instability has long been assumed to be absolutely unstable in a sheared magnetic field. We have derived an improved eigenvalue equation for the collisionless drift instability in tokamaks which does not rely on the often used perturbation expansion in the smallness of the growth rate (topic 2).

Numerical work has also been carried out to check this analytic result. We have concluded that, contrary to the prevailing view of drift waves as presented by Pearlstein and Berk,[31] the so-called "absolute universal instability" is not universal at all (topic 3). This startling finding is having a substantial effect on our understanding of the role drift waves may play in tokamak plasma confinement. Since present tokamak experiments operate near the transition between the banana and plateau regimes of collisionality, we have investigated the collisional effects on trapped electron instabilities (topic 4).

The usual treatments of the trapped electron instabilities ignore the fact that trapped electron orbits are concentrated around the outside of the torus; hence, the driving term has a poloidal angle dependence. If this poloidal variation is retained, the problem becomes two-dimensional. Until recently, only numerical solutions of this problem had been published in the literature. By ignoring the

ion magnetic drift term, we were able to obtain analytic solutions of the two-dimensional eigenvalue problem for trapped electron instability (topic 5).

The effects of impurities on the trapped electron mode have been investigated (topic 6). As a vehicle to investigate the relevant instabilities in tokamaks, we first derived the linearized gyrokinetic equation with collisions (topic 7).

Small resonant magnetic perturbations can cause significant distortions of the magnetic surfaces in tokamaks. It has previously gone unrecognized that since the high mode number, drift wave type turbulence is probably not purely electrostatic, it is, in fact, accompanied by magnetic perturbations that can induce densely packed magnetic island structures and thereby strongly affect radial plasma transport in tokamaks. The islands are discussed in topic 8. The ensuing anomalous electron transport due to field line "fluttering" is treated extensively in topic 9, the basic ideas of which have appeared in the open literature and as an invited paper at the 1977 DPP-APS meeting.

Finally, in topic 10 we report on the experimental demonstration of the diffusive nature of radial electron heat transport in a tokamak. In the original investigation of the space-time evolution of electron temperature perturbations induced by the internal disruptions (topic 10), it was found that while the electron heat transport is a diffusive process, the electron heat conduction coefficient governing it seemed to be about an order of magnitude larger than that governing the background. In more recent work (topic 11) this paradox was reconciled by: (1) a more careful treatment of the "initial conditions" prevailing after the internal disruption; (2) a more careful treatment of the region near the initial perturbation; and (3) refinement of the data. The net result was to produce a number of new methods for analyzing the data and a conclusive demonstration that radial electron heat transport in ORMAK was a microscopic, diffusive process.

Anomalous Alpha Particle Transport in Thermonuclear Tokamak Plasmas[32]

D. J. Sigmar H. C. Chan*

Due to the strong localization of the fusion-born alpha particles in velocity and configuration space and their coupling to Alfvén waves in the background plasma, the relaxation of alphas is anomalous. In a finite system, the enhanced electromagnetic fluctuations can produce rapid spatial losses of alpha population and energy. These losses prevent the alpha velocity distribution from attaining a stable collisional equilibrium, thus maintaining a steady-state turbulence level. A self-consistent numerical quasi-linear calculation is performed for a low frequency mode, showing the evolution of the alpha distribution and yielding the anomalous loss rates.

Improved Eigenvalue Equations for the Collisionless Drift Instability in Tokamaks[33]

P. J. Catto K. T. Tsang

Previous work has considered the validity of the perturbation theory technique of solving the radial differential equation for the collisionless drift wave in a tokamak only near marginal stability for the most unstable radial eigenmode. The present work extends the previous result and determines more exact eigenvalue equations (for all even and odd spatial modes) that are valid for arbitrary growth rates. Away from and perhaps near marginal

---

*Massachusetts Institute of Technology

stability, these more complete eigenvalue equations are required in order to accurately calculate growth rates.

"Absolute Universal Instability" Is Not Universal[34]

K. T. Tsang P. J. Catto
J. C. Whitson J. Smith

The roots of an improved analytic eigenvalue equation for the absolute universal or collisionless drift instability in a sheared magnetic field are found numerically and compared with the eigenvalues obtained from a numerical solution of the exact differential equation. The startling result is that both techniques predict stability, no matter how weak the shear or how large the transverse wave number, in contradiction to all previous work. Stability is due primarily to the stabilizing influence of the nonresonant electrons.

Collisional Effects on Trapped Electron Instabilities[35]

K. T. Tsang J. D. Callen
P. J. Catto

The effects of collisions on dissipative trapped electron instabilities are evaluated by distinguishing between the perpendicular and parallel electron velocity components when calculating trapped and untrapped electron contributions. The growth rate is obtained for all regimes of collisionality and reduces to previous results in appropriate limits. It is shown that the dominant effect of finite collisionality is to determine the number of trapped and untrapped electrons. It is also shown that collisional broadening removes the resonant electron response only for collision frequencies greater than or equal to ten times the wave frequency, $\nu_e \geq 10\omega$. For such large ν_e/ω, ion-ion collisions are found to exert a far stronger stabilizing influence than does broadening.

Analytic Solutions of the Two-Dimensional Eigenvalue Problem for the Trapped Electron Instability in Tokamaks[36]

K. T. Tsang P. J. Catto

The radial localization of the destabilizing trapped electron term that is caused by the differences in the pitch of the magnetic field and the mode structure is shown to result in a completely new form of the dispersion relation for the trapped electron instability.

Dissipative Trapped Electron Modes in the Presence of Impurities[37]

K. T. Tsang

The effect of impurities on low frequency drift modes of a toroidally confined plasma is investigated by the gyrokinetic equation. It is assumed that the electrons are in the banana and the ions in the plateau regime. Impurity collision damping is found to be significant in the usual trapped electron mode. A new instability due to the impurities can occur for normal profiles and impurities peaked at the center, and quasi-linear considerations show that impurities will be driven outward if such an instability occurs.

Linearized Gyrokinetic Equation with Collisions[38]

P. J. Catto K. T. Tsang

A like particle collision operator is derived for arbitrary values of the product of poloidal wave number times gyroradius by employing an ordering in which gyroradius corrections are retained in lowest order and the radial dependence appropriate for sheared magnetic fields is included. In addition,

neoclassical drift, finite beta (plasma pressure/magnetic pressure), and unperturbed toroidal electric field modifications are considered.

Magnetic island characteristics in tokamaks

J. D. Callen G. G. Kelley*
B. V. Waddell

The concept of a helical flux function is developed and utilized to investigate the magnetic topology in tokamaks when there are small, helically resonant magnetic perturbations present in the plasma. Generally speaking, the perturbations produce complicated magnetic island structures whose details depend on the character of the magnetic perturbation. Expressions are derived for the magnetic island width (δ), field line trajectory within an island, and length of field line required to trace out an island ($2\pi RN$). For helically resonant magnetic perturbations ($\tilde{B}$) which decrease as $x^{-\alpha}$ away from a rational surface, we find $\delta \sim (\tilde{B}/nq')^{1/(\alpha+2)}$ and $N \sim (nq'\delta)^{-1} \sim \tilde{B}^{-1/(\alpha+2)}(nq')^{-(\alpha+1)/(\alpha+2)}$, where q' is a measure of the magnetic shear and n is the toroidal mode number of the helical perturbation.

Possible Effects of Drift Wave Turbulence on Magnetic Structure and Plasma Transport in Tokamaks[39]

J. D. Callen

A new mechanism is proposed by which low level, drift wave type fluctuations, such as those observed in the ATC and TFR experiments ($e\tilde{\phi}/T_e \lesssim 10^{-2}$), can cause anomalous radial electron heat transport in tokamaks. The model is based on the fact that since transport processes parallel to the magnetic field are many orders of magnitude more rapid than perpendicular ones, very small, helically resonant magnetic perturbations (e.g., $\tilde{B}_r/B \geq \sqrt{\chi_\perp/\chi_\parallel} \sim 10^{-4}$) which cause field lines to move rapidly allow the parallel transport process to contribute to radial electron heat transport. We hypothesize that the small magnetic perturbations ($\tilde{B}_r/B \lesssim 10^{-3}$) accompanying drift waves at any nonzero plasma beta (ratio of plasma pressure to magnetic energy density) are large enough to produce significant effects in present tokamak experiments. The helical magnetic component of drift waves produces magnetic island structures whose spatial widths ($\delta \sim 0.5$ cm) can easily exceed the ion gyroradius. In a drift wave oscillation period, electrons circumnavigate a magnetic island, whereas the slower moving ions see only a tilt of the magnetic field lines. Thus, electrons try to diffuse radially more rapidly than ions; however, a radial potential builds up on a very short time scale to confine the electrons electrostatically and thereby keep the particle diffusion ambipolar. Nonetheless, this parallel electron diffusion process does cause net radial electron heat conduction through an ensemble of closely packed island structures. The heat conduction coefficient is estimated to be $\chi_e^\delta \sim (3/16)(\nu + \gamma)\delta^2$, where ν is the electron-ion collision frequency and γ is the drift wave growth rate, or inverse island correlation time. Other effects which these magnetic flutters may have on plasma transport and runaway electron processes are also discussed.

Experimental Measurement of Electron Heat Diffusivity in a Tokamak[40]

J. D. Callen G. L. Jahns*

Electron temperature perturbations produced by internal disruptions in the center of ORMAK are followed with a multichord soft x-ray detector array. The space-time evolution is found to be diffusive in character, but the conduction coefficient determined from a heat

*Special Projects

*General Atomic Company

pulse propagation model is larger by a factor of 2.5-15 than that implied by the measured gross energy containment time.

On Measuring the Electron Heat Diffusion Coefficient in a Tokamak from Sawtooth Oscillation Observations[41]

M. Soler J. D. Callen

A number of new methods are discussed for determining the electron heat conduction coefficient χ_e in a tokamak from the experimental observation of the space-time evolution of the temperature perturbations induced by internal disruptions. In ORMAK the various average values of χ_e and the radial dependence of χ_e are found to be consistent with and more precise than the $\chi_e(r)$ determined by conventionally analyzing the electron power balance equation. The net result of these measurements is to prove conclusively that the dominant radial electron heat transport mechanism in tokamaks is a microscopic, diffusive process.

4.3.3 Energetic Particle Orbits

Concomitantly with the success of the ORNL neutral beam development program we have maintained our theoretical effort in this area. The very high energy particle drift orbits due to injection or to the fusion process show significant deviations from standard orbit theory for thermal particles, necessitating extensions of the guiding center motion to higher order (topic 1). As an alternative to the very high energy beam development needed for heating of reactor-size machines, the concept of "ripple injection" will soon be tested. Here we report on a magnetic design for ripple-assisted beam injection into the ISX-B and TFTR tokamaks (topic 2). In this context two new computer codes were generated, both of which allow for the realistic magnetic field geometries needed for the next generation machines (topics 3 and 4).

Extensions of Guiding Center Motion to Higher Order[42]

T. G. Northrop* J. A. Rome

In a static magnetic field, some well-known guiding center equations maintain their form when extended to next order in the magnetic moment series. The differential equation for guiding center motion which describes both the parallel and perpendicular velocities correctly through first order in gyroradius is given. The question of how to define the guiding center position through second order arises and is discussed, and second order drifts are derived for one usual definition.

The toroidal canonical angular momentum, P_ϕ, of the guiding center in an axisymmetric field is shown to be conserved using the guiding center velocity correct through first order. When second order motion is included, P_ϕ is no longer a constant.

The above extensions of guiding center theory help to resolve the different tokamak orbits obtained, either by using the guiding center equations of motion or by using conservation of P_ϕ.

Magnetics Design for Ripple-Assisted Beam Injection into the ISX-B and TFTR Tokamaks[43]

R. J. Goldston† D. L. Jassby†
H. H. Towner† R. H. Fowler
J. F. Lyon‡ J. A Rome
T. Brown§

A test of ripple-assisted neutral beam injection will be performed on the ISX-B device in 1978-79, using a low power beam with $W_b \sim$ 10-20 keV, and possibly also on the TFTR device

---

*NASA/Goddard Space Flight Center
†Princeton Plasma Physics Laboratory
‡Tokamak Experimental Section
§Grumman Aerospace Corporation

ca. 1982 with a high power 80-keV beam. In both cases, the optimal coil configuration for establishing the required vertically asymmetric TF ripple consists of a pair of trapezoidal current loops located between the TF coils and the vacuum vessel and bracketing the vertically injected beam. This report describes the design of the ripple coils for ISX-B, the ripple contours in the elliptical ISX-B and circular TFTR plasmas, and the objectives and parameters of the ISX-B experiment. The formation of magnetic islands in the plasma is examined for an arbitrary number of ripple injection locations.

FLOC – A Field Line Orbit Code for the Study of Ripple Injection into Tokamaks[4]

R. H. Fowler D. K. Lee
P. W. Gaffney J. A. Rome

A computer code is described which is used to study ripple beam injection into a tokamak plasma. The collisionless guiding center equations of motion are integrated to find the orbits of single particles in realistic magnetic fields for ripple injection. In order to determine whether the ripple is detrimental to the plasma, the magnetic flux surfaces are constructed by integration of the field line equations. The numerical techniques are described, use of the code is outlined, a program listing is provided, and the results of sample cases are presented.

Monte Carlo beam deposition code

R. H. Fowler J. A. Rome

D. E. Post (PPPL) has developed a Monte Carlo beam deposition code (FREYA) which allows for arbitrary injection geometry. We modified this code to account for the noncircular, shifted flux surfaces which characterize high beta equilibria. This code now employs the equilibria calculated by the Oak Ridge Equilibrium Code to allow us to study injection scenarios which result from low density and/or small radius startup. This code is now undergoing further modification to account for the fast ion orbits.

4.3.4 The Collisional Plasma Model

C. O. Beasley, Jr. J. E. McCune
H. K. Meier K. E. Rothe
D. J. Sigmar W. I. van Rij

The CPM effort focuses on a computer code which solves the kinetic equation for each plasma species. Besides being used for a variety of production runs, the code and its underlying theory are presently extended to include the gyrokinetic equation (see topic 7). In 1977, fundamental papers defining the CPM were published (topics 1-3). Its first application, to neoclassical equilibria, was also reported or published (topics 4, 5). First results on the nonlinear evolution of drift modes are given in topic 6.

In the course of deriving the gyrokinetic equation for general equilibria using symbolic software techniques to handle the algebra, a completely new software package called WRITE was developed (topic 8).

The CPM: A Velocity Orthogonal Function Representation for the Distribution Function of a Collisional Plasma[5]

H. K. Meier W. I. van Rij
C. O. Beasley, Jr. J. E. McCune

A velocity-space, orthogonal function representation has been developed for the distribution functions of a collisional plasma. The choice of functions is determined by several criteria: (1) the functions must provide an accurate representation of the Coulomb collision operator; (2) the representation must be efficient, in that physical plasmas be represented by as few terms as possible in order to minimize both computer time and storage requirements; and (3) the collision and Vlasov operators must lead to simple expressions which can be rapidly and

easily calculated. The collision operator in the representation used here is developed both for the nonlinear (general distribution functions) and approximately linear (approximately Maxwellian distribution functions) cases. Some numerical results are discussed, and expressions for macroscopic observables in terms of the expansion amplitude are also given.

Kinetic Equations for the CPM[47]

W. I. van Rij — H. K. Meier
C. O. Beasley, Jr. — J. E. McCune

Using the CPM representation, expressions are derived for the Vlasov operator, both in its general form and in the drift kinetic approximation following the recursive derivation by Hazeltine. The expressions for the operators give easily calculated couplings between neighboring components of the CPM representation. Expressions for various macroscopic observables in the drift kinetic approximation are also given.

Numerical Study of Drift Kinetic Evolution of Collisional Plasmas in Tori[7]

C. O. Beasley, Jr. — J. E. McCune
H. K. Meier — W. I. van Rij

Preliminary numerical results for the dynamics of toroidally confined plasmas in the drift kinetic, Fokker-Planck description are discussed. These solutions were obtained by using the CPM (described in detail elsewhere). An initial value problem was solved in which collisions and particle dynamics compete in a given magnetic field to set up a quasi-equilibrium. The plasma (guiding center) distribution function and many macroscopic quantities of interest are monitored. Good agreement with corresponding but more approximate theories is obtained over a wide range of collisionality, particularly with regard to the neoclassical particle flux. Confirmation of earlier results for the distribution function is achieved when due account is taken of the differing collisionality of particles with differing energies.

Electrical Conductivity of Tokamak Plasmas Calculated by CPM Codes[48]

C. O. Beasley, Jr. — D. J. Sigmar
W. I. van Rij — H. K. Meier
J. E. McCune

We have used the CPM to calculate the parallel conductivity for several values of collisionality, Z_{eff}, and aspect ratio, using parameters characteristic of present experiments (e.g., ORMAK) as well as in the slideaway regime. The accurate treatment of the Fokker-Planck collision operator in combination with toroidal trapping effects, in the regime of finite values of $E/E_{DREICER}$, removes the ambiguities introduced by the *ad hoc* model treatment of this problem by Hui, Windsor, and Coppi.[49]

Calculation of a Self-Consistent, Low Frequency Electrostatic Field in Toroidal Geometry[50]

C. O. Beasley, Jr. — H. K. Meier
W. I. van Rij — J. E. McCune

We derive an asymptotic series in ω_p^{-2}, the inverse square plasma frequency, for the self-consistent, curl free, low frequency electric field in toroidal. The derivation is consistent with the drift kinetic ordering and may be used in either instability or equilibrium calculations. We also provide an interpretation of past formulations of the statement of quasi-neutrality as applied to neoclassical equilibria.

Numerical Study of Drift Mode Behavior Using a Self-Consistent Drift Kinetic Expansion[51]

W. I. van Rij — H. K. Meier
C. O. Beasley, Jr. — J. E. McCune

We derive the perturbed distribution function for low frequency drift modes in cylindrical plasmas, correct to first order in the $(k\omega/k_\parallel\omega_p)^2$ series expansion for the self-consistent electrostatic field derived in Ref. 50.

Starting w... solutions of the linear dispersion relations, ... have a numerical comparison of the expansion solution for the electrostatic field with the Poisson solution and i ve tigate the nonlinear behavior of drift modes.

Gyrokinetic equation using natural variables, part I

H. ... Meier

A drift kinetic equation for low frequency instabilities including finite Larmor radius terms $-k_\perp^2 \rho_i^2 \Phi$ derived for arbitrary (high beta) tokamak equilibria. In Part ... the Vlasov equation is first transformed (as Cat..o did) to magnetic field line velocity-space coordinates without specifying the MHD equilibrium. By constructing the eigenfunctions of the lowest order Vlasov operator (including the finite gyroradius term) such that its eigenfunctions are rigorously separable [$\propto \delta(\ldots) \exp(i\ldots - i\ldots)$, whe... ... is the gyroangle, ... and ... are a certain pair of poloidal and toroidal angles, and ... and ... are integers], the configuration space variables (..., ...) are defined rather than introduced arbitrarily. These natural variables and eigenfunctions permit a rigorous and numerically economic formulation of the gyrokinetic problem for arbitrary beta equilibrium. This will be shown in Part II.

"WRITE" (a DISSPLA Macroprogram) User's Manual[52]

H. K. Meier

A PDP10 program called WRIT... has been written which considerably simplifies the task to computer-generate text, slides, viewgraphs, etc., of complex mathematical expressions. This program constitutes an interface between the user and DISSPLA,[53] a widely used computer graphics software package.

4.4 TRANSPORT SIMULATION

T. Amano — J. T. Hogan*
D. E. Arnurius — W. A. Houlberg
S. E. Attenberger — H. C. Howe
J. D. Callen* — A. T. Mense
E. C. Crume, Jr. — J. K. Munro, Jr.

The continuing success of neutral injection heating has brought some key elements of the approach to an economically competitive tokamak reactor into sharper focus. The high power densities which are typical of recent reactor conceptual designs force detailed attention to be paid to the problems of impurity generation and transport, cold gas and pellet fueling, and transport in high beta plasmas. The path to the high beta tokamak reactor leads ... rectly through such contemporary experiments as ISX-A and ISX-B, however, and the testing of models for these processes against experimental results has improved our technical grasp of important issues in several areas in the past year.

The reactor high-Z impurity transport question can be studied by analyzing in detail the behavior in present experiments of lower-Z impurities (such as carbon, oxygen, aluminum, and neon), for which the basic neoclassical theory of transport can be tested as a reference. Advances (Sect. 4.4.1) on both the atomic physics and diffusion problems have been made, and a tentative recycling model has been proposed for comparison purposes (Sects. 4.4.2, 4.4.3).

The development of a successful strategy for reactor fueling for long pulse lengths requires the development of a more successful model for particle confinement. Anomalies which

*Group Leader
†Section 4.4 Coordinator

have been disclosed by present cold gas injection techniques may be resolved with the aid of multispecies neutral gas models developed in the past year (Sect. 4.4.2). Pellet injection into a tokamak discharge has been modeled for the first time and some features of the experiment predicted in advance (Sect. 4.4.2).

High beta FCT equilibria have been shown to be accessible, granted both presently favored and more pessimistic models for diffusive transport (Sect. 4.4.3). It has become clear as a result, however, that the limits to beta and confinement can be expected to come from new classes of MHD instabilities (such as ballooning), which will be triggered by increased pressure.

4.4.1 Physics Packages

D. E. Arnurius T. Amano
E. C. Cruse, Jr.

Numerical Calculation of Impurity Charge State Distributions[5]

E. C. Cruse, Jr. D. E. Arnurius

The numerical calculation of impurity charge state distributions using the computer program IMPDYN is discussed. The time-dependent corona atomic physics model used in the calculations is reviewed, and general and specific treatments of electron impact ionization and recombination are referenced. The complete program and two examples relating to tokamak plasmas are given on a microfiche so that a user may verify that his version of the program is working properly. In the discussion of the examples, the corona steady-state approximation is shown to have significant defects when the plasma environment, particularly the electron temperature, is changing rapidly.

Subroutines for impurity excitation, ionization, and recombination

D. E. Arnurius T. Amano
E. C. Cruse, Jr.

Additional subroutines for general use were developed for calculating nonequilibrium electron impact excitation, ionization, and recombination of impurity elements of significance to recent (e.g., ATC) and current (e.g., ISX, PLT, TFR) tokamak experiments. Among the new impurity elements treated are aluminum and neon for impurity injection experiments, and the subroutines for iron and oxygen were upgraded.

4.4.2 Tokamak Discharge Modeling

Two-species neutral transport model

H. C. Howe D. E. Arnurius

In a plasma consisting of two hydrogen isotopes (hydrogen and deuterium or deuterium and tritium), the neutral particle transport is described by a Boltzmann equation for each neutral species. These two equations are coupled by charge exchange of the neutrals of one species with the plasma ions of the other species. This provides each neutral population with a volume source and sink term in addition to electron ionization. We have developed a code which solves for the neutral density and energy profiles in a slab geometry using simplified collision operators to describe the charge exchange coupling. Global neutral particle and energy balances are calculated along with the energy balances are calculated along with the energy spectrum of emerging neutrals and the The code is being used to analyze charge exchange data from recent experiments in ISX-A in which deuterium was puffed into a hydrogen

plasma. Coupled with a two-species plasma transport code, the neutral routine is also being used to investigate whether an inward plasma pinch must be included in the density equation in order to reproduce the penetration of the puffed deuterium to the center of the hydrogen plasma.

Transport simulation of pellet fueling in ISX

H. C. Howe

A transport model of pellet injection provides a description of recent observations on ISX-A and predicts results for ISX-B. A new 1-D cylindrical transport code (PROCTR) uses a simple predictor-corrector method to solve the conventional time-dependent equations for density, temperatures, and fields. The pellet model, developed in connection with reactor fueling studies (Sect. 4.5.1), includes ablation and deposition of the injected hydrogen on flux surfaces; the ablation model agrees well with pellet injection results from ORMAK.

In the transport model, neutrals from the wall and from the gas injection valve create a plasma source in the outer regions of the plasma. The neoclassical pinch transports some of this plasma to the center, while most of the particles recycle to the wall (which acts as a partial getter). An arbitrary particle diffusion level balances both the neutral source and the neoclassical pinch and reproduces observed prepellet density levels for a diffusion coefficient of $D \approx 1$-10 cm^2/msec. The pellet model provides a density deposition profile. The addition of this density to the plasma density, combined with an adiabatic decrease of the plasma temperature, gives initial conditions for the evolution of the plasma after the pellet is injected.

The model predicts the two major experimental signatures of a pellet injected into ISX-A (see Sect. 6.8). The density increases by ~30% due simply to depositing all the pellet particles in the plasma, i.e., simple particle balance is obtained. The additional cold electrons instantaneously turn on electron-electron collision time scale, lower the plasma electron temperature, and the resulting increase in the plasma resistance causes a positive voltage spike. The observations and predictions from the model agree quantitatively for these two effects.

The model voltage decreases to the preinjection value in about one energy confinement time, while the current density profile is held constant by flux conservation. This decay time (~1.5 msec) is consistent with the observed decay time. The density behavior after the pellet is injected is more variable and is still being modeled.

Modeling of ISX-B pellet experiments indicates that flux conservation will prevent modification of the current density profile as long as the number of particles in a pellet does not exceed the number of particles in the plasma. Larger pellets cool the plasma enough to make the magnetic diffusion time less than the electron energy containment time. The resulting peaking of the current channel may lead to disruption and, in fact, large pellets caused greatly enhanced MHD activity in the ISX-A experiments. To sustain the ISX-B plasma solely with pellet injection in the presence of this theoretical limit to the pellet size will require multiple pellet injection. The modeling indicates that a pellet injection rate of one pellet every 10 msec would be sufficient to maintain a plasma density of $\bar{n}_e = 5 \times 10^{13}$ cm^{-3}.

Impurity recycling model for vuv spectroscopic data analysis

B. E. Armurius E. C. Crume, Jr.
H. C. Howe

An extension of an impurity recycling model used by the TFR Group[1] has been made to assist in the analysis of vuv spectroscopic data from ORMAK and ISX. The extension allows for more freedom in the choice of diffusion velocities

and impurity density profiles, and its use in the analysis of oxygen impurities in ORMAK is described in Sect. B.1.c of this report.

Impurity transport simulation

T. Ando E. S. Marmar, Jr.

An impurity transport simulation code has been considerably upgraded and extended to treat the transport of oxygen and iron and oxygen and injected aluminum in ATC and of various species, including aluminum and neon in ISX, and to treat impurity flow reversal experiments in ISX.

4.4.3 Tokamak Model Development

The Accessibility of High-Beta States

J. T. Hogan

Encouraging results with tangential neutral beam heating and adiabatic compression of tokamak plasmas have prompted interest in and a will study the attempt to achieve high-beta, high projected beta values based on magnetohydrodynamic equilibrium considerations. The models previously used for transport calculations will become inadequate. Two new models will be required to account for the modification of the magnetic geometry, along with the changes in plasma parameters.

We present an axisymmetric transport model which should be useful for studying the approach to higher beta values in tokamak experiments. Results from transport calculations with this model allow us to draw a parallel between observed behavior in two highly unrelated experiments: electron heating by neutral injection in the ORMAK device, and adiabatic compression in the ATC experiment. Finally, the nature of cross-field transport may be expected to change as significant beta values are reached. Enhanced transport from ballooning instabilities is likely to play a role as important as that now played by sawtooth ($m = 1$) and saturated $m = 2$ instabilities. New techniques for describing this transport are required.

Impurity Models for Tokamaks

J. T. Hogan

The performance of the majority of tokamak confinement experiments supports that impurities will play a key role in the behavior of controlled fusion reactors, while every effort is made to minimize impurity content and some promising techniques for prevention and control have been identified, it seems prudent to assume that a significant, residual impurity constituent will remain. This has led to develop and to test models for the various phases of the problem: ionization, recombination through the coronal-equilibrium level into the plasma transport in the plasma and effects of impurities on the plasma power, energy, and momentum balance. In this paper we describe the models for these basic processes which are used in computer studies of tokamak dynamics, and we discuss the areas where improvement is needed.

Atomic and Molecular Data Needs, Priorities, and Accuracies for Tokamak Beam Injection

J. T. Hogan

The tokamak magnetic geometry possesses satisfactory confinement properties and will form the basis for many large, new experiments in the next few years. The aim of all of these experiments is to explore the physics of hot, dense plasmas in conditions near to those for which significant thermonuclear energy production is a possibility. Some experiments, such as TFTR, may even attain breakeven, with energy produced from D-T fusion reactions equaling the energy input needed to sustain the plasma against losses.

It is a common assumption that some sort of external heating mechanism will be required to achieve high plasma temperature. While various forms of radio frequency and other wave heating techniques are being studied, the dominant emphasis is being placed on heating by the

injection of energetic beams of neutral hydrogenic particles. We will first discuss the processes which are important to an understanding of the neutral beam injection process in a tokamak, and then discuss those areas for which atomic and molecular data are particularly needed. We conclude with an assessment of the accuracies required and with some estimation of the priorities which should be assigned.

Tokamak Transport Simulation Models[61]

J. T. Hogan

We describe the Oak Ridge Tokamak Transport Code. This code computes the number, momentum, and energy balance for particles and follows the evolution of tokamak poloidal and toroidal fields. The magnetic geometry is two-dimensional, with solutions of the Grad-Shafranov equation providing flux surface topology. The velocity-space description of fast injected ions is also two-dimensional, and the Fokker-Planck equation is solved for the injected species. Transport *per se* involves six coupled nonlinear partial differential equations, while the treatment of the plasma-wall interface requires the solution of 14 zero-dimensional rate equations. The XSDRN neutron and photon transport code has been adapted to serve as a neutral gas transport module.

Some examples illustrating problems of current interest are presented.

A User's Manual for the Oak Ridge Tokamak Transport Code[62]

J. K. Munro, Jr. J. T. Hogan
H. C. Howe D. E. Arnurius

A 1-D tokamak transport code is described which simulates a plasma discharge using a fluid model which includes power balances for electrons and ions, conservation of mass, and Maxwell's equations. The modular structure of the code allows a user to add models of various physical processes which can modify the discharge behavior. Such physical processes treated in the version of the code described here include effects of plasma transport, neutral gas transport, impurity diffusion, and neutral beam injection. Each process can be modeled by a parameterized analytic formula or at least one detailed numerical calculation. The program logic of each module is presented, followed by detailed descriptions of each subroutine used by the module. The physics underlying the models is only briefly summarized. The transport code was written in IBM FORTRAN-IV and implemented on IBM 360/370 series computers at ORNL and on the CDC 7600 computers of the MFE Computing Center of Lawrence Livermore Laboratory. A listing of the current reference version is provided on accompanying microfiche.

Free-Expansion Experiment on ATC

L. P. Grisham* K. Bol*
J. T. Hogan

The transport of a tokamak plasma freed from contact with a material limiter is studied. A small compression in major radius of the plasma in the ATC tokamak produces a free-standing discharge, similar, except for scale, to a possible configuration of the TFTR. The density evolution is readily modeled by a numerical transport model calculation. The experiment provides a successful preliminary test of the feasibility of this technique.

4.5 PLASMA ENGINEERING

S. E. Attenberger Y-K. M. Peng
J. N. Davidson J. A. Rome
G. A. Emmert K. E. Rothe
W. A. Houlberg W. M. Stacey, Jr.
D. G. McAlees D. J. Strickler
J. R. McNally, Jr. N. A. Uckan†
A. T. Mense R. M. Wieland

Plasma engineering applies and coordinates specialized theoretical plasma physics techniques and models to applied areas of fusion

---

*Princeton Plasma Physics Laboratory
†Group Leader

energy research, development, and engineering as needs arise or are anticipated.

4.5.1 Plasma Systems Activity

A. T. Mense — J. N. Davidson
J. R. McNally, Jr. — S. E. Attenberger
W. A. Houlberg — S. L. Milora*

The Plasma Systems Activity this past year mainly concentrated on studying the effects of various "cold fuel" fueling profiles, including the self-consistent effects of discrete pellet fueling, on plasma behavior.

A preliminary study has been initiated to consider possible schemes for steady-state tokamak reactor operation by maintaining the plasma current during the transformer "recocking phase" with neutral beam-driven currents. The possibility of beam or fusion alpha-produced seed currents has also been addressed in preliminary studies.

The electrostatic plasma sheath problem (which may occur at divertor collector plates and limiters) has been generalized to include multispecies.

Effects of fueling profiles on plasma

W. A. Houlberg — A. T. Mense
S. L. Milora* — S. E. Attenberger

A summary of the plasma fueling study is presented here; the details of the study are reported in Ref. 64. The following points have been observed.

(1) There appears to be no experiential evidence or theoretical restriction (to date) which would dictate that cold fuel must be injected directly into the hot central core region of a tokamak. Even classical processes appear to be sufficiently fast to balance central ion losses due to fusions.

(2) By reducing the pellet penetration requirements in the plasma, a consequent reduction in pellet velocity is achieved. This reduction in pellet speed is on the order of ten and is independent of the ablation physics model for the pellet. Using the experimental work of Foster and Milora on pellet injection performed on ORMAK,[65] a suitable pellet velocity for a TNS device appears to be in the neighborhood of ~3 km/sec.

(3) Present-day microinstability theory[66] tends to indicate a potential problem which could develop in a reactor-grade plasma. The so-called dissipative trapped particle instabilities may occur, the nonlinear consequences of which may be anomalously high energy and particle loss rates. The lowest order form of the theory shows that these modes depend sensitively on the plasma density gradients. (They usually depend on temperature gradients in higher order.) Control of the cold fuel fueling profiles appears to have a profound effect on the density gradient dependencies of these instabilities. Edge fueling tends to flatten the density ($\nabla n \to 0$) over the hot central plasma regions. Near the edge, where ∇n is steep, the temperature is held low due to the dominance of the cold fuel. The net effect is to reduce the energy losses from the plasma due to these modes. In addition, self-consistent 1-D transport studies of neutral beam-heated, full-bore startup tend to indicate that gas puffing is a less than optimum way to fuel if these trapped particle modes are present; thus some degree of pellet injection appears necessary (see Figs. 4.11, 4.12).

(4) For a TNS-size device it was found that 2-mm radius, 1-km/sec-pellets did a suitable job of maintaining the plasma at any desired operating density. Typically, pellet injection rates on the order of 10 to 20 pellets/sec were required to maintain a volume-averaged density, $\bar{n}$, of 8×10^{13} cm^{-3}. The pellet deposition profile was computed self-consistently using the ablation theory of Parks, Foster, Milora, and Turnbull.[67,68] Oscillations in edge density and temperature occurred, but because they occur on a short time scale compared with the local energy confinement times, the local

*Plasma Technology Section

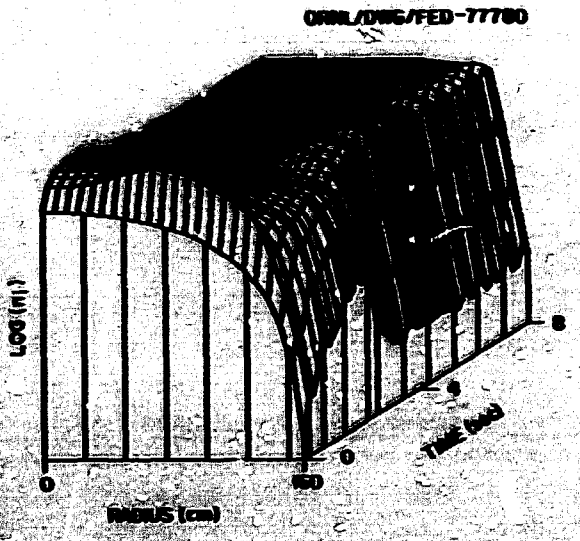

Fig. 4.11. Evolution of the density profile over 8 sec for a small pellet, high plasma density case. A 2-mm-radius pellet is injected at 10^3 m/sec whenever the plasma density drops below $n = 10^{14}$ cm^{-3}, resulting in 177 pellets injected during the simulation.

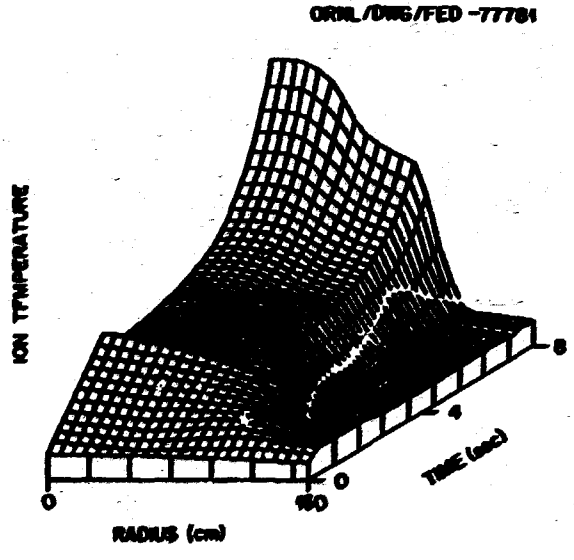

Fig. 4.12. Evolution of the ion temperature for the same case shown in Fig. 4.1. The hot ignited central core region (sharply defined because of local alpha heating) and the cold edge region resemble the low penetrating, continuous particle source results.

plasma beta (∝ density x temperature) was essentially unaffected. Also there were no fusion power oscillations because all the fusion events occur in the central plasma core and thus are not affected by edge oscillations (see Fig. 4.13). Deeper penetration would, of course, have a more instantaneous effect on the fusion power.

(5) There was at one time a concern about whether a significant fraction of neutral beam-injected power would be attenuated at the plasma edge due to the pellet ablation (density) spike. Our 1-D numerical studies seem to indicate that no problem exists here unless, of course, too large a pellet is used. In that case, the plasma properties used to decide the pellet ablation rate may be modified so quickly that the ablation physics analysis would become

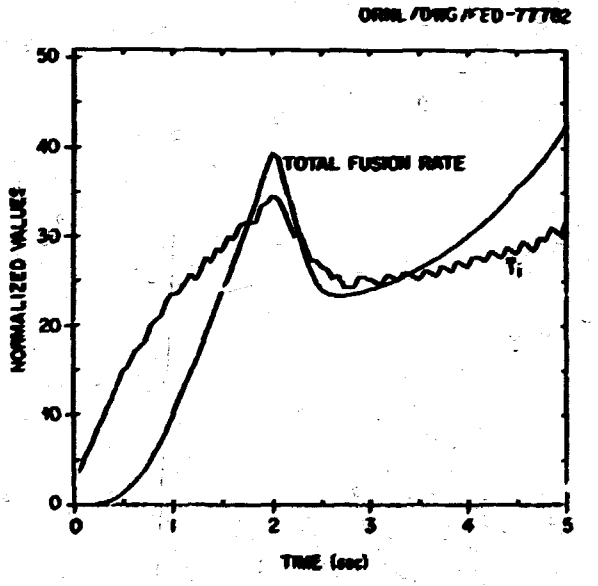

Fig. 4.13. The normalized values of the average ion temperature and total fusion rate as a function of time. The fluctuations in the ion temperature result from fluctuations (due to pellets) near the plasma edge. The fusion rate is very strongly centrally peaked and basically unaffected by the edge fluctuations.

suspect. However, for reasonable pellet sizes (e.g., pellets carrying ~10% of plasma density/pellet), we find negligible effects on beam attenuation.

Electrostatic Sheath Potential for a Hot, Multispecies Plasma[69]

J. N. Davidson A. T. Mense

The collisionless electrostatic sheath between a plasma and a wall has been investigated for the case in which the plasma contains several ion species and has a finite temperature. This modest extension of the analysis of Hobbs and Wesson[70] also incorporates secondary electron emission from the wall. The inclusion of impurity species in the plasma modifies the Bohm criterion so that the sheath potential is slightly increased and the total heat flow across the sheath is slightly increased. Because the energy carried from the plasma by the ions is increased, enhanced sputtering is a possibility.

4.5.2 Divertor Modeling[71]

A. T. Mense G. A. Emmert

One-dimensional transport studies using the Mense-Emmert divertor model have been carried out for large fusion reactors (e.g., EPR, UWMAK-II, UWMAK-III) and for smaller devices (e.g., PDX/ASDEX). To allow modeling of this inherently 2-D problem with a 1-D code, suitable expressions must be found for the particle and energy loss rates along the field lines to the collector plates. In the model used here this requires the replacement

$$\nabla_{\parallel} \cdot \Gamma_{\parallel} \rightarrow \frac{\Gamma_{\parallel}(r)}{L(r)} = \frac{nv_{\parallel}}{L} = \frac{n}{\tau_{\parallel}} ,$$

where $L(r)$ is the "average" distance which a particle must travel along the field before it is collected. Similarly one makes the replacement

$$\nabla_{\parallel} \cdot \left(\frac{3}{2} T_e \Gamma_{\parallel} + \tilde{Q}_{e\parallel}\right) \rightarrow \frac{Q_{e\parallel}}{L(r)}$$

and

$$\nabla_{\parallel} \cdot \left(\frac{3}{2} T_e \Gamma_{\parallel} + \tilde{Q}_{i\parallel}\right) \rightarrow \frac{Q_{i\parallel}}{L(r)} ,$$

where $\tilde{Q}_{\parallel}$ represents conductive loss and $3/2\ T\Gamma_{\parallel}$ is the convective loss along the field lines.

By requiring the net electrical current at each position along the collector plate to be zero, one can determine (approximately) the sheath potential ϕ_{max}. The expression $\vec{j} = 0$, which includes secondary electron emission effects, is given by

$$(\Gamma_{\parallel}^{+})_{elec} = (\Gamma_{\parallel}^{+})_{ion} \left(\frac{1 + \langle \varepsilon_i \rangle_{eff}}{1 - \langle \varepsilon_e \rangle_{eff}}\right)\left[1 - \frac{\langle \phi_\gamma \beta_\gamma \rangle}{(\Gamma_{\parallel}^{+})_{ion}}\right] ,$$

where $\langle \varepsilon_j \rangle_{eff}$ is the effective secondary electron emission coefficient of the collector plate material due to bombardment of the jth particle species. In addition $\langle \phi_\gamma \beta_\gamma \rangle$ gives the secondary electron emission due to a gamma ray or x-ray flux ϕ_γ. The resulting ϕ_{max} is given by

$$\phi_{max} = kT_e \ln \left[\frac{\left(\frac{m_i T_e}{m_e T_i}\right)^{1/2} \left(\frac{1 - \langle \varepsilon_e \rangle_{eff}}{1 + \langle \varepsilon_i \rangle_{eff}}\right)}{1 - \frac{\langle \phi_\gamma \beta_\gamma \rangle}{(\Gamma_{\parallel}^{+})_{ion}}}\right] .$$

Applying these results for the case of no secondary electron emissions, one arrives at the following expressions for the parallel fluxes:

$$\Gamma_{\parallel}(r) = \frac{n(r)}{4}\left[\frac{8\ kT_i(r)}{\pi\ m_i}\right]^{1/2} ,$$

$$Q_{\parallel i}(r) = 2kT_i(r)\Gamma_{\parallel}(r) , \text{ and}$$

$$Q_{\parallel e}(r) = 2kT_e(r)\gamma_E(r)\Gamma_{\parallel}(r) ,$$

where

$$\gamma_E(r) = 1 + \ln\left(\frac{m_i T_e}{m_e T_i}\right)^{1/4}$$

$$= 2.88 + 0.25 \ln\left(\frac{T_e A}{T_i}\right).$$

These expressions are then applied at a reasonable number of spatial nodes near the plasma edge in the 1-D transport code. It can clearly be seen that

$$\frac{Q_{\parallel e}}{T_e} > \frac{Q_{\parallel i}}{T_i} ,$$

which shows that the electrons "cool" faster than the ions; thus, energy deposition profiles across a collector plate are steeper than particle density profiles, i.e.,

$$\left(\frac{1}{T_e}\frac{\partial T_e}{\partial r}\right)^{-1} < \left(\frac{1}{n}\frac{\partial n}{\partial r}\right)^{-1}$$

across the collector plate. Two examples applying the above model are shown in Figs. 4.14 and 4.15.

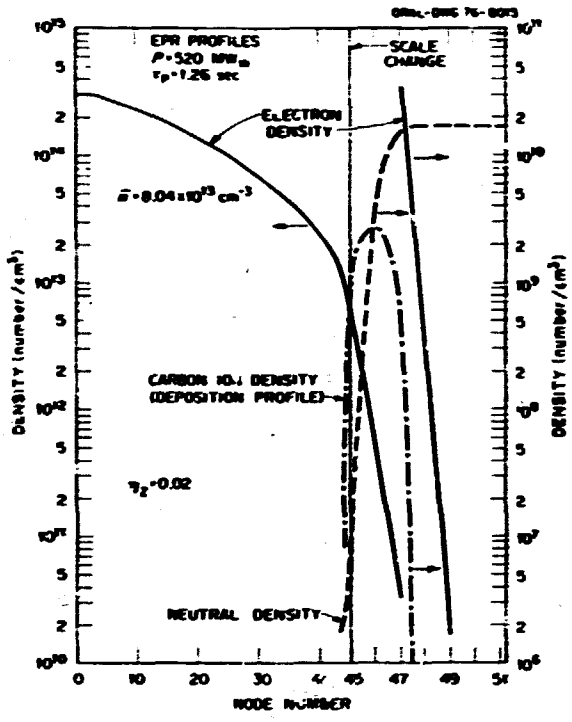

Fig. 4.14. Electron density, neutral density, and 20-eV carbon impurity deposition profiles. Note that $\eta_Z = 0.98$ implies a 98% shielding efficiency, i.e., only 2% of the wall-originated 20-eV carbon atoms makes it across the scrape-off zone into the main plasma.

4.5.3 Plasma Startup

W. A. Houlberg Y-K. M. Peng
S. K. Borowski T. Uckan

A comprehensive analysis of startup for large tokamaks has been initiated at ORNL. The primary objective of the study is to determine whether innovative startup scenarios can reduce or eliminate major technological problems associated with traditional techniques.

A three-phase startup procedure which has some very attractive features is being examined: (1) microwave breakdown of the plasma and electron heating near the upper hybrid resonance before the toroidal current is introduced, (2) continued microwave heating while increasing the toroidal current and density in a relatively small plasma, and (3) heating by neutral beams while simultaneously increasing the plasma size and current to final values.

Estimates of required microwave power levels for the first phase and theoretical estimates of relevant time scales for ohmically heated plasmas for the third phase have been made. One-dimensional transport calculations are now being developed for the second and third phases of startup to increase flexibility of the model.

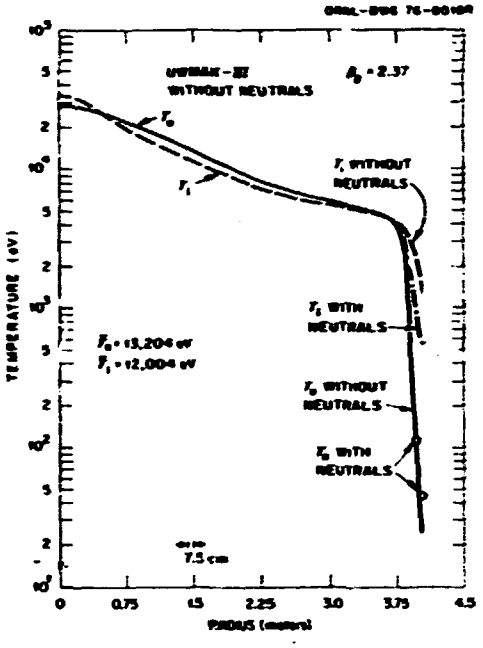

Fig. 4.15. Typical temperature profiles for a large fusion reactor. Note that recycling 10% of the divertor-collected flux back to the plasma as wall-originated neutrals causes a factor of two to three increase in ion temperatures in the divertor zone (where most charge exchange occurs) and little or no difference in bulk plasma temperature.

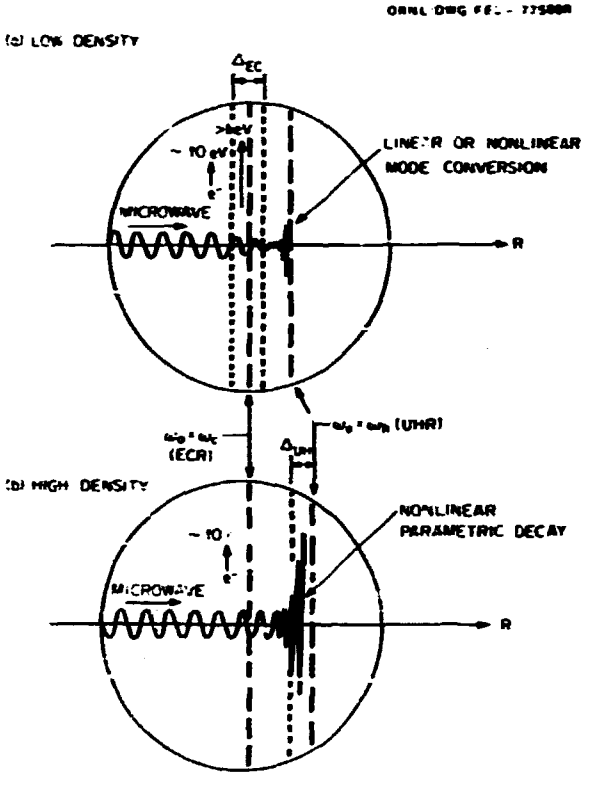

Fig. 4.16. The assumed mechanisms of microwave (as extraordinary mode) absorption near the ECR and the UHR in a currentless tokamak plasma; (a) in the low density regime, and (b) in the high density regime.

Microwave Startup of Tokamak Plasmas Near Electron Cyclotron and Urper Hybrid Resonances[72]

Y-K. M. Peng S. K. Borowski

The scenario of toroidal plasma startup with microwave initiation and heating near the electron cyclotron frequency is suggested and examined here (see Fig. 4.16). We assume microwave irradiation from the high field side and an anomalously large absorption of the extraordinary waves near the upper hybrid resonance. The dominant electron energy losses are assumed to be due to magnetic field curvature and parallel drifts, ionization of neutrals, cooling by ions, and radiation by low-Z impurities. It is shown by particle and energy balance considerations that electron temperatures around 250 eV and densities of 10^{12}-10^{13} cm^{-3} can be maintained, at least in a narrow region near the upper hybrid resonance, with modest microwave powers in ISX (120 kW at 28 GHz) and TNS (0.57 MW at 120 GHz). The loop voltages required for startup from these initial plasmas are also estimated. It is shown that the loop voltage can be reduced by a factor of five to ten from that for unassisted startup without an increase in the resistive loss in volt-seconds. If this reduction in loop voltage is verified in the ISX experiments, then substantial savings in the cost of power supplies for the OH and EF coils can be realized in future large tokamaks.

Small radius startup of ohmically heated tokamak plasmas with moving limiters[73,74]

T. Uckan

The problem of startup for a large tokamak plasma is studied with a moving limiter. The plasma transport with the presence of the electric field diffusion and heat conduction losses is investigated analytically by the separation of variables during this early phase of the discharge. The time evolution of the current density and temperature profiles is then obtained for this simple model. Expressions are also given for plasma discharge parameters such as the time evolution of the safety factor, the plasma current, the poloidal flux function, the skin time, the poloidal beta, the transformer flux, and the electron energy lifetime. The results are then applied to a typical tokamak (TNS-size) plasma. It is shown that a moving limiter may help ameliorate the possible problem of skin effects on the current profile.

4.5.4 Beam Heating Scenarios

J. A. Rome R. H. Fowler
J. A. Holmes Y-K. M. Peng

Possible "approach to ignition" scenarios for large and dense tokamaks have been studied. The primary scenario which has been adopted[75] starts with full-bore, low density plasma where beams can easily penetrate, so the heating profiles can be centrally peaked. As the plasma is heated and the density is increased, alpha heating and flux surface shifts seem to allow adequate beam penetration. Because of the centralized alpha particle heating (see Fig. 4.17), the need for full neutral beam penetration for $\bar{\beta} > 2\%$ may be eliminated.[75,76]

Another possible scenario starts with a dense, small-radius plasma which can be easily heated by the beams. As the radius is increased by gas puffing, the newly formed plasma is heated via beams. This scenario has the advantage of keeping the plasma away from the walls to (hopefully) control impurities and may allow some major radius compression to "kick" the core to ignition.

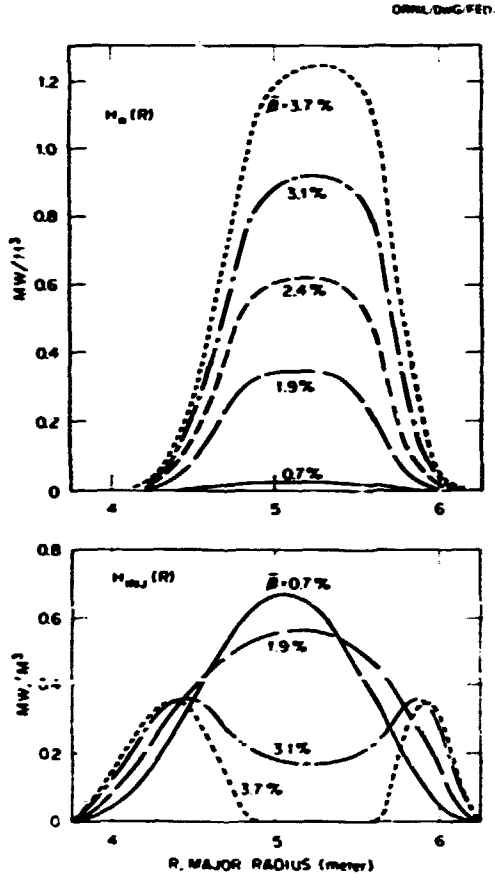

Fig. 4.17. Alpha particle heating and the required neutral injection heating profiles in a sequence of FCT equilibria in a TNS-size plasma from $\bar{\beta} = 0.7\%$ to 3.7%. Meanwhile, the peak plasma density (n_o) is assumed to increase from 1.2×10^{14} cm^{-3} to 2.1×10^{14} cm^{-3} in a linear fashion with $\bar{\beta}$ (from Ref. 76).

The sensitivity of beam injection to plasma density has been studied by using the Monte Carlo beam deposition code (Sect. 4.3.3). If the density is too low, the beam goes through the plasma and hits the far wall, while if it is too high, the beam will not reach the center of the plasma. As illustrated in Fig. 4.18, the range of acceptable plasma densities is quite narrow – only a factor of two to three. For effective heating during the approach to ignition, variable beam energy may be required.

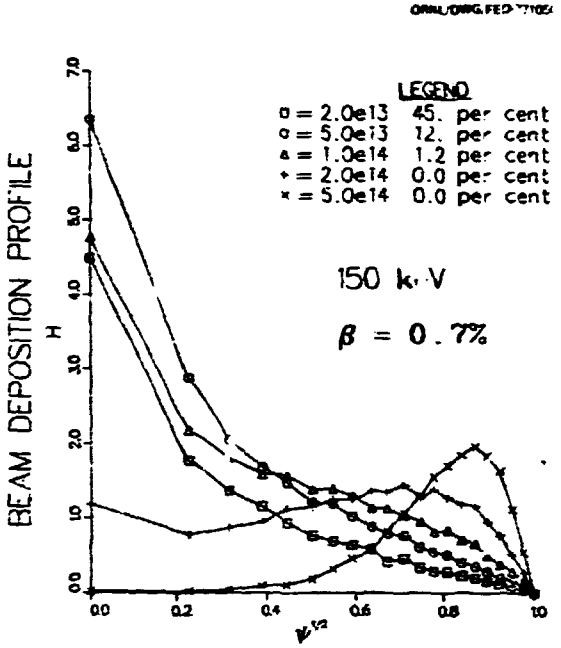

Fig. 4.18. For a given beam energy, the "density window" for acceptable beam penetration is small.

4.5.5 Advanced Fusion Fuels

J. R. McNally, Jr. K. E. Rothe

Advanced fusion reactors may permit the use of cleaner fusion fuels than the classical D-T. The reaction rate parameters as a function of ion temperature for many of the fuel cycles have been developed and are available in a subroutine on the NMFECC computer. A new ignition parameter Tn_τ and an energy multiplication factor k (analogous to the four-factor formula in fission) have been evaluated for D-T and for advanced fuel plasmas.

The Ignition Parameter Tn_τ and the Energy Multiplication Factor k for Fusioning Plasmas[77]

J. R. McNally, Jr.

Presented here are some novel interpretations of fusion plasmas which may be of interest to both fission and fusion scientists and engineers. A new fusion ignition parameter $(Tn_e\tau_E)_I$ is proposed which is proportional to β^2B^4 and inversely proportional to the charged particle fusion power density (P_{Fusion}) of a reacting plasma. Curves are given for many potential nuclear fusion fuels (see Fig. 4.19). The energy utilization factor in existing devices is defined as $f = P_{Fusion}/P_{Loss} = (Tn_e\tau_L)/(Tn_e\tau_E)_I$; in experimental plasmas, f has increased by about two orders of magnitude in the past decade and now exceeds 10^{-4}, while a "nearest" f* exceeds 10^{-3} (see Fig. 4.20). The f factor is also analogous to its fission counterpart in the four-factor neutron multiplication factor

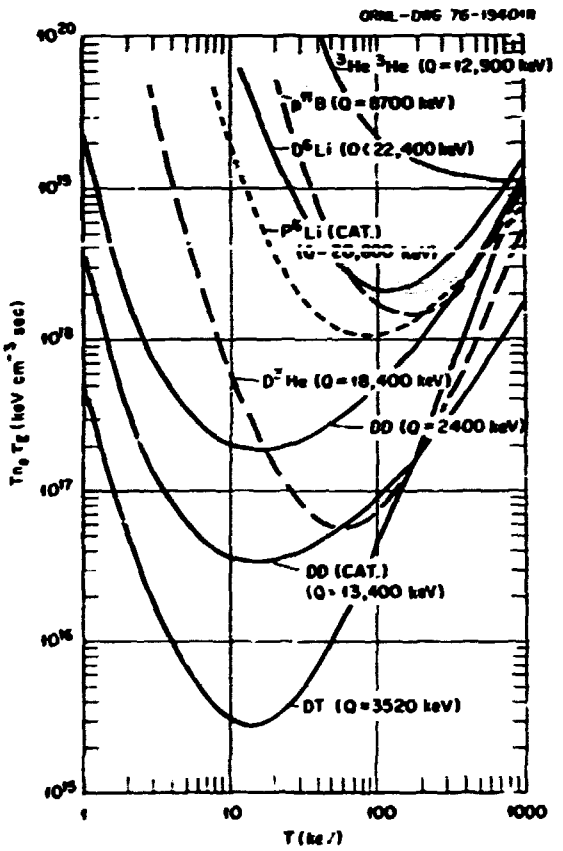

Fig. 4.19. The ignition parameter $(Tn_e\tau_E)_I$ vs kinetic temperature T with $T = T_i = T_e$. D^6Li, D^3He, and D-T do not include D-D side reactions.

ORNL/DWG/FED-77300R2

FUSION EXPERIMENTS PROGRESSING TOWARD GOALS OF BREAKEVEN AND IGNITION AS MEASURED BY $nT\tau_E$

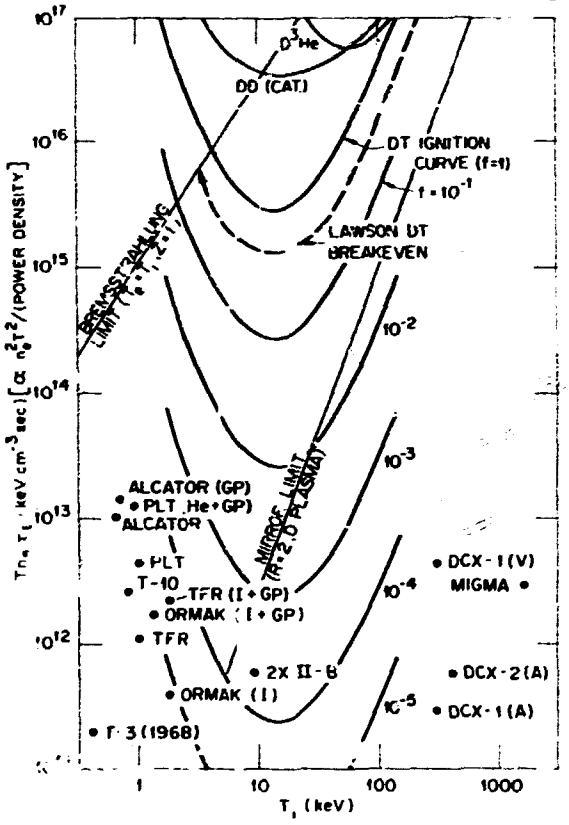

Fig. 4.20. Experimental $nT_e\tau_L$ points, Lawson breakeven curve, and three ignition curves. I = injection, GP = gas puff, He = helium, V = high vacuum buildup, A = arc breakup of H_2^+. Ignition curves must be below appropriate bremsstrahlung limiting curve. Mirrors must be partially closed in some way to be above mirror limit. [f^* is the ratio of the experimental ($nT_e\tau_L$) to 3 x 10^{15} keV cm^{-3} sec]. Laser pellet best experimental point is at 8 x 10^{12} keV cm^{-3} sec at 8 keV (Erik Storm, LLL, private communication, September 1977).

k = fnεp, where f is the neutron thermal utilization factor. Past, present, and future fusion experiments are discussed briefly in this context.

D^3He as a "Clean" Fusion Reactor[75]

J. R. McNally, Jr.

The prospects for relatively "clean" D^3He reactors (lean D, rich ^3He) are evaluated, with significant gains over a comparable power D-T reactor (14-MeV neutrons reduced by 135, all neutrons by 25, plasma tritium by $\sim 10^3$, tritium handling by $\sim 10^3$).

Energy Transfer from Ions to Electrons and the Coulomb Logarithm[75]

J. R. McNally, Jr.

Application of Chandrasekhar's stellar approach to plasmas reveals the importance of nondominant terms in both the energy transfer from ions to electrons and the form of the Coulomb logarithm. Figures 4.21 and 4.22 illustrate the role of dominant and nondominant terms in the neighborhood of electron velocity near the ion velocity.

4.5.6 Plasma Engineering Support of Advanced Systems

Advanced fusion systems design projects (see Sect. 8 of this report) receive fusion physics support and guidance from the plasma engineering group.

Plasma Engineering Considerations and Innovations for a Medium Field Tokamak Fusion Reactor[76]

S. E. Attenberger
W. A. Houlberg
Y-K. M. Peng
J. D. Callen
A. T. Mense
J. A. Rome
N. A. Uckan

Recent plasma engineering studies have ascertained a viable concept for TNS based on medium toroidal fields between 4 and 7 T at the plasma center, plasma $\bar{\beta}$ values up to 10%, and averaged densities between 0.6 x 10^{14} cm^{-3} and

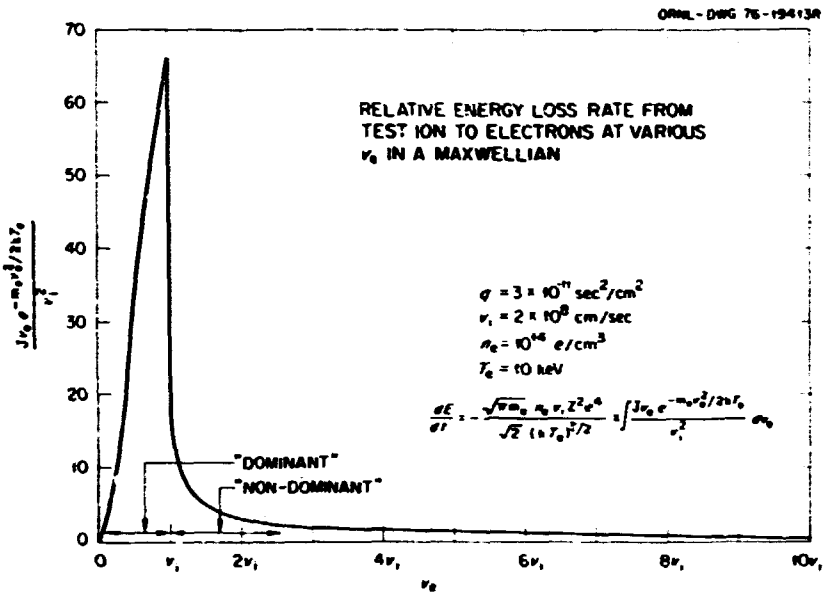

Fig. 4.21. Relative energy loss rate of a test ion to electrons of various v_e in a Maxwellian distribution at T_e = 10 keV, v_i = 2 x 10^8 cm/sec, n_e = 10^{14} e/cm^3, and $q = \lambda_D m_e/Ze^2$ = 3 x 10^{-11} sec^2/cm^2.

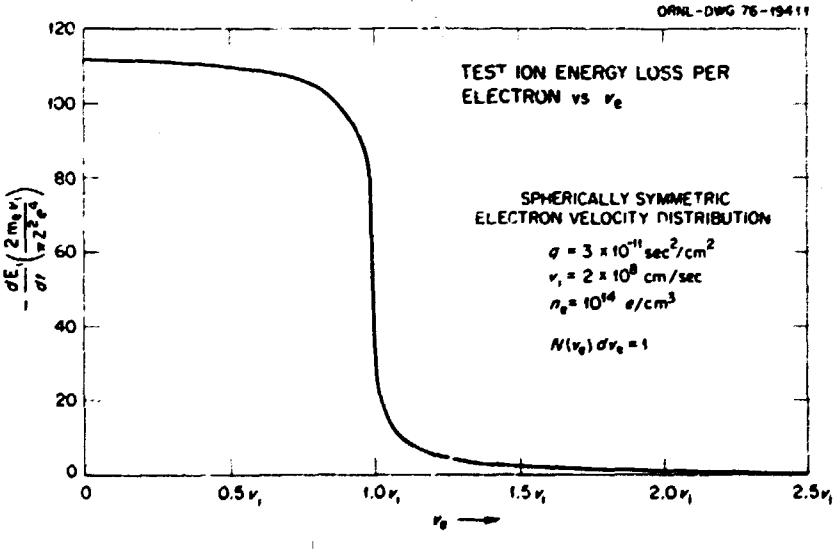

Fig. 4.22. Electron velocity dependence of the test ion energy loss rate per electron in a plasma at n_e = 10^{14} e/cm^3, T_e = 10 keV, q = 3 x 10^{-11} sec^2/cm^2, and test ion velocity v_i = 2 x 10^8 cm/sec.

2.5 x 10^{14} cm^{-3}. Plasma engineering innovations that can substantially reduce the size, cost, and complexity of TNS have been explored and are summarized in this paper. It is shown that the previously anticipated requirement of high pellet velocities can be substantially reduced (see Fig. 4.23); the TF ripple requirements may be relaxed to reduce the number of TF coils and improve machine access; hybrid EF coils have been shown to require building only small interior coils and to reduce the power supply required by the exterior coils; proper approaches of microwave plasma preheating may reduce the peak loop voltage for startup by an order of magnitude.

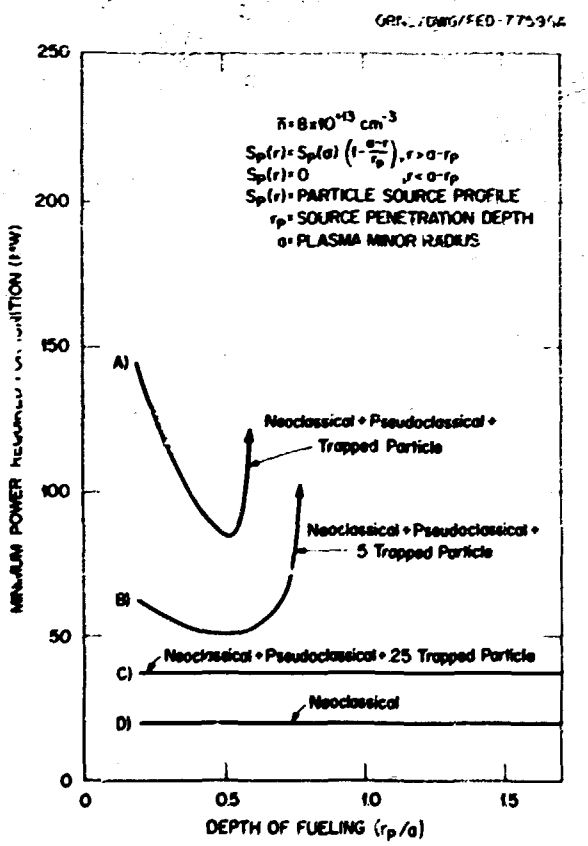

Fig. 4.23. The dependence of the minimum heating power (required for ignition) on the depth of fueling for various levels of trapped particle loss rates assumed in the 1-D transport calculations for TNS.

The reactor fluid TNS reactor concepts and the plasma engineering innovations discussed should be applicable to other designs of tokamak reactors; some of the suggested innovations will be tested in upcoming experiments.

Space-Dependent Thermal Stability of Reacting Tokamak Plasmas

W. A. Houlberg P. W. Conn*

A technique is presented for the analysis of thermal stability in reacting tokamak plasmas using a one-dimensional, time-dependent fluid transport model. Application is made to the analysis of density-related thermal instabilities in a neutral beam-driven, two-component plasma, TETR, and a conceptual reactor-size ignited plasma, UWMAK-III. A density-driven thermal instability can exist when the particle confinement varies as $\tau_p \propto n$. This condition is satisfied by the trapped ion mode diffusion model and an empirical model. A time delay in the heating due to finite alpha thermalization does not significantly alter the character of the instability at normal plasma densities. A linear feedback response for the particle source is found to provide a stabilized equilibrium in all cases. Strong radial variation of the transport and physical properties of the plasma is not found to introduce radial-dependent feedback requirements. Feedback on the average density is sufficient for stabilization with moderate response times (see Figs. 4.24 and 4.25).

Plasma Simulation and Modeling for EBTR

N. A. Uckan C. L. Hedrick

A simple model (time-dependent D-T point model) has been formulated to assess the energy balance in an EBTR plasma. The effects of the different scaling assumptions on EBTR performance and operating point have been analyzed.

*University of Wisconsin

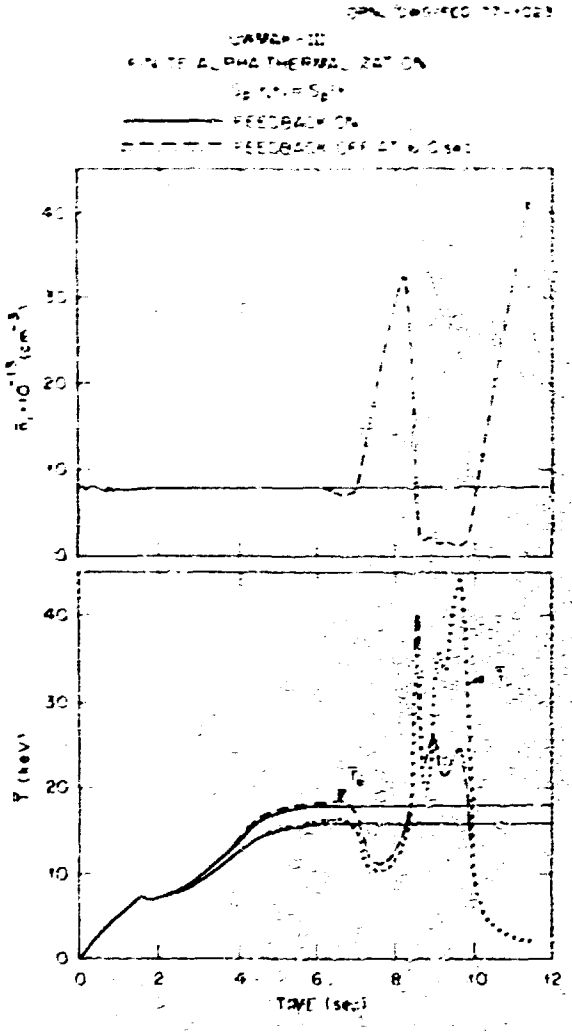

Fig. 4.24. Average density and electron and ion temperature for an ignited plasma with trapped particle transport, a spatially uniform particle source profile, and a finite thermalization time for the fusion alphas. The characteristics of the instability are changed by the finite thermalization time only when the density is low and the thermalization time becomes long.

Although in the present EBT device (EBT-I) plasma transport seems to be governed largely by neoclassical processes, hypothesized anomalous transport losses are included in the plasma simulation model in addition to neoclassical and/or classical transport in order to test the sensitivity of EBTR parameters. For the particular case studied, it is shown that the reference EBTR can accommodate anomalous losses

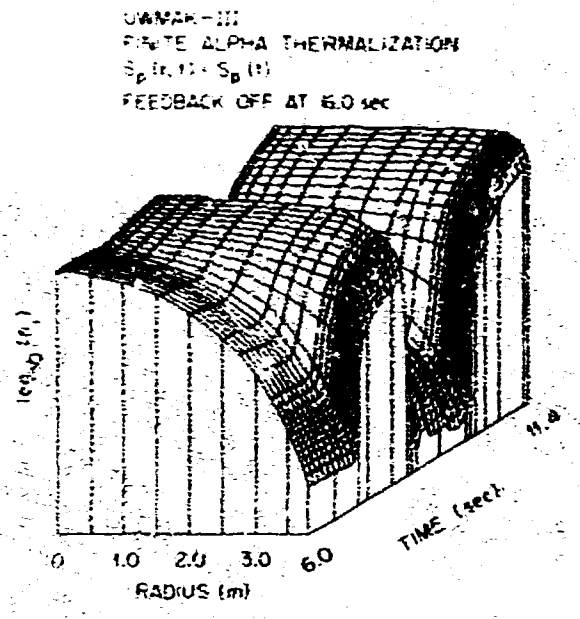

Fig. 4.25. Evolution of the density and electron and ion temperature profiles for the case shown in Fig. 4.24.

one to two orders of magnitude greater than the present neoclassical losses at the operating point (steady state). Results are discussed.

4.6 COMPUTER SUPPORT

T. Burnett, III	C. O. Kemper
R. D. Burris	D. R. Overbey
D. N. Clark	C. E. Parker
J. E. Francis, Jr.	J. W. Reynolds
R. K. Gryder	C. R. Stewart, Jr.
C. E. Hammons*	O. C. Yonts

4.6.1 User Service Center

C. E. Parker	T. Burnett, III
R. D. Burris	D. N. Clark

The User Service Center hardware was upgraded by the addition of 128 K words of memory, resulting in a system total of 320 K words. An additional RP06 disk system was added to further

*Group Leader

support the increasing data needs of the ISX experiment. Concurrently, the DF10 data channel was upgraded to a DF10C on a sales/exchange agreement in order to support the memory above 256 K. A dual dectape system was to provide Division researchers with personal file storage for backup purposes and intersystem transportability. The KI10 central processor was upgraded to the new model KL10-B cpu; a memory unit with an insufficient number of memory ports (64 K) was sales/exchanged in this process, leaving only the 256 K memory for the USC. The new central processor (which has an internal data channel to relieve data flow bottlenecks) was in full operation five days after arrival. A dual ported disk was installed at the same time as a requirement of the new central processor.

Necessary changes were made to the NMFECC software to make it compatible with the new processor's cache memory. The PDP11/45 experimental data coordinating computer was hardware interfaced to the USC to provide a more rapid data path to the USC from the Division experiments and the ORNL computer center. Software modifications to support this were begun and targeted for completion in early 78. A generalized Network Command Language and system PLOT command were made fully operational.

4.6.2 Experimental Data Handling

J. E. Francis, Jr. D. R. Overbey
O. C. Yonts J. W. Reynolds
C. R. Stewart, Jr. C. O. Kemper

New data handling requirements arose in the transition from ORMAK to ISX. A restructuring of the PDP12 operating system was necessary in order to accommodate additional communication links into the PDP12. This restructuring resulted in disk data spooling and allowed the comparison of data channels from different shots. This system modification required a new communications subprogram between the PDP11/45 and the PDP12 at ISX.

A PDP8 was interfaced to a residual gas analyzer for studying impurities in ISX. Software was developed so that scans could be taken automatically and a printed copy of the results could be obtained from a Tektronix 4010 terminal.

The PLT beam test stand data acquisition system was brought on line and is documented in a published paper.[8]

A data acquisition system which supports seven analog data channels for taking data from small cryogenic coils was developed for the Magnetics and Superconductivity Section. The incoming analog data are digitized and stored in memory, whereupon they can be processed or transmitted to either of two PDP10's for further analysis and storage. Preliminary calculations to show hysteresis loops can be made and the curves displayed on the PDP12 display unit.

REFERENCES

1. Abstract of paper published in Phys. Rev. Lett. 40, 866 (1978).
2. Abstract of ORNL/TM-6013, Oak Ridge, Tennessee (November 1977).
3. Abstract of report to be issued as an ORNL/TM, Oak Ridge, Tennessee.
4. Abstract of report to be issued as ORNL/TM-6215, Oak Ridge, Tennessee.
5. Abstract of ORNL/TM-5490, Oak Ridge, Tennessee (April 1977); see also Nucl. Fusion 17, 1237 (1977).
6. Abstract of ORNL/TM-5967, Oak Ridge, Tennessee (December 1977); submitted to Nucl. Fusion.
7. Abstract of report to be issued as ORNL/TM-6318, Oak Ridge, Tennessee.
8. Abstract of report to be issued as ORNL/TM-6320, Oak Ridge, Tennessee.
9. Abstract of ORNL/TM-6052, Oak Ridge, Tennessee (November 1977); submitted to Phys. Fluids.

10. Abstract of lecture presented by B. V. Waddell at the Trieste College in Theoretical and Computational Physics, March 22-April 9, 1977; to be published by the IAEA.
11. Nucl. Fusion 18, 735 (1978).
12. Nucl. Fusion 18, 609 (1978).
13. Abstract of ORNL/TM-6096, Oak Ridge, Tennessee (December 1977).
14. Abstract of report to be issued as ORNL/TM-6175, Oak Ridge, Tennessee.
15. Invited paper, Bull. Am. Phys. Soc. 22, 1104 (1977).
16. B. V. Waddell, G. L. Jahns, J. D. Callen, and H. R. Hicks, *Internal Disruptions in Tokamaks*, ORNL/TM-5840, Oak Ridge, Tennessee (May 1977); expanded version to be published in Nucl. Fusion.
17. B. V. Waddell, M. N. Rosenbluth, D. A. Monticello, and R. B. White, Nucl Fusion 16, 528 (1976).
18. Phys. Rev. Lett. 38, 829 (1977).
19. Phys. Rev. Lett. 39, 943 (1977).
20. Abstract of ORNL/TM-6289, Oak Ridge, Tennessee (January 1978).
21. G. Bateman, D. B. Nelson, D. J. Sigmar, and N. A. Uckan, *High Beta Tokamak Instabilities*, to be issued as part of ORNL/TM-6273, Oak Ridge, Tennessee.
22. Abstract of ORNL/TM-6271, Oak Ridge, Tennessee (December 1977).
23. A. G. Armstrong et al., *GFUN Users' Guide*, Report RL-76-029-A, Rutherford Research Laboratory, Chilton, Oxfordshire, United Kingdom (November 1976).
24. G. Vahala and L. Vahala, abstract of paper to be published in Phys. Fluids.
25. Abstract of paper published in Phys. Rev. Lett. 38, 70 (1977).
26. Abstract of report to be issued as ORNL/TM-6040, Oak Ridge, Tennessee; also submitted to Phys. Fluids.
27. Abstract of paper published in Phys. Fluids 20, 418 (1977).
28. Abstract of paper published in Phys. Fluids 20, 1680 (1977).
29. Abstract of paper published in Nucl. Fusion 17, 557 (1977).
30. Abstract of paper published in Nucl. Fusion 17, 797 (1977).
31. L. D. Pearlstein and H. L. Berk, Phys. Rev. Lett. 23, 220 (1969).
32. Abstract of report to be issued as ORNL/TM-6027, Oak Ridge, Tennessee.
33. Abstract of ORNL/TM-6045, Oak Ridge, Tennessee (November 1977).
34. Phys. Rev. Lett. 40, 327 (1978).
35. K. T. Tsang, J. D. Callen, and P. J. Catto, Phys. Fluids 20, 2113 (1977).
36. Abstract of paper published in Phys. Rev. Lett. 39, 1664 (1977).
37. Abstract of paper published in Nucl. Fusion 17, 261 (1977).
38. Abstract of paper published in Phys. Fluids 20, 396 (1977).
39. Abstract of ORNL/TM-5974, Oak Ridge, Tennessee (July 1977); see also Phys. Rev. Lett. 39, 1540 (1977) and Bull. Am. Phys. Soc. 22, 1104 (1977).
40. Abstract of paper published in Phys. Rev. Lett. 38, 491 (1977).
41. Abstract of ORNL/TM-6165, Oak Ridge, Tennessee (February 1978); to be published in Nucl. Fusion.
42. Abstract of ORNL/TM-5952, Oak Ridge, Tennessee (July 1977); to be published in Phys. Fluids.
43. Abstract of PPPL-1398, Princeton, New Jersey (November 1977); see also *Proc. 7th Symp. on Engineering Problems of Fusion Research*, Vol. II, p. 1333 (1977).
44. Abstract of report to be issued as ORNL/TM-6293, Oak Ridge, Tennessee.
45. Abstract of paper published in Plasma Phys. 19, 151 (1977).
46. Abstract of paper published in Plasma Phys. 19, 135 (1977).
47. Abstract of paper published in Plasma Phys. 19, 593 (1977).
48. Abstract of paper presented at the 1977 Annual Controlled Fusion Theory Conf., San Diego, California, May 4-6, 1977.

49. B. H. Hui, N. Windsor, and B. Coppi, *Collisional Theory of Electrical Resistivity in Trapped Electron Regimes*, NRL Memorandum 3349, Naval Research Laboratory, Washington, D.C. (August 1976).

50. Abstract of ORNL/TM-5724, Oak Ridge, Tennessee (March 1977); to be published in Plasma Phys.

51. Abstract of report to be issued as ORNL/TM-6325, Oak Ridge, Tennessee.

52. Abstract of report to be issued as ORNL/TM-6322, Oak Ridge, Tennessee.

53. Integrated Software Systems Corporation *DISSPLA [Beginners/Intermediate and Advanced Manuals]*, P.O. Box 9906, San Diego, California.

54. E. C. Crume and D. E. Arnurius, *Numerical Calculation of Impurity Charge State Distributions*, ORNL/TM-6050, Oak Ridge, Tennessee (September 1977).

55. Equipe TFR, Nucl. Fusion 17, 1297 (1977).

56. O. M. Okamato and T. Amano, J. Comput. Phys. 26, 80 (1978).

57. K. H. Burrell, Phys. Fluids 19, 401 (1976).

58. Abstract of report to be issued as ORNL/TM-6049, Oak Ridge, Tennessee.

59. Abstract of paper presented at Am. Nucl. Soc. 1977 Annual Meeting, New York, New York, June 12-16, 1977.

60. Abstract of review paper A1 in *Atomic and Molecular Data for Fusion*, IAEA-199, Vienna, Austria (1977).

61. Abstract of paper published in Nucl. Sci Eng. 64, 2 (1977).

62. Abstract of ORNL/TM-5262, Oak Ridge, Tennessee (March 1977).

63. Abstract of paper published in Nucl. Fusion 18, 3 (1978).

64. A. T. Mense, W. A. Houlberg, S. E. Attenberger, and S. L. Milora, *Effects of Fueling Profiles on Plasma Transport*, ORNL/TM-6026, Oak Ridge, Tennessee (April 1978).

65. C. A. Foster, R. J. Colchin, S. L. Milora, K. Kim, and P. J. Turnbull, *Solid Hydrogen Pellet Injection into the ORMAK Tokamak*, ORNL/TM-5857, Oak Ridge, Tennessee (June 1977).

66. S. O. Dean, J. D. Callen, H. P. Furth, J. F. Clarke, T. Ohkawa, and P. H. Rutherford, *Status and Objectives of Tokamak System for Fusion Research*, WASH-1295, U.S. Atomic Energy Commission, Washington, D.C. (1974).

67. P. B. Parks, R. J. Turnbull, and C. A. Foster, Nucl. Fusion 17, 577 (1977).

68. S. L. Milora and C. A. Foster, *ORNL Neutral Gas Shielding Model for Pellet-Plasma Interactions*, ORNL/TM-5776, Oak Ridge, Tennessee (May 1977).

69. Abstract of paper published in Bull. Am. Phys. Soc. 22, 1208 (1977).

70. G. D. Hobbs and J. A. Wesson, *Heat Transmission Through a Langmuir Sheath in the Presence of Electron Emission*, CLM-R-61, Culham Laboratory, Abingdon, Oxon, United Kingdom (June 1966).

71. Abstract of report to be issued as ORNL/TM-6279, Oak Ridge, Tennessee.

72. Abstract of ORNL/TM-6113, Oak Ridge, Tennessee (December 1977).

73. *A Study of Possible Separable Solutions for Plasma Transport in Ohmically Heated Tokamaks*, ORNL/TM-6065, Oak Ridge, Tennessee (October 1977).

74. *Small Radius Start-up of Tokamak Plasmas with a Moving Limiter*, ORNL/TM-6111, Oak Ridge, Tennessee (December 1977).

75. J. A. Rome, *Injection Scenarios for TNS*, ORNL/TM-5931, Oak Ridge, Tennessee (July 1977).

76. S. E. Attenberger, J. D. Callen, W. A. Houlberg, A. T. Mense, Y-K. M. Peng, J. A. Rome, and N. A. Uckan, *Plasma Engineering Considerations and Innovations for a Medium Field Tokamak Fusion Reactor*, ORNL/TM-6150, Oak Ridge, Tennessee (December 1977).

77. Abstract of paper published in Nucl. Fusion 17, 1273 (1977).

78. Abstract of paper published in Nucl. Fusion 18, 133 (1978).

79. Abstract of ORNL/TM-5803, Oak Ridge, Tennessee (September 1977).

80. Abstract of report to be issued as ORNL/TM-6297, Oak Ridge, Tennessee; research sponsored in part by Wisconsin Electric Utilities Research Foundation.

81. Abstract of ORNL/TM-6019, Oak Ridge, Tennessee (October 1977).

82. J. E. Francis, Jr. and C. E. Hammons, Proc. 7th Symp. on Engineering Problems of Fusion Research. Vol. II, p. 1217 (1977).

ATOMIC, MOLECULAR, AND NUCLEAR PHYSICS

C. F. Barnett[1]
D. H. Crandall[1]
H. B. Gilbody[2]
B. E. Hasselquist[3]
S. W. Hawthorne[1]
I. A. Howard[4]
H. J. Kim[1]
E. W. McDaniel[5]
R. H. McKnight[6]
F. W. Meyer[1]
T. J. Morgan[7]
R. A. Phaneuf[1]
E. W. Thomas[5]
M. I. Wilker[1]

Abstract. Measurements of electron capture cross sections were completed for multicharged ions of O, Si, Fe, Mo, Ta, W, and Au in H and H_2 in the energy range of 60-250 keV/amu (TFTR injection energy). The cross sections increased with increasing ion charge q and can be represented by a simple power law expression, $\sigma_{q,q-1} = \sigma_0 q^p$. For the heavier particles (Ta, W, and Au) the q-dependence exhibited an oscillatory structure superimposed on the power law q-dependence. The oscillations were attributed to the interaction of the captured electron with a Coulomb potential modified by a short-range term that accounts for the screening by ionic electrons. Low energy (1.25-8.45 keV/amu) electron capture cross sections were measured for ions of the He and Li isoelectronic sequences in H and H_2. These measurements indicated that in this energy range there was no uniform scaling with ion charge and no general behavior of the cross section with velocity or energy.

Hydrogen-like or completely stripped ions are difficult to obtain from conventional ion sources because of the large energy required to remove the electrons from the K-shell. To overcome this difficulty, we used a CO_2 laser beam to create a high temperature plasma from a C target. A power density of 4×10^9 W/cm^2 incident on a C solid target provided usable beams of C^{5+}. Equilibrium yields of D^- obtained by passing D ions and atoms through thick Cs vapor targets were reinvestigated in an attempt to remove discrepancies in the various measurements. Present D^- yields of 0.18 at a D energy of 300 eV are lower by approximately a factor of two than recent measurements of Schlachter et al.

Work continued on the collection, evaluation, storage, and retrieval of atomic data pertinent to the controlled fusion program.

5.1 HEAVY PROJECTILE ELECTRON CAPTURE CROSS SECTIONS: MEASUREMENTS WITH THE TANDEM VAN DE GRAAFF

We continued our measurements of total single electron capture cross sections using projectiles from the Tandem Van de Graaff accelerator incident on a high temperature atomic hydrogen target. The ion species investigated were O, Si, Fe, Mo, Ta, W, and Au, with collision velocities ranging from 2.2-6.2 x 10^8 cm/sec (or energies of 60-250 keV/amu). The original experimental method, described in last year's annual report,[1] was modified to extend the highest charge states investigated; cross sections for incident ion charge states up to q = 19 were measured.

1. Physics Division.
2. Consultant, Queen's University, Belfast.
3. Summer student, University of Wisconsin, River Falls, Wisconsin.
4. Summer student, Massachusetts Institute of Technology, Cambridge, Massachusetts.
5. Consultant, Georgia Institute of Technology, Atlanta, Georgia.
6. Consultant, California Polytechnic State University, San Luis Obispo, California.
7. Consultant, Wesleyan University, Middletown, Connecticut.

BLANK PAGE

The experimental cross sections for three representative ion species at 3.4 x 10^8 cm/sec (the collision velocity for TFTR neutral beam injection) are plotted vs initial ion charge q in Fig. 5.1. The results for lighter ions are similar to those previously reported;[2] except for sharp dips at charge q corresponding to closed shell configurations of the projectile ion, the cross sections $\sigma_{q,q-1}$ for Fe and Mo projectiles increase rapidly with incident charge q, and the increase can be well represented by a simple power law q^p. The straight lines which accompany the data shown in Fig. 5.1 are the least-squares fits using a two-parameter expression, $\sigma_{q,q-1} = \sigma_0 q^p$. Such a monotonic increase of $\sigma_{q,q-1}$ with charge q is predicted by the classical theory of Olson and Salop.[3]

The q-dependencies of the cross sections for the heavier projectiles are more complicated; superimposed on the simple power law scaling (as observed in the lighter projectile data), all three of the heavier projectiles investigated (Ta, W, and Au) exhibit a common oscillatory structure whose relative magnitude is apparently independent of ion species and velocity. This oscillatory behavior can be seen for Au projectile ions in Fig. 5.1. To emphasize this structure, the experimental cross sections $\sigma_{q,q-1}$, divided by the least-squares fits $\sigma_0 q^p$, are plotted vs q for Ta, W, and Au ions in Fig. 5.2. We attribute the oscillations to interference in the amplitude for scattering of the captured electron by a Coulomb potential modified by a short-range term that accounts for screening by the ionic electrons. A theoretical impulse model for the collision reproduces well the observed oscillations.[4]

The typical collision velocity dependence of the cross sections which characterizes all charge states and ion species investigated is

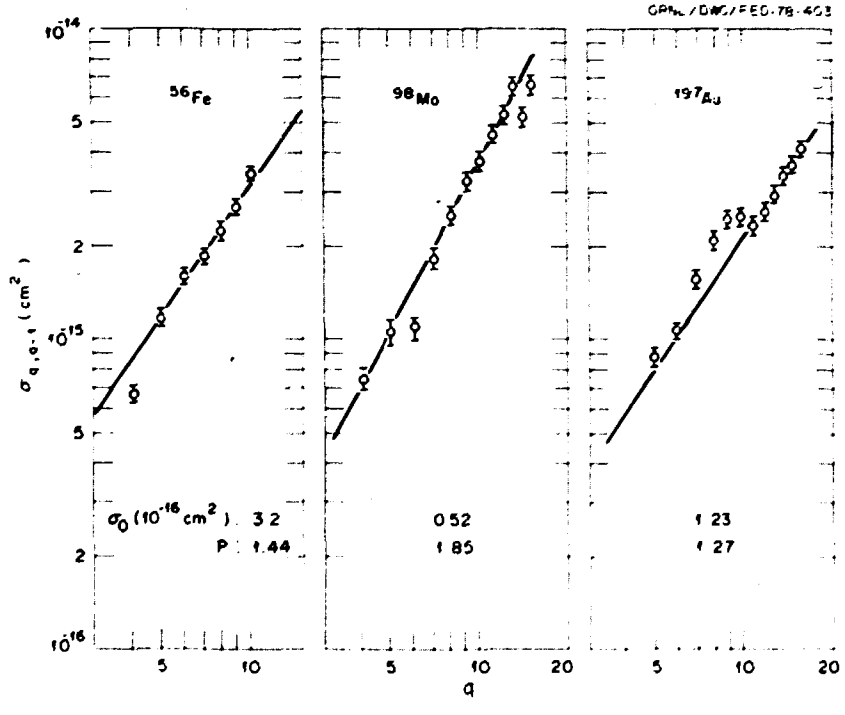

Fig. 5.1. Measured cross sections $\sigma_{q,q-1}$ for multicharged ^{56}Fe, ^{98}Mo, and ^{197}Au ions at v = 3.4 x 10^8 cm/sec plotted vs incident charge q. The straight lines are least-squares fits of the data to the expression $\sigma_0 q^p$.

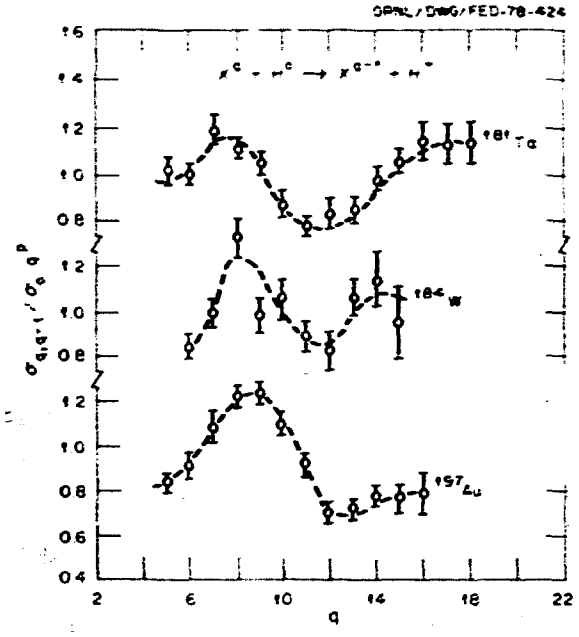

Fig. 5.2. Ratio of experimental electron capture cross sections $\sigma_{q,q-1}$ to power law least-squares fits ($\sigma_0 q^p$) for ^{181}Ta, ^{184}W, and ^{197}Au ions in atomic hydrogen vs ionic charge q. Collision velocity: v = 3.4 x 10^8 cm/sec for W and Au and 3.9 x 10^8 cm/sec for Ta ions.

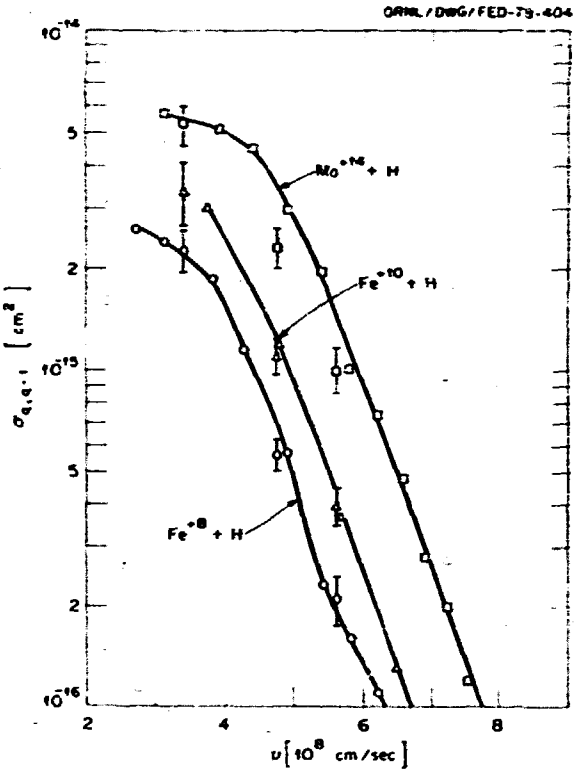

Fig. 5.3. Measured cross sections $\sigma_{q,q-1}$ for ^{56}Fe and ^{98}Mo vs collision velocity v. Solid points are measured results and open connected points are the theoretical results of Olson and Salop (Ref. 3).

illustrated in Fig. 5.3. The classical theory of Olson and Salop[3] reproduces the observed shape and the magnitude of the cross sections.

5.2 LOW ENERGY MEASUREMENTS OF ELECTRON TRANSFER FROM HYDROGEN ATOMS AND MOLECULES TO MULTICHARGED IONS*

The Penning Multicharged Ion Source Facility[5] located in the Physics Division at ORNL has been used for measurements of total cross sections for electron capture by various multicharged ions in atomic and molecular hydrogen gas targets at low velocities (v < 10^8 cm/sec). Apart from their relevance to plasma diagnostics and modeling, these measurements provide a basis for testing our understanding of inelastic processes such as electron transfer. Theoretical calculations at low velocities are difficult and are based on a quasi-molecular model for the collision.

The general experimental method and, in particular, the implementation and calibration of the atomic hydrogen target have been described in detail.[6] The experiments have concentrated on multicharged ions isoelectronic with He and Li; single electron capture data have been obtained for the ions B^{q+} (q = 2,3,4,5), C^{q+} (q = 3,4,5), N^{q+} (q = 3,4,5), O^{q+} (q = 5,6), and F^{q+} in collisions with hydrogen atoms and molecules in the velocity range of 0.5-1.3 x 10^8 cm/sec. Representative electron capture data

*This program was supported by ERDA jointly through DPR and DMFE.

for He-like B^{3+} and C^{4+} ions colliding with hydrogen atoms are shown in Fig. 5.4, along with the theoretical calculations of Olson, Shipsey, and Browne.[7] The theory utilizes *ab initio* potential energy curves in multistate close-coupling calculations and, within the combined uncertainties satisfactorily reproduces both the magnitudes and velocity dependencies of the experimental cross sections for B^{3+} + H and C^{4+} + H collisions.

magnitude and velocity dependence of the charge transfer cross section. Such an analysis also allows prediction of the most probable final electronic states of the multicharged ion. Since these are often excited levels which decay by short wavelength transitions and since the cross sections are large, charge transfer to multicharged ions is a potentially important mechanism for achieving population inversion in the x-ray region.[5]

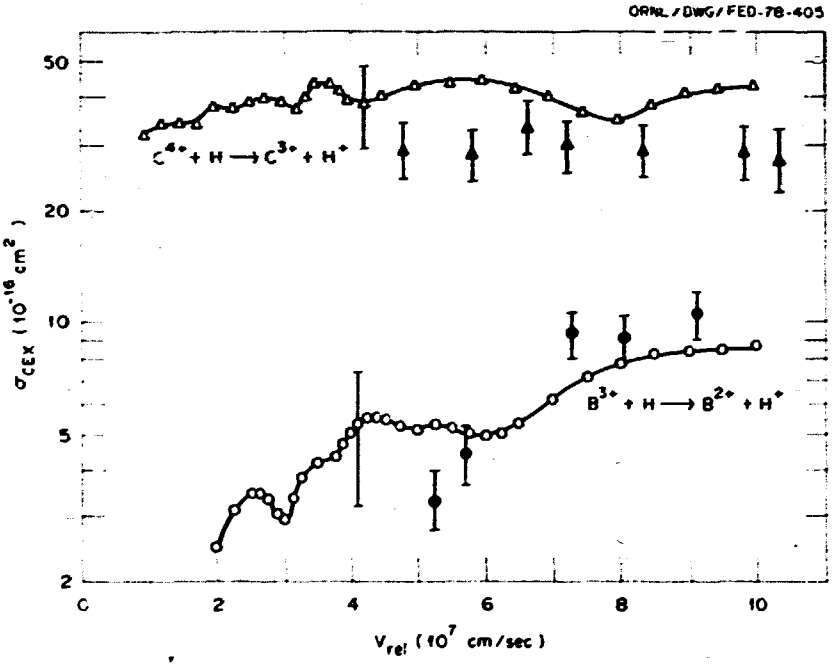

Fig. 5.4. Total cross sections for simple electron capture from hydrogen atoms by B^{3+} (circles) and C^{4+} (triangles). Solid points are experimental data and open points are the theory of Olson et al. (Ref. 7). Flags represent estimated total uncertainties.

In contrast to measurements made at higher velocities,[6,8] the cross sections at low velocities exhibit neither uniform scalings with ionic charge nor general behavior with velocity. Calculation of the potential curves relevant to each collision pair is necessary to predict the

..3 LASER ION SOURCE

To obtain hydrogen-like and completely stripped ions for collision studies in the very important low energy region, we assembled an apparatus to investigate the feasibility of

:s an ion source a pulsed laser beam
: vacuum onto a solid surface. Laser
:. search has revealed that highly stripped ions emerging from such plasmas account for a significant fraction of the energy deposited and of the target mass ablated by the laser beam.[10]

In the present experiments, a pulsed laser beam from a modest 10-J commercial TEA CO_2 laser was focused onto a solid target at power densities as high as 4×10^9 W/cm^2. An ion beam was collimated from the particle blow-off normal to the target surface, directed through a cylindrical electrostatic analyzer, and detected using a channel plate electron multiplier. The combination of time-of-flight and electrostatic analysis permits isolation and identification of ions with different charge-to-mass ratios. Typical energy distributions for the various charge states of carbon in the pulsed ion beam are plotted in Fig. 5.5 for a graphite target at a laser power density of 4×10^9 W/cm^2; note that hydrogen-like C^{5+} ions are produced even at relatively modest laser power levels. (Focused power densities in current laser fusion experiments are typically 10^{16} W/cm^2.)

Modifications to the CO_2 laser to permit fundamental mode operation and similar experiments with a ND:glass laser are expected to provide an order-of-magnitude increase in focused power and to yield fully stripped ions. The technique is suitable for producing ions of any element that exists as a solid or in a solid compound. Such laser produced plasmas are also a convenient source of the optical spectra of highly stripped ions.[11] We are currently implementing a computer data acquisition system to facilitate the development of the ion source and its application to cross-section measurements for such fundamental atomic processes as electron capture by fully stripped ions in the critical low energy region, where theory[12] has not been tested.

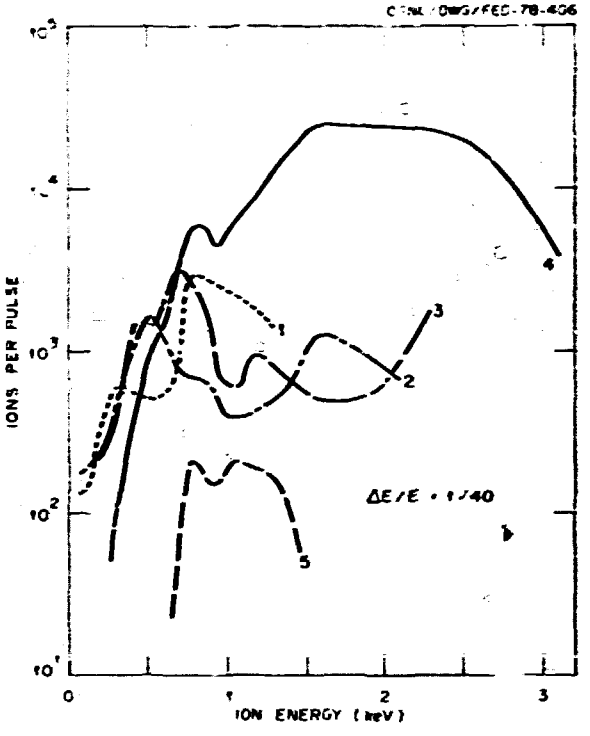

Fig. 5.5. Measured charge and energy distributions of carbon ions emerging from a laser-produced plasma. The CO_2 laser pulse was focused onto graphite in vacuum to a power density of 4×10^9 W/cm^2. The numbers represent the carbon ion charge.

5.4 H^- EQUILIBRIUM YIELDS IN A THICK Cs VAPOR TARGET

The equilibrium factor F^{∞}_{-1} for H^+ (or D^+) incident on a thick Cs vapor target is an important parameter in the design of charge transfer cells for use in MFE neutral beam injection schemes. Considerable disagreement exists in previously reported measurements of F^{∞}_{-1} for H^+ incident on Cs, particularly in the vicinity of the maximum in the equilibrium fraction curve at proton energies in the range of 200-500 eV.[13-15]

To determine whether excitation of the Cs(6p) state by H^+ significantly affects the thick target H^- yield, we have measured F^{∞}_{-} for

both H^- and H^+ incident on Cs in the energy range of 150-1000 eV. The cross section for H^- production from H^0 is about an order of magnitude larger for collisions with Cs(6p) than for collisions with Cs(6s). If Cs(6p) excitation by H^+ is an important mechanism in H^- formation, then differences in the Cs(6p) population due to variations in target cell geometries and incident H^+ intensities might explain the discrepant results in the existing F^{∞}_{-1} measurements.

In the present H^- yield measurements, an analyzed H^- beam of the desired energy was incident on a [illegible] target. The charge components of the beam emerging from the target were monitored as a function of the Cs target thickness π by a secondary emission detector located a short distance downbeam of the target. Appropriate biasing of high transmission grids in front of the detector allowed separate measurements of the H^+, H^0, and H^- beam fractions. Upon reaching the equilibrium target thickness where the beam fractions become independent of π, the incident beam was switched to H^+, and F^{∞}_{-1} was again determined.

During experimental runs, the secondary emission factors γ_+ and γ_- of the charged beam components incident on the detector were continuously monitored. The factors γ_+ and γ_- were observed to increase with the Cs target thickness, possibly due to the increased Cs coverage of the detector surface. Since the secondary emission factor γ_0 for H^0 incident on the detector could not be measured directly during an experimental run, a separate experiment was performed in the energy range from 100 eV to 2.5 keV to determine the ratios γ_-/γ_0 and γ_0/γ_+, which are believed to be independent of the detector surface condition. The results of these measurements are shown in Fig. 5.6. These results, together with measurements of γ_+ or γ_- during the equilibrium run itself, allowed continual calibration of the detector response to H^0 under all surface conditions.

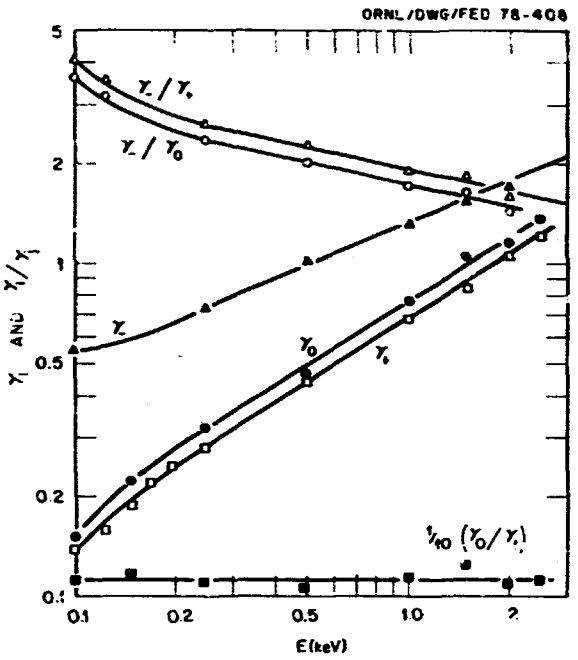

Fig. 5.6. The negative particle (e^- and/or D^-) ejection/reflection coefficients γ_+, γ_0, and γ_- for H^+, H^0, and H^- normally incident on "dirty" stainless steel, and the computed ratios γ_0/γ_+, γ_-/γ_0, and γ_-/γ_+ as a function of the incident hydrogen projectile energy.

Figure 5.7 shows the results of the equilibrium yield measurements and compares them with existing measurements. The yields F^{∞}_{-1} were found to be the same for H^+ and H^- incident on Cs, suggesting that Cs(6p) excitation by H^+ plays a negligible role in H^- formation in a thick target. Measurements of F^{∞}_{-1} with D^- incident showed no observable isotope effect, consistent with earlier observations[15] that the equilibrium yields for D^+ and H^+ incident on a thick Cs vapor target are the same for equal incident velocities. The discrepancy between the present measurements and those of Schlachter et al.[13] and Agafanov et al.[14] at low energies is not understood and will be the basis for further experiments.

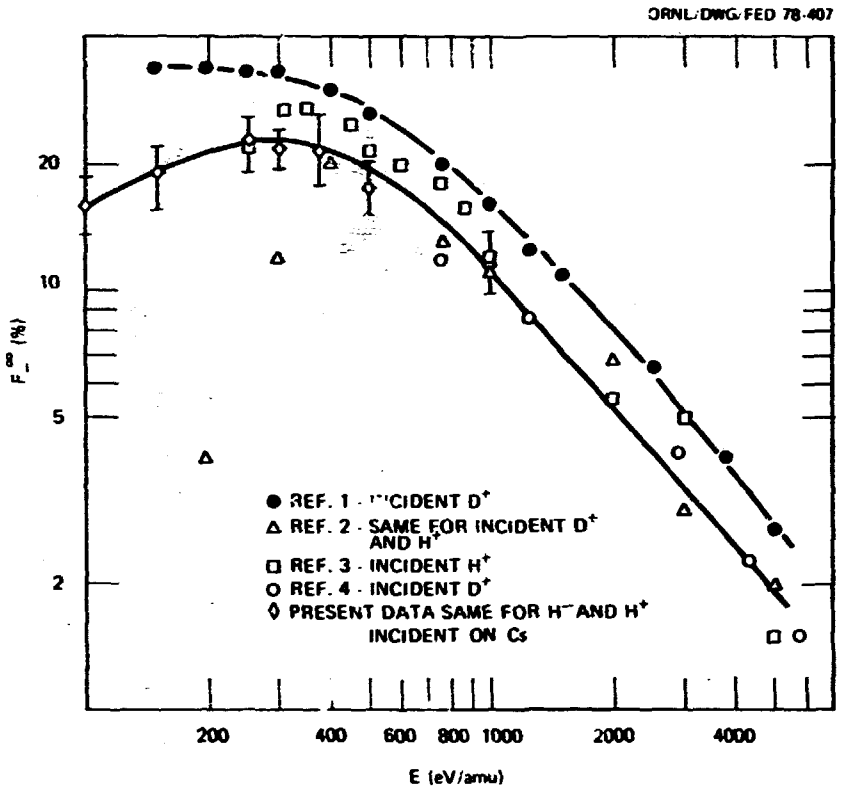

Fig. 5.7. The $H^-(D^-)$ equilibrium fraction F_{-1}^{∞} for $H^+(D^+)$ and H^- incident on a thick Cs vapor target as a function of the energy per nucleon of the incident ions [Ref. 1: textual Ref. 15; Ref. 2: textual Ref. 16; Ref. 3: textual Ref. 17; Ref. 4: F. W. Meyer and L. W. Anderson, Phys. Rev. A 11, 589 (1975)].

5.5 CONTROLLED FUSION ATOMIC DATA CENTER

The two-volume compilation of *Atomic Data for Controlled Fusion Research* is being updated with new and revised data. The compilation has been critically reviewed to remove mistakes made in the initial publication. We are now evaluating new sections of the compilation; these data concern charge exchange of multicharged ions, electron ionization, and excitation of multicharged ions. These sections will be published either as a third volume or as supplements to the "Atomic Data for Fusion" newsletter.

In cooperation with the Atomic Transition Probabilities Data Center at NBS, the bimonthly publication of "Atomic Data for Fusion" has continued. During the year, Volume 3 was completed and distributed. The newsletter is now sent to 475 scientists and libraries and, judging from the response we have received, is serving a useful purpose.

Searching, evaluating, and entering bibliographical data into the computer file have continued. Several hundred references were added into the computer file for 1950-1975. This file is as complete as it is possible to obtain without a significantly increased effort. From our studies we have determined that the file contains more than 90% of the atomic collision papers published during 1950-75. Tapes of this file are being transferred to the IAEA for use in publishing a composite bibliography. Four bibliographies of primary use to fusion

research will be published, including heavy-particle charge exchange, excitation, dissociation, and ionization. For the period 1976-77, 90% of open literature has been searched and evaluated. During a critical review of our bibliographical file, we found that in 1970 a serious error had been made in our retrieval program. This was corrected, and the decision was made to replace the computer program with an up-to-date, more universal format using an on-line computer terminal for input and output. This new system was placed into operation in January 1978. Significant time will be saved in the input operation and file editing.

Programming was completed to convert cross sections to reaction rates and to analytical expressions for systems where beam-Maxwellian and Maxwellian-Maxwellian distributions are applicable. Presently, the storage and retrieval system, including file management and editing, is being debugged on the ORNL PDP-10 computer for storage on the Livermore 7600 computer.

Cooperation has continued with the IAEA in its efforts to establish an Atomic Data for Fusion data center. We have been able to supply both advice and material for their newsletter and for the forthcoming bibliography.

REFERENCES

1. *Fusion Energy Division Annual Progress Report for the Period Ending December 31, 1976*, ORNL-5275, Sect. 2.10.3, pp. 89-90, Oak Ridge, Tennessee (June 1977).
2. *Fusion Energy Division Annual Progress Report for the Period Ending December 31, 1976*, ORNL-5275, Sect. 2.10.2, pp. 88-89, Oak Ridge, Tennessee (June 1977).
3. R. E. Olson and A. Salop, Phys. Rev. A 16, 531 (1977), and private communication (SRI International, 1977).
4. H. J. Kim, P. Hvelplund, F. W. Meyer, R. A. Phaneuf, P. H. Stelson, and C. Bottcher, "Observation of Coulomb Interference in Total Electron Capture Cross Sections," submitted to Phys. Rev. Lett.
5. M. L. Mallory and D. H. Crandall, IEEE Trans. Nucl. Sci. 23, 1069 (1976). This facility is fondly known as the ORNL PIG (Penning Ion Gauge).
6. R. A. Phaneuf, F. W. Meyer, and R. H. McKnight, Phys. Rev. A 17, 534 (1978).
7. R. E. Olson, E. J. Shipsey, and J. C. Browne, J. Phys. B. 11, 699 (1978).
8. *Fusion Energy Division Annual Progress Report for the Period Ending December 31, 1976*, ORNL-5275, pp. 88-91, Oak Ridge, Tennessee (June 1977).
9. W. H. Louisell, M. O. Scully, and W. B. McKnight, Phys. Rev. A 11, 989 (1975).
10. See, for example, A. W. Ehler, J. Appl. Phys. 46, 2464 (1975); E. A. McLean, R. Decoste, B. H. Ripin, J. A. Stamper, H. R. Griem, and S. E. Bodner, Appl. Phys. Lett. 31, 9 (1977).
11. L. F. Chase, W. C. Jordan, J. D. Perez, and R. R. Johnston, Phys. Rev. A 13, 1497 (1976).
12. C. Bottcher, J. Phys. B 10, L213 (1977); A. Salop and R. E. Olson, Phys. Rev. A 16, 1811 (1977); J. Vaaben and J. S. Briggs, J. Phys. B 10, L521 (1977).
13. A. S. Schlachter, K. R. Stalder, and J. W. Stearns, *Proc. 10th Int. Conf. on the Physics of Electronic and Atomic Collisions*, Vol. II, p. 870 (1977).
14. Yu. A. Agafanov, B. A. D'yachkov and M. A. Pavlii, Sov. Tech. Phys. Lett. 2, 296 (1976).
15. Yu. M. Khirnyi and L. N. Kochemasova, Prib. Tekh. Eksp. 3, 56 (1970).

PLASMA TECHNOLOGY

H. H. Haselton, Section Head

G. C. Barber	R. L. Johnson[2]	S. W. Schwenterly
W. R. Becraft[1]	A. R. Kemp[2]	T. E. Shannon[2]
C. W. Blue	J. Kim	E. Slaughter[2]
E. H. Bryant[2]	K. Leung[5]	S. J. Sosnowski[2]
D. D. Cannon[2]	T. Mann[2]	D. O. Sparks
J. S. Culver[2]	J. A. Mayhall[2]	L. D. Stewart[7]
W. K. Dagenhart	G. L. McDade[2]	W. L. Stirling
R. C. Davis	M. M. Menon	J. D. Stout[2]
R. B. Easter[2]	S. L. Milora	J. B. Talbot[3]
P. W. Fisher[3]	G. F. Pierce[2]	P. B. Thompson[2]
W. M. Fletcher[2]	N. S. Ponte[6]	C. C. Tsai
J. W. Forseman[2]	R. E. Potter	J. F. Watson[3]
C. A. Foster	C. C. Queen[2]	J. H. Whealton
W. L. Gardner	P. M. Ryan	J. W. Whitfield[2]
H. F. Glavish[4]	T. L. Ryan[2]	J. C. Whitson[8]
D. H. Gray[2]	D. E. Schechter	R. E. Wright
R. E. Hill[2]	G. Schilling[7]	W. L. Wright[2]

Abstract. The Plasma Technology Section has the responsibility for: (1) development of multi-megawatt neutral beam systems for plasma heating, (2) development of techniques for fueling the plasma using high velocity pellets, and (3) development of vacuum pumps of large pumping speeds ($\sim 10^6$-10^8 liters/sec) compatible with neutral beam and fusion devices. Significant advances have been made in each of these areas.

In the neutral beam area, four systems, each capable of delivering approximately 750 kW of neutral power into the tokamak plasma, were delivered to the Princeton Plasma Physics Laboratory. Two of the beam lines have already been used for injection into the Princeton Large Torus (PLT) and a record ion temperature of 2.2 keV has been attained with an injected power of 1.1 MW (D^0) at 38 keV, divided equally between the beam lines. The achievement was made possible by the development of modified duoPIGatron ion sources and appropriate beam transport systems. The three-grid duoPIGatron source has provided ion beams of up to 70 A at energies greater than 40 keV. The source is characterized by moderate filament and arc power requirements (1 A/kW), high gas efficiency (50%), and high reliability. A singular feature of the source is the high atomic yield (85%) it provides. An updated version, expected to deliver up to 100 A, is being developed. The beam transport system incorporates liquid helium cooled cryo-condensation pumps of 500,000 liters/sec pumping speed, and beam dumps and calorimeters using water cooled swirl tubes that operate at steady state and dissipate very high power densities (~ 5 kW/cm^2). Improvement of the beam optics is crucial in a high power neutral beam system. Experiments using a preaccelerating voltage

---

1. General Electric Company, Oak Ridge, Tennessee.
2. Engineering Division.
3. Chemical Technology Division.
4. Stanford University, Stanford, California.
5. Madison College, Harrisonburg, Virginia.
6. Lawrence Livermore Laboratory, Livermore, California.
7. Princeton Plasma Physics Laboratory, Princeton, New Jersey.
8. Computer Sciences Division.

between the plasma grid and the second anode produced substantial improvement (30%) in beam transmission efficiency. Similar improvements have also been obtained using shaped apertures on the plasma grid. A two-stage accelerating technique has been successfully employed to obtain good beam optics (0.3° HWHM) at energies up to 120 keV, using a single beamlet. Efforts are being made to produce high energy (120-keV), high current (50-A) beams using the two-stage accelerating technique. The development of high voltage, high power electrical systems switching megawatts of power at a high repetition rate has been a vital part of this program.

In the pellet fueling area, hydrogen pellets accelerated to high velocities (330 m/sec) using a pneumatic gun technique have already been successfully injected into the ISX tokamak plasma. The pellets penetrate 12 cm into the plasma, in agreement with theoretical prediction, and corresponding increases in plasma density have been observed. A pellet accelerator using a rotating arm concept is also under development.

In the vacuum components development area, cryocondensation pumps of enormous pumping speed ($\sim 10^5$ liters/sec) have demonstrated their usefulness as an integral part of the neutral beam systems. Alternate approaches using cryosorption techniques are being developed.

6.1 ION SOURCE DEVELOPMENT

6.1.1 Introduction

Injection of energetic neutrals (hydrogen isotopes) is the prime plasma heating technique for fusion devices. In practice, the neutral beams are produced from positive and/or negative ion beams via neutralization processes. Below ~200 keV, the present technology based on positive ion beams is favored. At higher energies, however, the high neutralization efficiency of negative ions encourages the development of negative ion sources. Our program has been heavily involved in the development of ion beams at energies up to 60 keV and currents up to 100 A, and development of higher energy positive and negative ion sources is also being pursued vigorously. The major achievements are reported below.

6.1.2 Positive Ion Sources

The duoPIGatron ion source[1-5] (15-A, 10-cm grid) developed for ORMAK injectors is reliable, efficient, and simple. Recently it was operated for studying its long pulse capability, and ion beams of 5.5 A/25 keV/2 sec and 9.5 A/29 keV/0.9 sec were extracted. The arc discharge corresponding to the latter beam condition was extended to 10 sec. Although the experiment was terminated due to malfunctioning of the vacuum system, the results indicate that the source components would withstand dc operation.

Employing a magnetic multipole line-cusp confinement,[6,7] the source has been scaled up to versions with 15-, 20-, and 22-cm grid diameters. The sources are capable of creating a uniform (±5% density variation over the grid diameter) and dense (about 2×10^{12} cm^{-3} at the extraction surface) plasma. For PLT injectors, the 22-cm version delivered beams of 60 A/40 keV/0.3 sec, as originally designated.[8] Beam parameters of 70 A, 45 keV, and 0.5 sec have also been independently achieved. The beam current density was found to be in the range of 0.3-0.4 A/cm^2. With the optimization of electrode dimensions and configurations, magnetic field arrangement, and gas feed, the source has provided a high arc efficiency (~1 A/kW) and 50% gas efficiency and has operated reliably without any maintenance over long periods of time (~50,000 beam pulses). The most unique feature of this source is the high atomic yield (85%) it provides.

A species model[7] was developed to explain the high proton yield. The essential factors are the high volume production of atomic ions due to the high gas pressure and the low ion loss rate due to the maximized ratio of the plasma volume to the electrode surface. The high production rate of atomic ions in the volume is essentially due to the dissociation processes of molecular ions by the cold plasma

electrons. Measured electron energy is <5 eV. The source performed equally well when hydrogen was substituted with deu rium.

An alternate ion source with tungsten filaments,[9] similar to the magnetic multipole line-cusp containment device, was studied experimentally. Ion beams of 14 A/18.5 keV (0.15 A/cm^2 current density) were formed. This source provided good radial density uniformity and low noise level (±0.5%) – characteristics that improve the beam transmission.[10] It is also capable of delivering beams with high atomic yields (90%). However, the large amount of tungsten vapor released by the filaments could cause impurity problems in the fusion plasma. Hence, the electron source must be improved.

An 80-keV/40-A ion source with a plasma generator similar to PLT injectors and a two-stage ion accelerator with an 18-cm grid were fabricated (Fig. 6.1). Initial operation of this source delivered ion beams of 64 keV/20 A.

A plasma generator with a 35-cm -c chamber has been operated successfully and is expected to deliver an ion beam of 100 A from a 25-cm grid.[11] Ion sources (circular as well as rectangular cross section) are also being designed for beam currents up to ~100 A at energies up to 120 keV. These sources are intended for neutral beam injectors for ISX-B at ORNL, PDX at PPPL, and TNS.

6.1.3 Negative Ion Sources

The ORNL negative ion source program is composed of several new and unique ideas[12,13] for generating plasmas from which negative ion

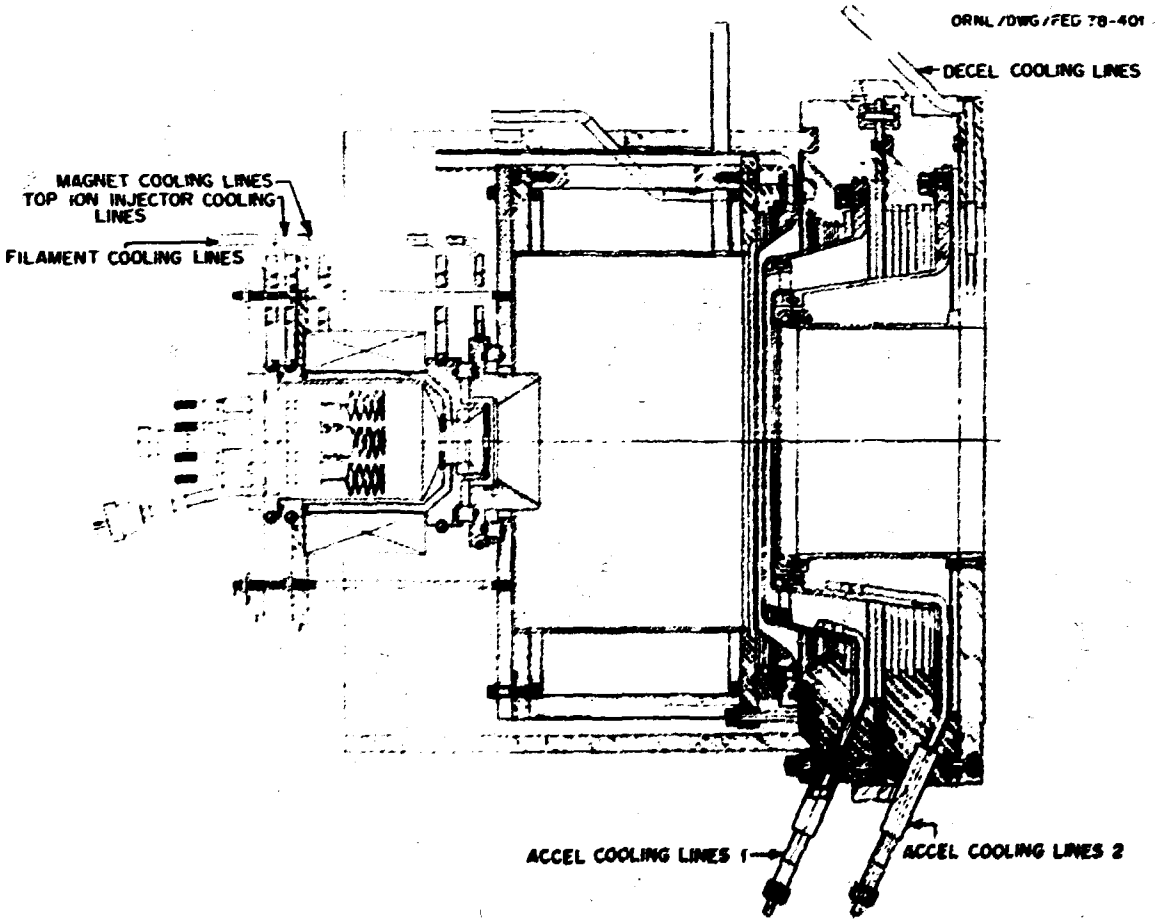

Fig. 6.1. A two-stage ion source.

beams may be produced. There are two well established methods by which negative ion beams are generated: (1) direct extraction, and (2) two-stage or double charge exchange extraction. In direct extraction, an electric field is used to extract negative ions directly from the ion source plasma. However, in the double charge exchange method, relatively low energy positive ions are extracted from the ion source plasma; the ions then charge exchange while passing through an alkali vapor cell. The resulting negative ions are then accelerated to the desired energy. The ORNL program deals with three separate ideas which fall under the direct extraction category and one under the double charge exchange method. A discussion of these ideas and their status was recently issued.[14]

6.2 MEDIUM ENERGY NEUTRAL BEAM SYSTEMS

6.2.1 PLT Neutral Beam Systems

Four ORNL/PLT neutral beam systems (Fig. 6.2) had been delivered to PPPL as of January 1978. These beam lines are rated at a nominal 750 kW of neutrals to the PLT plasma at 60 A and 40 keV for 300 msec. Test stand operation of beam lines one and two at ORNL achieved these performance criteria.[7,15] Initial operation of beam lines one and three on PLT delivered a total 1.1 MW of D^0 and H^0 to the plasma, resulting in a rise in T_i from 0.9 to 2.2 keV. Final operation of all four beam lines on PLT should result in over 3 MW of neutral power to the tokamak plasma by early summer 1978.

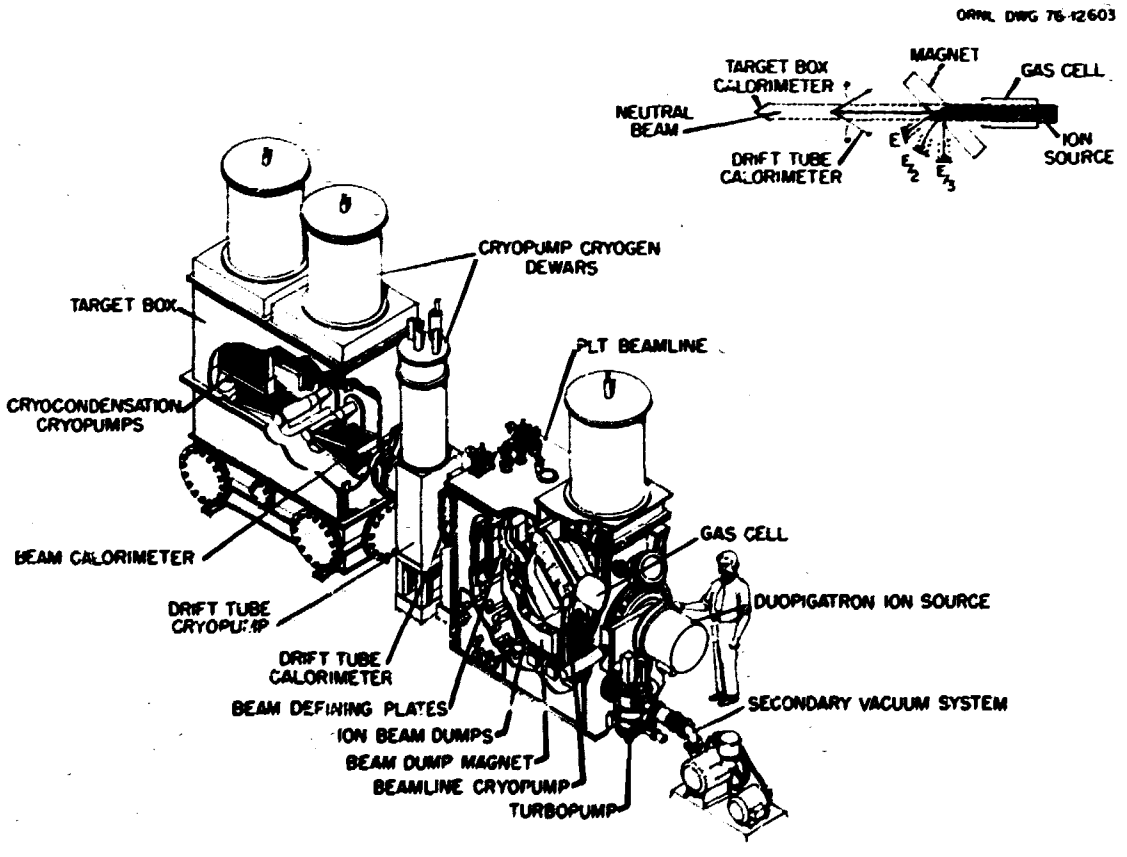

Fig. 6.2. ORNL/PLT beam line and ORNL test facility target box.

Significant performance parameters of these beam lines as demonstrated at ORNL include:

(1) Neutral power from a single source through a PLT-size (20 x 25 cm) aperture at 4.10 m.

50 A, 40 kV, 300 msec	550-kW neutrals
60 A, 45 kV, 200 msec	700-kW neutrals
70 A, 40 kV, 100 msec	750-kW neutrals

(2) Species ratios of the ion beams as extracted from the ion source of $H^+:H_2^+:H_3^+$ = 85:12:3 (very easily reproduced) are to be compared to previous best values of 55:25:20 from ORNL/ORMAK sources.

(3) Beams of up to 60 A have been produced with 15 Torr liters/sec of H_2 (including neutralizer).

(4) Beam power deposition has been measured calorimetrically with 18 channels which have accounted for 90-95% of I-V power for well focused beams.

(5) The 500,000 liters/sec LHe cryocondensation pumps have performed flawlessly in concert with neutral beam operation.

(6) Arc power required was 1 kW per ampere of beam current.

(7) Swirl tube targets on the ion dump have held up with power densities exceeding 5.4 kW/cm^2 for 300 msec.

(8) The ORNL modified duoPIGatron has operated for over 50,000 pulses on the beam line before needing new filaments, even after accidental exposure to water vapor between runs.

The power flow along the beam line was monitored by sensing the cooling water flow rate and the rise in temperature on various elements. A PDP-11/40 computer was used for data acquisition. A typical plot of power deposition as a percentage of the input electrical power is shown in Fig. 6.3. With the help of such plots appropriate operating parameters can be selected to optimize the power reaching the target.

Approximately 600 kW of neutral power has been collected on the inertial target kept 4.1 m downstream under optimum conditions. The highest power (power supply limited) that has been measured at the target with hydrogen as the working gas was 750 kW when the source was operating at 40 kV and 70 A. With a precel voltage of 100 V (see Sect. 6.4.2), 830 kW of neutral power has been measured at the target using deuterium gas when the source was operating at 45 kV delivering 54 A. This will translate to almost 1 MW of neutrals at the PLT plasma because the solid angle subtended by the machine is greater than that afforded at our test facility.

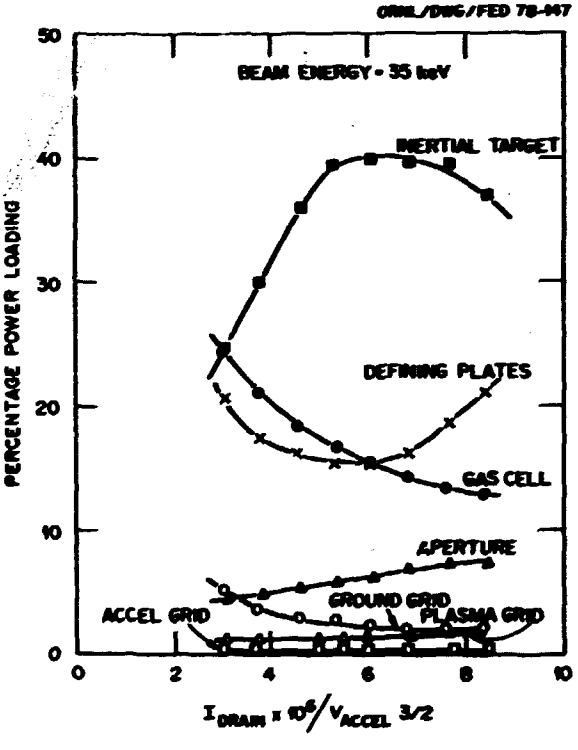

Fig. 6.3. Typical data from PLT ion source and beam line.

6.2.2 ISX-B Neutral Beam Systems

A cryogenically pumped beam line was added to the Medium Energy Test Facility to produce a system similar to the ORNL developed PLT beam line.[15] This system simulates very closely the 4.15-m ISX-B beam line and is being used to qualify two 40-kV, 60-A injectors for the ISX-B

experiment. The injectors are identical to the 22-cm PLT injectors[7] and should deliver about 700 kW of neutral power per beam line.

Operation of the METF beam line has begun and the first ISX-B injector has undergone preliminary testing of 50-A output at 42 kV. Optics studies to maximize the neutral power output are proceeding. Both ISX-B sources are to be ready for installation by July 1, 1978.

An added feature of the METF beam line is the capability to test a 28- to 30-cm-diam source of 100-A output. Both the beam defining plates and the drift tube calorimeter have been modified to accept a larger beam. Testing of a 100-A injector for possible ISX-B use will begin in August 1978.

6.2.3 PDX Neutral Beam Systems

The Poloidal Divertor Experiment at Princeton Plasma Physics Laboratory will have attached to it four operational ORNL neutral beam systems by early 1980. Each 4.2-m-long system will deliver 1.5 MW of neutral power (through a 30 x 35-cm rectangular aperture) to the plasma for 0.5 sec. To achieve this injected neutral power the Plasma Technology Section is developing a 50 keV/100 A/0.5-sec source with a >80% atomic ion yield and having a 30-cm-diam grid pattern. This source is a relatively modest extrapolation of existing sources and should provide no major development problems. In addition, the beam line design is a relatively straightforward upgrade to the successful PLT design to accommodate the higher power beams.

6.3 HIGH ENERGY NEUTRAL BEAM DEVELOPMENT

The High Power Test Facility[16] and its associated electrical systems[17] were completed on schedule. The test stand was utilized for two-stage beam optics[18] study as well as for investigation of two-stage beam steering.[19] An 18-cm, two-stage source designed to deliver 40 A at 80 keV is currently being tested at the facility. Beam currents up to 20 A at energies of ~65 keV have already been extracted. A 120-kV, 50-A, two-stage source is being fabricated and will be installed on the test stand after the limits of the present source are tested. The test stand is also being updated to incorporate various diagnostic facilities.

6.4 BEAM OPTICS STUDIES

6.4.1 Theoretical Work

In the ion optics code a new iteration scheme for treating the source plasma was implemented.[20,21] Compared to the previous scheme[22] touted last year,[23] it is a panacea. Figure 6.4 shows the accuracy and expedience of the scheme as compared to the previous one. Briefly, it is a Newton SOR iteration scheme which has proven global convergence and uniqueness properties for the problem at hand. Note that even the previous scheme has enormous advantage over st earlier iteration schemes[24] (see Fig. 3 of Ref. 23).

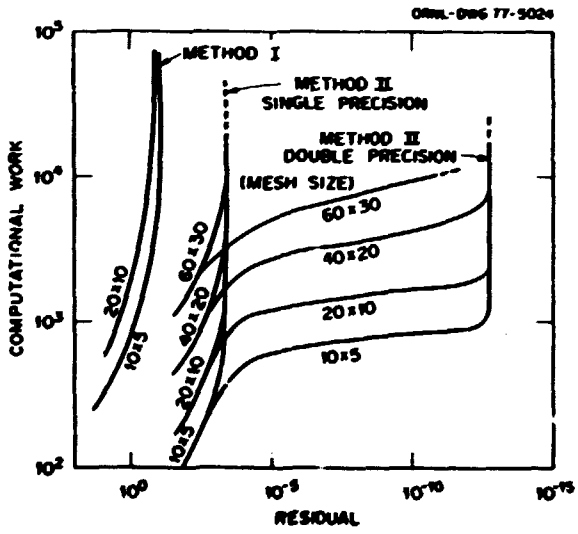

Fig. 6.4. Comparison of computation works vs accuracy of last year's and this year's scheme.

The code has been used to verify,[25-28] predict,[28] and explain[10,29-31] experimental findings. Specifically, a study was made of the

dependence of ion optics on plasma parameters,[35] along with electrode shape,[36] tetrode voltage distribution and geometry,[37] plasma electrode preacceleration with and without an insulator coating,[38] and source plasma density fluctuations.[39] An important result is that a small preacceleration will noticeably diminish the beam divergence under actual operating conditions. The code has also been used to consider the effects of a collector plasma in a direct recovery device.[31]

Other studies completed include a linear theory of ion beamlet steering,[33,34] reionization losses in drift tubes,[32] beamlet-beamlet interaction in the accelerator region,[36] and mitigation of residual space charge in the neutralizer.[37]

6.4.2 Experimental Work

Two-stage ion beam optics

Extensive investigations using a two-stage acceleration technique[16] were carried out to determine the beam optics. The beam optics in such a scheme is a function of the ratio of the voltage gradients across the individual stages (Γ/f), the beam perveance in the extraction gap, and the aspect ratio of the grid structure (see Fig. 6.5). The beam divergence is also influenced by the magnitude of the decel voltage, the total energy of the beam, and the background pressure. The divergence of a single beamlet was examined to elucidate the parametric dependence of the above quantities for beam energies up to 120 keV. The variation of divergence angle with extraction perveance for different values of Γ is shown in Fig. 6.6. Under optimum conditions, the HWHM divergence angle can be reduced to about 0.3°. Also, near the optimum conditions the beam divergence is not seriously affected by plasma density fluctuations.

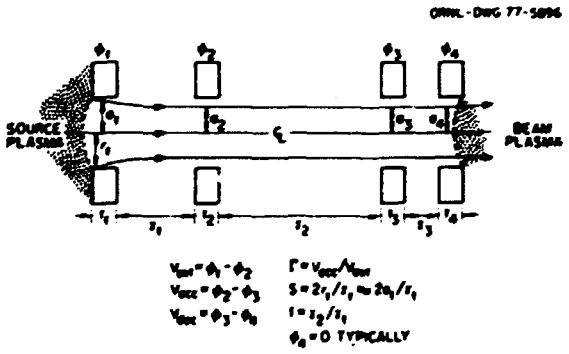

Fig. 6.5. Schematic representation of a two-stage accelerator.

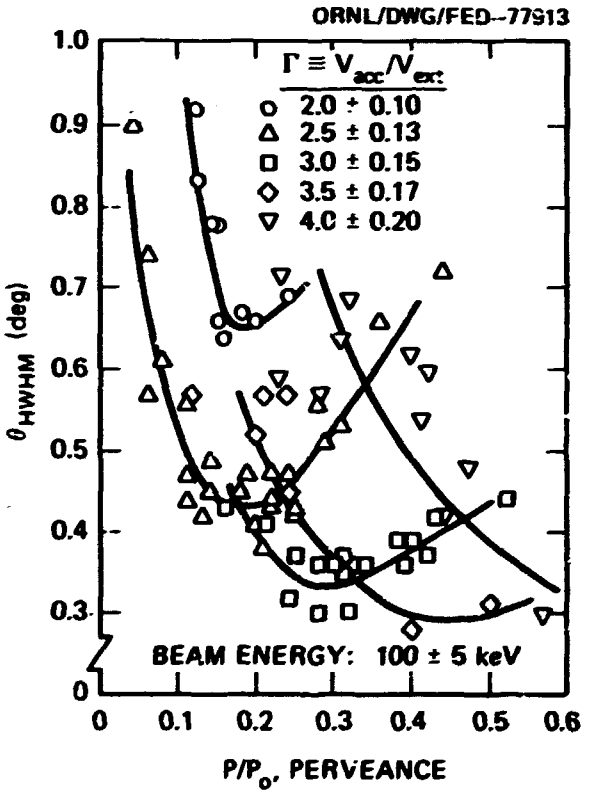

Fig. 6.6. Divergence angle vs extraction perveance for different values of Γ.

Beam optics with precel voltage

Substantial improvement in beam optics was realized by employing a precel voltage between the plasma grid and the second anode.[35] For a 22-cm ion source of the type used for injection into PLT, the total transmission efficiency through an aperture of 20 x 25 cm located 4.1 m

downstream increased by 30% when a precel voltage of 175 ± 25 V was applied (see Fig. 6.7). No deleterious effects were noted on power loading at the grids with the precel voltage. However, application of the precel voltage lowered the optimum perveance value by ~10-15%. The beam transmission efficiency was also found to improve when the plasma electrode was tied to the arc negative. The arc supply in effect acted as the precel supply.

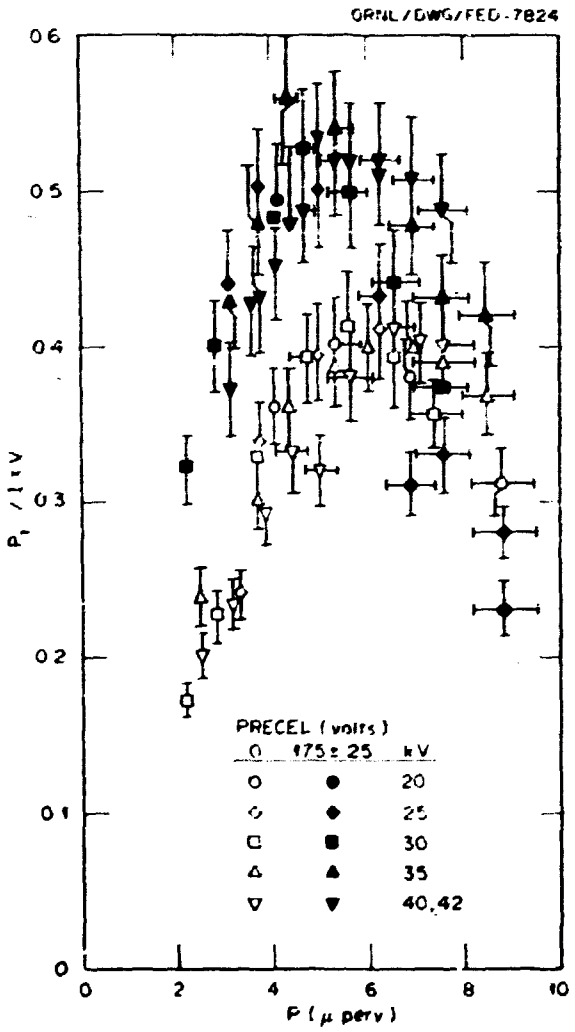

Fig. 6.7. Transmission efficiency vs beam perveance with and without precel voltage.

Shaped apertures

Previous studies indicated substantial improvement in beam optics with shaped apertures.[39] A 22-cm PLT type source was fabricated with shaped apertures on the plasma grid to utilize this effect. Each hole was tapered from 125 mil on the plasma side to 150 mil on the other side, leaving a straight section of 15-20 mil facing the plasma. (The total thickness of the plasma grid was 75 mil.) Preliminary investigations show about 30% improvement in transmission efficiency when compared with straight circular apertures.

6.5 BEAM DIAGNOSTICS

6.5.1 Plasma Source Diagnostics

An essential diagnostic of a discharge plasma source is the measurement of the plasma density variation across the plasma column from which an ion beam is extracted, since the plasma density uniformity is extremely important for stable ion beam extraction. A simple, moveable, cylindrical Langmuir probe has become an integral part of every ion source, providing information on the plasma density, the electron temperature, and the density fluctuation.

6.5.2 Species Measurement

The ion beam species composition has been successfully analyzed by using the deflection magnet in a beam line as a sweeping magnet and by monitoring the signal from a calorimetric probe (see Fig. 6.8). A typical species composition of 85% H_1^+, 12% H_2^+, and 3% H_3^+ has been determined at the source using this technique and known cross sections for the atomic processes present in the equilibrium length, charge exchange cell. The proton fraction was nearly independent of beam current (arc current) above

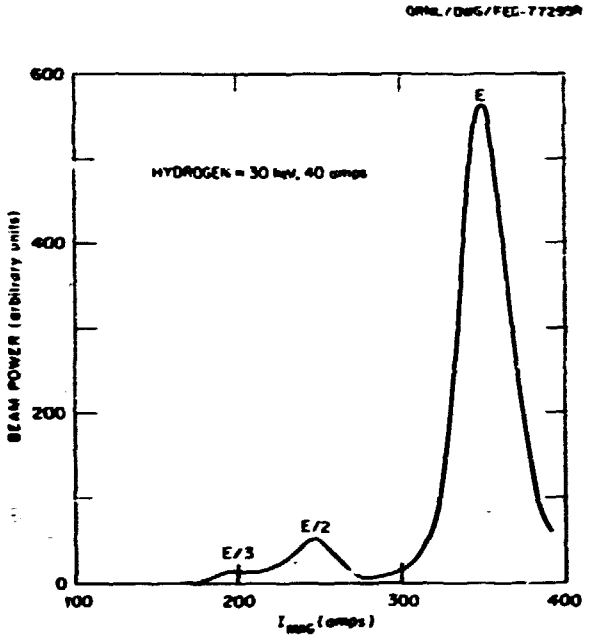

Fig. 6.8. Calorimetric scan of the full, half, and third energy ion peaks emerging from the gas cell.

30 A. At lower currents the third energy component increased at the expense of the primary energy component.

6.5.3 Power Monitoring Along the Beam Lines

In our cryogenically pumped METF, the essential parts intercepting the beam along the beam line are calorimetrically monitored and the information is processed and stored in a CAMAC/PDP-11 computer system. This diagnostic proved to be exceedingly valuable in studying the beam transmission and ion source tuning, and in monitoring the power loading on various elements of the beam line.

6.5.4 Target Profile Scanner

Faraday cup arrays have been used behind a target plate to resolve the beam profiles by sampling the beam through corresponding pinholes. This type of scanner was effectively used in the study of two-stage beam optics up to 120 keV. Thermocouple arrays embedded on a target plate are in use at the METF to resolve the neutral beam profile for the ISX-B injectors.

6.5.5 Photodiode Array

An indirect measurement of the beam profiles has been successfully made[6-0] using an array of photodiodes detecting the amount of excitation light from well collimated chords across the beam. The prototype ISX beam line has a narrow and long Pyrex window spanning the entire beam cross section for the on-line photodiode array measurements at the location of the drift tube.

6.5.6 Gas Pressure Monitor and Analyzer

A gas spectrum analyzer and a time-resolved absolute pressure monitor were used for the prototype PLT beam line and also are in use at the prototype ISX beam line.

6.5.7 Pinhole Camera

This technique has been revived from our previous work[6-1] as a potential diagnostic for examining individual beamlets. The camera is now under development at the prototype ISX beam line.

6.5.8 Fast Neutron Measurements

During the last phase of the PLT beam injector development, deuterium beams were tested for comparison with the hydrogen beam performance. Fast neutrons from D-D reactions from targets and other parts were measured[6-2] by a system consisting of a ^{3}He counter, a fission chamber, and TLD's.

6.5.9 Computer Data Processing

A CAMAC/PDP-11 system is constantly used to process and store data from the METF, where the PLT neutral beam injectors were developed and the ISX neutral beam injectors are now under testing.

6.6 ELECTRICAL TECHNOLOGY DEVELOPMENT

6.6.1 High Power Test Facility

The installation of the 168-kV, 50-A, dc accel power supply was completed as scheduled. The three power modules were tested independently to full power (56 kV, 50 A) on a water cooled resistive load. All other tests were made and were in agreement with specification ES-YEE-8301-1.

Installation of the 150-kV, 50-A modulator, crowbar system was completed and tests conducted up to 90 kV 30 A into a resis d. The system has operated into an levels of 65 kV and 30 A. Althoug ith series operation of vacuum te voltages and currents, the prob insurmountable.

The 20-kV, 5-A decel power supply sts were completed and accepted as outlined in specification TD SP-131. All isolated power and control systems were tested and turned over to operations as a complete operating neutral beam test facility.

To upgrade the test facility from 50-A to 100-A ion sources, a new 220-V, 1500-A, dc arc power supply is under construction. A similar arc power supply will be used on the ISX injectors for future 100-A neutral beam systems. Completion is expected in spring 1978.

6.6.2 Medium Energy Test Facility

With the completion of the PLT beam line program, the test facility will be upgraded for development of 100-A ion source systems for PDX and ISX neutral injection experiments. The accelerating power will share the same 168-kV, 50-A power supply with the High Power Test Facility. The three power modules will be series/parallel connected providing 84 kV, 100 A.

The performance of the 60-kV, 60-A modulator for the METF has been excellent. For PLT source development the modulator has delivered 40 kV, 60 A at pulse lengths up to 300 msec. Independent parameters of 50 kV, 70 A, and 500 msec have been attained. No major failures have occurred and the maintenance required has been minimal.

In conjunction with 100-A ion source development, an 80-kV, 100 A modulator is presently being designed. The modulator will utilize two Eimac X-2062d vacuum tetrodes connected in parallel to realize these parameters. Anticipated completion of this project is about September 30, 1978.

A 300-V, 2500-A, dc arc power supply is being developed for the METF upgrade program. It will deliver enough arc power for ion sources with a grid structure up to 40 cm and beam currents up to 200 A. The isolated deck is being redesigned to accommodate larger ion sources. The design and construction are under way for the upgrade.

6.6.3 Other Developments

A power system was designed and constructed to operate an MIT ion source. There are similarities to the ORNL duoPIGatron ion source. The major differences were in the arc power supply and the filament power supply. The arc required pulsed 600 V(dc) at 100 A, and the filament required 75 V(dc) at 4 A opposed to 100 V(dc) at 800 A and 12 V(dc) at 200 A, re-
tively. Results of the experiment are reported elsewhere.

A complete MacKenzie ion source will be studied; the power and control systems have been designed and built to operate it. The major difference in power requirements from those of a duoPIGatron is the filament power. The MacKenzie source requires 12 V(dc) at 1200 A due to the large number of tungsten filaments. The filaments must be ed at a low temperature, and prior to ion extraction they must be pulsed to full power. The system is ready for installation.

A precel experiment was conducted with the PLT ion source to test for improved beam transmission efficiency. A 300-V(dc), 100-A pulsed power supply was designed and constructed for

connection between the second anode and the plasma grid. Results indicated a 30% improvement in transmission efficiency.

6.7 VACUUM COMPONENTS DEVELOPMENT

6.7.1 Introduction

The objective of the Vacuum Components Development (VCD) Program is development and construction of integrated high speed (~10^5-10^6 liters/sec) pumping systems for near-term fusion experiments with applicability to future fusion reactor requirements. Since getters, cryosorption, and cryocondensation have many complementary characteristics, it is probable that a fusion vacuum system would employ a combination of these techniques. Currently the most favorable applications appear to be in neutral beam injectors, tokamak divertors, and direct energy convertors. These systems will be designed to pump hydrogen isotopes, helium, and other contaminants as cleanly as possible. Simple and rapid regeneration will be provided in anticipation of the requirements of machines using tritium. Close attention will be given to economical industrial fabrication.

6.7.2 Performance Tests on AEDC Cryocondensation Pumps

Seven cryocondensation pumps cooled by 4.2-K liquid helium were fabricated for the PLT injectors (Fig. 6.2) by Arnold Engineering Development Center (AEDC) under subcontract. These were designated as types "A" (5 m^2), "B" (0.5 m^2), and "C" (2.5 m^2) and were installed in the source tank, drift tube, and METF target tank, respectively. The numbers in parentheses give the pump inlet areas. During injector system tests at ORNL, the helium consumption per pump varied from 3 to 5 liters/hr, depending on operating conditions. Continuous flow hydrogen pumping tests on a "C" pump indicated a maximum pumping speed of about 2 x 10^5 liters/sec (Ref. 43) after proper ion gauge sensitivity corrections were applied. No evidence of pump instability was observed during high power neutral beam pulses, and typical maximum beam line pressures remained in the range of 10^{-7} Torr. Other design and performance details are given in Ref. 43.

6.7.3 Beam Line Cryosorption Pump

Construction is proceeding on a large cryosorption pump with an inlet area of two square meters.[44] The pump (Fig. 6.9) is very similar in configuration to the AEDC type "C" cryocondensation pumps, and will be tested in the METF target chamber in direct comparison with the existing "C" pump. The pump is fabricated by Excalibur Corp. of Waltham, Massachusetts; delivery is expected in early summer 1978. The pump panels will be maintained at temperatures between 10 and 20 K by 3-atm supercritical helium gas circulated through a liquid

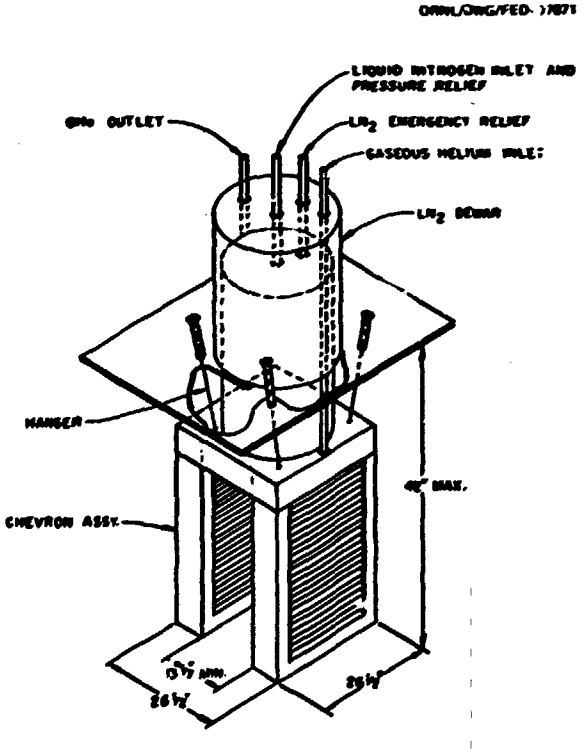

Fig. 6.9. Excalibur 2-m^2 cryosorption pump.

helium bath by a room temperature compressor coupled to the cold loop through a heat exchanger. Design and most of the procurement for this loop are complete, and fabrication should be finished by the time the Excalibur pump arrives.

6.7.4 Vacuum Engineering Data Studies

Engineering data on molecular sieve materials for cryosorption are being obtained in collaboration with the ORNL Chemical Technology Division. Sample panels 10 cm in diameter are being tested in a Variable Panel/Temperature Cryostat (Fig. 6.10). The first tests were carried out on a sample of type 5A molecular sieve (5-Å pores) in 1.5-mm-deep grooves on a stainless steel substrate. A total of 82 five-minute test runs with hydrogen gas were completed at panel temperatures ranging from 12 to 35 K. No evidence of panel degradation was observed. Figure 6.11 gives average speeds vs pressure at various hydrogen flow rates and panel temperatures. It can be seen that the highest speeds are obtained at the lowest panel temperatures. The minimum 15-K speed amounts to about 2 liters/sec/cm^2 at 10^{-4} Torr. This rather low value is due to rapid falloff of the pumping speed as material accumulates in the surface pore layers and indicates that 5A sieve will probably not be acceptable for fusion applications. Some preliminary tests with type Na-Y sieve (7-Å pores) on a similar stainless steel substrate indicate that larger pores give an order of magnitude better pumping speed at 15 K. This sieve will be used on the 2-m^2 Excalibur pump.

The pumping systems for the divertor and main plasma chamber will have to handle gas mixtures containing as much as 15% helium produced by the fusion "burn." Pumping speed tests with a D-5% He mixture were performed on a molecular sieve 5A panel at 4.2 K.[5] The results indicated that the sieve will not pump both gases at once -- the deuterium plugs the sieve pores and the helium accumulates, leading to cryogenic runaway. When an intermediate

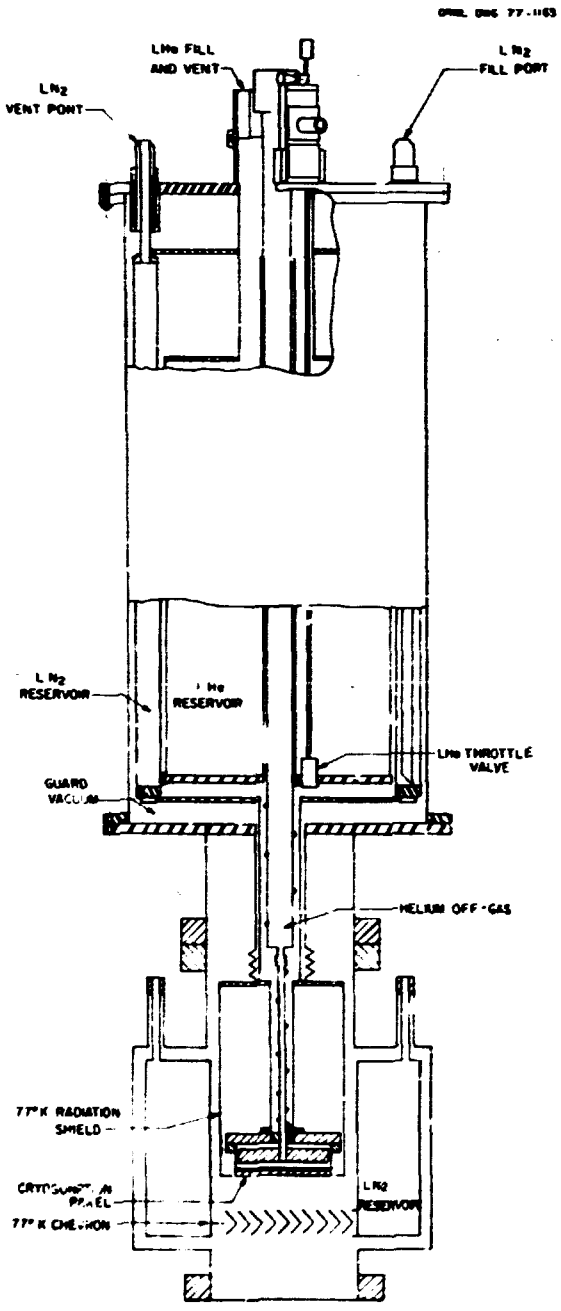

Fig. 6.10. Variable panel/temperature cryostat.

chevron cooled with 4.2-K helium gas was interposed, pumping speeds comparable to those for pure deuterium were obtained. Hence, compound pumps having separate stages for each gas component will be required for mixed gases.

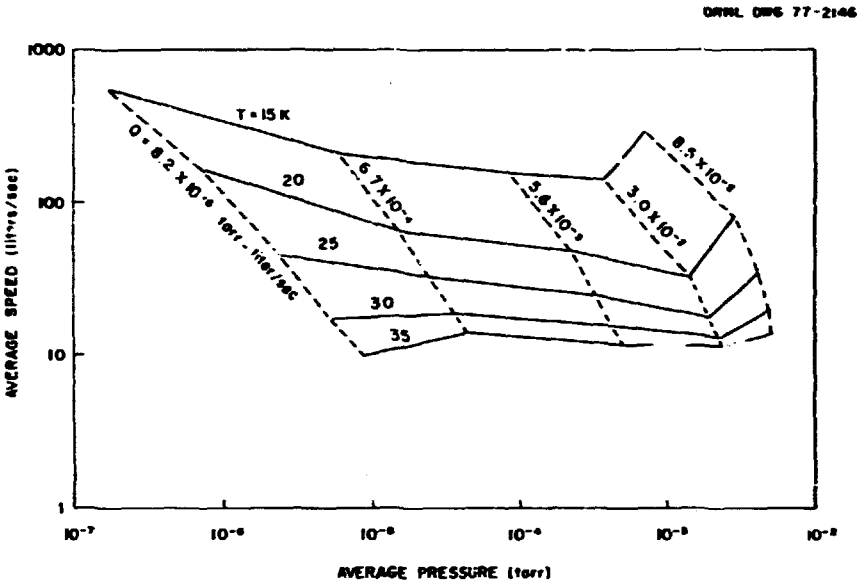

Fig. 6.11. Average pumping speeds for a 5-min run vs pressure for a 10-cm-diam type 5A molecular sieve cryosorption panel.

6.8 PELLET FUELING

6.8.1 Introduction

The ORNL pellet fueling program is developing solid hydrogen pellet injection devices for use in pellet-plasma interaction studies. The immediate objective is to develop equipment which can be applied to contemporary tokamak confinement devices in an effort to determine empirical pellet fueling criteria. The ultimate goal is the realization of a practical device that can be used to sustain ignited plasma conditions in a tokamak power reactor. The status of the various pellet acceleration programs and results of recent pellet injection studies on ISX are reported below.

6.8.2 Mechanical Pellet Injector Program

Conceptually, the mechanical injector accelerates extruded solid hydrogen pellets on the surface of a high speed rotating disc to speeds approaching 1000 m/sec.[46] A schematic of the prototype device which is nearing completion is shown in Fig. 6.12. A continuous stream of pellets is formed by the extruder/cutter disc mechanism which is situated along the vacuum spin tank assembly. These pellets are to be injected past the spin tank lid and onto the surface of the spinning aluminum arbor. A uniquely shaped groove machined in the disc surface carries the pellets from the central hub region to the outer periphery, where they exit tangentially with a velocity that is twice as large as the arbor trip speed. In this way, pellets would be fed continuously into the tokamak drift tube at a rate sufficient to sustain the plasma discharge.

To date, the arbor has been operated reliably at the design speed of 470 m/sec. The pellet feed mechanism, which is nearing completion, will be tested separately; if these tests are successful, the two systems will be combined in the coming year to form a prototype pellet injector system.

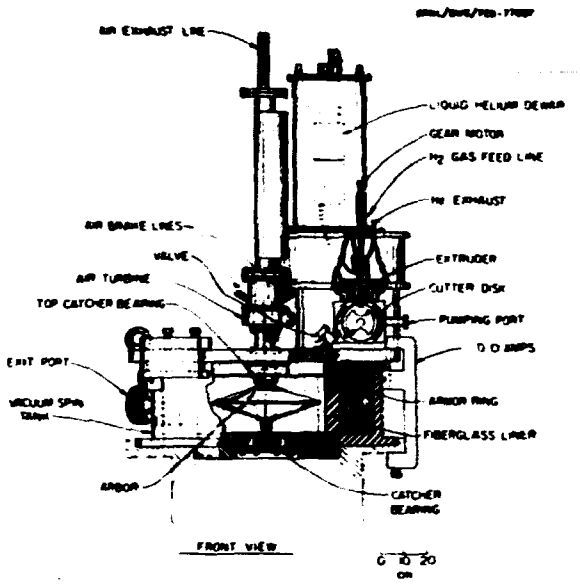

Fig. 6.12. Mechanical pellet injection system.

6.8.3 Pneumatic Pellet Injector Program

A gun type pellet injector has been developed for use in near-term pellet injection experiments; it operates on the principle of accelerating a frozen hydrogen pellet in a miniature gun barrel with pressurized gaseous propellant. This device has been operated successfully in the laboratory at speeds as high as 430 m/sec with 0.6-mm-diam cylindrical hydrogen pellets. Presently, this device is capable of injecting a single pellet during each tokamak discharge. In the future, its capabilities will be extended to multiple pellet injection for the purpose of sustaining the plasma density during the tokamak discharge.

6.8.4 Pellet Injection Studies on ISX

Hydrogen pellets were injected into the ISX plasma at velocities of 330 m/sec to test the pellet ablation dynamics and to determine the effect of abrupt density increases on the plasma discharge. Photographs of the discharge indicate that pellets penetrated nominally 12 cm into the plasma, which is in agreement with pellet ablation scaling laws developed from previous pellet injection experiments.[6,7] The much deeper penetration, combined with the larger mass of the pellets, appears to indicate that the plasma density can be efficiently and significantly increased without deleterious effects on the discharge. Figure 6.13 shows typical recorded line average densities during pellet injection into high and low density discharges. Pellets enter the plasma at 77 msec, which results in an abrupt increase in plasma density. In the high density case, a 30% increase is noted; the background density is maintained in this example by gas puffing. In

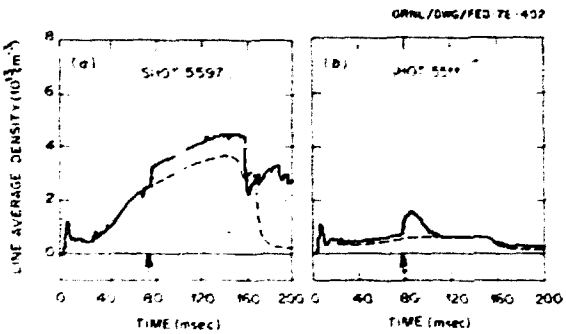

Fig. 6.13. Line average density records during pellet injection into ISX-A. (a) typical high density case, (b) typical low density case (shots 5597 and 5511).

the low density example, gas puffing was discontinued to produce a nominal plasma density of 7×10^{12}/cm^3. Introduction of the fresh fuel is seen to nearly double the plasma density momentarily. An overall increase in MHD activity brought about by pellet injection is apparently responsible for the decrease in density seen after injection. The plasma returns to its nominal density in about 20 msec.

These preliminary results indicate that relatively large pellets can be injected into the tokamak plasma. If these observations are correct, technological requirements based on reactor fueling devices will be greatly relieved.

REFERENCES

1. O. B. Morgan et al., "The Development and Application of Neutral Injection Heating for ORMAK," invited talk given at the International School of Plasma Phys. Symp. on Plasma Heating and Toroidal Devices, Varenna, Italy, September 6-17, 1976.
2. T. C. Jernigan et al., *Proc. 2nd Symp. on Ion Sources and Formation of Ion Beams*, paper VI-9 (1974).
3. W. L. Stirling et al., *Proc. 2nd Symp. on Ion Sources and Formation of Ion Beams*, paper VI-10 (1974).
4. R. C. Davis, T. C. Jernigan, O. B. Morgan, L. D. Stewart, and W. L. Stirling, Rev. Sci. Instrum. 46, 576 (1975).
5. C. C. Tsai, W. L. Stirling, and P. M. Ryan, Rev. Sci. Instrum. 48, 651 (1977).
6. W. L. Stirling, C. C. Tsai, and P. M. Ryan, Rev. Sci. Instrum. 48, 533 (1977).
7. C. C. Tsai et al., *Proc. 7th Symp. on Engineering Problems of Fusion Research*, Vol. I, p. 278 (1977).
8. H. H. Haselton et al., *Proc. 6th Symp. on Engineering Problems of Fusion Research*, p. 865 (1976).
9. P. M. Ryan, C. C. Tsai, and W. L. Stirling, Bull. Am. Phys. Soc. 22, 1083 (1977).
10. J. H. Whealton and C. C. Tsai, Rev. Sci. Instrum. 49, 495 (1978).
11. W. L. Stirling, R. C. Davis, P. M. Ryan, D. E. Schechter, and C. C. Tsai, Bull. Am. Phys. Soc. 22, 1083 (1977).
12. J. H. Whealton, C. C. Tsai, L. R. Grisham, and W. L. Stirling, *Proc. Symp. on the Production and Neutralization of Negative Hydrogen Ions and Beams*, p. 129 (1978).
13. C. C. Tsai, W. L. Stirling, and R. C. Davis, *Proc. Symp. on the Production and Neutralization of Negative Hydrogen Ions and Beams*, p. 340 (1978).
14. W. L. Stirling, "The ORNL Negative Ion Program," paper presented at the OFE Workshop on Plasma Heating Requirements, Washington, D.C., December 5-7, 1977; proceedings to be published.
15. W. K. Dagenhart, W. L. Gardner, H. H. Haselton, M. M. Menon, D. E. Schechter, W. L. Stirling, and C. C. Tsai, *Proc. 7th Symp. on Engineering Problems of Fusion Research*, Vol. I, pp. 533-538 (1977).
16. W. L. Gardner, J. Kim, M. M. Menon, and G. Schilling, *Proc. 7th Symp. on Engineering Problems of Fusion Research*, Vol. II, pp. 1545-1548 (1977).
17. G. C. Barber, A. Y. Broverman, R. E. Hill, C. M. Loring, N. S. Ponte, G. Schilling, and R. E. Wright, *Proc. 7th Symp. on Engineering Problems of Fusion Research*, Vol. II, pp. 1142-1146 (1977).
18. M. M. Menon, W. L. Gardner, and J. Kim, Bull. Am. Phys. Soc. 22, 1082 (1977).
19. W. L. Gardner, J. Kim, M. M. Menon, and J. H. Whealton, Rev. Sci. Instrum., in press.
20. J. C. Whitson, J. Smith, and J. H. Whealton, J. Comput. Phys., in press.
21. J. C. Whitson, J. Smith, and J. H. Whealton, Bull. Am. Phys. Soc. 22, 1082 (1977).
22. J. H. Whealton, E. F. Jaeger, and J. C. Whitson, J. Comput. Phys. 27, 32 (1978).
23. *Fusion Energy Division Annual Progress Report for Period Ending December 31, 1976*, ORNL-5275, Oak Ridge, Tennessee (1977).
24. E. F. Jaeger and J. C. Whitson, *1975 Numerical Simulation for Axially Symmetric Beamlets*, ORNL/TM-4990, Oak Ridge, Tennessee (1975).
25. J. H. Whealton, E. F. Jaeger, and J. C. Whitson, Rev. Sci. Instrum. 48, 829 (1977).

26. L. R. Grisham, C. C. Tsai, J. H. Whealton, and W. L. Stirling, Rev. Sci. Instrum. 48, 1037 (1977).
27. J. Kim, J. H. Whealton, and G. Schilling, J. Appl. Phys. 49, 517 (1978).
28. J. H. Whealton, L. R. Grisham, C. C. Tsai, and W. L. Stirling, J. Appl. Phys. 49, 3091 (1978).
29. J. H. Whealton, "Reduction in Residual Aberration Effects on Ion Optics in Neutral Beam Generators," paper presented at the Annual Controlled Fusion Theory Conference, San Diego, California, May 4-6, 1977.
30. J. H. Whealton, L. R. Grisham, J. Kim, W. L. Stirling, and C. C. Tsai, "Space Charge Ion Optical Systems," paper presented at the IEEE Int. Conf. on Plasma Science, Troy, New York, May 23-25, 1977.
31. J. H. Whealton and J. C. Whitson, Bull. Am. Phys. Soc. 23, 151 (1978).
32. G. G. Kelley, O. B. Morgan, G. Schilling, and J. H. Whealton, "Steady State Space Charge Blowup and Recovery of Intense Ion Beams," Nucl. Instrum. Methods, in press.
33. J. H. Whealton, Rev. Sci. Instrum. 48, 1428 (1977).
34. W. L. Gardner, J. Kim, M. M. Menon, and J. H. Whealton, Bull. Am. Phys. Soc. 22, 1082 (1977); W. L. Gardner, J. Kim, M. M. Menon, and J. H. Whealton, Rev. Sci. Instrum., in press.
35. J. H. Whealton, H. H. Haselton, and W. L. Stirling (Oak Ridge National Laboratory), private communication, 1977.
36. J. H. Whealton, Appl. Phys. Lett. 32, 353 (1978).
37. J. H. Whealton, Rev. Sci. Instrum. 49, 9999 (1978).
38. J. H. Whealton, C. C. Tsai, W. K. Dagenhart, W. L. Gardner, H. H. Haselton, J. Kim, M. M. Menon, P. M. Ryan, D. E. Schechter, and W. L. Stirling, "Effect of Preacceleration on Intense Ion Beam Transmission Efficiency," submitted to Appl. Phys. Lett.
39. L. R. Grisham, C. C. Tsai, J. H. Whealton, and W. L. Stirling, Rev. Sci. Instrum. 48, 1037 (1977).
40. P. M. Ryan and J. Kim, Bull. Am. Phys. Soc. 21, 1119 (1976).
41. P. M. Ryan, R. C. Davis, W. L. Stirling, and C. C. Tsai, Bull. Am. Phys. Soc. 20, 1365 (1975).
42. J. Kim et al., "D-D Neutron Measurements from ORNL/PLT Neutral Beam Injector," paper presented at the IEEE Int. Conf. on Plasma Science, Monterey, California, May 15-18, 1978.
43. S. W. Schwenterly, W. K. Dagenhart, H. H. Haselton, W. L. Stirling, and C. C. Tsai, Trans. Am. Nucl. Soc. 27, 56 (1977).
44. S. W. Schwenterly, *Proc. 7th Symp. on Engineering Problems of Fusion Research*, Vol. II, pp. 1793-1795 (1978).
45. P. W. Fisher and J. S. Watson, *Proc. 7th Symp. on Engineering Problems of Fusion Research*, Vol. II, pp. 1816-1819 (1977).
46. C. A. Foster and S. L. Milora, "ORNL Pellet Acceleration Program," paper presented at the Fusion Fueling Workshop, Princeton, New Jersey, November 1-5, 1977.
47. S. L. Milora and C. A. Foster, "Pellet Experiments at ORNL," paper presented at the Fusion Fueling Workshop, Princeton, New Jersey, November 1-5, 1977.

LCP AND SUPERCONDUCTING MAGNET TECHNOLOGY

M. S. Lubell, Section Head, Magnetics and Superconductivity Section
P. N. Haubenreich, Manager, Large Coil Program

J. E. Akin[1]	R. B. Jacobs[1]	H. Pih[1]
L. Alley, Jr.	W. J. Kenney	C. C. Queen[2]
J. K. Ballou	J. F. Kois[2]	J. P. Rudd
R. L. Brown	D. M. Kroeger[3]	T. L. Ryan[2]
P. B. Burn[2]	M. H. Kumselman[2]	R. E. Schwall[6]
W. D. Cain[2]	C. G. Lawson[4]	S. S. Shen
L. Dresner	C. D. Long[3]	R. E. Stamps[2]
D. S. Easton[2]	J. C. Lottin[5]	R. C. Stewart[2]
J. F. Ellis	J. W. Lue	W. C. T. Stoddart[2]
W. A. Fietz	J. N. Luton, Jr.	P. B. Thompson[2]
C. M. Fitzpatrick	T. L. Mann[2]	W. H. Wagner
W. M. Fletcher[2]	J. R. May[7]	P. L. Walstrom
W. F. Gauster[1]	J. R. Miller	R. J. Wood[2]
J. S. Goddard[2]	L. W. Nelms[2]	R. B. Wysor[2]
W. H. Gray	R. E. Nelson[2]	H. T. Yeh

Abstract. In this year our efforts were focused primarily in support of the LCP and in advanced development of superconductor. We also carried out smaller but important design tasks in support of the TNS, EBT-S, EBT-II, and EBTR programs. As a result of our collaborative efforts with commercial superconductor manufacturers, we were able to procure the first long length of 8-T, 10-kA NbTi conductor. A second type more analogous to the GE-LCP conductor is expected early in 1978. Three CPFF subcontracts were arranged with industry to develop Nb_3Sn and forced flow conductor. Our small-scale experiments on conductor stability, ac losses, and pulse coils, and the theoretical work in support of these experiments have contributed to a better understanding of the design of conductor for TF coils. The instrumentation development concentrated on testing of strain gages and evaluating the previously developed MCDT on a real system, ISX-A. New facilities were designed and construction initiated to enable us to evaluate properly the full-size conductor chosen by the three LCP participants. Capital facilities such as power supplies, a computer, and a large refrigerator/liquefier were received. The structural analysis and 3-D eddy current and magnetic field code development carried out in support of the ongoing projects also provided an extended capability for the future. A major effort was expended on getting the LCSTF set up. Practice winding of the first segment coil was completed and plans were formulated for winding the subsequent coils. The project was on schedule for completion (in July 1978) and within budget at the close of the year, but a cut in funds required a hold to be put on the project.

1. Consultant.
2. UCC-ND Engineering.
3. Metals and Ceramics Division.
4. Energy Division.
5. Sabbatical from Saclay.
6. Present address: Intermagnetics General Corporation, Guilderland, New York.
7. Grumman Aerospace Corporation.

7.1 CONDUCTOR DEVELOPMENT

7.1.1 Development Contracts

Three contracts for forced flow conductor development were awarded for TF coil work. One is with Supercon to develop a forced flow NbTi

conductor using the Ukonite process for jacketing the cable. The second is with Airco for forced flow NbTi and Nb_3Sn, concentrating on the Nb_3Sn using Airco's own jacketing process. The third is with IGC to develop a novel concept for Nb_3Sn forced flow conductor using two copper braid heat exchangers flanking an Nb_3Sn braid or cable. These contracts were signed in August-September 1977 and will run into CY 1978.

7.1.2 Conductors Purchased

Orders were placed for two 600-m lengths of 10-kA, 8-T TF pool boiling conductors. The first, consisting of seven parallel compacted cables, was received in September 1977. The second, similar to the GE/IGC concept for LCP use, is expected early in 1978. In addition ~250 m of practice conductor, a physical duplication of the second TF conductor, was received for use in setting up the winding facility. Other conductors purchased and received in 1977 for test and evaluation were 8000 kA-m of 8-T conductor suitable for pulse application and 300 kA-m of aluminum stabilized conductor.

7.1.3 Conductors for Tokamak Toroidal Field Coils[1]

This paper describes six conductors which are being developed for use in superconducting TF coils of tokamak fusion machines. Included are three pool boiling and three forced flow concepts. Research and development programs on several of the conductors are under way, jointly involving ORNL and conductor manufacturers. Conductors will be tested in short lengths and in the form of 2.7 x 2.0-m LCS tests. The conductor development and testing are closely coordinated with the LCP at ORNL.

7.2 STABILITY EXPERIMENTS AND THEORY

7.2.1 Current Transfer in Built-up Conductors

Superconductors carrying 10 kA or more have been widely suggested for use in fusion research and reactor magnets. Built-up or cable conductors have been proposed in which superconductor is concentrated in part of the conductor or part of the strands while the stabilizer occupies the rest. This scheme leads to substantial savings in manufacturing cost and to reduction of ac losses. We have constructed a simple theory that predicts a reduction in cold end stability by extra heating in resistive layers joining stabilizer and composite. Two types of conductors were constructed for the experimental test. Triplex conductors consisting of either three superconducting wires or two superconducting wires plus one copper wire were used to simulate cables. Laminated superconductor and copper strips with different soldering bonds were used for built-up conductors. Normal zone propagation and recovery experiments have been performed and the results compared with theory. The predicted decrease appears to be small in the cases considered, and experimental evidence suggests that the effect is even smaller than predicted, i.e., the theory is conservative. In fact, other parameters that are difficult to control, such as effective heat transfer, appear predominant.[2] This is an important result because it gives the conductor designer more freedom to reduce manufacturing difficulties, improve conductor performance, and reduce ac losses by segregation of composite and stabilizer. It also indicates that stringent quality control of soldering in built-up conductors is probably not necessary from an electrical standpoint.

7.2.2 Vapor Locking

Recently Wilson and Walters suggested that it seemed "worthwhile to investigate stagnant two-phase cooling." Their suggestion was based on the assumption that "gas is free to vent but no new liquid enters the zone during the pulse." Subsequent experiments by Iwasa et al. showed that in narrow channels the gas did not vent freely but expelled liquid instead. Were no new liquid to enter and no gas to vent at all, the helium would then have only about one-seventh the energy absorbing capacity as supposed by Wilson and Walters (because of the seven-fold volume expansion upon vaporization). For all practical purposes, heat transfer stops when the channel is filled with vapor. If recovery is to occur, it must occur before this happens.

The heat delivered to the helium in a temperature excursion is the sum of the initial heat pulse that created the normal zone and the Joule heat produced during recovery. If recovery is fast, Joule heat production may be kept small, and the bulk of the energy absorbing capacity of the helium may be devoted to the initial pulse. Rapid recovery is fostered by a large cooled surface such as is typified by cable-in-conduit conductors which have been proposed for use with supercritical helium in forced flow; this work is concerned with the recovery processes in such conductors.

Vapor locking has been observed to limit the stability of superconductors in narrow tubular channels. This limitation is consistent with an analysis based on reduction of cooled surface by vapor formation. In very long channels ($L/D > 50$), however, it was found that stability increases. When the superconductor inside long sheathed sections recovers from the resistive state, it recovers faster than in open section. This is believed to be due to the increase of the heat transfer coefficient and heat capacity caused by pressure buildup and relief inside the sheath.[3]

7.2.3 Design of Force Cooled Conductors for Large Fusion Magnets

One of the central problems in designing conductors force cooled by supercritical helium is to maintain an adequate stability margin while keeping the pumping power tolerably low. A method has been developed for minimizing the pumping power for fixed stability by optimally choosing the matrix-to-superconductor and the metal-to-helium ratios. Optimized conductors have acceptable pumping power requirements for fusion-size magnets. The mass flow and hence the pumping losses can be varied through a magnet according to the local magnetic field and magnitude of the desired stability margin. Force cooled conductors also give flexibility in operation, permitting, for example, higher fields to be obtained than originally intended by lowering the helium temperature or increasing the pumping power or both. This flexibility is available only if the pumping power is low to begin with. The design method is explained in detail (with examples).[4]

7.2.4 The Effect of a Continuous Resistive Transition on Self-Field Instability

As transport current increases, composite superconductors develop resistance continuously rather than discontinuously. This means that the distribution of current among the filaments in a composite conductor is determined not only by their inductive coupling but also by the longitudinal resistance they develop as they begin to carry current. The current distribution has been calculated, taking into account the continuous nature of the resistive transition for the following two cases: (1) a composite clamped suddenly across a constant current source, and (2) a composite being charged at a uniform rate. The results of problem (2) have been used to show that slowly charged conductors

are much more stable against self-field instability than is indicated by purely inductive calculations.[5,6]

7.3 ac LOSSES AND PULSE COIL MEASUREMENTS

In CY 1977, the setup, building, and instrumentation efforts of the previous year were brought to fruition as stability and loss results were obtained on a wide variety of pulsed coil conductors.

Stability measurements early in the year were concentrated on the 2000-A cables produced in CY 1976. The results show that solder filling does improve cable stability but that stability with insulated strands was equal to or better than that obtained with bare strands. Evidence of additional loss due to impurities or superparamagnetism in the Cu-30% Ni matrix of some conductors was also found. Loss measurements on triplex and seven-strand cables demonstrated that solder coated cables had essentially the same losses as those made with insulated strands. Solder filled cables had much higher losses. A transformer model, which was devised to solve the transient losses in normal conductor and superconducting composite, was found to describe all the results quite well. Very interesting results were obtained in measurements of the saturation magnetization of the triplex cables, and these have led to a more systematic investigation of the influence of superconductor distribution within a strand or cable on the pulsed loss. This project is coordinated with our efforts to produce low cost, low loss, high stability cables by incorporating pure copper strands with the composite strands.

A design study for a fast ramp superconductor initiated in 1976 at IGC led to a very fruitful collaboration this year. A promising "self-ventilating," pancake-wound braid coil design has been developed. This design for a TNS-size PF coil obtains effective cooling without the use of interturn spacers. When combined with the high stability, low loss braid described below, this promises to be a viable method for winding full-size PF coils. The second result of the ORNL-IGC collaboration was the high Cu:SC "finned" conductor. This design provides low loss in strands that are individually cryostable and which may thus be incorporated into an insulated braid. A test billet of this conductor was successfully extruded and drawn to wire, and fabrication of a full-size billet was initiated.

Our plans for 1977 called for fabrication of a 300-kJ test coil to be tested early in 1978 and the construction of a second such coil incorporating state-of-the-art mixed matrix conductor by April 1978. Budgetary restrictions have made it impossible to plan for either coil. However, based on the successful production of the "finned" conductor, it was decided to proceed directly to the mixed matrix coil. A short length (≈100 ft) of 2000-A braid similar in size and Cu:SC ratio to that needed for the coil was produced, and extensive stability measurements were made to determine the proper degree of compaction and the detailed coil design. An insulation previously not used in superconductivity (Essex Wire Co. GP-200) was tested and found to have the abrasion resistance necessary for braiding. Mechanical design and structural analysis of the coil (designated as ORPUS-III) have been performed.

A contract for a 2000-A, 300-V bipolar power supply was placed at the beginning of FY 1977, and an acceptance test of the supply was witnessed at the vendor's plant in November 1977. Delivery to Oak Ridge was accomplished in December and final checkout will be completed in February 1978.

7.3.1 Losses and Transient Field Effect in Superconducting Cables for PF and TF Coils[7]

This paper presents results of transient loss measurements on some seven-strand cable conductors. In addition to the filamentary coupling in a single composite strand, we have observed appreciable interstrand coupling in the cables filled with solder. We also have found that the interstrand coupling depends on the

arrangement of the strands. Coupling loss results are analyzed in terms of a diffusion time constant associated with the coupling mechanism. Deduction of effective resistivity is also presented and discussed.

7.3.2 An Apparatus to Examine Pulsed Parallel Field Losses in Large Conductors

Conductors in tokamak TF coils will be exposed to pulsed fields both parallel and perpendicular to the current direction. These conductors will likely be quite high capacity (10-20 kA) and therefore probably will be built up out of smaller units. We have previously published measurements of losses in conductors exposed to a pulsed parallel field, but those experiments necessarily used monolithic conductors of relatively small cross section because the pulse coil, a torus that surrounded the test conductor, was itself small. Here we describe an apparatus that is conceptually similar but has been scaled up to accept conductors of much larger cross section and current capacity. The apparatus consists basically of a superconducting torus that contains a movable spool to allow test samples to be wound inside without unwinding the torus. Details of apparatus design and capabilities are described, and preliminary results from tests of the apparatus and from loss measurements using it are reported. A novel winding technique used in the construction of the pulsed torus is described in Sect. 7.6.1.

7.3.3 Superconductors for Tokamak Poloidal Field Coils[9]

The PF system in a tokamak fusion device provides a time varying flux which is used initially to break down the plasma and build up the plasma current and subsequently to compensate for plasma losses in sustaining the burn. Although the coil parameters vary somewhat from device to device, maximum fields up to 7 T and field sweep rates up to 7 T/sec are common. This combination of maximum field and field sweep rate is somewhat beyond the state of the art and, when combined with the large size of the magnets (stored energy $\sim 10^9$ J), presents a rather demanding technological challenge. In this paper we present stability and loss measurements on superconducting cables similar to those that could be used in PF coils. A model which aids in the interpretation of the loss is also presented.

7.3.4 Fast Ramp Superconductor for Ohmic Heating Coils[10]

The present study was conducted to consider practical 10,000-A conductor designs to meet the operating constraints for the OH coils of TNS and experimental tokamak reactors. The conductor must simultaneously meet the requirements for mechanical support, cryostabilization, high overall winding current density, low mechanical and electrical losses, and mechanical and electrical integrity for cyclic pulsed operation from -7 T to +7 T in 1 sec.

Our suggested winding is a set of nested tubes, each made up of a stack of pancake-wound bobbins. Each pancake is comound of a flat open superconductor braid, steel tape, and Kapton insulation. The strands of the braid consist of sectored copper regions separated by copper-nickel and surrounding a mixed matrix copper, copper-nickel, and NbTi multifilament core. Strands 1.5-mm-diam provide conservative cryostabilization at overall winding current densities adequate for the OH winding of an EPR-I or TNS-size coil ($\sim$1500 A/cm^2). Eddy current and coupling losses are at acceptable levels, and hysteresis losses can be reduced to within acceptable limits with 10-μm-diam filaments, provided the winding is graded, tube to tube. The basic conductor and winding concept can be extended to provide conductors of higher currents.

A 2000-A model conductor has been fabricated from 0.94-mm-diam strands and tested in a reinforced pancake configuration. The measured maximum recovery current corresponds to a current density of 3500 A/cm^2 over the entire coil cross section.

7.3.5 Mechanical Design of ORPUS-III[11]

ORPUS-III is the third in a series of pulsed superconducting solenoids built to test construction techniques applicable to tokamak PF coils. The present coil is designed to be charged to a maximum field of 7 T in 1 sec, and stored energy is approximately 300 kJ. The conductor is a high copper-superconductor ratio, mixed matrix material developed for this application. In this paper we present a mechanical design which uses distributed reinforcement to support a self-ventilating braid conductor. Using this design, it has been possible to obtain a high overall current density and a low heat flux in a fully normal zone. In order for the stress to be kept within acceptable limits in the reinforcing material, a programmed winding tension schedule has been calculated. The deflection, stress, and strain of the windings are predicted using the STANSOL-II computer code.

7.4 INSTRUMENTATION AND DATA ACQUISITION

A small-scale effort in testing instrumentation for magnet testing in LCSTF and LCPTF continued through 1977. In addition, a data acquisition system for coil testing (based on a PDP 11/60 minicomputer) was designed and purchased, and work on software development was begun.

Platinum-tungsten strain gages were tested in fields up to 7.5 T and were found to have an acceptably low magnetoresistance; this, together with their low temperature coefficient of resistance, makes them good candidates for magnet strain measurement.

A second prototype voltage tap signal conditioning unit, capable of amplifying and compensating inductive signal components in millivolt signals superimposed on a 2000-V common mode background, was breadboarded and bench tested. The first prototype has unacceptably large phase shifts.

A double shielded transformer isolation scheme for strain gages and other transducers on or near high potential surfaces (i.e., the windings of an LCP magnet during a quench) was under development in 1977. The system is designed for use with stranded carrier amplifiers.

Deflection measurements were made on three of the TF coils of ISX during the magnet system test using two devices developed in the magnet program. The measured deflections agreed well with the values predicted by finite element stress analysis.

Finally, a significant part of the instrumentation effort was dedicated to monitoring and review of the instrumentation efforts of the three large coil contractors.

7.5 LARGE COIL SEGMENT

7.5.1 Test Facility

LCSTF is a facility for testing superconducting "segment coils" – coils nearly as large in diameter as the coil for LCP and with the same transport current (10–15 kA), but with approximately one-tenth of the cross section and less than one-tenth as much superconductor. Since the self-field of the segment coils is low (about 1 T), four superconducting niobium-tin, tape-wound coils salvaged from the IMP facility are used to produce a maximum total field of 7.5 T over a 60-cm length of the test coil windings. In addition to the background coil and support structure, the facility includes a large vacuum chamber (the old ORMAK vacuum vessel with modifications), vacuum pumps and valves, liquid helium and nitrogen supply lines, an LN_2-cooled cold wall, vapor-cooled current leads, buswork, dump circuits, a diagnostic and control system, and miscellaneous utilities.

At the end of November 1977, the project was placed on a hold status because of lack of funding. At this time, costs were within projected levels, and the project was on schedule

for a completion date of July 1978. Construction for various parts of LCSTF was in various states of completion; overall, about 95% of the engineering design was finished and approximately 20% of the fabrication was complete. Major procurement for LCSTF was about 25% complete.

The revised schedule for LCSTF, assuming that work on the project resumes at the start of FY 1979, calls for completion in June 1979.

7.5.2 Segment Fabrication

The bobbin for the first coil was fabricated and delivered along with the balance of the steel case, which will be welded to form the entire coil case after winding. Insulation material, epoxy fiberglass, Kapton, and epoxy were purchased and received. Detail design of the first coil, including instrumentation, was completed. Practice winding, including insulation insertion, was initiated.

7.5.3 Design of a 3-m, 7.5-T Superconducting Segment Test Facility[1]

The design of a test facility for so-called segment coils is described. The segments are D- or oval-shaped test coils, up to 3 m in major diameter, and can have a maximum winding cross section of 14-cm axial length and 30-cm radial build, which is approximately one-tenth that of a coil for LCP. A background field of 6 T, which when added to the 1.5 T available from the segment self-field yields a peak total field of 7.5 T in the segment, is produced by a set of niobium-tin, tape-wound dipole magnets mounted on either side of the test segment and cooled with boiling helium. The high field region is approximately 30 cm in length and is centered in the straight or largest radius portion of the test coil. The test coil and background field coils are suspended with a horizontal axis orientation in a vacuum vessel with a liquid nitrogen-cooled liner to provide thermal isolation.

The first segment coil to be tested in the facility will be wound from a cryostable conductor rated at 10 kA at 8 T and will be cooled by boiling helium. When combined with a helium pump loop, the facility is designed to provide essential design data on the stability of high current (10-15 kA) conductors of the LCP-TNS generation in an environment which simulates the cryogenics and heat transfer aspects of a tokamak TF coil (including horizontal axis, long cooling channels, transverse convection effects, and asymmetric field distribution).

The magnetic analysis, facility description, and structural, cryogenic, instrumentation and control, power supply, and coil protection systems designs are described.

7.6 COIL FABRICATION DEVELOPMENT

Some time was spent in the early part of the year relocating the large coil winding facility in the large bay area of Bldg. 9204-1. Alterations and additions were made in some of the equipment to improve its performance. Three types of conductor have been used for practice winding on D-shaped bobbins. One conductor with square copper strands, spiral wrapped around a heavy stainless steel ribbon, almost exactly duplicates the superconductor to be used in the first LCS coil. The design and winding techniques are substantially in hand for winding the LCS coil when the superconductor arrives. Subsequent LCS coils will have jackets wrapped around them and be cooled by forced flow.

In other coil development work, several small test coils were fabricated for pulsed coil investigations and conductor stability experiments. Also a spliceless pancake winding scheme was demonstrated by fabricating a four-pancake prototype coil. Pancake-wound coils have certain fabrication advantages over layer-wound coils if numerous splices can be avoided. They may also withstand magnetic forces well, and for some applications cooling methods may be better

and more reliable. Parts for winding a 40-pancake coil (76-cm bore) have been made and are ready to wind.

Some coil winding innovations developed at ORNL are attractive to the LCP contractors. General Electric plans to fabricate its coil using almost the same kind of equipment that was developed for winding the LCS coils. The conductor, insulations, and design of their windings can hardly be distinguished from the first LCS coil. Westinghouse has wound a small prototype D-shaped coil that demonstrates the feasibility of the spliceless winding method using its Nb_3Sn conductor. Also, a suggestion for simplifying and reducing the expense of fabricating end-of-layer splices will probably be adopted by General Dynamics.

7.6.1 Superconducting Coil Fabrication Development at ORNL[13]

Superconducting coils may be essential for minimizing power consumption in very large magnet systems. In fusion devices, the requirements vary over a wide range. Some coils will be operated at steady state and will have unsymmetrical shapes, while other coils will be pulsed. Furthermore, many test coils will be needed for experimental purposes.

A large coil winding facility (>2-m OD) is devoted to developing equipment for winding steady-state TF coils having D or oval shapes. Some activities for this facility are discussed.

Novel techniques have been developed for winding spliceless pancakes that may have immediate applications for pulsed PF coils. The concept is also applicable for many other coils, including room temperature coils and coils with odd shapes.

Also, a unique method of winding small TF test coils has been developed. This method of winding suggests possibilities for remote winding of coils, which may be useful in fusion devices.

In all superconducting coils, the windings must be securely supported against magnetic forces and conductor motion that could cause frictional heating. It is important that sufficient space be reserved to maintain adequate liquid helium cooling. A bonus for any coil is to keep the number of splices to a minimum. The selection of suitable superconductors and structural materials is a continuing concern, but the emphasis of this work is on the development of fabrication methods.

7.7 CRYOGENICS AND REFRIGERATION

7.7.1 Helium Liquefier and Refrigerator

The 3.5-K helium refrigerator/liquefier is being purchased to supply helium coolant in support of the LCPTF, the LCSTF, and other experiments where the use of a closed cycle helium refrigerator is cost effective. The refrigerator has a nominal capacity of 866 W and 125 liters/hr of LHe at 3.5 K.

All components of hardware have been delivered to ORNL including the helium compressor, the coldbox, the control panel, and all spare parts for the compressor and the gas bearing expansion turbine. All detailed designs for construction have been completed by the architect-engineer, approved by UCC-ND.

7.7.2 Helium Pump Development

The LCPTF requires a method to pump helium through the magnets cooled by the forced flow of supercritical subcooled helium. The use of a cold helium pump is the preferred method of force flowing the helium through the coils. A single-stage, preprototypical piston pump has been obtained from Gardner Cryogenics Company for test and evaluation purposes. This pump has a variable flow capacity of from ~4 to 20 g/sec and can develop a head of ~3 atm. The unit is designed to pump single-phase supercritical and subcooled helium with a suction pressure >2.5 atm. A pump test assembly has been designed for costing purposes. The loop is designed to operate either as a closed loop isolated from the refrigerator by a helium boiler or as part of the refrigerator circulating system. The

loop will contain a calorimeter for flow calibration of the pump and of flow meters for LCPTF that are located in series with the pump flow. Heat exchangers, thermocouplers, and pressure transducers will be located to permit measurement of mass pump efficiency.

7.7.3 The Helium Liquefier-Refrigerator and Distribution System for the Large Coil Program Test Facility[14]

The LCP has the objectives of obtaining and testing superconducting magnets of a size and in an environment that demonstrate feasibility of application for TNS. These magnets are to be in a toroidal array which may include from one to six magnets and are to be cooled by either pool boiling or forced convection of helium. The toroidal array will be housed in a large vacuum vessel measuring about 11 m in diameter and 11 m high. The magnets will be modified D-shaped coils and will have a bore of 2.5 by 3.5 m.

The program objectives require a versatile and sophisticated liquid helium supply and cryogenic distribution system to meet the test requirements. The liquid helium supply system consists of a high pressure gas storage system; a 1050-kW, two-stage compressor; a refrigerator coldbox capable of delivering helium at two thermodynamic states; and a 19,000-liter helium storage dewar with the associated piping and controls. The refrigerator built by CTI is designed to supply the experimental load with either supercritical helium at temperatures to ~3.5 K or as saturated liquid down to ~3.5 K. The compressor system is an oil-flooded rotary screw unit capable of operating to 0.5-atm suction pressure. The first and second compression stage sizes are 300 kW and 750 kW, respectively, and they may be used either independently or in tandem. The features of the refrigerator-liquefier are described in this paper. The features of the helium distribution system and cryogenic systems are described in Sect. 7.7.4.

7.7.4 The Helium Distribution System for the Large Coil Program Test Facility (LCPTF)[15]

The helium distribution system of the Large Coil Program Test Facility is designed to establish and maintain the thermal environment of the toroidal array of superconducting magnets throughout the initial test and evaluation period of the test program.

The refrigeration and liquefaction requirements for the LCPTF will be discussed including both the usual cooldown, lead cooling, thermal conduction and radiation and Joule heating losses, and the unusual losses due to simulated nuclear heating, magnetic coupling losses due to the transient fields of the driving magnets, and pumping losses due to fluid resistance and pump inefficiency.

The flow system is designed with separate cooldown and steady-state flow systems, and to simultaneously circulate helium under steady-state conditions through coils cooled by boiling liquid or supercritical helium at ~4.0 K and >2.5-atm pressure. Separate helium storage dewars are utilized for vapor cooling of the current leads to the magnets, with the effluent gas being stored after compression in high pressure storage tanks. The flow diagram will be presented in simplified form to show the salient features of the cryogenic system.

7.8 STRUCTURAL ANALYSIS AND MATERIAL EVALUATION

7.8.1 Material Evaluation

The first experimental phase of investigation to determine the effect of irradiation damage on organic electrical insulators at liquid helium temperatures has been completed.

Involvement continued in support of local projects such as LCP and LCS in selecting appropriate materials and fabrication technology. Participation in external liaison activities for OFE such as the DOE/OFE Task Group on Special

Purpose Materials continued, along with an expanded involvement with NBS (Boulder, Colorado) in their work for DOE/OFE.

Mechanical testing was performed on the behavior of the superconductor to be used in the ORPUS-III pulse coil experiment, and preparation was made to test LCS/LCP prototype conductors.

Interactions Between Conductor Strain and Other Magnet System Design Parameters[16]

A simple closed form electromechanical analysis of a TF coil is used to calculate current density in the conductor plus coolant (J_{con}) and fraction of the cross section allotted to structure (λ_{st}) as functions of important machine parameters, including the Young's modulus of the structural material, allowable elastic strain, system aspect ratio, major radius, and maximum field. The analysis is used to assess trade-offs between conductor strain and other machine parameters and to identify ways in which strain tolerant superconductor can increase flexibility in the system as a whole. Both J_{con} and λ_{st} are regarded as figures indicating feasibility of a particular set of magnet parameters. In particular, high strain conductors allow the use of less stiff structural materials (aluminum alloys rather than stainless steel, for example). High strain conductors also significantly impact attainable field and usable aspect ratio. The analysis allows straightforward calculations of the manner in which the system is affected when parameters are varied.

Mechanical Characterization of Selected Adhesives and Bulk Materials at Liquid Nitrogen and Room Temperatures[17]

This paper presents the results of a series of mechanical tests on selected adhesives and bulk materials. The materials tested are of general interest to designers of magnets for cryogenic service and include several epoxies, a varnish, a B-stage glass cloth, insulation papers, and commercially available fiber reinforced composites. These tests were performed at room temperature (293 K) and at liquid nitrogen temperature (77 K) and include both simple tension tests and lap shear tests with various adherends. The parameters critical to tensile or bond strength were varied as part of the test program. The procedures used to manufacture and test these specimens and the results of the tests are reported in this paper.

7.8.2 Structural Analysis

Much work has been previously reported on the "best" shape for TF coils for tokamaks. W. H. Gray has derived a new coil shape based on a shell approach. The resulting coil shape approaches a circle quite closely for aspect ratios currently under consideration. This concept would result in a very efficient structure for the resistance of out-of-plane loading of TF coils. Additional investigations of this concept are being planned.

As part of the joint U.S.A./U.S.S.R. scientific exchange in fusion, a series of calculations was made on the TF coils for the U.S.S.R. T-10M over a period of three weeks. The ORNL staff interacted with Drs. Churakov and Klimenko to produce results for circular and oval TF coils under normal and perturbed field conditions. During a similar exchange, T. E. Shannon of ORNL Engineering was told while in the U.S.S.R. that the work done by ORNL was highly appreciated and quite useful.

A new approach was developed for the analysis of magnetoelastic stability. The methodology developed results in a force/deflection relationship much like an ordinary stiffness matrix in the finite element method. Work was started to implement this approach into an analysis code.

Bending Free Toroidal Shells for Tokamak Fusion Reactors[18]

Several authors have suggested novel shape for the TF coils of a tokamak fusion reactor. Collectively, these magnet shapes have become referred to as the "Princeton D-coil." This coil shape can be derived by assuming that for a thin conductor to be in a state of "pure tension," its

radius of curvature must be proportional to the toroidal radius. A principal disadvantage of this derivation is that out-of-plane support, a necessary feature in the design of a tokamak fusion reactor, is neglected.

In this paper, a derivation of a bending free toroidal shell for a tokamak fusion reactor is presented. The out-of-plane structure is considered to be an integral part of the fusion reactor, and therefore its shape is optimized to produce a bending free stress distribution. This shape, which is nearly circular for aspect ratios greater than 2.5, is derived by solving the equilibrium, constitutive, and kinematic relationships for a uniform toroidal membrane. This membrane is subjected to a magnetic pressure which is inversely proportional to the square of the toroidal radius. A comparison between this bending free shape and the D-shape is presented.

A Preliminary Structural Analysis of the Toroidal Field Coils for T-10M[19]

A structural analysis of the T-10M tokamak TF coil system has been performed. Two TF coil shapes were proposed, one oval and the other circular. Each TF coil system is composed of 24 coils. The oval TF coil system has a 2.4-m major radius with a minor bore diameter of 2.15 m and a major bore diameter of 3.28 m. The circular TF coil system has a 2.5-m major radius with a 2.2-m bore diameter. The cross sections of both TF coil shapes have rectangular dimensions of 0.4 x 0.26 m with a 0.35- x 0.22-m winding cavity symmetrically placed within the cross section. The current of each coil is 1.75 MA. Either geometry produces a magnetic field of 3.5 T on axis, 2.4 m from the machine center line.

This study (a part of the joint U.S.A./U.S.S.R. scientific exchange) reports the results of a cooperative investigation to determine which TF coil shape operates in a minimum stress configuration. The scope of the analysis covers only the in-plane force distribution produced by the magnetic field.

Based upon the preceding conditions, the oval TF coil shape appears to be superior to the circular. Further, the oval TF coil shape in its present design has a significant safety margin between working and yield stress under normal operating conditions. The circular design, however, is less sensitive to magnetic field perturbations which may be encountered in proof testing.

Magnetoelastic Energy Calculations for Finite Element Analysis of Superconductors[20]

It has been shown that the high current density and magnetic flux density associated with superconductors can make the magnetoelastic energy a significant portion of the total energy in a structural system. The present work offers a procedure for evaluating this magnetoelastic energy for use in the finite element analysis of the structural dynamics and stability of the superconductor. A simple, special case of the element matrices is illustrated.

Finite Element Stress Analysis of Orthotropic Solenoids[21]

The mechanical behavior of superconducting magnets deviates from isotropy due to their construction techniques, which involve the layering of superconductor, insulation, and sometimes structural reinforcement within the windings. This paper describes a finite element stress analysis which has been extended to consider the effects of orthotropic material properties, as well as differential thermal contraction and spatially varying magnetic body forces. The procedure is applicable to all arbitrarily shaped axisymmetric magnets. A comparison between the finite element stress analysis and an analytical solution for a rotationally transversely isotropic solenoid is presented. Good agreement is obtained within the limits of the analytical solution.

7.8.3 Support Calculations

Personnel and equipment were made available during the check-out phase of ISX-A to ascertain the agreement between predicted and actual mechanical behavior due to electromagnetic loads. The close interaction between the experiment operators and Magnetics and Superconductivity Section personnel with support from ORNL Engineering was instrumental in the rapid startup of this tokamak.

The existence of the iron yoke in the ohmic heating circuit of ISX results in appreciable contributions to the magnetic fields, and calculations using the ORNL version of RHEL's GFUN-3D were made to evaluate this effect. Both static and transient experimental data were gathered for comparison purposes. In the course of these comparisons the effect of grain orientation in the iron laminations was identified. In recognition of the limitations of the validity of the GFUN-3D results for this type of problem, work was begun to establish a transient/anisotropic saturable material analysis capability.

Detailed structural analysis was performed on the LCS background coil support structure and LCS coil case.

A number of contractor reviews were attended and documents reviewed in this project. Section staff assisted in the decision making activity of the Large Coil Program and performed analyses of the effects of fringe fields on ferromagnetic materials in the vacinity of the LCP facility.

Magnetic Field Computations for ISX Using GFUN-3D[22]

This paper presents a comparison between measured magnetic fields and the magnetic fields calculated by the three-dimensional computer program GFUN-3D for ISX. Several iron models are considered, ranging in sophistication from 50 to 222 tetrahedra iron elements. The effects of air gaps and the efforts made to simulate effects of grain orientation and packing factor are detailed. The results obtained are compared with the measured magnetic fields, and explanations are presented to account for the variations which occur.

Structural Analysis of the Large Coil Segment Test[23]

The purpose of the LCS test is to verify that the present knowledge of superconducting composite conductors is adequate for designing the large coils which are proposed for future tokamak fusion reactors. Background coils will be used to impose high magnetic fields locally on a test coil to simulate the external fields expected in a TF coil configuration. Due to offset centerlines between the LCS and the background coil, large magnetic forces will be produced and tend to pull the background coils toward the test coil centerline.

The purpose of this study was to predict these loads, resulting displacements, and stresses in the LCS and background coil support structure, and thus to ensure that an adequate margin of safety is provided in each structure. Prediction of these displacements and stress patterns is particularly important since these parameters will be monitored during the test and used as criteria for higher levels of testing (i.e., before applying full current, measured stress at lower levels must correlate with predictions).

7.9 EDDY CURRENT CALCULATIONS

A package of 3-D eddy current code was developed with the capability to handle calculations of pulse coils with arbitrary coil shape and waveform.

The existence of a surface barrier in a conductor significantly modifies the flow pattern of eddy currents. This surface effect is determined by solving a singular 3-D Laplace equation with Neumann boundary condition.

A local field code has been modified to include calculation of vector potential due to circular arc and straight conductors of rectangular cross section. One application was to

estimate the eddy current-induced loss and mechanical loadings in the TNS vacuum tank due to the simultaneous discharge of three TNS coils.

The eddy current code development last year for thin plates was limited to the pulse field of a ramped dipole. This code has also been updated to handle a field due to coils of arbitrary shape and pulse waveform.

7.9.1 A Perturbation-Polynomial Expansion Formulation of 3-D Eddy Current Problems[24]

A pulsed magnetic field is required in tokamak fusion machines, but eddy currents produced by the pulsed field may produce undesirable effects (e.g., in the mechanical loading of the vacuum vessel, heating in the magnet and structure, and field ripple in the plasma region). A method was developed earlier to calculate the eddy current produced in a thin object by the linear ramping of a magnetic dipole. We report here extension of the method to calculate the eddy current induced in three-dimensional objects and by pulse coils of general shape. Examples are given.

7.10 DESIGN PROJECTS

7.10.1 EBTR

EBTR magnets are designed to be cryostable and consistent with present and near-term technology. The emphasis in this year's EBTR magnet design was in optimization, improvements, and more detailed design. Some highlights of the design are listed below.

Without violating the plasma constraints, the coil dimension has been optimized to give the maximum access space between coils. This eases the problem of remote handling, divertor design, and diagnostics. The axial length of each coil is now reduced to 2.1 m.

Conductors are made of monolithic multifilamentary NbTi composite with built-up copper strips. More copper and shorter slot size are used in the strip to improve cryostability and mechanical stability. The peak compressive stress in the winding is now reduced to 7.6 ksi.

Magnets are circular coils made of tightly wound pancakes with pool boiling cooling. A fabrication procedure for coil winding and the attachment of electrical leads and cryogenic piping has been worked out. A detailed stress profile was also computed. Peak stress and strain in the winding are respectively 19.7 ksi and 0.11%, both of which are within the design limit of materials used.

The cryogenic load is increased to 63.4 kW at 4.2 K (31.7 MW at 300 K), mainly due to the new eccentric shield design and the large conduction surface area structure support. The vapor-cooled lead loss is, however, significantly reduced by avoiding coil segmentation.

A flexible electrical connection scheme was adopted. Coils are discharged in different ways according to whether the discharge is normal, a quench, or a lead/conductor failure. The out-of-plane load during quench is minimized by reconnecting coils via switching into groups which interleave with each other.

Toroidal Magnet System Conceptual Design for the ELMO Bumpy Torus Reactor[25]

The EBTR is a fusion reactor device based on the concept of toroidally linked mirrors. To minimize engineering uncertainties, the EBTR superconducting magnet system is designed so that it could be built with existing or near-term technology. The design uses identical coils in standard modules, thus facilitating commercialization. The reference design uses 48 modules and produces 4000 MW(th).

Each of the 48 TF coils has an inner radius of 2.95 m, axial length of 2.6 m, and current density in the winding of 1.5 kA/cm^2. The coils produce a peak field of 4.5 T along the plasma center line, a mirror ratio of 1.8, and a peak field in the winding of 7.3 T. All coils are

circular in shape, with pancake-wound construction and natural convection pool boiling cooling. EBTR is expected to operate in steady state, and the TF coils are not exposed to pulsed fields.

Cryostability of the magnet is achieved by building up monolithic multifilamentary NbTi composite with formed copper strips. The copper strips are punched with slots to increase the wetted surface area and to improve coolant circulation. A high operating current (25 kA) was chosen to hold the terminal voltage during discharge to 2 kV, and four conductors are wound in parallel to maintain a reasonably small conductor and large heat transfer surface. The four conductors are interleaved in a spiral fashion such that inductances are equalized and the total current is evenly divided between conductors. The design provides 35% helium space, interconnected helium passages with a minimum cross-sectional dimension of 0.25 cm, and a surface heat flux of 0.14 W/cm^2 when the entire current is in the stabilizer. Quench detection is based on voltage taps, with pickup coils on the current leads of all power supplies to compensate the inductive voltages and leave only the resistive component. Eight consecutive magnets are charged with a single power supply. Each coil is individually protected by an external dump resistor, which is switched into the circuit on the detection of a quench in any coil.

7.10.2 TNS

In the ORNL/Westinghouse TNS effort, our role was to provide program guidance and consultation and to review the technical work done at Westinghouse. In addition to this, the work on iron cores for large tokamak devices was begun as an alternative to the air core systems used in most large-scale tokamak studies. It appears at this time that the iron core system will allow design simplification and reduce the power requirements for the poloidal systems.

A Comparison Between an Air Core and an Iron Core Ohmic Heating System for The Next Step

Conceptual studies of EPR and TNS tokamak devices have shown that air core poloidal coil systems are expensive and may require the development of large superconducting pulse magnets; development of reliable, low cost, high power switches; and power supply options in addition to large SCR systems. These studies indicate that a considerable fraction of the total capital cost of the device will be in the power supplies and magnets of the poloidal coil system. The high cost of these systems is due to the very large power required to initiate the plasma and the smaller, but still large, power required in the OH system to establish plasma current. There is considerable work being done on alternative ways to initiate the plasma with lower power requirements, such as small radius startup, closely coupled equilibrium coils, and microwave heating. This paper considers initiating the plasma with a high voltage induced by the OH system.

Another way to reduce the required power that may be used with all of the options just mentioned is to use an iron core that forms a complete magnetic circuit around the plasma. Smaller tokamak devices such as ORMAK, ISX, and TEXT use an iron core to improve the coupling between the plasma and the PF magnets, and a saturated iron core is proposed for JET. The FCT concepts put forward by ORNL allow devices to be built with aspect ratios on the order of four to five, which leaves considerable space in the bore of the device for an iron core to be operated in a less saturated state than in the JET proposal.

The purpose of this paper is to compare the costs of the major components of an air core and iron core OH system. The comparison will be done for the OH system by replacing the air core OH magnets with a set of magnets to operate an

iron core. Both air and iron core systems will be operated in the same mode, i.e., they will be required to supply the same volt-seconds on the same schedule and will use the same equilibrium field coil system. (The comparison is not between two optimized systems but between two systems which differ only in the type of OH system they use.) The comparison will be made on the basis of the peak power required in the OH power supply circuits necessary for initiation of the plasma and on the basis of the peak stored magnetic energy.

7.10.3 EBT-S

It is desired to test the effect on the plasma of changing the torus aspect ratio of the existing EBT-S machine without changing the major radius. This can be simulated by adding a set of ARE coils. By adjusting the current in the ARE coils, one can change the field configuration and thus the apparent aspect ratio of the torus, although the design options are restricted because EBT was constructed before the ARE coil concept was conceived. Several arrangements and shapes of magnets have been investigated and the most promising one chosen. The magnetic design of a pair of copper canted ARE coils inside each of the 24 microwave cavities is nearing completion, but problems of spatial interference still exist.

7.10.4 EBT-II, EBT-IIA

The mirror coil magnetic design was done for several EBT-II models as the requirements were refined. Several months ago the magnetic design had been modified so that the mirror coils appeared to be just within the state of the art for superconducting solenoids. Now EBT-II is to have ARE coils and have its name changed to EBT-IIA. This magnet system composed of both mirror and ARE coils appears to be much more difficult, and the entire magnet system is being reconsidered. The new problems include asymmetric loading on the mirror coils, greater difficulty in reducing field errors to a minimum, restricted access to the machine because of the presence of the ARE coils, and more complicated machine assembly; furthermore, if the ARE coils are resistive, their design will be limited by their power consumption and there will be a requirement to restrain magnetic forces between coils at cryogenic and r temperatures.

The coil parameters for one version are listed in Table 7.1 and the refrigeration loads in Table 7.2. A more complete description of EBT-II is presented elsewhere in this annual report.

Table 7.1. EBT-II magnet dimensions

Number of coils (N)	48
Major radius of torus (R_o)	4.88 m
Mirror ratio (MR)	2.249
Magnet coil inner radius (A_1)	0.176 m
Magnet coil outer radius (A_2)	0.275 m
Total coil width (B)	0.213 m
Current (I)	1500 A
Current density (J)	9500 A/cm^2

Table 7.2. Summary of EBT-II refrigeration requirements

Liquefaction requirement	
Lead cooling (4.2-300 K)	202 liters/hr
Refrigeration required at 3.5-K helium (W)	
Joint resistance (3 per coil)	~4
Thermal radiation (pipes and valves)	400
Gamma radiation losses	50
Structural supports	35
Instrument leads	30
	~520 W
Including 50% contingency, refrigeration load is	300 liters/hr 750 W
Nitrogen requirements (steady state)	
Cold wall temperature cooling	760 W (18 liters/hr)
Conduction losses	240 W (6 liters/hr)
Refrigerator precooling	
Total LN_2 usage with contingency	(487 litrrs/hr)

7.10.5 Large Coil Program

The Large Coil Program was established by DMFE early in 1976 as the central element of the U.S. program for the development of superconducting toroidal magnets for tokamaks. The objectives and rationale of the LCP are described briefly in last year's annual report[27] and more fully in the *Plan for the Large Coil Program*.[28] In 1977 the program contracted with three industrial teams to design and construct three different tokamak-relevant test coils. These will be assembled (with three coils to be procured later) in the Large Coil Test Facility at ORNL and fully tested to determine and demonstrate their operational characteristics. With the exception of plasma effects, every aspect of the tokamak TF coils and their environment will be either reproduced, approximated, or simulated.

Requirements for the test coils, based originally on EPR studies and later on TNS studies at ORNL and elsewhere, were incorporated in technical specifications that were issued in January 1978. The first column of Table 7.3 lists major items of interest for TNS coils. The second shows the consensus values of these parameters where the various TNS studies were in agreement, and a range otherwise. The third column shows the requirements of the LCP coil specifications. The difference in bore between the listed TNS and the LCP requirements is a factor of two, which was considered by the LCP, DMFE, and their advisory panels as being a reasonably sized scaling step to be made after LCP results were known. The conductor and winding cross section are full-size, and current density is the same as in TNS concepts. The peak field of 8 T at the conductor in the LCP specification was chosen as being the largest step that could be prudently taken from the existing state of the art (near the upper limit with NbTi at 4.2 K). Use of either NbTi or Nb_3Sn conductor was allowed in order to encourage development of the latter, which is capable of higher fields but is less widely used. (In anticipation of later procurement and testing of higher field coils, the LCTF design was required to be adaptable for tests up to 12-T peak field.) The choice of pulsed field for the LCP tests was necessarily a compromise, since predictions of pulsed field to which TNS coils will be exposed vary by an order of magnitude depending on the tokamak design. The LCP value of 0.14 T/sec is roughly at the logarithmic midpoint of the range.

Proposals for the conceptual design, detailed design, verification testing, and construction necessary for the production of an LCP test coil were received in February 1978 from five industrial teams. The proposals were judged by a panel of specialists on the basis of a preexisting set of criteria and weighting factors. The successful proposals were submitted by General Dynamics/Convair Division, supported by Intermagnetics General Corporation and Magnetic Engineering Associates; General Electric, supported by Intermagnetics General Corporation and Chicago Bridge and Iron Nuclear Company; and Westinghouse Electric Company, supported by Airco. Although all three teams are working to the same set of performance specifications, these specifications deliberately avoided foreclosing the contractor's design options in the expectation that the LCP coils would address a variety of promising design approaches. That this was successful is shown by Table 7.4, which compares the major design features of the three conceptual designs. Originally the Westinghouse reference design used NbTi, with Nb_3Sn as an alternate. Westinghouse was subsequently instructed to proceed with the alternate. Fuller descriptions of the conceptual designs of the three coils and the LCTF are given in the twelve papers comprising Session O of the Seventh Symposium on Engineering Problems of Fusion Research, Knoxville, Tennessee, October 25-28, 1977.[29]

All three industrial teams completed conceptual designs in 1977 and began verification testing of key features. Each also prepared a detailed schedule, revised from the original proposal to account for anticipated funding constraints. Delivery dates were thereby shifted from 1979 to 1980 and 1981. (Part of the stretch-out of the Westinghouse schedule was

Table 7.3. Test coil specifications aim at TNS requirements

	TNS requirement	LCP specification
Shape	Minimum bending D or oval	Minimum bending D or slight modification
Size	~5 x 7 m	2.5 x 3.5 m
Field distribution	Toroidal array with low aspect ratio	Toroidal array with low aspect ratio
Peak toroidal field	8-12 T	8 T
Ampere-turns	~7 x 10^6	~7 x 10^6 (implied)
Conductor current	10-15 kA	10-15 kA
Pulsed field	0.05-0.5 T/sec	0.14 T/sec
Stability	Cryostable	Cryostable (recovery from half-turn normalcy is a minimum requirement)
Cooling	Helium, either pool boiling or forced flow	Helium, either pool boiling or forced flow
Radiation heating	Up to 8 x 10^{-4} W/cm^3 (actual)	Up to 8 x 10^{-4} W/cm^3 (simulated)
Radiation damage	4 x 10^{16} neutrons/cm^2 (E < 0.1 MeV) 6 x 10^6 rad	Assume 5 x 10^{16} neutrons/cm^2 in stability analysis (not in test), 1 x 10^7 rad in insulation selection
Cooldown time	120 hr	120 hr
Warmup time	60 hr	60 hr
Design life	10 years, including 10^5 pulse field cycles	10 years, including 50 thermal cycles, 300 charging cycles, 3 x 10^6 pulse field applications, and operation in alternate modes for testing

Table 7.4. LCP test coil concepts

Design	General Dynamics/Convair	General Electric	Westinghouse
Conductor material	NbTi	NbTi	Nb_3Sn
Helium conditions	Pool boiling, 4.2 K	Pool boiling, 4.2 K	Supercritical forced flow 4-6 K
Winding concept	Cable soldered in extended surface stabilizer, layer wound	Conductor subelements spiralled around stainless steel strip, pancake wound	Compacted cable in conduit wound in spiral grooves in pancake plates
Structure concept	Coil case	Coil case	Plates bolted together
Structural material	Type 304L stainless steel	Type 316LN stainless steel	Aluminum 2219-T87

associated with the change from NbTi to Nb_3Sn conductor, which involved additional development.)

As described in last year's progress report, a six-coil compact torus was chosen as the optimum arrangement for coil testing. (Fewer coils can be tested by the use of spacers.) Figure 7.1 shows the test stand, which will be located inside an 11-m (35-ft) cylindrical vacuum vessel to provide thermal isolation. A conceptual design of the complete facility including all support systems (to be located in Building 9204-1, Y-12 Plant) was completed, cost estimates were made, and a major project proposal was submitted to DMFE. Approval was given for construction of those

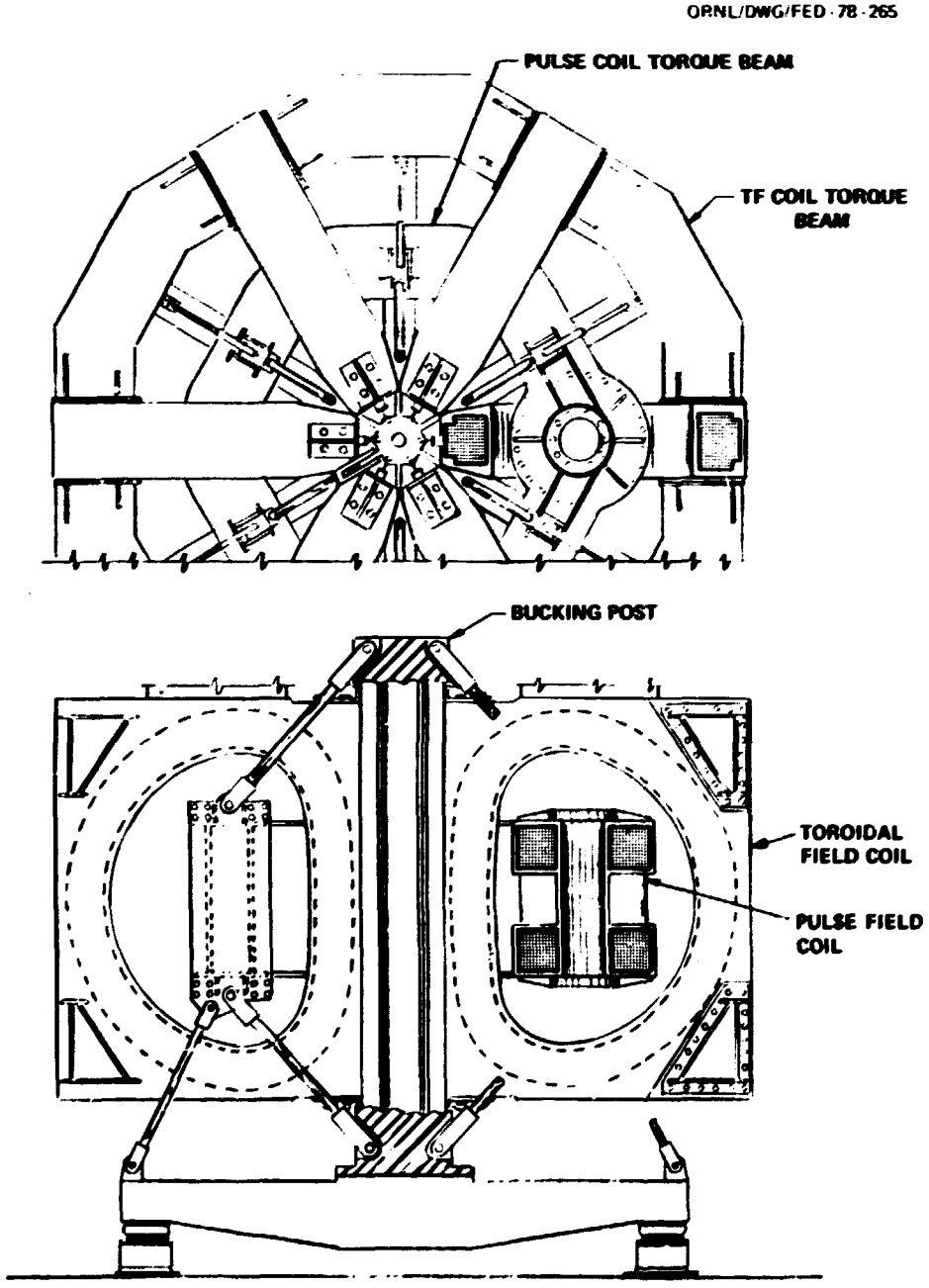

Fig. 7.1. LCTF test stand.

portions of the facility required for testing three coils, with the understanding that the additional equipment for testing six coils in pulsed fields would be approved later. Specifications were prepared and a contract was competitively awarded for design and construction of the large vacuum vessel. Part of the stainless steel plate for the vessel was also procured.

Through the International Energy Agency an implementing agreement for a program of research and development on superconducting magnets for fusion was drawn up and was signed by the U.S. and EURATOM in October. The implementing agreement provides for annexes, each of which will define a separate task, including the obligations of the participants to that annex and information to be shared among the participants. The agreement also sets up an executive committee composed of a representative from each participant of any annex. The first annex defines the Large Coil Task, in which the U.S. will act as operating agent for the LCTF and each other participant will furnish at least one coil for testing in the LCTF. The participants will share specified categories of information from the manufacture and testing of all coils, and each will bear its own cost. Thus the agreement not only stimulates cross-fertilization of ideas and technology but also provides each participant with detailed information on design, manufacture, and performance of several different coils. It is planned that the U.S. will supply three coils and other participants one each. (In addition to EURATOM, Japan and Switzerland expressed their intentions of participating.)

The Magnetics and Superconductivity Section assisted the LCP as called upon by providing analytical tools, computational aid, technical advice, results of pertinent small-scale experiments, and interaction with the three industrial subcontractors. The work involved both the test coils and the test facility. Particular items were: presentations concerning the coil specifications at the bidders' conference in January; aid in bid evaluations; post-award discussions with the successful and unsuccessful bidders; preparation and revision of the program plan for the LCP and its presentations to OFE; Phase I midterm and final reviews with each of the contractors, including joint "splinter group" meetings with the contractors and posing written questions for the contractors' consideration; participation in a workshop on structure with the three contractors; and conducting a workshop on forced flow conductor testing with Westinghouse.

Design of Superconducting Toroidal Magnet Coils and Testing Facility in the U.S.A.[3]

The U.S. plans to achieve controlled ignition of a D-T plasma in a device of the tokamak type in the next decade. It is required that reliable and economic superconducting coil designs be developed and proven in time for incorporation in this machine. Several different designs of superconducting coils are being evaluated for use in the toroidal magnet of this machine, which, according to the designs from both ORNL and General Atomic Company, will have approximately 18 TF coils of 5 x 7.5-m bore and a total stored energy of about 10 GJ. Part of the OH and plasma shaping coils are inside the TF coils, permitting designs with relatively low pulse fields (due almost entirely to the vertical plasma positioning field) at the windings of the TF coils. In the U.S. Large Coil Program, three industrial teams are presently designing test coils to general specifications prepared by ORNL with guidance from DOE. Each test coil is approximately half the bore size of reactor coils, is oval- or D-shaped, and has a bore of 2.5 x 3.5 m. The dimensions and operating requirements are identical for all test coils. The coils are designed to produce a peak field of at least 8 T at the winding of a selected coil operated at its design current. This condition is met when the selected coil is operated at design current in a compact toroidal array of six coils, with the other five coils being operated at 0.8 of their design current. The six coils are of three different designs;

both pool boiling and forced flow designs are included. The coils are housed in a single large vacuum chamber for economy and testing convenience. Auxiliary coils provide a pulse field over the test coil winding volume. This auxiliary system is designed to produce a pulse field which rises to a peak of 0.14 T in 1 sec. With the exception of material damage due to neutron irradiation, all reactor requirements and environments will be either duplicated, approximated, or simulated. The test facility is being designed to accept coils producing up to 12 T in later phases of the program.

7.10.6 Magnetic Field Codes

When a number of magnetic systems must be investigated quickly, it is desirable to have a set of magnetic field codes that operate from a unified data base (UDB). The UDB is a single collection of data sets used by each code in the system. This is important because the same data used to produce the 3-D plots of the magnet configuration (to check input magnet system geometry visually) are also used to calculate the field and forces. The code allows solenoids and noncircular coils to be mixed in the same magnetic system. The suite of codes provides the following features (at this time the system cannot handle problems with iron):

- 3-D plots of magnet configurations (hidden lines removed),
- magnetic field and force calculations,
- 2-D and 3-D flux line plots, and
- node and element generation of magnet windings for finite element structural analysis.

7.10.7 Superconducting Magnet Development for Tokamaks[31]

The tokamak is a toroidal plasma machine which is the main line approach of DOE/OFE to obtain controlled thermonuclear power. Experimental power reactors based on tokamaks have been designed by ORNL and others. All use superconducting toroidal dc magnetic field systems (plasma confinement), and many also use superconducting poloidal pulsed field systems (plasma ohmic heating and shaping). The Next Step in the U.S. Fusion Program precedes the EPR and is an ignition test reactor which will also employ superconducting magnet systems. The present state of the art and rate of technological progress of superconducting magnet technology will be compared with the requirements of the next generation of fusion machines in order to provide a basis for evaluating the scope of the needed development program. A development program is under way to provide the physics understanding and engineering data necessary to design, fabricate, and test large superconducting magnet systems which will serve as model systems. The required TNS confining field system is a toroidal array of 14 to 20 identical coils having an average bore of 5 to 7 m and operating at a maximum field of 8 to 12 T. The magnetic force on each coil tending to push it to the torus axis is extremely large, and because of the superimposed pulsed fields of the OH and vertical field systems, the out-of-plane forces tending to warp and tilt the coil are also significant. The pulsed fields also produce ac losses in the conductor and structure, appreciably influencing the coil design and the required refrigeration capacity. The pulsed field magnet systems are arrays of nonidentical coils having the torus major axis as their axis of symmetry, with the bulk of the amp-turns in a central solenoid about 3 to 5 m in diameter and producing a maximum field of about 5 T changing at a rate of 5 T/sec. Even though the pulse systems are axisymmetric, the coils outside the central solenoid are subjected to bending loads due to the presence of the TF coils. Because the coil bores, stored energy, and rate and amplitude of the field change are all large, the challenge of the pulsed coil system, particularly with respect to power supplies, structure (probably nonmetallic), and stability (preferably cryostatic), may be even greater than for the TF system. For all tokamak coil systems, the large stored energy, inductively coupled magnets, and the need for long-term, reliable

performance and safe discharge provide a challenge to the designer of the protection system. Decisions for the coil designer include: superconductor material – NbTi or Nb_3Sn; conductor configuration – monolithic or cable; helium coolant condition – boiling, supercritical, or superfluid; helium circulation – natural convection or forced flow; type of winding – layer or pancake; structural material – metallic or nonmetallic; structural reinforcement – distributed or lumped; and, for the toroidal coils, shape of coil – modified D or oval. The final choices can be verified and the design optimized only after much testing at a significant size, but the existence of viable options provides optimism that the program will be successful.

7.10.8 Development of Superconducting Magnet Systems for Fusion Power Generators[32]

Of the many concepts of magnetic confinement being pursued at the present time, the tokamak fusion machine is the most promising for extrapolation to a power producing reactor. The recent conceptual design studies on tokamak experimental power reactors by ORNL and others have led for the first time to a fairly clear understanding of the requirements for both the toroidal (or confining) and poloidal (or plasma heating) magnet systems.

It has been generally acknowledged that the TF system and most, if not all, of the PF system will have to employ superconducting windings if net power is to be obtained economically from a thermonuclear reactor. Now it is recognized that large superconducting magnet systems must be developed for TNS, a D-T ignition test reactor. In order to provide a basis for evaluating the scope of the needed development program, both the rate of technological advancement and the present state of the art of superconducting magnet technology will be compared with the requirements for TNS.

REFERENCES

1. W. A. Fietz, abstract of paper published in *Proc. 7th Symp. on Engineering Problems of Fusion Research*, Vol. II, pp. 1278-81 (1977).
2. J. R. Miller, L. Dresner, and J. W. Lue, *Proc. 7th Symp. on Engineering Problems of Fusion Research*, Vol. II, pp. 1282-87 (1977).
3. J. W. Lue, J. R. Miller, and L. Dresner, "Vapor Locking as a Limitation to the Stability of Composite Conductors Cooled by Boiling Helium," to be published in Adv. Cryog. Eng.
4. L. Dresner and J. W. Lue, "Design of Force Cooled Conductors for Large Fusion Magnets," paper presented at the 6th Int. Conf. on Magnet Technology, Bratislava, Czechoslovakia, August 29-September 2, 1977; proceedings to be published.
5. L. Dresner, *The Effect of Flux Flow on Self-Field Instability*, ORNL/TM-5986, Oak Ridge, Tennessee (August 1977).
6. L. Dresner, *Proc. 7th Symp. on Engineering Problems of Fusion Research*, Vol. I, pp. 719-22 (1977).
7. S. S. Shen and R. E. Schwall, abstract of paper published in *Proc. 7th Symp. on Engineering Problems of Fusion Research*, Vol. II, pp. 1293-96 (1977).
8. J. R. Miller and S. S. Shen, abstract of paper published in *Proc. 7th Symp. on Engineering Problems of Fusion Research*, pp. 1297-1300 (1977).
9. R. E. Schwall, S. S. Shen, J. W. Lue, J. R. Miller, and H. T. Yeh, abstract of paper presented at the Cryogenic Engineering Conference, Boulder, Colorado, August 2-5, 1977.
10. M. S. Walker and B. A. Zeitlin (Intermagnetics General Corporation), and R. E. Schwall, abstract of paper published in *Proc. 7th Symp. on Engineering Problems of Fusion Research*, Vol. II, pp. 1310-14 (1977).

11. R. E. Schwall, W. H. Gray, and C. J. Long, abstract of paper published in *Proc. 7th Symp. on Engineering Problems of Fusion Research*, Vol. II, pp. 1326-28 (1977).
12. P. L. Walstrom, P. B. Burn, B. E. Nelson, T. L. Ryan, and P. B. Wysor, abstract of paper published in *Proc. 7th Symp. on Engineering Problems of Fusion Research*, Vol. I, pp. 354-59 (1977).
13. R. L. Brown, abstract of paper published in *Proc. 7th Symp. on Engineering Problems of Fusion Research*, Vol. I, pp. 723-27 (1977).
14. C. G. Lawson and J. P. Kois, abstract of paper published in *Proc. 7th Symp. on Engineering Problems of Fusion Research*, Vol. II, pp. 966-68 (1977).
15. C. G. Lawson and J. R. May (Grumman Aerospace Corporation), abstract of paper published in *Proc. 7th Symp. on Engineering Problems of Fusion Research*, Vol. I, pp. 737-40 (1977).
16. C. J. Long, abstract of paper published in *Proc. 7th Symp. on Engineering Problems of Fusion Research*, Vol. I, pp. 776-79 (1977).
17. C. M. Fitzpatrick and W. C. T. Stoddart, abstract of paper published in *Proc. 7th Symp. on Engineering Problems of Fusion Research*, Vol. II, pp. 1025-29 (1977).
18. W. H. Gray, W. C. T. Stoddart, and J. E. Akin, abstract of paper published in *Proc. 7th Symp. on Engineering Problems of Fusion Research*, Vol. I, pp. 855-61 (1977).
19. W. H. Gray, J. K. Ballou, W. C. T. Stoddart, G. F. Churakov (Efremov Institute, Leningrad, U.S.S.R.), and E. Y. Klimenko (Kurchatov Institute, Moscow, U.S.S.R.), abstract of paper published in *Proc. 7th Symp. on Engineering Problems of Fusion Research*, Vol. I, pp. 756-61 (1977).
20. J. E. Akin and W. C. T. Stoddart, abstract of paper published in *Proc. 7th Symp. on Engineering Problems of Fusion Research*, Vol. I, pp. 772-75 (1977).
21. W. H. Gray and J. E. Akin, abstract of paper published in *Proc. 7th Symp. on Engineering Problems of Fusion Research*, Vol. I, pp. 851-53 (1977).
22. W. D. Cain, abstract of paper published in *Proc. 7th Symp. on Engineering Problems of Fusion Research*, Vol. II, pp. 1362-66 (1977).
23. W. D. Cain, W. H. Gray, W. R. Hendricn, B. E. Nelson, and W. C. T. Stoddart, abstract of paper published in *Proc. 7th Symp. on Engineering Problems of Fusion Research*, Vol. I, pp. 751-55 (1977).
24. H. T. Yeh, abstract of paper published in *Proc. 7th Symp. on Engineering Problems of Fusion Research*, Vol. II, pp. 1381-85 (1977).
25. J. N. Luton and H. T. Yeh, abstract of paper presented at the 6th Int. Conf. on Magnet Technology, Bratislava, Czechoslovakia, August 29-September 2, 1977; proceedings to be published.
26. J. K. Ballou and J. H. Schultz (Westinghouse Electric Corporation), abstract of paper published in *Proc. 7th Symp. on Engineering Problems of Fusion Research*, Vol. II, pp. 1605-07 (1977).
27. *Fusion Energy Division Annual Progress Report for Period Ending December 31 1977*, ORNL-5275, pp. 273-280, Oak Ridge, Tennessee (June 1977).
28. P. N. Haubenreich, W. C. Anderson, J. N. Luton, and P. B. Thompson, *Plan for the Large Coil Program*, ORNL/TM-5824, Oak Ridge, Tennessee (February 1977).
29. *Proceedings*, 7th Symp. on Engineering Problems of Fusion Research, Knoxville, Tennessee, October 25-28, 1977.
30. J. N. Luton, P. N. Haubenreich, and P. B. Thompson, abstract of paper presented at the 6th Int. Conf. on Magnet Technology, Bratislava, Czechoslovakia, August 29-September 2, 1977; proceedings to be published.
31. J. N. Luton and M. S. Lubell, abstract of paper presented at the Int. Magnetics Conf., Los Angeles, California, June 6-9, 1977.
32. M. S. Lubell, abstract of paper presented at the World Electrochemical Conf., Moscow, U.S.S.R., June 21-25, 1977.

ADVANCED SYSTEMS

D. Steiner, Manager

M. Roberts, Deputy Manager

S. E. Attenberger[1]
J. K. Ballou[2]
J. M. Barnes[2]
D. B. Batchelor[3]
W. R. Becraft[4]
E. S. Bettis[5]
R. N. Cherdack[6]
R. A. Dandl[7]
Engineering Design Team[8]
C. A. Flanagan, Project Mgr.
T. C. Varljen, Eng. Mgr.
G. Gibson, Applied Physics Mgr.
J. W. French, Mechanical Eng. Mgr.
F. M. Heck, Electrical Eng. Mgr.
W. R. Hamilton[9]
C. L. Hedrick, Jr.[3]
T. J. Huxford[1]
G. A. Krist[2]
K. C. Liu[3]
J. W. Lue[10]
D. G. McAlees[11]
F. B. Marcus[12]
J. May[13]
H. E. McCoy[9]
A. T. Mense[2]
P. Mohr[14]
L. W. Owen[2]
Y-K. M. Peng[3]
R. L. Reid[15]
J. A. Rome[3]
R. T. Santoro[3]
G. Schilling[3,††]
J. L. Scott[2]
T. E. Shannon
P. T. Spampinato[13]
N. A. Uckan[3]
J. S. Watson[2]
H. L. Watts[2]
W. M. Wells[1]
R. W. Werner[13]
F. W. Wiffen[9]
R. B. Wysor[2]
H. T. Yeh[2]

---

1. Computer Sciences Division.
2. Magnetics & Superconductivity Section.
3. Plasma Theory Section.
4. General Electric Co., Philadelphia, Pennsylvania.
5. UCC-ND Engineering.
6. Burns & Roe, Paramus, New Jersey.
7. EBT Program.
8. Westinghouse Electric Co., Pittsburgh, Pennsylvania.
9. Metals and Ceramics Division.
10. Consultant, Exxon Nuclear Co., Inc.
11. Grumman Aerospace Corp., Bethpage, New York.
12. Visiting Scientist, Lawrence Livermore Laboratory.
13. Neutron Physics Division.
14. Plasma Technology Section.
15. Chemical Technology Division.

†Present address: General Atomic Co., San Diego, California.

††Present address: Princeton Plasma Physics Laboratory, Princeton, New Jersey.

Abstract. The Advanced Systems Program includes three major activities: (1) the TNS program, (2) the Fusion Power Demonstration Study, and (3) the ELMO Bumpy Torus Reactor (EBTR) Study.

The Next Step (TNS) Program. The TNS program established by DOE's Office of Fusion Energy at ORNL in early 1976 has two principal objectives:

(1) to implement in the next decade a facility with a fusion reactor core that can be extrapolated to an economically viable fusion reactor, and
(2) to provide a near-term means of focusing the efforts of the national fusion program to achieve the first objective.

During the FY 1977 period the Oak Ridge TNS program pursued these objectives through efforts in three broad areas: plasma engineering, systems modeling, and program planning.

Based on the findings of the FY 1977 efforts, it has been judged that continued activities in the Oak Ridge TNS program should be directed toward preconceptual design with particular emphasis placed on engineering feasibility. As a point of departure for the FY 1978 activities we selected a baseline design based on the efforts of last year. The baseline design represents both the culmination of the FY 1977 activity and the starting point for the FY 1978 preconceptual design activity.

Fusion Power Demonstration Study. The major emphasis of the Oak Ridge Fusion Power Demonstration Study in FY 1977 was in the application of current and near-term technology as the most logical path to near-term demonstration of tokamak fusion power. In addition we pursued a number of concepts to simplify the tokamak reactor and thus make it more acceptable to the utility industry as a future source of energy. These concepts focus on the areas having the greatest overall impact on reactor feasibility: overall size and power output, remote maintenance considerations, electrical power supplies, blanket design, and economics.

Two specific recommendations resulting from the FY 1977 study were selected for an in-depth design study in FY 1978 to evaluate engineering feasibility: (1) the design of a blanket system for a fusion reactor based on stainless steel as the structural material, liquid lithium as the breeding material, and helium gas as the coolant; and (2) an evaluation of the committed-site, multiple-unit concept as a strategy for carrying out the various phases of fusion power demonstration. The engineering is being subcontracted to private industry under ORNL management to get outside expertise in power plant technology.

ELMO Bumpy Torus Reactor (EBTR) Study. The experimental results from EBT have motivated a consideration of the EBT concept as the basis for a potential reactor. This study played a substantial role over the past several years in the development of the EBT concept into a most promising alternative for fusion power. Since the first round of conceptual EBT reactor design in FY 1976, there has been considerable progress in design improvements which incorporate increased understanding from plasma research.

A power producing EBTR system is especially attractive from the viewpoint of reactor design because of its steady-state operation at high plasma pressure, its modular construction, its relatively large aspect ratio, and its favorable geometry for ease of maintenance. On the basis of trade-off studies among the plasma physics requirements and uncertainties, engineering design, and technological capabilities, a self-consistent set of plasma parameters and a range of machine characteristics have been obtained. An economic evaluation of the EBTR indicates that its capital costs are comparable to those of a tokamak reactor.

8.1 THE NEXT STEP PROGRAM

TNS, The Next Step after the Tokamak Fusion Test Reactor, is intended to be a reactor core experiment forcing fusion technology. In order to place our TNS program in perspective, it is useful to consider the evolution of our advanced systems studies. Previous advanced systems studies started with point designs (CRMAK F/BX I and II),[1] explored the design issues of the tokamak Experimental Power Reactor scoping studies,[2] and culminated in an evaluated EPR reference design.[3] With this basis, the TNS activities were directed at characterizing the design space between TFTR and EPR with a fundamental emphasis on higher beta plasma systems than previously projected, i.e., $\bar{\beta} \sim$ 5-10% as compared with 1-3%. The orientation toward smaller sized, higher beta systems rather than larger systems at the lower beta has come from an engineering judgment that the larger systems are both mechanically and economically impractical. This judgment was quantified in our Fusion Power Demonstration Study.[4] The characterization of this TFTR-EPR design space has proceeded by plasma engineering investigations of the dynamics of the higher beta plasmas and the requirements on technology of heating and

fueling,[7] by developing consistent, feasible engineering models of systems of different size and magnetic field strength,[8] and by program planning studies of the steps required to implement the designs.[9]

In the first area, plasma engineering, early indications were that very stringent requirements would be placed on physics achievements (i.e., $\bar{\beta} \sim$ 10-15%), on beam technology (i.e., ~500 keV), on fueling technology (i.e., ~10,000-m/sec pellet velocities to reach the plasma center), and on a large system size. Rather than pursue these difficult requirements with even more difficult technology development programs, high risk physics, or high cost solutions, we reexamined the basis for the requirements. We found that as more realistic models of the higher beta plasma are used (specifically going from 0-D to 1-D models with spatial profiles), the lower the requirements on achievable beta, neutral beam energy, and fueling technology become. Under the constraint of a fixed, no-divertor TF coil shape, an innovative design concept for a compact poloidal divertor was developed that may have significant impact on the options available to plasma engineers.[7]

In the second area, system modeling, the principal questions were, "What is the cost variation with size?" and "How does cost depend upon the TF coil technology used?" Based on fairly comprehensive engineering models as opposed to optimized point designs, curves of relative cost vs the principal geometric and operating characteristics have been produced. With the costing and sizing model,[9] the cost sensitivity to any of the assumptions can be investigated and modifications made. With respect to the second question – impact of TF coil type – the result was that the principal differences between the use of superconducting and copper coils were those of objectives and risks, and not cost alone. These differences and the relative costs for the Cu, Nb_3Sn, NbTi, and a concentric hybrid arrangement of NbTi/Cu options were roughly as shown in Table 8.1.

With respect to the differences between NbTi and Nb_3Sn systems, a closer examination of similar physical devices indicated that the balance of plant is the dominant factor and that the choice of coil technologies is of great concern but as yet has little quantified economic impact.

In the third area, program planning, various elements of a preliminary program plan were initiated and identified the central programmatic questions. In particular, an assessment of both the generic[10] and design specific[11] R&D needs for TNS was made, and recommendations for more emphasis on existing programs and for new initiatives were made and documented. Planning schedules for integration of the TNS project with the supporting R&D work and the subsequent reactor devices were developed as well.[12] From this came the findings that plasma physics and decision making are probably the true critical paths and that a route to achievement of improved engineering reliability must be laid out and implemented for a successful program.

Based on the findings in these three areas, it is judged that continued activities in the Oak Ridge TNS program should be directed toward

Table 8.1. Approximate, relative, total plant costs of four systems with different TF coil options

Coil type	Cu	Nb_3Sn	NbTi	NbTi/Cu (hybrid)
Approximate relative cost	1	1.3	1.5	1.5
Most suitable objective	Ignition alone	Reactor prototype	Reactor prototype for $\beta > 5\%$	Reactor prototype not dependent upon Nb_3Sn

preconceptual design with particular emphasis placed on reducing the technological requirements through innovations in plasma engineering (such as microwave assisted startup, and refinements in the calculations (such as the TF coil ripple constraint), on making cost reductions, and on achieving increased engineering feasibility through simpler, more maintainable designs. This represents a shift in emphasis from systems modeling to preconceptual design with improved integration of the plasma engineering and program planning activities.

8.1.1 Plasma Engineering

The purpose of the plasma engineering studies within this program has been to establish credible ranges of physics parameters for an ignition test reactor as the next step beyond TFTR. Our reactor concept is based on medium toroidal fields[1] (B_T = 4-7 T), high plasma densities[1] ($\bar{n}$ = 0.6-2.5 x 10^{20} m^{-3}), and high tokamak betas (β = 5-10%).

Use of medium field strengths is compatible with the introduction of a large amount of neutral beam power, which in turn is important to high density. With large neutral beam power, the plasma is expected to heat up in a time scale much shorter than the plasma skin time, resulting in a flux conserving tokamak.[1] Calculations in D-shaped FCT[1] have produced equilibria at β above 20% with the safety factor up to 5. Although MHD instabilities may limit β to lower values, β values substantially above a few percent are expected to permit the use of medium field and/or to reduce the reactor size.

To ensure the consistency of our physics parameters, we have studied several important subjects in plasma engineering for synthesis with the design engineering and planning considerations as summarized below.

The empirical energy confinement scaling derived from studies in ATC, ORMAK, and Alcator has been used in a 0-D study[17] to choose a reference reactor with the parameters shown in Table 8.2.

The effect of density profile on the effective ion charge (Z_{eff}) is studied with a 1-D multi-[illegible] transport code incorporating particle and energy balances. It is found that $(Z_{eff} = 1)$ is not critical for reasonable density profiles, supporting the use of $(Z_{eff} = 1)$ in the 0-D scaling studies. The 1-D study (see Table 8.2) also indicates that burn conditions can exist over a wide range of density and fusion power levels, in contrast with a single operating point in the 0-D model.

The evolution of equilibria by injection to ignition and burn is studied with the flux-surface averages of the particle and energy balance equations together with the axisymmetric FCT equilibria. It is found that the centrally localized α-particle heating density can exceed the injection heating density at relatively low values of $\bar{n}$ = 2.5. This fact, when combined with the constraint to use current positive ion source beam heating technology, has led to the following line of reasoning.

Because of the centralized α-particle heating, the need for full neutral beam penetration beyond $\bar{n}$ = 2.5 is eliminated. An injection procedure[1] is found that starts with low density to facilitate penetration (Fig. 8.1). The density is then increased with the accompanying acceptable decrease in penetration. It is found that beam energy from 150 to 200 keV may be sufficient for perpendicular injection at Z_{eff} = 1.5. This is in sharp contrast to the requirements of 300-500 keV developed from the initial 0-D model calculations.

MHD ballooning modes are expected to place limits on β. Recent calculations[1] show a stable β near 5% for a D-shaped FCT equilibrium, while improvements beyond these values seem possible. Current estimates for β are between 5% and 10% with shaping and profile modifications. This β range overlaps that calculated for steady-state D-T burns.

A poloidal field system[1] in an FCT that maintains plasma D shape despite large and rapid changes in β has been obtained. In TNS, coils

Table 8.2. [illegible] parameters for a D-shaped, medium-field ignition test reactor

	Unit	Parameters based on the [illegible] model	Parameters refined with 1-D transport, MHD equilibrium, and stability
[illegible] ratio	[illegible]	[illegible]	[illegible]
[illegible] ratio	–	1.5	1.5
Aspect ratio		4	4
[illegible]		1.6	1.6
[illegible] on axis	T	[illegible]	4.3
[illegible] at coil	T		[illegible]
[illegible] low	MA	4	4
[illegible] burn	MA	6	4.5-6.5
q		3	3
n, low	[illegible]	0.5 × 10	0.3-0.5 × 10
n, ignition and burn	[illegible]	2.7 × 10	0.8-2.5 × 10
T, low	keV	2	1-2
T, ignition	keV	11	4-7
T, burn	keV	13	5-10
[illegible] ignition		11	3-5
Injection power	MW	75	50-75
burn		15	3.5-10
Collisionality, low		0.5	0.14-0.96
Collisionality, burn		0.02	0.01-0.15
n[illegible] burn	[illegible] sec	3 × 10	0.6-3 × 10
Average fusion power density	MW/[illegible]	6	0.4-8
Plasma volume	[illegible]	250	250
Average neutron wall loading	MW/[illegible]	3.7	0.3-5
Total fusion power	MW	1500	100-2000

more than 3 m away from the plasma edge can be properly located to produce D-shaped equilibria. However, the power supply required by these coils is around ten times that required by coils 0.6 m away, and a systems analysis for overall balance is therefore required.

Based on these considerations, self-consistent parameters are established and given in Table 8.2. Upcoming tokamak experiments will refine stability limits of [illegible] and plasma confinement scaling laws. Since B_T = 4.3 T is near the lower end of the medium field strength, a large margin of reliability can be achieved by using B_T [illegible] 6 T. This field strength is within reach of present-day coil technologies and development programs.

In conclusion, the imposition of technology/economics constraints resulted in creative improvements in plasma engineering models:

(1) Detailed energy deposition calculations support the use of existing 150-keV injection technology, thus providing an alternative to the pursuit of difficult, costly, risky, and time-consuming [illegible]500-keV technology.

(2) The inclusion of profiles has reduced beta requirements (Table 8.2).

(3) A compact poloidal divertor concept has been developed within nominal "D" TF coil geometry.

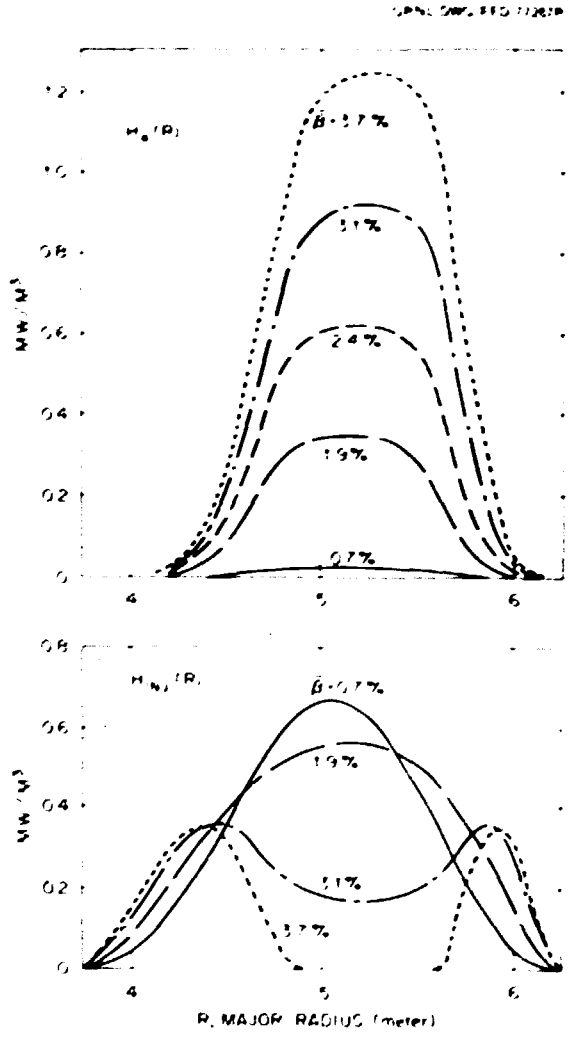

Fig. 8.1. Low density injection procedure facilitates penetration.

8.1.2 Design Engineering

A series of parametric trade studies was performed to evaluate consistently the relative costs and performance parameters of D-T burning tokamaks over a range of plasma sizes and TF coil technologies. Four different types of TF coil technologies have been investigated: water-cooled copper coils (called TNS-1), superconducting NbTi (TNS-3) and Nb_3Sn (TNS-4) coils, and a "hybrid" coil arrangement (TNS-5) consisting of a normal conducting Cu coil nested within a superconducting NbTi coil. In order to arrive at a reasonable size for the set of distinctly different options identifying the TNS alternatives, it was considered that plasma size, a measure of cost and capability, and TF coil technology treatment as the widest range of key technology options, were the most important characteristics to investigate in the initial trade studies.

In performing these trade studies for TNS tokamaks, in a consistent way to develop data suitable for a comparison of respective costs, complexity, risk, and availability, certain engineering ground rules were established including constant-tension D-shaped coils, water-cooled copper PF coils located within the TF coil bore, and auxiliary plasma heating by neutral beams.

The device sizes considered in these trade studies covered a range in the plasma radius from 0.75 m to 2.5 m, spanning the range from TFTR-size plasmas to those chosen for recent ESS design studies. The device major radius was varied from 3.9 m down to some lower limit (4.4 m for a = 0.9 m to 4.6 m for a = 2 m) which was consistent with the ground rules and still allowed a viable engineering design. The plasma beta value was chosen as the main parameter on which to judge the performance or "confidence of success" of each ignition device and was allowed to vary in the range from 2% to 15%. Two different plasma scalings were used to specify the physics parameters for an ignition device: empirical scaling and trapped particle mode scaling.

The major tool used in performing these trade studies was a computer code designated COAST,* written to permit COsting And Sizing of D-T burning Tokamak systems through detailed treatment of all major components of the total plant.

In these studies, we determined that for each coil technology and plasma beta at ignition there is some minimum cost device at a specific a, R_0, and B_{max} (Fig. 8.2). The reasons for the slight cost difference between NbTi and Nb_3Sn devices are shown in Table 8.3 for a typical

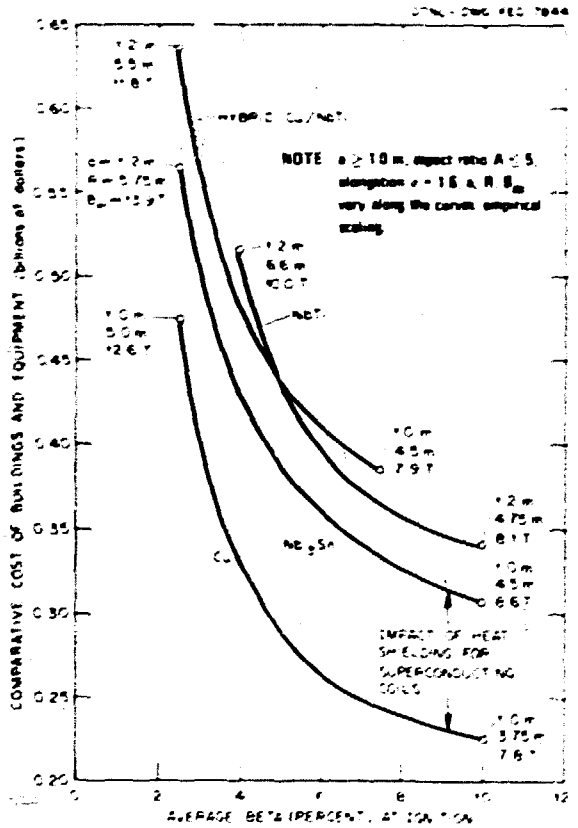

Fig. 8.2. Minimum cost devices for four TF coil technologies vs average plasma beta at ignition.

Table 8.3. Comparison of costs for similar NbTi + Nb_3Sn devices indicates overwhelming role of balance of plant

Item	NbTi	Nb_3Sn	NbTi-Nb_3Sn
TF coil cost	85	92	-7
Conductor[a]	24	37	-13
Structure and dewar	61	55	6
Refrigeration cost	50	23	27
"Balance of plant"	235	233	2
Total cost (M$)	370	348	22

[a]Based on $100/kg for Nb_3Sn and $50/kg for NbTi.

machine with $a = 1.2$ m, $R_0 = 5.0$ m, and $B_{max} = 9.0$ T. Note that the TF coil conductor cost is larger than the Nb_3Sn, as expected; however, the TF coil structure cost is larger for the NbTi because its radial build is larger due to its lower current density limitation. The main cost item difference is in the liquid helium refrigeration costs, which are about twice as high for the NbTi due to its lower thermal operating margin. The most important finding of this particular cost comparison, however, is that the balance of plant overwhelmingly dominates the total cost and makes the technological differences between NbTi and Nb_3Sn insignificant from a cost point of view.

Representative parameters and costs for four TNS point designs[13] that achieve ignition at an average beta of 5% are given in Table 8.4. The maximum field at the TF coil for each design is about 10-11 T; this would require the NbTi superconductor to be designed to operate below 4 K and would permit an Nb_3Sn design at a modest maximum field value. An NbTi superconducting design which would operate with a maximum field of 8 T at the TF coil would require a larger and more costly size at a $\bar{\beta}$ of 5% or would require operation at an average beta of ~7.5% in devices of the size shown in Table 8.4.

For a chosen plasma beta operating value, there seem to be two main conclusions possible for the best choice for a tokamak TNS, depending upon the perceived objective of TNS. If the main goal of TNS is to demonstrate ignition with a minimum of technology development in the shortest time, then water-cooled Cu coils at moderate field strengths (10-11 T) and with moderate physics demand (i.e., assuming $\bar{\beta} \sim 5\%$) seem the best choice. If, on the other hand, the goal of TNS is, in addition to ignition, demonstration of the science and technology required for reactors (i.e., sustained burn dynamics, beam power handling, and systems integrated superconducting coils which would

Table 8.4. Comparison of representative parameters for four TNS point designs

	TNS-1	TNS-3	TNS-4	TNS-5
TF coil conductor	Cu	NbTi	Nb_3Sn	Cu/NbTi
Plasma minor radius, a (m)	1	1.2	1.2	1
Plasma major radius, R (m)	4	5.7	5	4.5
Plasma elongation, σ (-)	1.6	1.6	1.6	1.6
Aspect ratio, A (-)	4	4.7	4.2	4.5
Field at TF coil, B_m (T)	10.4	9.9	10.9	9.7
Field on axis, B_t (T)	5.8	5.3	5.3	5.3
Toroidal beta, β_t (%)	5	5	5	5
Plasma current, I_p (MA)	4.1	3.8	4.9	3.6
Mean electron density, $\bar{n}_e$ (m^{-3})	1.6×10^{20}	1.3×10^{20}	1.3×10^{20}	1.6×10^{20}
Mean ion temperature, $\bar{T}_i$ (keV)	13	13	13	13
Energy confinement time, τ_E (sec)	1.5	1.8	1.8	1.5
$\bar{n}_e\tau_E$ (m^{-3} sec)	2.4×10^{20}	2.4×10^{20}	2.4×10^{20}	2.4×10^{20}
Total volt-sec	41	55.2	51.6	43.5
Plasma volume, V_p (m^3)	126.3	259.2	227.6	142.1
Neutron wall loading (MW/m^2)	1.50	1.28	1.28	1.5
Total fusion power (MW)	558	795	698	628
Fusion power density (MW/m^3)	3.7	2.6	2.6	3.7
Neutral beam power (MW)	40	57	50	45
Steady-state burn time (sec)	16	16	16	16
Time between pulses (sec)	300	300	300	300
TF coil vertical bore (m)	6.1	7.4	7.6	9.5
TF coil horizontal bore (m)	3.8	5.1	4.9	5.7
Plasma energy/energy consumed	0.32	0.85	1.57	0.51
Number of TF coils	20	20	20	20
Cost, building and equipment (M$)	280.7	434.4	388.3	436
Relative cost	1	1.5	1.34	1.51
Annual utility cost (M$)	4.1	3	2	3.4

extrapolate to a power reactor), then the Nb_3Sn TF coil devices seem the best choice, at a cost about 30% higher than for the Cu device. The lower field NbTi devices generally result in larger and more expensive devices, as do the more complex hybrid NbTi/Cu options, and hence are not as attractive as the Cu or Nb_3Sn. The choice of Nb_3Sn would imply an associated technological risk, although the benefits of its higher field capability and larger thermal margin make it very desirable for fusion power reactor applications. Table 8.4 indicates that the purely superconducting TF coil cases have the more favorable energy balances; with the particular performance parameters chosen to give minimum cost size, the Nb_3Sn case does show more than breakeven.

Although the quantitative basis for the selection of Nb_3Sn does come from the costing analysis, the selection process is not a straightforward one of minimizing calculable costs. Running as a thread through these discussions is the matter of risk. Physics performance risk is minimized by providing flexibility and extended ranges of technological parameters such as magnetic field. The use of Nb_3Sn coils in the

range of 8-11 T with a corresponding range of demand on $\bar{\tau}$ ~ 10-5 provides a margin of reserve field to be tapped later if required. Technological or engineering performance risk is minimized by using experience proven techniques with adequate backup positions. Economic risk is minimized by operating at the lowest possible level of technology that is required. Programmatic risk is minimized by pursuing paths that are as widely applicable as possible. The latter three risks do not appear minimizable simultaneously. We judge that with the incentives for NbTi and Nb_3Sn equally strong in reactor applications, for different reasons, and with NbTi and Nb_3Sn technology and coils being demonstrated in LCP, the choice of Nb_3Sn is appropriate for two primary reasons:

(1) it provides a larger plasma performance, and

(2) it provides greater emphasis on development of the Nb_3Sn option within the context of a coordinated NbTi and Nb_3Sn development and demonstration program.

Clearly these capital cost comparisons have forced us to confront the real questions - the choice of objectives (i.e., "ignition" or "reactor core") and resolution of the judgmental issues both quantifiable and semiquantifiable. As shown in Table 8.5, capital cost is but one of five quantifiable issues, and the risk and extrapolation issues are but four of seven, no one of which has yet been dealt with satisfactorily. An attempt to quantify[1] these judgmental issues has resulted in support for the qualitative conclusions discussed in this work.

Quantitative systems engineering emphasizes the importance of the overall program context.

(1) Comparative costing illuminates the impact of different technologies and highlights high cost impacts.

(2) Comparative costing indicates the dominant role of "balance of plant."

(3) Costing exercises have illuminated the real program questions - objectives plus judgments.

Table 8.5. The important cost factors are many more than capital cost alone

Quantifiable[a]	Semiquantifiable[b]
Capital cost [c]	Mechanical complexity
Operation cost	Technical risk
Size	Assembly/maintenance
Performance	Operational flexibility
Schedule	Cost/schedule risk
	Reactor technology
	Extrapolatability

[a]Quantified in present study.

[b]First attempts at quantification made in present study.

[c]Principal target in present study.

8.1.3 Project Planning

Development of a practical means of synthesizing and building on the advances made in plasma engineering and design engineering is the focus of the TNS planning activity. In developing a draft TNS program plan,[7] we came to three conclusions:

(1) The physics and technology base does exist from which to start the TNS design as a central fusion program goal.

(2) We have specific recommendations for new emphasis in certain physics and technology areas to minimize R&D program gaps.

(3) TNS conceptual design must be started now, and a close look at organizing the fusion program around a TNS project is essential to support operation in the mid-1980's.

On the first point — support base — sufficient strides have been made in both fusion physics achievement (in plasma density, energy confinement, plasma temperature, and effective impurity level) and operational understanding to encourage us to begin a serious planning effort. Even though we do not now have a working theoretical framework that allows us to extrapolate present-day plasma parameters into the low collisionality, high density fusion plasma regime with confidence, we can examine many of

the specific physics areas expected to be important in the TNS design process and begin to specify the kind of information required in that area during each major design period. Sound technology program bases from which to start exist in the three key areas for TNS (i.e., TF magnets for LCP, 150-keV beams for TFTR, and tritium handling for the Tritium Systems Test Assembly).

On the second point – principal gaps – we find three principal areas in physics and between seven and fifteen areas in technologies requiring attention.[19]

- A comprehensive impurity and particle control plan must be formulated and implemented on a timely basis to identify the best way to proceed in this most uncertain area.
- The need for experimental investigation of configuration maintenance (long pulse) and optimization in high beta, high temperature plasmas is not now being met in any existing or near-term facility.
- The applied theoretical program in impurity dynamics, plasma transport, and, most critically, coupled equilibrium, stability, transport, and heating simulation of ignition scenarios must be intensified in the existing plasma theory base program.
- Seven areas need initiation of programs or new emphasis in exploratory studies to ensure an acceptable technology base for TNS final design under any scenario.

Programs	Studies
Compound gas pump development	Limiter materials improvement
Neutral beam switch tube pulse lengthening	Plasma configuration sensing and control
Increased neutral beam power and pulse length source	Abnormal control operations
PF electrical systems (for cost reductions)	

- Six other programs related to Nb_3Sn TF coils, NbTi PF coils, active impurity controls, 300-keV beams, and >2 km/sec pellet fuel injectors might need increased emphasis depending upon TNS design decisions.
- The NbTi TF coil and pellet injector programs have critical timing questions in the generally compressed project schedule and must be closely examined further.

On the third point – implementation – development of a comprehensive work breakdown structure, a master schedule based on the work breakdown structure, and a first draft of the ingredients of the program plan have yielded six fundamental features:

- A ten-year schedule to operation from today requires an aggressive program.
- The principal, quantifiable critical path is construction of and machine assembly (basically the TF coils) within the main test cell (tokamak building).
- A phased approach, specifying main test cell first and tokamak device two years later, is essential to the achievement of the most rapid, logical schedule beginning in FY 1980.
- A reference design (i.e., an initial selection of principal design features such as plasma-size TF coil technology, etc.) with backup should be chosen now, and preparations for conceptual design of the facilities (main test cell, etc.) must be made in FY 1978 to match an FY 1980 schedule.
- A central project management is necessary to integrate all the program elements into a coordinated effort.
- The planning efforts have provided the preliminary schedules linking the project with R&D support with which to develop the necessary information supporting the reference design choice.

Underlying the discussion of adequacy and timeliness are two crucial factors. One is the requirement to tie the project schedule projections and project decisions to the institutional commitments, achievements, and level of effort in the support R&D program. The other is the fundamental importance to the design philosophy of basing all design on a firm criterion of reliable assembly and maintenance in a D-T environment. The assembly and maintenance program is based on four parts: TFTR experience, models and mockups, an intermediate superconducting tokamak experiment, and good design practice coupled with utility experience.

Program planning is identifying critical programmatic questions:

- Project planning is based on detailed work breakdown structure.
- Systematic analysis highlights problem areas.
- Plasma physics and decision making are probably true critical paths.
- A route to engineering reliability must be laid out.

8.1.4 Future Directions

On the basis of our studies thus far, the direction of future work is clear even though the pace is not. The first order of business is to reexamine the key requirements that have led to high cost, high technology design solutions. The second step is then to initiate a conceptual design leading to the construction project. Proceeding with the first step involves reconsideration of the startup voltage and PF system power requirements as well as further examination of the various divertor options, startup options, and design trade-offs for reliable assembly and maintenance. As an example in the former category, the PF system, based on an iron core magnetic circuit rather than an air core circuit, may well have considerably reduced power supply requirements. In the latter category, placement of the coils of the PF system outside the TF coils can significantly reduce the maintenance difficulties. In both cases, however, a systems analysis is required to balance the conflicting demands of mechanical, electrical, and plasma engineering.

In addition to pursuing these potential reductions in the design requirements, we will also be continuing the development of the baseline design and the program planning charts in selected systems as a systems focus for the study. Figure 8.3 illustrates the baseline design configuration selected for the FY 1978 study. The baseline parameters are displayed in Table 8.6.

The TNS program continues to be an ORNL/industry effort focused on initiating preconceptual design for the the next step in the tokamak program after TFTR.

8.1.5 Concluding Summary

Integration of engineering reality is bringing us closer to a realizable reactor:

- Imposition of technology/economics constraints has resulted in creative improvements in plasma engineering models.
- Quantitative systems engineering is emphasizing the importance of maintaining an awareness of the overall program context.
- Program planning is identifying critical programmatic questions.
- Based on this year's work, our current work tasks are confronting major "Go/Difficult Go" decision issues.
- Industrial participation is being used to strengthen the early design process.

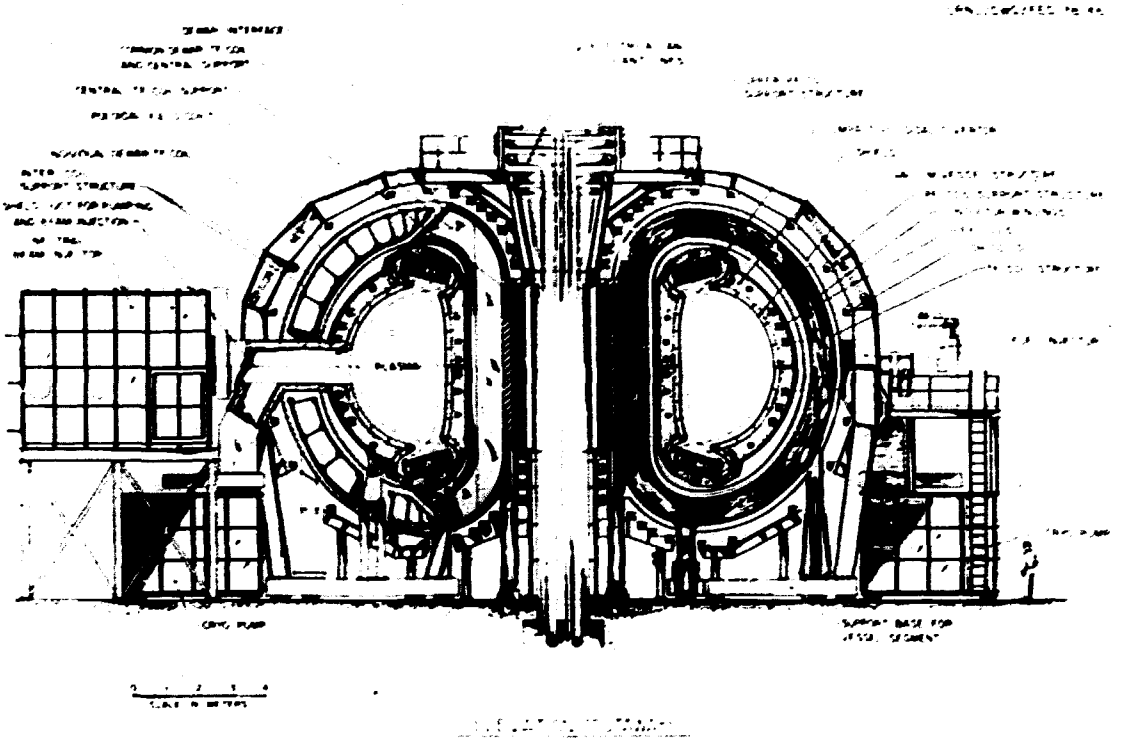

Fig. 8.3. TNS baseline configuration typical section.

Table 8.6. Baseline design parameters

Baseline Parameters	0-D estimates (used in TNS-4)	Ranges of self-consistent values
I_p, ohmic (MA)	4.9[a]	4.9
I_p, burn (MA)	5.6[a]	5.2-6.5
n, ohmic (m^{-3})	0.5 x 10^{20}	0.3-0.5 x 10^{20}
n, burn (m^{-3})	1.3 x 10^{20}	0.6-3.0 x 10^{20}
T, ohmic (keV)	2	1-2
T, burn (keV)	13	5-12
ε, burn (%)	5	2.6-10
Collisionality (ohmic)	0.5	0.4-1
Collisionality (burn)	0.02	0.01-0.20
$\bar{n}\tau$, burn (m^{-3} sec)	2.4 x 10^{20}	0.6-3.6 x 10^{20}
P_{D-T}/V (MW/m^3)	2.6	0.4-12
W_L (MW/m^2)	1.3	0.3-7.5
P_{D-T} (MW)	700	100-3000
R_o (m)	5	5
A (m)	1.2	1.2
b/a (-)	1.6	1.6
B_m (T)	10.9	10.9
B_t (T)	5.3	5.3
σ_s (-)	3.5	3.5

[a] I_p determined through MHD equilibrium calculations of D-shaped FCT plasmas.

8.2 ORNL FUSION POWER DEMONSTRATION STUDY

The major emphasis of the ORNL Fusion Power Demonstration Study has been in the application of current and near-term technology to the most logical path to near-term demonstration of tokamak fusion power. In addition we have pursued a number of concepts to simplify the tokamak reactor to make it more acceptable to the utility industry as a future source of energy. These concepts focus on the areas having the greatest impact on reactor feasibility: (1) overall size and power output, (2) remote maintenance considerations, (3) electrical power supplies, (4) blanket design, and (5) economics.

The tokamak device, by nature of its configuration and pulsed operation, is an exceptionally complex engineering design problem. We have concluded that innovative design concepts are essential to cope with this basic complexity, and we feel that the feasibility of tokamak fusion power has been significantly improved by these design approaches.

In FY 1978, the program has moved away from overall reactor system studies and is focusing on two specific design studies suggested by this approach. The major thrust is to produce a preliminary design of a blanket system of a tokamak reactor which will operate under a reasonable selection of reaction conditions and to assess performance and reliability aspects of the resultant design in utility service. In keeping with the logic of near-term demonstration, the study is constrained by the following guidelines austenitic stainless steel for structure, static lithium as the fertile material, and circulating helium as the coolant.

The second study will consider the impact of a committed site on the commercialization of fusion power. The concept of a single site dedicated to the development of fusion reactors from an elementary reactor device (TNS) through a prototype of a commercial power producing reactor has many benefits. In the absence of a clear, common understanding of the characteristics of the eventual fusion reactor, the site would serve as a focus for the various efforts taking place at existing laboratories and should lead to increased cooperation among them. Significant cost savings could be achieved by using many of the same facilities for a series of devices, particularly buildings and costly power handling and conversion systems. Significant schedule compression compared with serial development of several sites could also result from a single, committed site for multiple, sequential steps. Both of these studies are being conducted primarily with industrial subcontracts.

8.2.1 Introduction

The ORNL Fusion Power Demonstration Study was initiated in FY 1976 with the objective of providing a basis for planning a path to tokamak power demonstration. It is recognized that there is no unique set of technological directions, engineering designs, or plasma parameters which offers promise for the demonstration reactor. Several such sets no doubt do exist. In this study, we seek to define one promising set of technologies, design approaches, and plasma characteristics. We have stressed the need to simplify the overall design approach.

It is our judgment that the number of new technologies and facilities required for demonstration must be minimized. In carrying out the study we have emphasized the application of current and near-term technologies.

Since the projected cost of fusion power must be evaluated in competition with other advanced energy systems, we have performed systems analysis and costing evaluation as the justification for component sizing and selection. A computer model was developed to scale plasma parameters, design configuration, and component cost.

8.2.2 Plasma Physics Considerations

The feasibility of tokamak fusion power is more uncertain in the plasma physics performance than with limitations in technology and engineering. We have taken an optimistic outlook

for the plasma physics in selecting operating characteristics which lead to an attractive physical size and power output. These characteristics are consistent with present theoretical understanding of tokamak plasma behavior, but the definitive answers must be verified in tokamak experiments.

A representative set of parameters is presented in Table 8.7.

Table 8.7. Tokamak power reactor parameters

Average beta, β	0.1
Neutron wall loading, L	2.75 MW/m^2
Safety factor, q	3
Aspect ratio, A	4
Delta, Δ	2 m
Space between plasma and first wall	0.2 m
Plasma radius, a	1.55 m
Plasma elongation, σ_p	1.6
Field on axis, B_t	3.4 T
Maximum field at TF coil, B_{max}	8 T
TF coil horizontal bore	7.1 m
TF coil vertical bore	9.6 m
TF coil elongation, σ_{TF}	1.35
Ripple (at plasma edge)	2%
Burn time	23 min
Power (burn), P_B	865 MW(e)
Power (average), P_A	825 MW(e)
Duty factor	0.95
Thermal efficiency, η_T	~0.35

8.2.3 Simplified Design Approach

The following design concepts are representative of the approach taken to simplify the overall reactor design and improve its reliability for commercial application.

Size reduction

Our plasma engineering studies indicate that the reactor size for ignition is essentially in the range of a moderate sized commercial power plant [500-1000 MW(e)]. Assuming that beta values of 5-10% can be obtained, the overall size of the reactor can be quite small in comparison with other recent reactor concepts. Figure 8.4 illustrates the size comparison between the UWMAK II design of 1975 and the reference design of this study. Also note that a Combustion Engineering pressurized water fission reactor is shown to illustrate current power and utility industry experience in reactor size. This overall size reduction has major implications in enhancing the practicality of tokamak power reactors.

Vacuum topology

We are proposing that the tokamak reactor system be enclosed in a vacuum building. By eliminating the atmospheric pressure on the toroidal plasma vessel, the requirement for leak tightness becomes insignificant since the pressure on both sides is nearly equal. This approach will virtually eliminate the complex remote maintenance and assembly problem associated with welding and inspection of the plasma vacuum vessel.

To establish the engineering feasibility of this concept, we have located an existing vacuum building constructed by NASA near Cleveland, Ohio. In Fig. 8.5, the Demo reactor is superimposed in this facility to illustrate that the basic size and containment are within reasonable extrapolation. In addition to the assembly, disassembly, and repair advantages, the vacuum building also improves the ability to contain and control tritium.

Iron core option

Our initial evaluation of an iron core option indicates a reduction in power supply requirements as well as improvements in design. The additional cost of fabrication and construction of the iron core must be carefully evaluated with the reduced cost of power supplies. However, the iron core eliminates the air core windings under the tokamak device, for which maintenance and repair are major concerns (see Fig. 8.6).

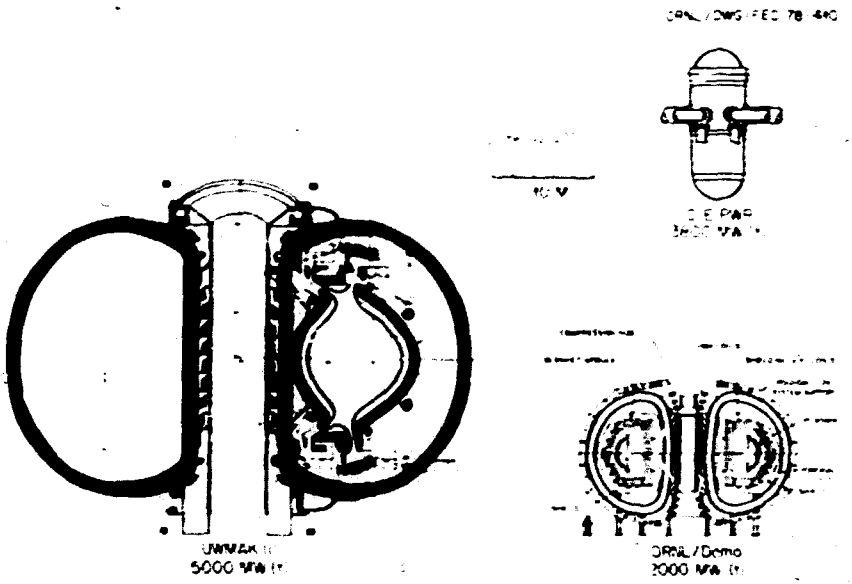

Fig. 8.4. Improvement in plasma performance leads to reduction in reactor size.

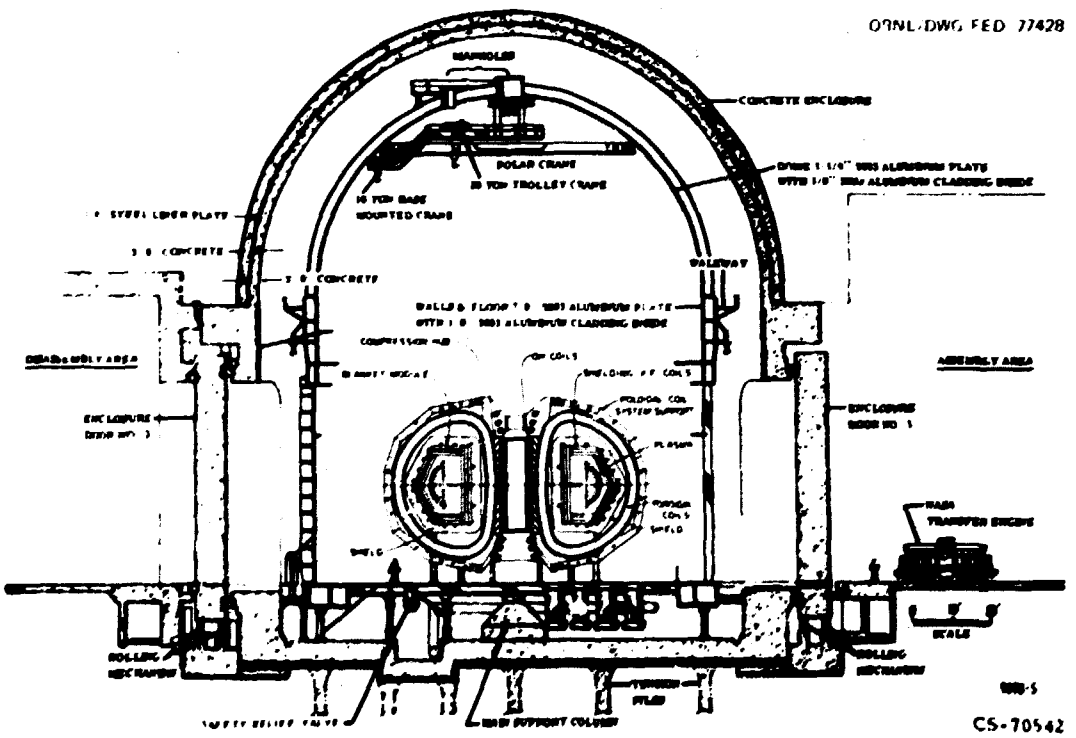

Fig. 8.5. Tokamak reactor superimposed on existing NASA facility to illustrate feasibility of vacuum containment building.

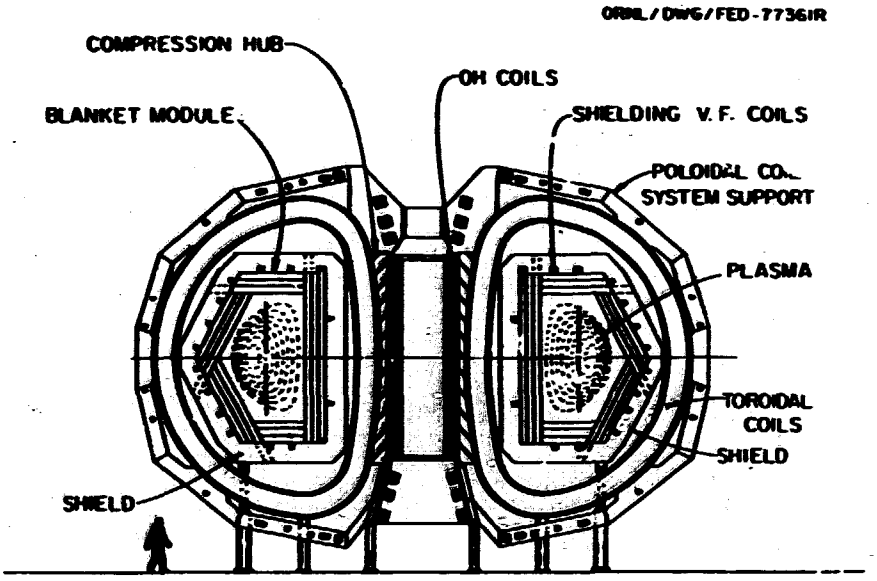

Fig. 8.6. Iron core eliminate OH windings under the tokamak.

Blanket modular approach

In order to minimize down time and facilitate maintenance, the blanket design philosophy has been to seek a modular approach which eases the problems of remote maintenance. Thus, remote maintenance has been identified as a major objective and design consideration in the development of the engineering design for the blanket configuration. In this context, we are stressing small, easily replaced individual blanket modules. Figure 8.7 is an illustration of one concept under study.

8.2.4 Application of Current or Near-Term Technology

The primary technology for the demonstration reactor is listed in Table 8.8. The following concepts were identified in this study.

Blanket structural material and coolants

It is our judgment that an alloy similar to type 316 stainless steel will be capable of achieving an integral wall loading of 10-20 MW-yr/m^2. This is accomplished primarily by limiting the first wall temperature to 400°C to minimize radiation effects. Moreover, the unique helium production reactions associated with nickel bearing alloys in thermal neutron fluxes allow an excellent simulation of fusion reactor neutron radiation effects in existing fission reactors. Gaseous helium now appears to be the most attractive blanket coolant for a stainless steel system with lithium as the breeding material.

Power conversion system

The recommended power conversion system would consist of a primary and intermediate heat transfer loop coupled to a conventional steam cycle. Assuming a primary loop exit temperature of about 450°C, a steam cycle thermodynamic efficiency of ~35% can be achieved.

Pulsed electrical system

Our studies indicate that the primary energy storage requirements can be satisfied with conventional motor-generator flywheel sets. Advanced energy storage concepts such as homopolar generators and superconducting energy

ORNL/DWG/FED-77427

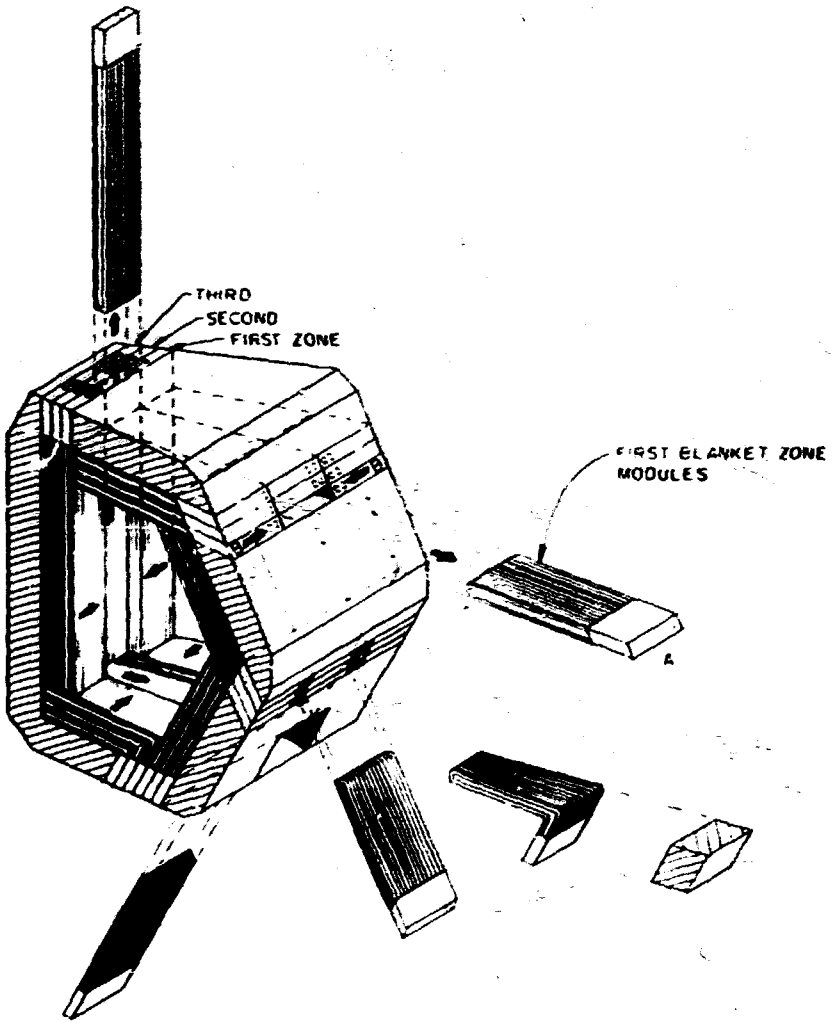

Fig. 8.7. Small blanket modules ease remote maintenance requirements.

Table 8.8. Technology base for near-term applications

System	Technology	Base
Magnet	NbTi and Nb_3Sn	Large Coil Program
Plasma heating	Neutral beam injection	TFTR
Blanket structure	Austenitic stainless steel	Alloy Development Program
Tritium handling	Cryopumping and extraction	Tritium Systems Test Assembly
Pulsed power supplies	Motor generator flywheel sets (~500 MVA and ~2 GJ)	TFTR
Energy conversion	Steam cycle (T_s ~ 750°F and η ~ 35%)	Industry

storage devices may offer some cost savings but do not appear to be necessary for commercial feasibility.

8.2.5 Economics

The results of the tokamak plant cost studies indicate the following:

(1) Direct capital costs are comparable to other advanced energy systems [1000-2000 $/kW(e)] (see Fig. 8.8).
(2) Plasma size of 1-2 m and maximum fields of 6-11 T are required.
(3) The power output of tokamak reactors can be in the range of 500-1000 MW(e).
(4) In contrast to fission reactors, unit capital costs for tokamak reactors do not necessarily favor larger power levels.
(5) Multiple reactor units sharing common equipment can significantly reduce unit capital cost compared with the single reactor unit case.
(6) Neutron wall loadings in the range of 2-4 MW/m^2 with material lifetimes of 10-20 $MW\text{-}yr/m^2$ will result in near-optimum plant costs.
(7) A three-phase program, built around a single-site, multiple-unit concept, offers a viable strategy for demonstrating the commercial feasibility of tokamak fusion power.

8.2.6 Conclusions

The concepts evolving from the ORNL Fusion Power Demonstration Study are providing a basis for planning a path to tokamak power demonstration. In particular, this study has provided the following conclusions (Refs. 4, 24-28):

(1) Optimistic assumptions on plasma physics performance (β of 5-10%, a of 1-2 m) result in reactor size and power levels in the range of present power and utility industry experience.
(2) The use of a vacuum building improves the reliability and safety of the reactor and significantly improves the problem of remote maintenance and assembly of the blanket vacuum vessel.
(3) An iron core ohmic heating system eliminates the troublesome coils under the tokamak device and offers the potential of reduced cost by reduction in power supplies.
(4) A modular approach to the blanket design eases the problems of remote maintenance.
(5) The technology base for the demonstration reactor can be founded upon current and near-term technologies.
(6) The economics of fusion plant design favors multiple tokamak units which share a common electrical plant.

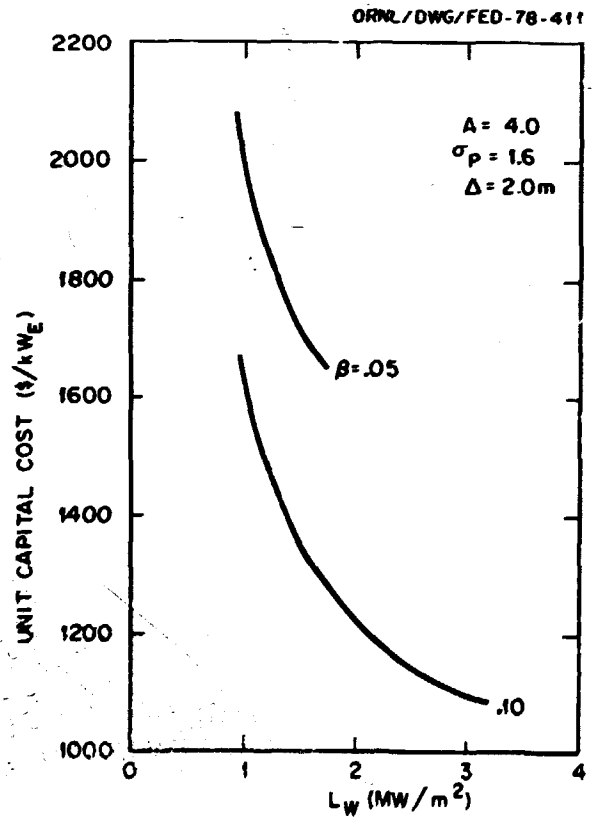

Fig. 8.8. Unit capital costs for tokamak power plants.

8.2.7 New Directions for Future Work

Two specific recommendations resulting from the FY 1977 study have been selected for an in-depth design study to evaluate engineering feasibility. The engineering is being subcontracted to private industry under ORNL management to get outside expertise in power plant technology.

Blanket design study

Westinghouse Electric Corporation has been selected to produce, within programmatic constraints, a reference design for the blanket system of a tokamak concept reactor which will operate under a reasonable selection of reactor conditions and to assess performance and reliability aspects of the resultant design in utility service. The study is limited to consideration of blanket concepts incorporating the most characteristic combination of elements, i.e., stainless steel structure, liquid lithium moderator, and helium gas coolant. It is intended to carry the process of conceptual engineering design of fusion reactor blanket systems one step further in comprehensiveness toward a feasible preliminary design. It is also intended to provide guidance to the development of fusion reactor test systems and to provide a benchmark against which the development of competing design concepts may be measured. It is not intended to be another parametric design study but will, in the initial phase, exercise some design point selections within the ranges identified by existing parametric studies. The results of this design are expected to lay the groundwork for component design and testing in FY 1979 and 1980.

Committed fusion site study

A three-phase program, built around a single committed-site, multiple-unit concept, offers a viable strategy for demonstrating commercial feasibility of tokamak fusion power. Commercial feasibility in this context means demonstrating the reliability and economic competitiveness of power generation under practical utility conditions. The three-phase program consists of (1) ignition demonstration (central pulsed electrical plant plus a single ignition device), (2) power technology demonstration (power conversion system added), and (3) commercial prototype demonstration (additional tokamak units added and tied to central pulsed electrical plant). We feel that such a strategy is rational because the plasma requirements for ignition are essentially the same as those associated with commercial plant operation. That is, plasma physics does not indicate that successively larger devices must be constructed proceeding from ignition to power demonstration and then to prototype commercial demonstration. Based on our cost estimates, it appears that such a program could be implemented in this century with a total facility cost of approximately $2-3 billion (in 1976 dollars). This does not include engineering and contingency costs nor does it include development costs. When engineering, contingency, and development costs are included, the total facility cost is estimated to be $5-8 billion (in 1976 dollars). Escalation through the three-phase program results in an estimated facility cost in the range of $10-20 billion.

An architect-engineer subcontractor will be selected in the spring of 1978 to make a technical evaluation of this concept. To do this, we wish to engage an organization familiar with site development for large facilities with strong interactions with electric power grids, large heat rejection requirements, significant environmental impacts, and potential radiological hazards. In other words, we need an engineering firm with nuclear power plant experience to perform this task of establishing site requirements and characteristics under UCC-ND supervision.

8.3 ELMO BUMPY TORUS REACTOR STUDY

The experimental results from EBT[29] have motivated a consideration of the EBT concept as the basis for a potential reactor.[30,31] This

study played a substantial role over the past couple of years in development of the EBT concept into a promising alternative concept for fusion power. Since the first round of conceptual EBT reactor design in 1976,[30] there has been considerable progress in design improvement which incorporates the increased understanding from the plasma research.

A power producing EBTR system is especially attractive from the viewpoint of a reactor designer because of its steady-state operation at high plasma pressure, its modular construction, its relatively large aspect ratio, and its favorable geometry for ease of maintenance.

The following set of design parameters is specified in order to select the reference design: from the utilities point of view, power output is limited to 2000-6000 MW(th); neutron wall loading is in the range of 1-2 MW/m^2 from lifetime considerations; the mirror ratio for annulus formation is typically the limiting plasma pressure is in the of 25-50%;[32] and the device should be capable of ignition and should use, if possible, 150-keV TFTR neutral beams or 120-GHz EBT-II microwave sources for the toroidal plasma and 70-GHz EBT-II microwave sources for the sustaining of annuli. On the basis of trade-off studies among the plasma physics requirements and uncertainties, engineering design, and technological capabilities, a self-consistent set of plasma parameters and a range of machine characteristics, given in Table 8.9, are obtained. A plan view of the entire EBTR plant is shown in Fig. 8.9. In view of the uncertainties involved in each area, plausible estimates have been made to retain flexibility so that the system can accommodate changes as the physics and technology evolve with time. The essential features of the EBTR are described below.

Table 8.9. EBTR parameters

Plasma radius (m)	1
Mirror ratio	1.8
Magnetic field (midplane/mirror) (T)	2.5/4.5
Aspect ratio	30-60
Number of sectors	24-48
Particle density (m^{-3})	1.4×10^{20}
Ion/electron temperature (keV)	15
Toroidal plasma β (%)	27
Neutron wall loading (average) (MW/m^2)	1.47
Total fusion power [MW(e)]	1000-2000
Cold zone (m)	0.2
Blanket thickness (m)	0.6
Shield thickness (m)	0.55
Coil inner radius (m)	3
Coil outer radius (m)	3.7
Coil half axial length (m)	1
Current density (A/cm^2)	1525
Neutral beam energy (keV)	150[a]
Neutral beam power (MW)	50-200[a]
Microwave frequency (GHz)	
Toroidal plasma	~120[a]
Hot electron annuli	~70
Microwave power (MW)	
Toroidal plasma	50-200[a]
Hot electron annuli	5-10

[a]A toroidal plasma will be heated to ignition conditions using either microwaves or neutral beam injection. Power required for ignition is in the range of 50-200 MW (total) depending on the startup procedures.

annuli produce a local magnetic well which provides stability for the toroidal plasma.[32] Hence an EBT contains two different groups of particles: a comparatively small number of mirror-trapped energetic electrons (several hundred kilovolts) and a higher density (both ions and electrons) toroidal plasma. The fusions occur between the toroidal plasma ions.

The power density which will dictate the desirable characteristics for the plasma in a D-T burning system is given by

$$\frac{P_{TH}}{V} = N_i^2 \frac{\langle \sigma v \rangle}{4} Q_F \propto \beta^2 B^4 \frac{\langle \sigma v \rangle}{T^2}, \qquad (8.3.1)$$

where Q_F = 17.6 MeV. The trade-offs between β and B have been considered,[31] and high-β and low-B (the minimum field strength assumed feasible is ~25 kG) operation is found to be desirable.

8.3.1 Plasma Performance

The basic EBT operation requires a toroidal bumpy magnetic field structure with an electron-cyclotron heated, hot electron ring (annulus) contained in each bump of the field. These

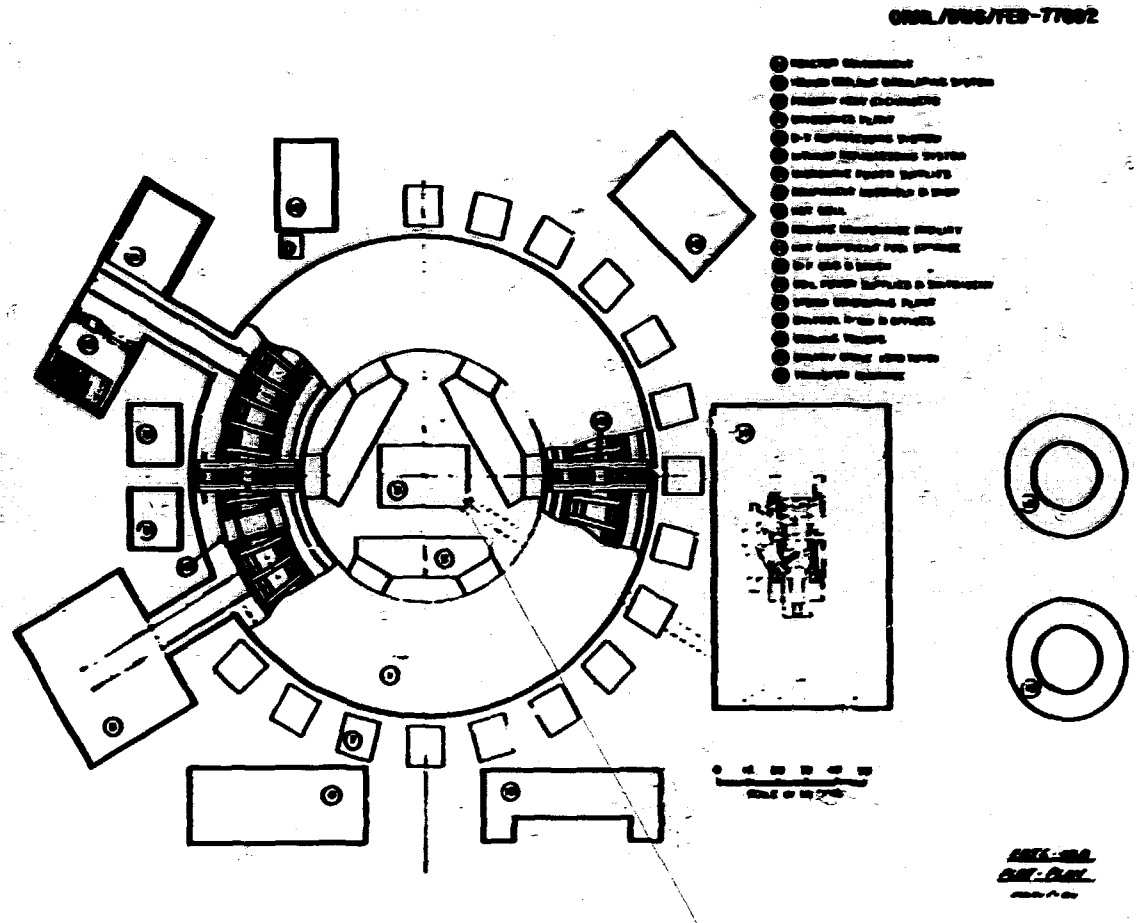

Fig. 8.9. EBTR plan view.

Startup scenarios consistent with microwave cutoff (120 GHz) or neutral beam penetration (150 keV) requirements have been derived to take advantage of high-β operation in EBT. At T = 15 keV, a β of <0.35 is required for 120-GHz microwave penetration. Similarly, neutral beam attenuation, which is proportional to exp (-nσχ), also places a restriction on maximum density if hollow density profiles are to be avoided. The dynamics of the EBTR system have been analyzed to establish procedures for achieving a high-β operating point at acceptable density, consistent with constraints imposed by other reactor support systems.

Steady-state plasma performance parameters are obtained from a consistent solution of the equilibrium and the plasma particle and power balance equations.[33] The scaling laws which will ultimately apply to the EBTR plasma are presently uncertain. A simulation model which retains the essential physics of the phenomena has been developed[33] to assess the plasma behavior. The reactor plasma simulated in this model is consistent with the results obtained from EBT-I experiments:[29,35] a toroidal core with nearly uniform density and temperature within the plasma radius, which is determined by the stabilizing hot electron annuli. Although

in the present EBT device plasma transport seems to be governed largely by neoclassical processes, hypothesized anomalous transport losses are included in the plasma simulation model in order to test the sensitivity of EBTR parameters.

From appropriate transport coefficients, confinement times are given by

$$\tau^{-1} = \gamma_{NC}\tau_{NC}^{-1} + \gamma_A\tau_A^{-1} . \qquad (8.3.2)$$

The γ factors permit consideration of different containment times, where the subscripts NC and A correspond to neoclassical and anomalous processes, respectively. The scaling of confinement time with density (n) and temperature (T) for neoclassical and anomalous processes is given by[33,34]

$$\tau_{NC} \propto \frac{3}{4}\left[\frac{R_T}{R_c}(i + Z_j\eta)\right]^2\left(\frac{1 + \nu_j^2/\Omega_j^2}{\nu_j}\right) \quad j = e,i , \qquad (8.3.3)$$

$$\tau_A \propto \frac{n^s}{T^p} , \qquad (8.3.4)$$

where

$$\nu_j = 3.8 \times 10^{-17}\frac{Z_j^2 n_j}{\sqrt{A_j}T_j^{3/2}} ,$$

$$\Omega_j = 10^3\frac{T_j}{Z_j B R_c a}(1 + Z_j\eta)$$

with

$$\eta = 10^{-3}\frac{E_r R_c}{T_j} .$$

All units are mks (temperatures and in keV). R_T and R_c are the toroidal and minor radii of curvature, and s and p are constants. From Eq. (8.3.2) one can arrange to have

$$\left(\frac{\gamma_A}{\tau_A}\right) = \frac{T^p}{n^s}\left[\left(\frac{n^s}{T^p}\right)_o\left(\frac{\gamma_{NC}}{\tau_{NC}}\right)_o F\right] , \qquad (8.3.5)$$

where the subscript o corresponds to the operating point values (steady state) and F (anomaly factor) is an adjustable constant which is chosen to yield physically plausible solutions. The results of the calculations for various values of the anomaly factor F and electric field parameter η are given in Fig. 8.10. It is shown that the selected parameters for EBTR are flexible enough to accommodate anomalous losses one to two orders of magnitude greater than the present neoclassical losses at the operating point.

Power requirements to sustain the stabilizing annuli need to be examined in detail, although preliminary calculations show that this is not a problem because the ring plasma occupies a relatively small volume.[30,31] In steady state, the annulus power balance is $P_{\mu A} = P_{\tau A} + P_{BA} + P_{CA}$, where $P_{\tau A}$ is thermal conduction and convection, P_{BA} is bremsstrahlung losses, P_{CA} is synchrotron (cyclotron) radiation, and $P_{\mu A}$ is the microwave power required to sustain the annulus. The calculations show that the synchrotron emission from the hot electron annulus accounts to a few tens of kilowatts per sector at worst, compared with a few tens to a few hundreds of kilowatts of transport losses for the data chosen.[29,30] It is important, however, that this subject be reviewed frequently as more information becomes available about the annuli (and their scaling laws) from the future experiments.[29]

From equilibrium requirements and efficiency of use of the magnetic field, a displaced-aperture inner wall design was adopted this year. Figure 8.11 shows the mod-B contours and field lines for one sector of EBTR for the straight cylindrical wall design (original wall design from last year's study) and for the displaced aperture flux following wall design (without finite beta). In the latter case, the

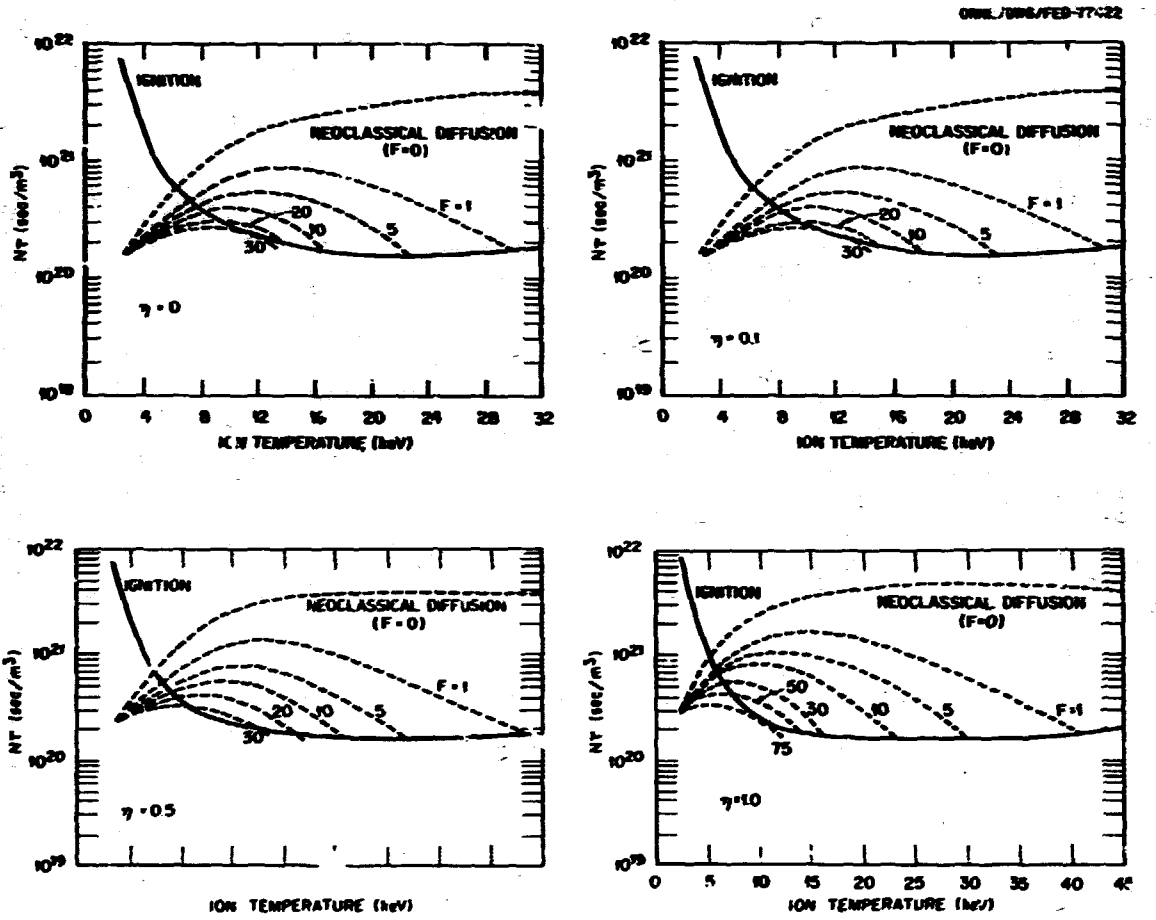

Fig. 8.10. $N\tau$ vs ion temperature T_i for different values of anomaly factor F and the electric field parameter.

plasma is shifted about 25 cm from the coil toward the major axis. This change leads to a usable volume of ~100%,[31] compared with 50%[30] for the straight cylindrical case.

8.3.2 Magnetics

The magnetic field in the EBTR is produced by 24 (48) 6-m-bore NbTi superconducting coils with a maximum field of ~7.8 T at the coil. The magnetic fields at the magnet throat and at the midplane (confining magnetic field) are 4.5 T and 2.5 T, respectively, which gives a mirror ratio of 1.8. As long as the ratio of the reactor major radius to the number of coils is constant, the axial field strength produced is not sensitive to the size of the reactor. Thus, an important advantage of an EBTR is that the same module magnet design can be used in reactors of different size and output. Also, EBT has a large aspect ratio, so that the magnetic field is reasonably uniform at the coils and the magnetic forces are nearly symmetrical. All coils are circular in shape and are made of tightly wound pancakes with pool boiling cooling.

Cryostability of the magnet is achieved by building up monolithic multifilamentary NbTi composite with formed copper strips. The copper strips are punched with slots to increase the wetted surface area and to improve coolant circulation. A high operating current (25 kA) was chosen to hold the terminal voltage during discharge to 2 kV, and four conductors are wound in parallel to maintain a reasonably small

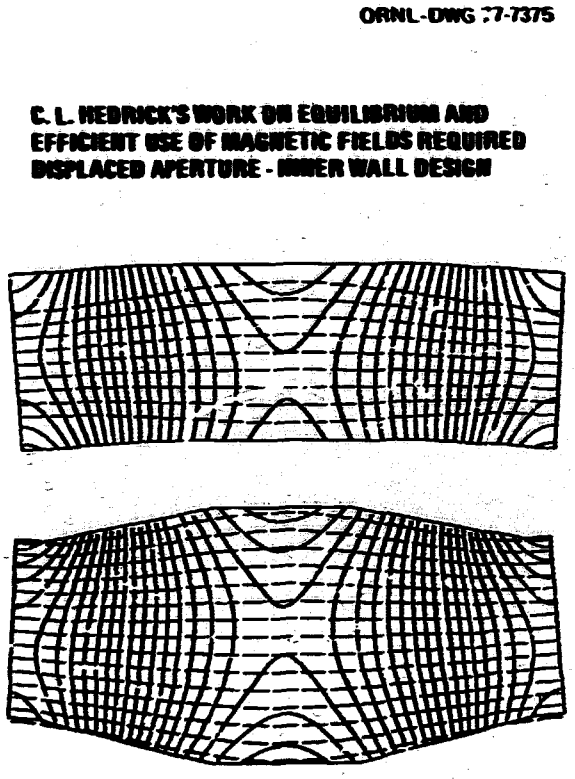

Fig. 8.11. Mod-B contours (solid lines) and field lines (dashed lines) in the equatorial plane for one sector of EBTR for straight cylindrical (upper curve) and displaced aperture (lower curve) inner wall design. In the upper curve, the boundary is the inner wall (and the coil planes). In the lower curve, the aperture has been moved toward the major axis about 25 cm so that its projection along field lines into the midplane lies on mod-B contours.

conductor and large heat transfer surface. The four conductors are interleaved in a spiral fashion in such a way that inductances are equalized and the total current is evenly divided between conductors. In EBT, it is important that the field errors be small. The winding scheme adopted (see Fig. 8.12) gives lower field errors than if only one conductor were used. Furthermore, compensation of field errors due to the crossover currents is possible. Stray fields are further reduced by careful use of the leads as compensation for each other and for axial current component with the winding. The design provides 35% helium space, interconnected helium passages with a minimum cross-sectional dimension of 0.25 cm, and a surface heat flux of 0.15 W/cm^2 when the entire current is in the stabilizer. Quench detection is based on voltage taps, with pickup coils on the current leads of all power supplies to compensate the inductive voltages and leave only the resistive component. Eight consecutive magnets are charged with a single power supply. Each coil is individually protected by an external dump resistor, which is switched into the circuit on the detection of a quench in any coil. Details of the EBTR magnets are discussed in Refs. 30, 31, and 35.

8.3.3 Mechanical Design

Conceptual designs of EBT reactors based on the modular concept are studied for a wide range of sizes.[30,31] Each module consists of one superconducting magnet coil, a shield of articulated cylindrical units, and multiple blanket modules (roughly conforming to the plasma shape), as well as vacuum pumping and microwave injection ports.

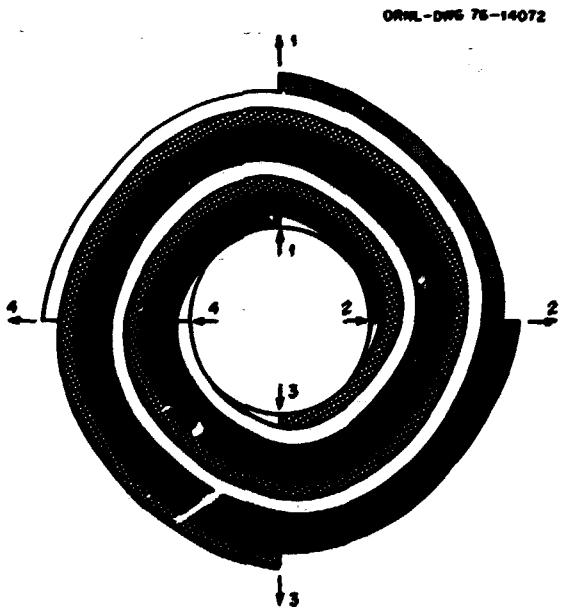

Fig. 8.12. Schematic diagram for spiral winding of four conductors in parallel in a pancake.

For the blanket, the following material choices and design constraints have been adopted:[36]

(1) stainless steel (modified 316) for all structures,
(2) metallic normal lithium as the fertile material,
(3) high pressure gaseous helium as coolant,
(4) first wall temperatures limited to 400°C,
(5) high pressure helium coolant doubly contained for protection of blanket buckets, and
(6) thin first wall to handle surface energy deposition.

The blanket is divided into segments both poloidally and toroidally. There are nine toroidal segments in one module, and each segment consists of twelve buckets arranged in a circular frame. A cross section of blanket bucket is shown in Fig. 8.13. The blanket is of uniform thickness, 60 cm, for all segments. The buckets are filled with lithium for neutron absorption and tritium production, and the back section of each bucket has stainless steel spheres mixed with lithium for gamma absorption. In order to contain the high pressure helium and prevent damage to the blanket buckets, double wall (concentric) cooling tubes are coiled in the buckets. Helium gas at 70 atm is circulated through the blanket to remove the heat for steam generation. The entire blanket structure is 316 stainless steel with a small addition of titanium. The shield sections are made of stainless steel containers (tanks) filled with stainless steel spheres around which borated water is circulated for heat removal. These tanks are divided into appropriate shapes and sizes to permit relatively easy access to the blanket.

The torus is assembled in a concrete moat, which is evacuated to provide a secondary vacuum enclosure for the machine. This vacuum environment greatly simplifies the assembly procedure and, more importantly, eases the remote maintenance problem, since it is not necessary to

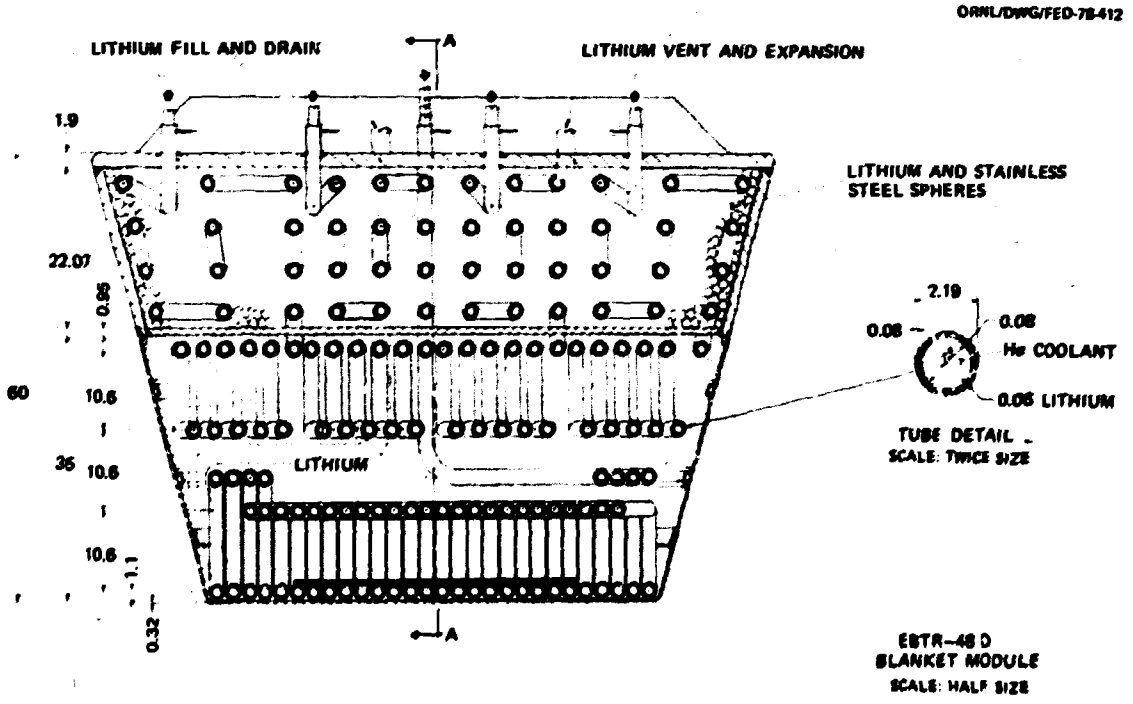

Fig. 8.13. Cross section of EBTR blanket bucket. First wall is at bottom of figure.

provide a vacuum-tight primary enclosure for the plasma. Thus, it is not required that the individual blanket segments be welded together. Also, the numerous penetrations through the blanket need no welding to the blanket wall. All assembly and remote maintenance operations are performed from above the moat. Two gantry cranes capable of rotating completely around the moat are mounted on a continuous circular track. A general plan view of the entire EBTR plant is shown in Fig. 8.9.

The coils are installed in a concrete "picture frame." The gravity load and the magnetic centering forces are transmitted to the picture frame through laminated load-bearing pads of insulating material and a liquid nitrogen-cooled buffer zone. A plan view of the components of the torus is shown in Fig. 8.14. After the coils are installed, the articulated shield pieces are installed, except for the center clamshell sections between coils. These are put in after the blanket sections have been put in place.

The plasma region is maintained at a lower pressure than the moat by two vacuum pumping ports between each TF coil. Microwave injection is made through these same vacuum ports. The vacuum system for the plasma region is located in tunnels running radially under the moat. The large area encircled by the moat is used for microwave generators and power supplies, cryogenic refrigerators, primary heat exchangers, and other equipment. This central location minimizes the lengths of lines running to these auxiliaries.

8.3.4 Neutronic Performance

Neutronics calculations were carried out to assess the ability of the lithium-laden blanket assembly to recover the kinetic energy of D-T fusion neutrons and secondary gamma rays in the form of heat and for breeding tritium. Also, the blanket and the shield assembly were evaluated in terms of their combined shielding ability to protect the magnet assembly from the intense plasma radiation.[37]

The calculations were performed in a 1-D cylindrical geometry using the discrete ordinates code ANISN[38] with a P_e-S_{12} approximation. The neutron and gamma ray transport cross sections were taken from the DLC-37[39] library and collapsed to a 35-neutron and 21-gamma ray energy group subset. All of the nuclear responses were obtained using the latest available ENDF/B-IV data. The reactor has a 60-cm-thick blanket assembly consisting of lithium in a 316 stainless steel structure and cooled with high pressure helium. The blanket surrounds a 100-cm-radius plasma region with a 20-cm cold zone. The shield is 55 cm thick and is separated from the blanket by a 30-cm-thick maintenance void. The shield is composed of 316 stainless steel (65%) and water (35%) and is supported by a stainless steel structure. Surrounding the blanket and shield is a magnet assembly consisting of NbTi/Cu coils and supported by stainless steel. All of the data were normalized to a first wall neutron loading of 1.47 MW/m^2.

The blanket assembly recovers 96% of the neutron and secondary gamma ray energy in the form of heat. Approximately 4% of the energy is deposited in the shield, and the remainder (7×10^{-4}%) is deposited in the magnet assembly. The total heating rate in the reactor is 1.47×10^5 W. The peak heating rate in the blanket is 13.5 W/cm^3 and drops off to 0.34 W/cm^3 at the front of the shield. The shield reduces the nuclear heating by nearly four orders of magnitude, and at the front of the magnet assembly the peak heating is down to 5.8×10^{-5} W/cm^3.

Natural lithium is used as the fertile material in the blanket. The tritium breeding ratio is 1.29 tritium nuclei per incident neutron, with 56% of the breeding resulting from neutron reactions with ^6Li.

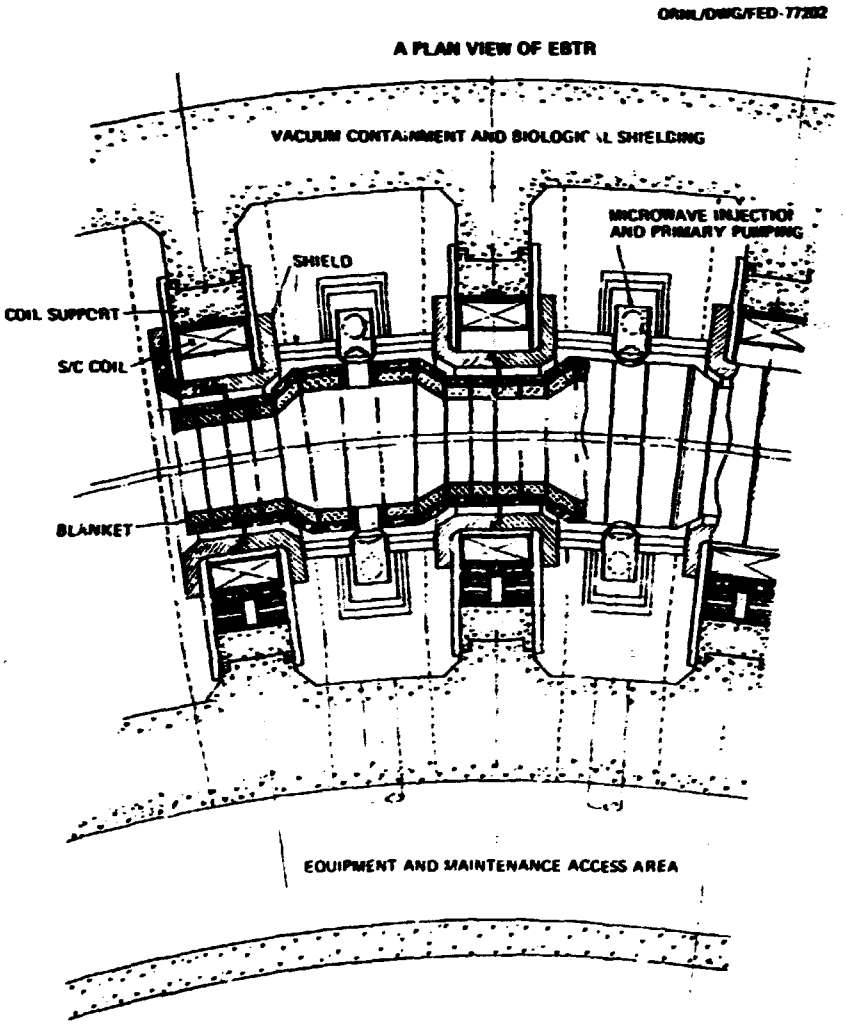

Fig. 8.14. A plan and section elevation view.

The radiation damage in the stainless steel structural components at various locations in the reactor is summarized in Table 8.10. Details of the nuclear performance of the EBTR are discussed in Refs. 31 and 37.

8.3.5 Thermal Hydraulics and Stress Analysis

Thermal hydraulic design space for the blanket module discussed has been examined in detail.[36] Specifically, a parametric study was performed to determine all the relevant hydraulic parameters, such as heat transfer coefficients, pumping power, etc.

In addition, calculations were made to determine the operating temperatures of the blanket structure. In this respect, the design goals were as follows:

(1) Limit maximum temperatures anywhere in the stainless steel structure to ~600°C.
(2) Limit the temperatures in areas experiencing the most severe radiation damage (first wall) to ~400°C.
(3) Minimize thermal stresses by arranging the coolant tubes to provide favorable temperature gradients in the blanket structure.

Table 8.10. Summary of radiation damage in stainless steel structural components

Location	Neutron wall loading = 1.47 MW/m^2		
	Atomic displacement rate[a] (dpa/yr)	Hydrogen gas production rate (appm/yr)[b]	Helium gas production rate (appm/yr)
First structural wall	10.9	913	276
Center of blanket	4.62	127	34.7
Rear of blanket	7.70×10^{-1}	7.43	1.91
Front of shield	2.16×10^{-1}	1.45	3.62×10^{-1}
Rear of shield	4.92×10^{-2}	1.11×10^{-1}	2.74×10^{-2}
Front of magnet coil	3.51×10^{-2}	5.13×10^{-2}	1.26×10^{-2}
Rear of magnet coil	6.26×10^{-3}	7.76×10^{-3}	1.67×10^{-3}

[a]Based on an effective displacement energy of 40 eV.

[b]Atom parts per million per year.

Figure 8.15 shows some of the results of hydraulic calculations. In this figure, the effects of wall loading, tubing size, and inlet pressure are parametrized with respect to the ratio of pumping power used to thermal power produced. Also indicated in Fig. 8.15 is a series of horizontal lines intersecting each of the curves of constant neutron wall loading. These lines indicate the maximum diameter tube that can be used and still maintain the first wall maximum temperature at less than 400°C. One should note that the first wall temperature of 400°C cannot be achieved for either 1.8- or 2-MW/m^2 cases. To operate at wall loading higher than 1.6 MW/m^2, the maximum temperature should be relaxed somewhat.

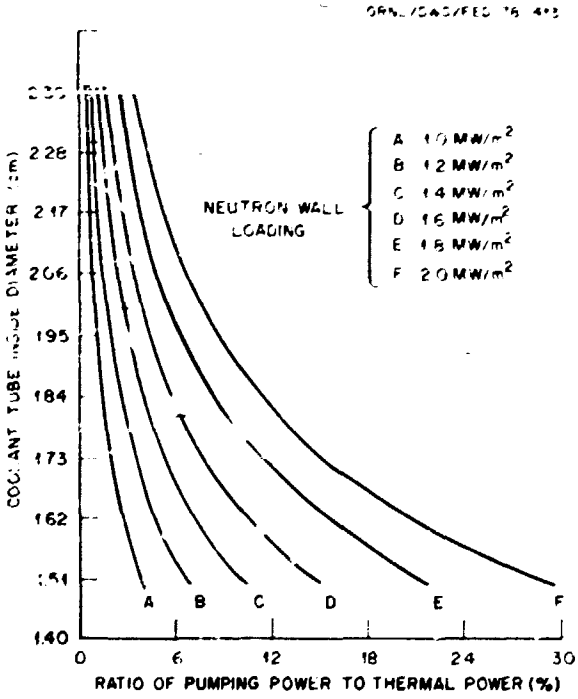

Fig. 8.15. Hydraulic parameters for: P_{inlet} = 1000 psig, T_{in} = 66°C, ΔT = 415°C.

Steady-state temperature distribution in the blanket bucket structure is shown in Fig. 8.16 for a neutron wall loading of 1.4 MW/m^2. For this wall loading the stresses and stress intensities derived for three critical points in the blanket module are summarized in Table 8.11. These values are in all cases below the allowable limits with a large margin of safety.

8.3.6 Economic Analysis

In order to establish the economic potential of the EBT reactor, two independent system costing models have been developed.[49] The first model relies on an explicit model of EBTR, discussed here, to compute the cost of the reactor itself and on the United Engineers and Constructors 1972 plant cost estimate developed for the LMFBR (suitably inflated for 1977

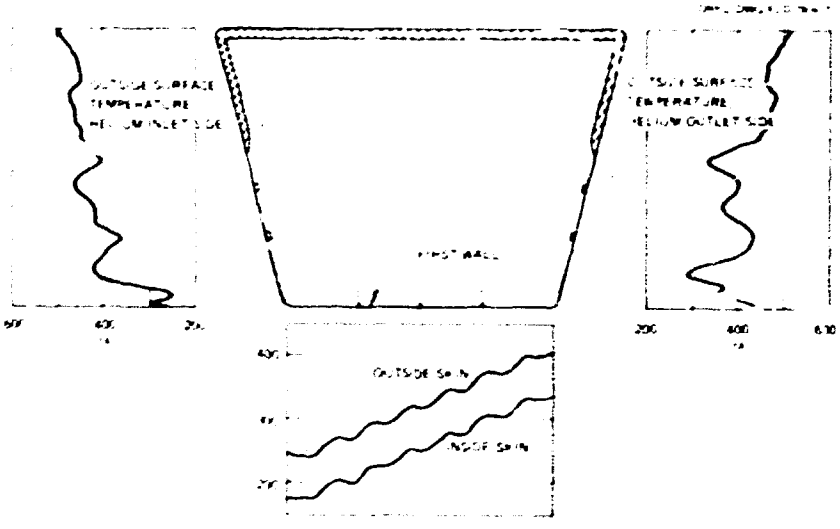

Fig. 6.16. Steady-state temperature distribution in the blanket bucket structure at a neutron wall loading of 1.4 MW/m².

Table 6.11. Stresses and stress intensities for three critical points in blanket module

	First wall		Side wall
Location	Center	Corner	Outlet side
Temperature, °C	320	400	431
P_m, psi[a]	150	150	150
P_b, psi[b]	±1,650	±1,650	±800
Q_1, psi[c]	4,500	0	16,800
Q_2, psi[d]	±17,900	±20,300	±17,690
$P_m + P_b$	1,800	1,800	950
$P_m + P_b + Q$	24,200	22,100	35,400

[a] P_m = membrane stress.
[b] P_b = bending stress.
[c] Q_1 = thermal membrane stress.
[d] Q_2 = thermal bending stress.

dollars) to compute the costs of the balance of the plant. The sensitivity of the reactor cost (nuclear island cost) to the design is then examined by parametric variations. To relate the results for comparison with the tokamak system, a second cost estimate was made using the model developed for the tokamak system.[2] The results of the two models, which are discussed in detail in Ref. 10, are in general agreement and predict capital costs of approximately $300-400/kW(th). Figure 8.17 shows capital costs as a function of aspect ratio, wall loading, beta, and power output for fixed plasma radius and magnetic field. Since the efficiency of the power conversion system varies and has yet to be demonstrated, cost estimates are given on the basis of dollars per kilowatt thermal instead of dollars per kilowatt electric.

In comparing the EBTR cost to the tokamak reactor cost,[2] cost savings of the EBTR over the tokamak system are realized by the lack of poloidal coil and driving systems and of the economic penalty of a duty factor associated with pulsed operation. These costs include neither the expected increased maintenance cost associated with the much more complex tokamak system and operating cycle nor the advantages of favorable EBTR geometry for ease of maintenance. In comparison, therefore, the EBT concept appears competitive both among fusion reactor concepts and among different power plants.

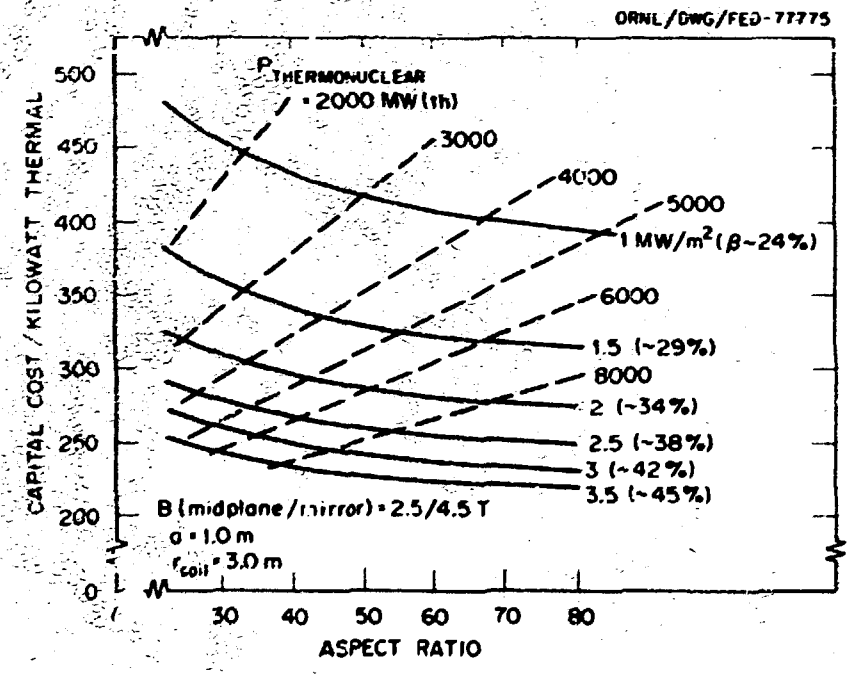

Fig. 8.17. Variation of unit capital costs with aspect ratio and wall loading.

REFERENCES

1. P. N. Haubenreich and M. Roberts, eds., *ORMAK F/BX, A Tokamak Fusion Test Reactor*, ORNL/TM-4634, Oak Ridge, Tennessee (June 1974).

2. M. Roberts (Program Manager), *Oak Ridge Tokamak Experimental Power Reactor Study Scoping Report*, ORNL/TM-5038, Oak Ridge, Tennessee (March 1977).

3. *Oak Ridge Tokamak Experimental Power Reactor Study – 1976: Parts 1-6*, ORNL/TM-5572-5577, Oak Ridge, Tennessee.
   Part 1 – M. Roberts et al., *EPR Summary*, ORNL/TM-5572 (April 1977).
   Part 2 – D. G. McAlees et al., *Plasma Engineering in a Deuterium-Tritium Fueled Tocamak*, ORNL/TM-5573 (October 1976).
   Part 3 – J. W. Lue et al., *Magnet Systems*, ORNL/TM-5574 (February 1977).
   Part 4 – C. A. Flanagan et al., *Nuclear Engineering*, ORNL/TM-5575 (December 1976).
   Part 5 – T. E. Shannon et al., *Engineering*, ORNL/TM-5576 (February 1977).
   Part 6 – M. Roberts et al., *Research, Development, and Demonstration Needs*, ORNL/TM-5577 (January 1977).
4. D. Steiner et al., *ORNL Fusion Power Demonstration Study: Interim Report*, ORNL/TM-5813, Oak Ridge, Tennessee (March 1977).
5. Y-K. M. Peng et al., *ORNL TNS Program: Plasma Engineering Considerations and Innovations for a Medium Field Tokamak Fusion Reactor*, ORNL/TM-6150, Oak Ridge, Tennessee (December 1977).
6. D. L. Chapin, *TNS Engineering Trade Study Analysis*, WFPS-TME-069, Pittsburgh, Pennsylvania (October 1977).
7. M. Roberts, *Plan for TNS Part I*, ORNL/TM-5982, Oak Ridge, Tennessee (October 1977).
8. T. F. Yang et al., *Westinghouse Compact Poloidal Diverter Reference Design*, WFPS-TME-042, Pittsburgh, Pennsylvania (May 1977).
9. D. A. Sink and E. Iwinski, *COAST, A Code for the Costing and Sizing of D-T Burning Tokamaks*, WFPS-TME-062, Pittsburgh, Pennsylvania (September 1977).
10. Oak Ridge TNS Program Staff, *Draft Program Plan for TNS – The Next Step After the Tokamak Fusion Test Reactor: Part II R&D Needs Assessment*, ORNL/TM-5983, Part IV, Oak Ridge, Tennessee (December 1977).
11. TNS Engineering Staff, *Program Plan for TNS, Part III – Project Specific R&D Needs*, WFPS-TME-044, Pittsburgh, Pennsylvania (March 1977).
12. W. B. Wood, ORNL/TM-5984, Part IV, Oak Ridge, Tennessee, in preparation.
13. D. L. Chapin et al., "Reactor System Size and Cost Trends for TNS Tokamaks," paper presented at the ANS Winter Meeting, San Francisco, California, November 27-December 2, 1977.
14. M. Murakami, J. D. Callen, and L. A. Berry, Nucl. Fusion 16, 347 (1976).
15. J. F. Clarke and D. J. Sigmar, Phys. Rev. Lett. 38, 70 (1977).
16. R. A. Dory and Y-K. M. Peng, Nucl. Fusion 17, 21 (1977).
17. F. B. Marcus and S. E. Attenberger (Oak Ridge National Laboratory), private communication, 1977.
18. A. T. Mense, S. E. Attenberger, and W. A. Houlberg, "Fueling Profile Sensitivities of Trapped Particle Mode Transport for TNS," paper presented at the ANS Winter Meeting, San Francisco, California, November 27-December 2, 1977.
19. J. A. Rome et al., *Injection Heating Scenarios for TNS*, ORNL/TM-5931, Oak Ridge, Tennessee (July 1977).
20. Glenn Bateman and Y-K. M. Peng, Phys. Rev. Lett. 38, 829 (1977).
21. Y-K. M. Peng and D. J. Strickler, "Poloidal Field Coils and Free-Boundary MHD Equilibrium Considerations for TNS," paper presented at the ANS Winter Meeting, San Francisco, California, November 27-December 2, 1977.
22. D. L. Chapin et al., *Trade Study Analysis for TNS Tokamaks*, WFPS-TME-056, Pittsburgh, Pennsylvania (October 1977).
23. T. C. Varljen et al., *Engineering Parameters for Four Ignition TNS Tokamak Reactor Systems*, WFPS-TME-058, Pittsburgh, Pennsylvania (October 1977).

24. P. W. Werner, *ORNL Fusion Power Demonstration Study: Arguments for a Vacuum Building in Which to Enclose a Fusion Reactor*, ORNL/TM-5664, Oak Ridge, Tennessee (December 1976).
25. A. P. Fraas and A. S. Thompson, *ORNL Fusion Power Demonstration Study: Fluid Flow, Heat Transfer, and Stress Analysis Considerations in the Design of Blankets for Full-Scale Fusion Reactors*, ORNL/TM-5960, Oak Ridge, Tennessee (January 1978).
26. R. W. Werner, *ORNL Fusion Power Demonstration Study: The Concept of the Cassette Blanket*, ORNL/TM-5964, Oak Ridge, Tennessee (October 1977).
27. W. M. Wells, *ORNL Fusion Power Demonstration Study: Lithium as a Blanket Coolant*, ORNL/TM-6214, Oak Ridge, Tennessee (January 1978).
28. W. B. Wood et al., *ORNL Fusion Power Demonstration Study: An Illustrative Example of Planning for the Demonstration of Tokamak Fusion Power*, ORNL/TM-6212, Oak Ridge, Tennessee (January 1978).
29. R. A. Dandl et al., *Research Program for Plasma Confinement and Heating in ELMO Bumpy Torus Devices*, ORNL/TM-4941, Oak Ridge, Tennessee (June 1975); *The ELMO Bumpy Torus Program*, ORNL/TM-5451, Oak Ridge, Tennessee (April 1976).
30. D. G. McAlees et al., *The ELMO Bumpy Torus Reactor (EBTR) Reference Design*, ORNL/TM-5669, Oak Ridge, Tennessee (November 1976).
31. N. A. Uckan et al., *The ELMO Bumpy Torus (EBT) Reactor*, ORNL/TM-6084, Oak Ridge, Tennessee (to be published).
32. D. B. Nelson and C. L. Hedrick, *Macroscopic Stability and Beta Limits in the ELMO Bumpy Torus*, ORNL/TM-5967, Oak Ridge, Tennessee (December 1977).
33. N. A. Uckan and C. L. Hedrick, *Plasma Simulation and Modeling for ELMO Bumpy Torus Reactor*, ORNL/TM-6013, Oak Ridge, Tennessee (October 1977).
34. I. M. Kovrizhnykh, Sov. Phys.-JETP 29, 475 (1969).
35. J. N. Luton and H. T. Yeh, "Toroidal Magnet System Design for the ELMO Bumpy Torus Reactor," paper presented at the 6th Int. Conf. on Magnet Technology, Bratislava, Czechoslovakia, August 29-September 2, 1977; proceedings to be published.
36. E. S. Bettis, J. M. Barnes, T. J. Huxford, K. C. Liu, R. T. Santoro, and H. L. Watts, "A Practical Blanket Design for a Toroidal Fusion Reactor," *Proc. 7th Symp. on Engineering Problems of Fusion Research*, Vol. II, p. 1453 (1978).
37. R. T. Santoro and J. M. Barnes, *Nuclear Performance Calculations for the ELMO Bumpy Torus Reactor (EBTR) Reference Design*, ORNL/TM-6085, Oak Ridge, Tennessee (December 1977).
38. W. W. Engle, Jr., *A User's Manual for ANISN, a One-Dimensional Discrete Ordinates Code with Anisotropic Scattering*, Report K-1693, Computing Technology Center, Union Carbide Corporation (1967).
39. W. E. Ford et al., *Modification Number One to the Coupled 100n-21γ Cross-Section Library for EPR Calculations*, ORNL/TM-5249, Oak Ridge, Tennessee (March 1976).
40. J. T. Yno, N. A. Uckan, and L. M. Lidsky, "Economic Analysis of EBT Reactor," *Proc. 7th Symp. on Engineering Problems of Fusion Research*, Vol. I, p. 681 (1978).

MATERIALS

J. T. Bell*,[1]
B. L. Bishop[2]
E. E. Bloom[3]
D. N. Braski*,[3]
R. R. Coltman, Jr.*,[4]
J. H. DeVan*,[3]
H. L. Dodds, Jr.[5]
T. A. Gabriel*,[2]
M. L. Grossbeck[3]
T. J. Hoffman[6]
D. T. Holmes[7]
J. A. Horak[3]
M. J. Kania[3]
J. R. Keiser[3]
P. H. Kernohan[7]
K. C. Liu[3]
C. J. Long*,[3]
P. J. Maziasz[3]
C. J. McHargue[3]
O. S. Oen[4]
D. L. Olson[7]
J. D. Redman*,[3]
T. C. Reuther[3]
M. T. Robinson*,[4]
T. K. Roche*,[3]
J. L. Scott[3]
J. E. Selle[3]
J. O. Stiegler[3]
J. M. Swanks[8]
F. W. Wiffen[3]
J. W. Woods*,[9]
A. F. Zulliger[10]

Abstract. The radiation effects program during the past year was heavily involved with DOE and other contractor personnel in defining the program for Alloy Development for Irradiation Performance. The goal of this program is to select and develop one or more alloys (from the multitude of candidate materials) that will serve successfully in fusion reactors producing economical electrical power. The basis for this experimental program is a continuing reappraisal of the materials requirements for fusion reactors – the maintenance of a program to calculate radiation damage parameters in conceptual fusion reactor designs and in fission reactors and other available experimental facilities. Irradiation experiments for this program are conducted in three fission reactors, EBR-II, HFIR, and the ORR. The past year saw the recognition by DOE of the value of ORR to the Fusion Materials Program and resulted in the first experiments for ORR irradiation of Fusion Reactor Program materials being built. The HFIR irradiation program continued, exploiting the unique ability of this reactor to produce high levels of helium during the irradiation of alloys containing nickel. Irradiation experiments in EBR-II continue with many different alloys reaching high levels of displacement damage at temperatures of interest.

The measured effects of irradiation on the engineering properties of candidate alloys are evaluated to serve three goals: (1) to set the direction of further experimental investigation, (2) to identify promising directions for alloy improvement by control of chemistry or microstructure, and (3) to identify limitations that material properties impose on fusion power systems. Available data indicate that limitations on ductility after extended periods of irradiation will restrict both the operating temperatures and the allowable strains during reactor operation. Cyclic loading imposed by temperature changes during a reactor operating cycle can be expected to further limit the reactor structure lifetime. The most important single result of this analysis is to highlight the shortage of data relevant to fusion reactor design or performance prediction. Finally, examination of the effect of modifying type 316 stainless steel by the addition of small amounts of titanium shows

---

*Part-time.

1. Chemistry Division.
2. Neutron Physics Division.
3. Metals and Ceramics Division.
4. Solid State Division.
5. University of Tennessee, Knoxville, Tennessee.
6. Computer Sciences Division.
7. Colorado School of Mines, Golden, Colorado.
8. Department of Energy, Washington, D.C.
9. ORNL Operations.
10. UCC-ND Engineering.

that this is a promising approach to be pursued in the search for alloys that meet the demands of fusion power systems.

The resistivity of several commercial organic insulators decreased promptly by a factor of ~10^3 under intense gamma ray irradiation, but the insulators showed little further change during irradiation at 4.8 K to a dose of 2×10^8 R. Postirradiation testing of electrical and mechanical properties at 300 K showed little change over preirradiation values.

9.1 THE PROGRAM FOR ALLOY DEVELOPMENT FOR IRRADIATION PERFORMANCE IN FUSION REACTORS[1]

J. O. Stiegler T. C. Reuther

Because the fusion reactor environment is outside the range of our experience and because the properties required by reactor design are not yet identified, the Alloy Development for Irradiation Performance Task Group is taking a broad approach in which four distinct classes of materials are investigated in parallel:

Path A – austenitic alloys
Path B – higher strength Fe-Ni-Cr alloys
Path C – reactive/refractory metal alloys
Path D – innovative concepts.

The Division of Magnetic Fusion Energy has established the planning and organizational basis for the development and testing of these alloys for the intense high energy neutron flux that will be encountered in the first wall of a fusion reactor. Because of the lack of fusion testing environment, most irradiations for obtaining engineering data will have to be carried out in fission reactors. A key element of the program is the Li (d,n) neutron source, which will allow relationships to be established between the fission and fusion environments. Because such a source supplies a broad spectrum of neutrons extending up to about 40 MeV, extensive cross-section measurements are required in order for it to be used effectively to develop alloys for fusion reactors.

9.2 MATERIALS REQUIREMENTS FOR FUSION REACTORS[2]

C. J. McHargue J. L. Scott

Once the physics of fusion devices is understood, which is expected to be achieved in the early 1980's, one or more experimental power reactors (EPR) are planned which will produce net electrical power. The structural material for the device will probably be a modification of an austenitic stainless steel. Unlike fission reactors, whose pressure boundaries are subjected to no or only light irradiation, the pressure boundary of a fusion reactor is subjected to high atomic displacement damage and high production rates of transmutation products, e.g., helium and hydrogen. Hence, the design data base must include irradiation materials. Because *in-situ* testing to obtain tensile, fatigue, creep, crack growth, stress rupture, and swelling data is currently impossible for fusion reactor conditions, a program of service temperature irradiations in fission reactors followed by postirradiation testing, simulation of fusion conditions, and low fluence 14-MeV neutron irradiation tests is planned. For the demonstration reactor (Demo) expected to be built within ten years after the EPR, higher heat fluxes may require the use of refractory metals, at least for the first 20 cm. A partial data base may be provided by high flux 14-MeV neutron sources being planned. Many materials other than those for structural components will be required in the EPR and Demo. These include superconducting magnets, insulators, neutron reflectors and shields, and breeding materials. The rest of the device should utilize conventional materials except that portion involved in tritium confinement and recovery.

9.3 SUMMARY OF RADIATION DAMAGE CALCULATIONS

T. A. Gabriel B. L. Bishop

In order to plan radiation damage experiments in fission reactors (such as ORR, HFIR, and EBR-II) keyed toward fusion reactor applications, it is necessary to have available for these

facilities displacement per atom (dpa) and gas production rates for many potential materials. In a previous paper,[3] the calculated irradiation response (dpa and gas production) for a fusion reactor first wall neutron spectrum was obtained. Similar calculated data are now being obtained for various locations within the fission reactors mentioned above. These data, when considered with those in Ref. 1, will make available better information for planning and evaluating fission reactor experiments in the light of fusion reactor needs. Some of the calculated data for the ORR reactor are given in Table 9.1.

In order to maintain good basic data on which the above type calculations are based, the sensitivity of primary knock-on atom (PKA) spectra and dpa cross sections to different secondary neutron energy and angular distributions and "in-groun" weighting schemes was investigated.[4] It was shown (see Table 9.2) that for some variables such as secondary neutron angular distributions, the sensitivity is reasonably large and there exists a need for further theoretical and experimental data and development.

9.4 USE OF FISSION REACTORS FOR FUSION REACTOR FIRST WALL STUDIES[5]

J. A. Horak J. H. Swank

The purpose of the work presented is to demonstrate one of the more important uses of existing fission reactors for the magnetic fusion reactor (MFR) first wall alloy development program. The most important properties of the first wall are resistance to fracture and to swelling while operating in the MFR environment. One of the more important effects of the fusion reactor environment is the high He/dpa produced in the first wall. The first wall must operate in the temperature range from ~0.3 to ~0.5 T_m, where it has been demonstrated that ductility and swelling are sensitive to helium concentration, dpa, and the He/dpa.[6-8]

In mixed spectrum fission reactors where both the fast (E > 0.1 MeV) and thermal neutron fluxes are ≥3 x 10^{14} neutrons/cm^2/s, both helium and dpa levels equal to and greater than those anticipated for an MFR at an operating level of

Table 9.1. dpa and gas production rates in the elemental constituents of fusion candidate alloys for the reactor spectrum: ORR/C-3 (midplane)

Element	Effective displacement threshold energy (eV)	Displacement damage (dpa/sec)	Helium (appm/sec)	Hydrogen (appm/sec)
Fe	40	2.13 x 10^{-7}	6.23 x 10^{-8}	1.07 x 10^{-6}
Ni	40	2.25 x 10^{-7}	8.88 x 10^{-7}	1.36 x 10^{-5}
Cr	40	2.41 x 10^{-7}	2.27 x 10^{-8}	3.14 x 10^{-7}
Mn	40	2.65 x 10^{-7}	2.46 x 10^{-8}	2.47 x 10^{-7}
V	40	2.65 x 10^{-7}	4.68 x 10^{-9}	1.90 x 10^{-7}
Nb	60	1.43 x 10^{-7}	1.55 x 10^{-8}	1.10 x 10^{-7}
Mo	60	1.63 x 10^{-7}	1.54 x 10^{-8}	2.99 x 10^{-8}
Ti	30	3.45 x 10^{-7}	3.11 x 10^{-8}	5.06 x 10^{-8}
Zr	50	1.63 x 10^{-7}	4.32 x 10^{-10}	6.13 x 10^{-8}
Al	25	4.28 x 10^{-7}	1.42 x 10^{-7}	7 31 x 10^{-7}
Mg	40	2.72 x 10^{-7}	5.40 x 10^{-7}	2.37 x 10^{-7}
Cu	30	2.92 x 10^{-7}	6.11 x 10^{-8}	3.25 x 10^{-6}
Co	40	2.50 x 10^{-7}	3.18 x 10^{-8}	5.35 x 10^{-7}

Table 9.2. Sensitivity of the Fe(n,n' unresolved) dpa cross sections to different neutron angular distributions and energy spectra

Neutron group number	dpa cross sections (barns)			
	$\frac{d\sigma}{d\Omega} = 1^a$ $\frac{d\sigma}{dE} = A$	$\frac{d\sigma}{d\Omega} = 2$ $\frac{d\sigma}{dE} = A$	$\frac{d\sigma}{d\Omega} = 3$ $\frac{d\sigma}{dE} = A$	$\frac{d\sigma}{d\Omega} = 1$ $\frac{d\sigma}{dE} = B$
1	460	376	346	394
2	472	385	356	410
3	504	412	381	444
4	565	463	428	506
5	689	566	524	631
6	955	791	736	906
7	1309	1099	1028	1289
8	1485	1259	1183	1492
9	1395	1181	1109	1410
10	1261	1066	1000	1277
11	1112	939	881	1129
12	936	792	744	956
13	730	622	585	751
14	512	442	419	533
15	308	271	259	323
16	144	130	126	152
17	27.5	25.4	24.8	28.3

[a] 1 = constant; 2 = 75% forward, 25% backward; 3 = 1 + cos θ.

A = ENDFB/IV; B = $Ee^{-E/T}$, where T(eV) = $3.22 \times 10^3 \sqrt{E'/A}$, A is the atomic number of the target, E' is the incident neutron energy in eV, and E is the energy of the emitted neutron. (All energy and angular distributions are for the center of mass system.)

at least 1 MW/m^2 can be produced in alloys that contain nickel, as shown in Fig. 9.1 for type 316 stainless steel. The fast neutrons produce the dpa; the helium is produced by the process $^{58}Ni + n_t \xrightarrow{\approx 4b} {}^{59}Ni + n_t \xrightarrow{\approx 12b} {}^{56}Fe + a$.[9,10] However, as shown in Fig. 9.1(a), irradiation in a mixed spectrum reactor where the thermal-to-fast-neutron ratio is approximately constant during the entire irradiation, the same He/dpa as that in an MFR first wall of type 316 stainless steel is achieved at only one time during irradiation. The helium concentration increases approximately as $(\phi_t \cdot t)^{\approx 1.5}$ and the dpa increases linearly with $\phi_f \cdot t$. Hence, the time when the He/dpa in a fission reactor exceeds that in an MFR is a function of the thermal-to-fast-neutron ratio. To utilize fission reactors for MFR first wall development of materials that contain niobium, it is necessary that the He/dpa during the entire irradiation closely match that anticipated in an MFR.

For several valid reasons it is becoming increasingly obvious that a member of the type 316 stainless steel family will be utilized for the first wall of the early generations of MFRs.[11-15] In Fig. 9.1(b) is shown the calculated He/dpa in type 316 stainless steel for an MFR at 1 MW/m^2 and for irradiation in two of the high flux positions (E-5 and C-3) of the Oak

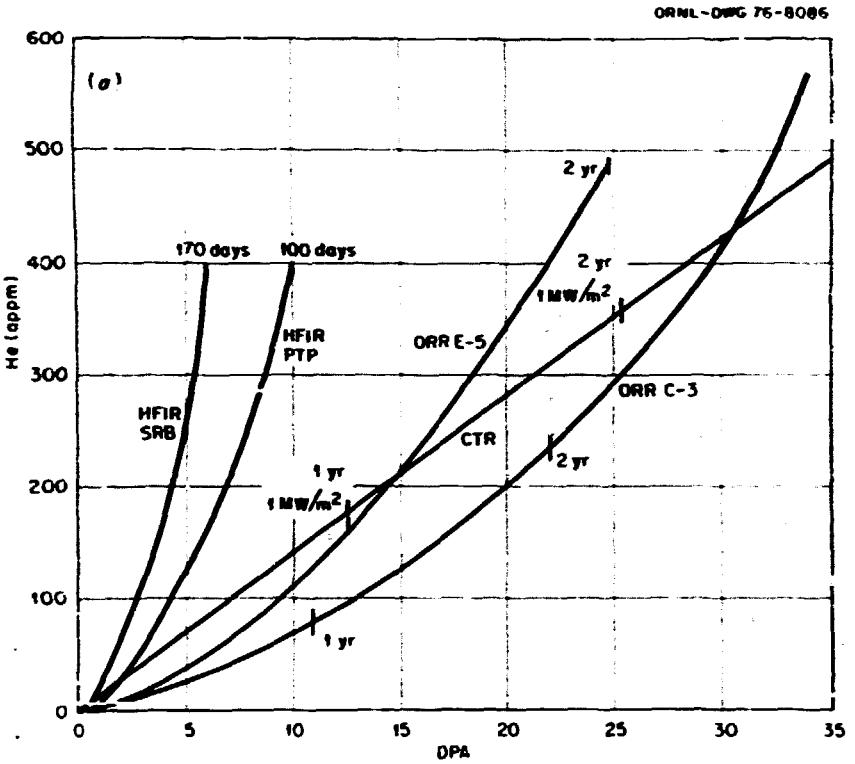

Fig. 1(a). Helium concentration as a function of displacements per atom in type 316 stainless steel for an MFR first wall and for irradiation in two HFIR and two ORR positions.

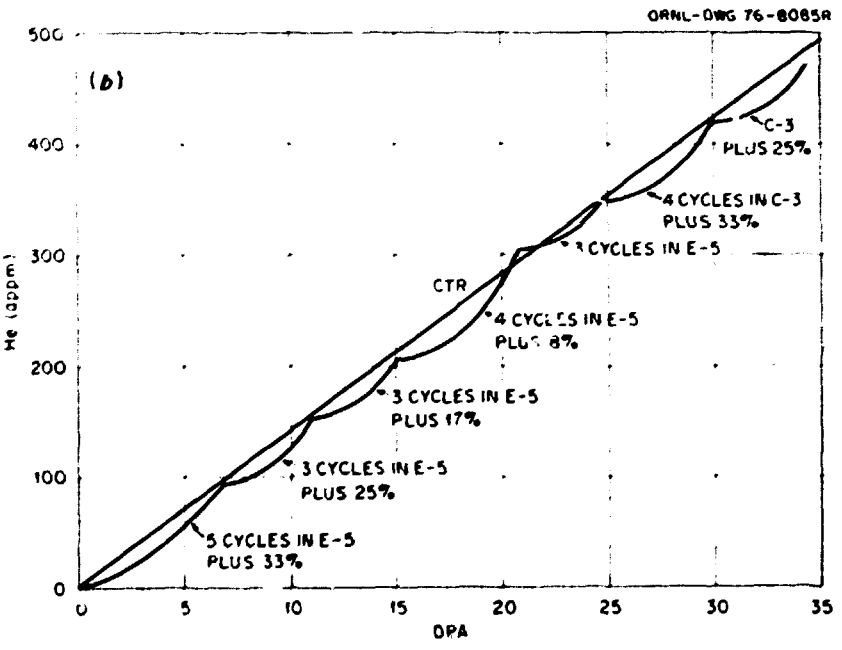

Fig. 1(b). Helium concentration as a function of displacements per atom in type 316 stainless steel for an MFR and for irradiation in two positions of ORR with spectrum tailoring. Percentage values are for the increases in the thermal neutron flux produced by varying the moderation between the reactor fuel and the test samples.

Ridge Research Reactor (ORR). The He/dpa for type 316 stainless steel irradiated in the central irradiation positions of ORR can be maintained as close to that of an MFR as thought necessary. This is accomplished by varying the thermal-to-fast-neutron ratio as often as desired during the irradiation.

The ORR core loading arrangement is designed to be extremely flexible. The spectrum tailoring required to produce the correct helium and dpa production rates and the He/dpa can be controlled through the number of fuel elements in the core, the mass of ^{235}U per fuel element, the thickness and species of moderator between the fuel and the test samples, and through the insertion of thin pieces of aluminum containing ≈10 at. % ^{235}U between the fuel and test samples. In the example shown in Fig. 9.1(b), extremely simple spectrum tailoring of the present ORR was used. No attempt was made to optimize the spectrum tailoring to produce a He/dpa closer to the MFR value. It is not known at this time how closely the He/dpa must be controlled to simulate the effects of the MFR environment. It would be relatively easy to have the He/dpa value for ORR irradiation of type 316 stainless steel as close to that of an MFR as desired.

In summary, high flux mixed spectrum fission reactors such as the ORR can provide relevant simulation of the helium concentration, dpa, and He/dpa expected in an MFR. These reactors will be an important part of the OFE alloy development program for first wall materials that contain nickel, for at least the next five to ten years.

9.5 THE UNIQUE ROLE OF HFIR IN FUSION REACTOR MATERIALS EVALUATION[16]

P. J. Maziasz F. W. Wiffen

The lack of irradiation facilities with neutron flux and spectrum that match a D-T fueled fusion reactor requires the use of simulation techniques in examining irradiation effects in fusion reactor first wall and structural materials. The purpose of this paper is to examine the place of irradiations in the HFIR in evaluating the effects of the fusion reactor environment and to examine the results of experiments exploiting the HFIR advantages.

The High Flux Isotopes Reactor is a 100-MW(th) flux trap reactor. The highest fast neutron flux is 1.4×10^{15} neutrons/cm^2/sec (>0.1 MeV); the thermal flux at the same position is 2.3×10^{15} neutrons/cm^2/sec. Temperatures above the water coolant temperatures are achieved by gradients across gas gaps between the nuclear heated specimen and the specimen holder in thermal contact with the water. Irradiation temperatures from 280-950°C have been achieved by this method.

Neutron irradiation of a metal results in the displacement of atoms, mainly through elastic collisions, and transmutation of target atoms initiated by neutron captures. In a fusion reactor, the accumulated displacement damage and the helium produced in (n,α) reactions will be the most important components of the irradiation response. In HFIR irradiation fast neutrons result in a high level of displacement damage, and the high thermal neutron flux results in significant yields for any reactions having a high thermal neutron cross section. A unique reaction sequence of interest here is helium production from the major isotope of nickel. The two-stage thermal neutron reaction sequence is $^{58}Ni(n,\gamma)^{59}Ni$, $^{59}Ni(n,\alpha)^{56}Fe$. The calculated irradiation response during HFIR irradiation of two alloys of interest is given in Table 9.3 and is compared with calculated damage production rates in a tokamak fusion reactor first wall.

Irradiations in the HFIR offer the only method of achieving helium levels equivalent to long service in a fusion reactor. Although these helium levels are accompanied by a lower dpa level than would be achieved in the long fusion reactor service, the dpa level is as high as achievable in any other fission reactor. These unique advantages of HFIR can be exploited in evaluating the importance of high helium levels in determining the irradiation response of some metals; in addition, in cases where helium level

Table 9.3. The simulation of fusion reactor irradiation response by HFIR irradiation of nickel-containing alloys

Irradiation time and response parameter	Calculated response	
	Type 316 SS	PE-16
One HFIR cycle (23 days)		
Displacement damage	2.25 dpa	2.25 dpa
Fusion equivalent	0.2 MW-yr/m^2	0.2 MW-yr/m^2
Helium generation	30 appm	101 appm
Fusion equivalent exposure	0.2 MW-yr/m^2	0.7 MW-yr/m^2
One year in HFIR (at 92%)		
Displacement damage	33.7 dpa	33.7 dpa
Fusion equivalent exposure	2.9 MW-yr/m^2	2.9 MW-yr/m^2
Helium generation	1920 appm	6370 appm
Fusion equivalent exposure	13 MW-yr/m^2	44 MW-yr/m^2

can be shown to control the irradiation response, the results can be used to predict fusion reactor service behavior.

Samples of type 316 stainless steel, Inconel 600, and PE-16 have been irradiated at temperatures in the range 300-730°C. Postirradiation examination has resulted in the following conclusions:

(1) At levels of helium anticipated in fusion reactor service, the irradiation response is not adequately predicted by irradiations that produce only displacement damage.[1]

(2) Swelling is controlled by helium content, with cavities in equilibrium with the helium pressure.[6,8] As a result, swelling is relatively temperature independent throughout the normal range of swelling temperatures, but larger swelling is observed at higher temperatures.

(3) Ductility reductions are greater than observed after fast reactor irradiation. At elevated temperatures, embrittlement is clearly dominated by helium content, with near zero elongation resulting from intergranular fractures.[7]

Future HFIR irradiations will be directed at more completely defining the helium effects on irradiation response and comparing the response of candidate alloys to the unique regime of irradiation parameters achievable in this reactor. The results will be translated to performance limits on planned fusion reactors and will be used in the development of alloys more resistant to degradation in fusion reactor services.

9.6 MECHANICAL PROPERTY DEGRADATION OF STRUCTURAL MATERIALS DURING FUSION REACTOR OPERATION[17]

F. W. Wiffen

The reliability and economics of electricity supplied by fusion power reactors will in large measure be determined by the lifetime of the reactor structural materials. This lifetime will be set by projected changes in the mechanical properties of the structure during service in the reactor neutron flux. In general, irradiation hardens the material and leads to a reduction in ductility. An exception to this is in some complex engineering alloys, where either hardening or softening can be observed depending on the

alloy and the irradiation conditions. Regardless of this restriction, irradiation usually leads to a reduction in ductility. Available tensile data show that significant ductility reduction can be expected for irradiation conditions typical of fusion reactor operation. Consideration of these effects shows that extensive work will be needed to fully establish the in-service properties of reactor structures. This information will be used by designers to develop conditions and design philosophies adapted to avoid the most deleterious operating conditions and to minimize design stresses. The information will also be used as input to alloy development programs with goals of producing materials more resistant to property degradation during irradiation.

9.7 COMPARISON OF 316 + Ti WITH 316 STAINLESS STEEL IRRADIATED IN A SIMULATED FUSION ENVIRONMENT[18]

P. J. Maziasz E. E. Bloom

Fracture of the first wall in a fusion reactor is a shutdown condition, and ductility and swelling are important parameters in evaluating the fracture resistance. In a fusion reactor, 14-MeV neutrons from the D-T plasma will produce displacement damage and helium in the first wall and structural materials. The High Flux Isotope Reactor simultaneously produces high levels of helium and dpa in alloys containing nickel and can help evaluate the fusion reactor response.[16] Previous studies[6-8,19] have shown that titanium additions can improve the irradiation response under fast reactor irradiation and that 20% cold working can improve the response relative to solution-annealed material after HFIR irradiations.

Samples of annealed and 20% cold-worked 316 and 316 modified by the addition of 0.23 wt % Ti (TiM 316) were irradiated in HFIR at 550-800°C to fluences producing 30-60 dpa and 2000- to 4000-appm He. Lower fluence irradiations at 600°C produced 1.5-3.0 dpa and 30- to 80-appm He. Swelling was determined by immersion density; the specimens were then tensile tested at a strain rate of 0.0028 min^{-1} at temperatures near the irradiation temperature, and the microstructures and swelling were evaluated by electron microscopy.

Limited data show increased ductility in annealed TiM 316 compared to 316 for tests above 550°C, while at 575°C, 20% cold-worked TiM 316 irradiated to low fluences also shows increased ductility relative to 20% cold-worked 316 (see Table 9.4). Ductility is lower in 316 irradiated in HFIR than in EBR-II, which produces much lower helium levels at similar temperatures and fluences.[7]

Swelling is reduced in annealed TiM 316 relative to 316 irradiated in HFIR (Table 9.4). Swelling is also reduced in 20% cold-worked TiM 316 relative to 316 for irradiation at 600°C to 1.5-3.0 dpa and 30- to 80-appm He. In both microstructural conditions, the concentration of intragranular cavities is reduced in TiM 316 relative to 316, while the cavity size remains about the same. In irradiations of the annealed material, the grain boundary cavities are much smaller in TiM 316 than in 316. Swelling is greater in 316 irradiated in HFIR than it is in EBR-II at similar temperatures and fluences.[6,8]

The precipitation responses of annealed TiM 316 and 316 are quite different. Intragranular precipitates in TiM 316 include TiC and some $M_{23}C_6$ after irradiation at 550-680°C. In contrast, precipitates identified in 316 include chi phase and some $M_{23}C_6$ for irradiation from 480-600°C. Both alloys exhibit $M_{23}C_6$ at the grain boundaries for irradiations below 600°C and sigma phase above 600°C. The TiC precipitate particles in the modified alloy are rod shaped and appear to be preferential nucleation sites for cavities. Their role as collection sites for helium affects both ductility and swelling.

In summary, the addition of titanium to 316 stainless steel improves both the total tensile elongation and the swelling response for irradiation to helium and dpa levels similar to those predicted for a fusion reactor first wall environment. The improvement results from differences in the microstructural accommodation of the helium.

Table 9.4. Swelling and postirradiation ductility of 316 and titanium-modified 316 irradiated in HFIR

Helium content (appm)	Displacement damage (dpa)	Test temperature (°C)[a]	Total tensile elongation (%)	Cavity volume fraction (%)
		Annealed 316		
4100	60	575	0.82	[8][b]
3200	45	650	0.2	
4240	61	650	0	7 ± 3
3400	48	750	0.14	[8][b]
		Annealed 316 + Ti		
1850	28	575	4.5	1 ± 0.3
2450	39	650	0.7	
3300	47	650	1	3 ± 0.8
3300	45	700	1.1	[3.4][b]
3420	48	750	0	9 ± 3
		20% cold-worked 316		
34.0	1.5	575	2.5	[0.4][b]
51.0	2.5	575	2.85	
86.0	3.3	575	0.5	0.06 ± 0.03
		20% cold-worked 316 + Ti		
30	1.5	575	5.6	[0.2][b]
70	3	575	5.1	0.02 ± 0.006

[a]Irradiation temperatures were near the test temperatures shown.
[b][ ] indicated swelling measured by immersion density change.

9.8 MECHANICAL PROPERTIES OF STRUCTURAL MATERIALS

K. C. Liu

Fusion power reactors must be guarded from thermal cyclic fatigue and designed against failure by the interaction of fatigue and creep at high temperatures where the effects of thermal and radiation creep on the mechanical properties of structural materials are significant. For concepts with short burn times, high cyclic lifetime is required. For others with longer burn times, the interaction of creep and fatigue is important. In any case, creep-fatigue damage is a strong function of thermal stresses. Decreasing thermal stresses will decrease creep-fatigue and consequently increase structural lifetime.

A recent panel[20] discussed the nature of thermal stress problems in a thin walled fusion blanket and demonstrated that the severity of the thermal stress is strongly dependent on the arrangement of cooling circuits. Requirements for acceptance of a design on the basis of existing design codes were also discussed. Unfortunately, these codes do not include the effects of fast neutron irradiation, which are essential to fusion component designs.

Structural integrity of the first wall/blanket system is a crucial factor that could influence the economy of fusion power. Damages by cyclic fatigue and creep-fatigue are likely the design limitations that govern the structural life of fusion blanket systems. In designing components for fusion reactors, design analysts

are faced with a difficult task of predicting structure lifetime because the complex problems of creep-fatigue have not been well understood and the existing methods of lifetime estimates are not adequate for their design applications.

Problems of assessing cyclic creep-fatigue damage in fusion blankets and current methods of lifetime prediction have also been addressed.[21] There are difficult problems associated with using these methods in current design applications. Several methods which are still under development commonly yield a dispersion of results when applied to the same design situation. There is also a common deficiency in the treatment of stress multiaxiality, which will generally exist in the structure during operation, whereas supporting design data are mostly derived from ideal uniaxial test conditions performed in relatively short periods. The most serious deficiency in the current treatment of creep-fatigue interaction is the lack of knowledge of the effects of neutron radiation. A development effort to fill gaps in existing knowledge of the effects of neutron radiation on creep-fatigue damage needs immediate attention.

9.9 IRRADIATION EXPERIMENTS IN PROGRESS

E. E. Bloom — M. J. Kania
F. W. Wiffen — M. L. Grossbeck
A. F. Zulliger — J. W. Woods

The Radiation Effects Program is continuing to use irradiation experiments in available fission reactors to evaluate the effects on material properties that will be encountered in fusion reactor first wall and structural components. Experiments are currently under irradiation in two thermal spectrum reactors, ORR and HFIR, and in the fast spectrum reactor, EBR-II.

The first experiment for the irradiation of fusion reactor program materials in the ORR, experiment ORR-MFE-1, was built late in 1977 for irradiation beginning in 1978. The experiment contains austenitic stainless steels, austenitic stainless steel welds, nickel base, and titanium base alloys. These samples are intended for postirradiation testing to determine swelling, microstructures, tensile properties, fatigue properties, and fracture modes. The samples selected provide coverage of alloy types, compositional variations, and microstructural variations. The irradiation parameters include the temperature range 350-650°C.

Experiments in the FTP of HFIP continued through 1977. During the year 11 experiments were loaded into the reactor, and 12 experiments were removed with their scheduled irradiation completed. These experiments contained specimens of type 316 stainless steel, welds in type 316 stainless steel, Inconel 600, and PE-16. The range of irradiation temperatures was 55-700°C, and specimens included will be used for the determination of swelling, microstructures, tensile properties, and postirradiation fatigue in uniaxial, fully reversed loading.

The EBR-II row 8 experiment, for which LASL was the major experimenter, was discharged from the reactor early in 1977. ORNL specimens of type 316 stainless steel, PE-16, and several refractory alloys have been returned for tensile and microstructural examination. This sample set will provide information on the effects of helium injected prior to irradiation in the postirradiation properties of several alloys. The row 7 experiment for EBR-II was put into the reactor in January 1977, and will continue under irradiation until early 1979. This experiment includes 316 stainless steel, PE-16, and a number of vanadium and niobium base alloys. Many of the samples have helium introduced by α-injection or ^{3}T β decay. The range of irradiation temperatures is 400-700°C, and the goal maximum fluence is 4×10^{26} neutrons/m^2 (>0.1 MeV).

9.10 SPUTTERING CALCULATIONS WITH THE DISCRETE ORDINATES METHOD[22]

T. J. Hoffman — M. T. Robinson
H. L. Dodds, Jr. — D. K. Holmes

The purpose of this work is to investigate the applicability of the discrete ordinates (S_N) method to light ion sputtering problems. In

particular, the neutral particle discrete ordinates computer code ANISN was used to calculate sputtering yields. No modifications to this code were necessary to treat charged particle transport. However, a cross-section processing code was written for the generation of multigroup cross sections; these cross sections include a modification to the total macroscopic cross section to account for electronic interactions and small scattering angle elastic interactions. The discrete ordinates approach enables calculation of the sputtering yield as functions of incident energy and angle and of many related quantities such as ion reflection coefficients, angular and energy distributions of sputtering particles, the behavior of beams penetrating thin foils, etc. The results of several sputtering problems as calculated with ANISN are presented.

9.11 COMPUTER SIMULATION OF RADIATION EFFECTS IN METALS

M. T. Robinson

The computer program MARLOWE generates collision cascades in crystalline and amorphous media using the binary collision approximation to generate individual particle trajectories. The numerical model was improved in a number of respects, and both the running time and the memory requirements were significantly reduced. The program (originally written for IBM System/360 equipment) was adapted to CDC 7600 hardware and was tested on a machine at LLL using the national MFE computing network. The code runs about one-third faster on a CDC 7600 than it does on a 360/195 but is much larger. At present, displacement cascades in copper could be run on a CDC 7600 up to about 50 keV, whereas on the 360/195, energies as high as 300 keV can be achieved without reprogramming. If adequate access to the NMFECC can be assured, it can be used very effectively in damage analysis applications.

9.12 COMPUTER SIMULATION OF THE REFLECTION OF HYDROGEN, DEUTERIUM, AND TRITIUM FROM AMORPHOUS AND POLYCRYSTALLINE SOLIDS[23]

O. S. Oen M. T. Robinson

The reflection (backscattering) of 0.01 to 5-keV hydrogen, deuterium, and tritium ions (atoms) from amorphous and polycrystalline solids has been studied using the binary collision cascade program MARLOWE. Incident ions striking the target are followed collision by collision until they either emerge through the target surface or their energy falls below 1 eV. Each collision with a target atom consists of an elastic part described by a Thomas-Fermi potential and an inelastic part which is proportional to the velocity of the projectile. The targets chosen were Be, Fe, Mo, W, and composite materials such as FeH. For the latter, the sputtering yield of the light atom constituent was also calculated by following the complete collision cascade as it developed in the solid.

The reflection coefficients increase with increasing target atomic number. For 100-eV tritium ions, for instance, the reflection from amorphous tungsten is an order of magnitude larger than from beryllium. Hydrogen reflection decreases as the hydrogen content of the target increases (replacing metal atoms by hydrogen) and the reflection of hydrogen from a pure hydrogen target becomes vanishingly small. With increasing hydrogen content of the target, the sputtering yield of hydrogen increases, passes through a maximum, and then decreases almost to zero. This result may be explained by noting that most of the sputtering is produced by the reflected projectiles as they emerge through the surface.

The reflection increases with increasing incident angle such that total reflection occurs for angles greater than a critical angle. With increasing incident angle, the sputtering yield of the light atom constituent increases, goes

through a maximum, and subsequently decreases. The calculated energy spectra of reflected ions and light sputtered atoms will be discussed.

9.13 RADIATION EFFECTS ON INSULATORS FOR SUPERCONDUCTING MAGNETS

R. H. Kernohan R. R. Coltman, Jr.
C. J. Long

In order to determine the radiation stability of electrical insulation that could be used in a superconducting magnet for containment of the plasma in a fusion energy device, 55 specimens of eight types of organic insulation were irradiated to a dose of about 2×10^8 R (2×10^6 J/kg) at a temperature of 4.8 K in the Low-Temperature Irradiation Facility in the Bulk Shielding Reactor at ORNL. Four of the specimens were monitored for changes in electrical resistivity during the irradiation. The initial resistivities, which were of the order of 10^{14} Ω-cm, decreased to about 10^{13} Ω-cm under the influence of a weak radiation field. At full power reactor operation (2 MW), the resistivities dropped to about 10^{11} Ω-cm but changed little during the irradiation. Because of residual radioactivity near or in the experiment assembly, the resistivities increased after irradiation, but not to the initial values. Restoration to near the initial resistivity values was later observed upon warming the specimens to room temperature and purging the irradiation chamber. The latter result may be related to outgassing induced by the irradiation.

9.14 TRITIUM PERMEATION AND STEAM GENERATORS

J. T. Bell J. D. Redman

The tritium permeation and steam generator program is new beginning in FY 1978. The objectives are to measure tritium permeation rates through steam generator materials under conditions that are anticipated in fusion power plants and to determine effective permeation barrier characteristics of oxide coatings that are formed by the steam oxidation of the heat exchanger material. An experimental system is being designed and will be constructed by mid-FY 1979.

The initial design of the system for measuring tritium permeabilities of steam generator materials at high temperatures (400-600°C) and under dynamic high steam pressures was accomplished. This system will consist of He-T_2 feed gas flowing around or through tube type samples with steam flowing respectively through or around the tubes. Tritium that permeates from the feed gas into the steam will be determined by analysis of condensed water samples.

9.15 LITHIUM COMPATIBILITY RESEARCH - STATUS AND REQUIREMENTS FOR FERROUS MATERIALS

J. E. Selle D. L. Olson

Studies to date on lithium corrosion in ferrous materials show that lithium is more corrosive toward stainless steels than is sodium. Pure iron has excellent resistance to lithium, but the corrosion rate increases with increasing nickel content. Solution, intergranular, and dissimilar metal mass transport mechanisms limit the maximum operating temperature of different alloy systems. Nitrogen is an especially detrimental impurity in lithium and causes accelerated mass transport in type 316 stainless steel loops. Getters such as calcium, which tie up the nitrogen, can reduce the adverse effects considerably. Aluminum additions to lithium result in the formation of intermetallic compounds on the surface of type 316 stainless steel and reduce the weight loss at 600°C by a factor of four. Extensive work is needed to define the corrosion limits for ferrous materials of interest for fusion reactor applications.

9.16 COMPATIBILITY STUDIES OF POTENTIAL MOLTEN SALT BREEDER REACTOR MATERIALS IN MOLTEN FLUORIDE SALTS

J. R. Keiser

This report summarizes the molten fluoride salt compatibility studies carried out during the period 1974-76 in support of the Molten Salt Reactor Program. Thermal convection and forced circulation loops were used to measure the corrosion rate of selected alloys. Results confirmed the relationship of time, initial chromium concentration, and mass loss developed by previous workers. The corrosion rates of Hastelloy N and Hastelloy N modified by the addition of 1-3 wt % Nb were well within the acceptable range for use in an MSBP.

REFERENCES

1. J. O. Stiegler and T. C. Reuther, "The Program for Alloy Development for Irradiation Performance in Fusion Reactors," pp. 51-57 in *Symposium on Neutron Cross-Sections from 10 to 40 MeV*, held at Brookhaven National Laboratory (May 3-5, 1977), ed. M. R. Bhat and S. Pearlstein, National Nuclear Data Center, Brookhaven National Laboratory, Upton, N.Y., July 1977.
2. C. J. McHargue and J. L. Scott, "Materials Requirements for Fusion Reactors," *Metall. Trans.* 9A:151-59 (February 1978).
3. T. A. Gabriel, B. L. Bishop, and F. W. Wiffen, *Calculated Irradiation Response of Materials Using a Fusion-Reactor First-Wall Neutron Spectrum*, ORNL/TM-5956, Oak Ridge, Tennessee (June 1977); to be published in *Nucl. Technol.*
4. T. A. Gabriel and B. L. Bishop, *Sensitivity of Primary Knock-on Atom Spectra and Displacement per Atom Cross Sections to Different Secondary Neutron Energy and Angular Distributions and "In-Group" Weighting Schemes*, ORNL/TM-6108, Oak Ridge, Tennessee (January 1978).
5. J. A. Horak and J. H. Swanks, "Use of Fission Reactors for Fusion Reactor First-Wall Studies," (Summary) *Trans. Am. Nucl. Soc.* 26(TANSAO 26), 187-88 (June 1977).
6. F. W. Wiffen and E. E. Bloom, "Effect of High Helium Content on Stainless-Steel Swelling," *Nucl. Technol.* 25, 113-23 (1975).
7. E. E. Bloom and F. W. Wiffen, "The Effects of Large Concentrations of Helium on the Mechanical Properties of Neutron-Irradiated Stainless Steel," *J. Nucl. Mater.* 50, 171 (1975).
8. P. J. Maziasz, F. W. Wiffen, and E. E. Bloom, "Swelling and Microstructural Changes in 316 Stainless Steel Irradiated Under Simulated CTR Conditions," *Rad. Eff. and Tritium Tech. in Fusion Reactors*, CONF-750989, Vol. I, pp. 259-88 (1976).
9. J. A. Horak, "Use of Fission Reactors for CTR Bulk Radiation Effects Studies," pp. 830-41 in *Proc. Int. Conf. Radiation Test Facilities for the CTR Surface and Materials Program*, at Argonne National Laboratory, ANL/CTR-75-4.
10. J. A. Horak, J. O. Stiegler, and F. W. Wiffen, "Evaluation of Fission Reactors for CTR Materials Development," *Trans. Am. Nucl. Soc.* 22(TANSAO 22), 172-74 (November 1975).
11. E. E. Bloom, F. W. Wiffen, P. J. Maziasz, and J. O. Stiegler, "Temperature and Fluence Limitations for a Type 316 Stainless-Steel Controlled Thermonuclear Reactor First Wall," *Nucl. Technol.* 31, 115-22 (1976).
12. M. Roberts et al., *Oak Ridge Tokamak Experimental Power Reactor Study Reference Design*, ORNL/TM-5042, Oak Ridge, Tennessee (November 1975).
13. W. M. Stacey, Jr. et al., *Tokamak Experimental Power Reactor Studies*, ANL/CTR-75-2 (1975).
14. *Experimental Power Reactor Conceptual Design Study 12-Month Progr. Rep. June 1, 1974 through June 30, 1975*, GA-A13534 (1975).

15. *Summary of the Proceedings of the Workshop on Conceptual Design Studies of Experimental Power Reactor-1*, Oak Ridge, Tennessee, Sept. 9-10, 1975, M. Murphy and J. Neff, Eds., ERDA-69 (November 1975).

16. P. J. Maziasz and F. W. Wiffen, "The Unique Role of HFIR in Fusion Reactor Materials Evaluation," (Summary) *Trans. Am. Nucl. Soc.* 26(TANSAO 26), 189-90 (June 1977).

17. F. W. Wiffen, abstract for an invited presentation given in the Panel Session, "Structural Mechanics Problems of Fusion Power Reactors," at the *4th International Conference on Structural Mechanics in Reactor Technology*, San Francisco, August 15-19, 1977.

18. P. J. Maziasz and E. E. Bloom, "Comparison of 316 + Ti with 316 Stainless Steel Irradiated in a Simulated Fusion Environment," (Summary) *Trans. Am. Nucl. Soc.* 27(TANSAO 27), 268-69 (November-December 1977).

19. E. E. Bloom, J. M. Leitnaker, and J. O. Stiegler, "Effect of Neutron Irradiation on the Microstructure and Properties of Titanium – Stabilized Type 316 Stainless Steels," *Nucl. Technol.* 31, 232-43 (November 1976).

20. E. S. Bettis et al., *Proc. 7th Symp. on Engineering Problems of Fusion Research*, Vol. II, pp. 1453-1458 (1977).

21. K. C. Liu, ibid., Vol. II, pp. 1495-1500 (1977).

22. Abstract of paper presented at the American Nuclear Society Winter Meeting, San Francisco, California (November 29, 1977).

23. Abstract of paper to be presented at the *3rd Int. Conf. on Plasma Surface Interactions in Contr. Fusion Devices*, Culham Lab., Abingdon, Oxfordshire, U.K. (April 3-7, 1978).

NEUTRON TRANSPORT

R. G. Alsmiller, Jr.[1]
J. Barish[2]
J. M. Barnes[2]
B. L. Bishop[2]
G. T. Chapman[1]
T. A. Gabriel[1]
R. A. Lillie[1]
B. F. Maskewitz[1]
J. T. Mihalczo[3]
G. L. Morgan[1]
E. M. Oblow[1]
F. G. Perey[1]
R. W. Roussin[1]
R. T. Santoro[1]
Y. Seki[4]
J. S. Tang[2]
D. K. Trubey[1]

Abstract. The neutron transport program is primarily analytic, but it also includes an experimental program. The experimental program is designed to provide the data necessary to verify the analysis methods and cross section data that are used at ORNL and throughout the United States for fusion reactor neutronics design calculations. During the past year a variety of neutronics calculations have been carried out in support of design work at ORNL and at the Princeton Plasma Physics Laboratory.

10.1 BLANKET AND SHIELD INTEGRAL EXPERIMENT AND ANALYSIS

G. T. Chapman
E. M. Oblow
R. T. Santoro
G. L. Morgan
F. G. Perey
Y. Seki

The design and construction of the 14-MeV neutron integral experiment facility was completed in 1977. The facility will produce up to 10^{10} neutrons/sec, and measurements of both neutron and gamma ray transmissions through up to 1 m of shield material can be measured (i.e., up to 10^6 material plus geometric attenuations). Preliminary measurements were made without shield materials in place, and these agreed well with two-dimensional transport calculations modeling the whole facility.

Analytic activity focused on the preanalysis of the first two experiments planned for 1978. A preliminary design for the first attenuation experiment was completed, and work was initiated to design the first streaming experiment. The attenuation experiment was designed to resemble a size-optimized inner toroidal shield for a large tokamak reactor (i.e., TNS). The experimental shield will consist of 35 cm of stainless steel followed by 25 cm of alternating 5-cm layers of stainless steel and borated polyethylene. Neutron and gamma ray spectral measurements will be made with an NE-213 detector at various stages of construction of the full 60-cm shield (six intermediate experiments are currently planned). Sensitivity studies for all of these planned measurements were also carried out to see what radiation transport and production processes are most important in such a shield. Very high sensitivity to 14-MeV neutron transport was observed.

10.2 TFTR NEUTRAL BEAM INJECTOR SHIELDING

R. T. Santoro
R. G. Alsmiller, Jr.
R. A. Lillie
J. M. Barnes

Two-dimensional discrete ordinates and three-dimensional Monte Carlo radiation transport calculations were carried out to estimate

---

1. Neutron Physics Division.
2. Computer Sciences Division.
3. Instrumentation and Controls Division.
4. Visiting scientist from the Division of Thermonuclear Fusion Research, Japan Atomic Energy Research Institute, Tokai Research Establishment, Japan.

the spatial dependencies of the nuclear heating rates and neutron and gamma ray scalar fluxes in the components of the neutral beam injectors being designed for the TFTR.[2] The nuclear responses were obtained for the radiation streaming from the plasma through the injector port and for the radiation leaking through the concrete igloo shield that surrounds the reactor. The analysis was performed using accurate representations of the radiation sources, and the neutral beam injector was modelled in the detail commensurate for each radiation transport calculation. The nuclear heating rates in the cryopanels that line the injector were found to range from $\sim 5 \times 10^{-3}$ W/cm^3 at the front of the injector to $\sim 6 \times 10^{-6}$ W/cm^3 at the rear of the injector.

10.3 NEUTRON COLLIMATOR DESIGN CALCULATIONS

R. A. Lillie R. G. Alsmiller, Jr.
J. T. Mihalczo

The TFTR at Princeton University and the ORMAK Upgrade at Oak Ridge National Laboratory will require neutron collimators to obtain spatially resolved neutron spectrum measurements that can be used to infer such quantities as ion temperature and toroidal drift motion. To aid in the design of these collimators, a number of SS-316 right circular cylindrical shells of varying lengths were analyzed using the two-dimensional discrete ordinates DOT[3] code system together with first and last flight particle estimator techniques to determine direct and background detector responses.

The results of this investigation identified the 14-MeV neutrons that scatter in the SS-316 immediately adjacent to the collimator opening (air column liner) as the dominant contributor to detector background.[4] Although collimator lengths greater than 60 cm were sufficient to attenuate uncollided background neutrons, lengths over 100 cm were needed to reduce the 14-MeV scattered background to acceptable levels. The calculated lower energy neutron background and the photon background levels were not found to be significant.

10.4 NEUTRONICS ANALYSIS FOR FUSION REACTOR DESIGN

R. T. Santoro J. S. Tang
T. A. Gabriel J. M. Barnes

Neutronics analyses have also been carried out in support of a variety of fusion reactor designs. These include TNS, EBTR, and ORMAK Upgrade. Calculations were carried out to identify the effects of shield penetration on a generic class of fusion reactors.[5] Calculations for EBTR were performed as part of a design team effort to identify a plausible design concept. The results of one-dimensional calculations identified the nuclear heating, radiation damage, and tritium breeding parameters for a lithium laden stainless steel-supported blanket design.[6] A study of the sensitivity of the first wall radiation damage to blanket composition to the first wall thickness also resulted from the EBTR studies.[7]

Two-dimensional discrete ordinates calculations were performed to identify a suitable biological shield design for an upgraded ORMAK machine.

10.5 RADIATION SHIELDING INFORMATION CENTER

B. F. Maskewitz R. W. Roussin
D. K. Trubey

The Radiation Shielding Information Center (RSIC), established in 1962, serves its user community by collecting, organizing, processing, evaluating, packaging, and disseminating information related mainly to reactor and weapons radiation. The scope includes the physics of interaction of radiation with matter, radiation production and transport, radiation detectors and measurements, engineering design techniques, shielding materials properties, computer codes useful in research and design, and nuclear data compilations. Originally established to support research related to fission, RSIC now supports fusion reactor technology. The major activities include (1) operating a computer-based information system and answering inquiries; (2) collecting, testing, packaging, and distributing

computer codes; and (3) those activities associated with evaluated and processed nuclear data libraries.

All RSIC activities contribute to the fusion technology program, but perhaps the most significant are those associated with the DOE-OFE Data Center. The Center includes a clearinghouse for evaluated cross sections and the generation, packaging, and distribution of a general purpose coupled neutron and gamma ray cross-section library for use in radiation transport and neutronics studies. In CY 1977, DLC-41/VITAMIN C, a 171-neutron, 36-gamma ray group, 36-materials data library was validated and made generally available. Several more problem-dependent data libraries were derived from this fine group set.

The RSIC data base increased in each subtask during the year:

(1) literature – 6000 citations[6] may be accessed on DOE-RECON, 40 RSIC reports issued with several volumes in series;
(2) codes collection – 309 complex shielding code packages[9] and 116 auxiliary data processing packages;[10]
(3) data collection – 51 data library packages[11] and additional working cross-section libraries maintained for DOE-OFE and DNA sponsors.

The RSIC newsletter distribution is ~1400. Volume V of the shielding bibliography series[8] was issued.

RSIC latest user statistics (FY 1977) indicate that 3307 separate letters and telephone calls (~13.2/workday) were processed during the year, a 50% increase over the previous year, and 96 visitors were received. The fusion research community accounted for ~15% of the total number of requests.

REFERENCES

1. Y. Seki, R. T. Santoro, E. M. Oblow, and J. L. Lucius, "Macroscopic Cross Section Sensitivity Study for the TNS Integral Experiments," submitted for presentation at the Annual Meeting of the American Nuclear Society, San Diego, California, June 18-23, 1978.
2. R. T. Santoro, R. A. Lillie, R. G. Alsmiller, Jr., and J. M. Barnes, "Two- and Three-Dimensional Neutronics Analysis of the TFTR Neutral Beam Injectors," submitted for presentation at the Annual Meeting of the American Nuclear Society, San Diego, California, June 18-23, 1978.
3. W. A. Rhoades and F. R. Mynatt, *The DOT III Two-Dimensional Discrete Ordinates Transport Code*, ORNL/TM-4280, Oak Ridge, Tennessee (1973).
4. R. A. Lillie, R. G. Alsmiller, Jr., and J. T. Mihalczo, Trans. Am. Nucl. Soc. 27, 797 (1977).
5. R. T. Santoro et al., Nucl. Tech. 37, 65 (1978).
6. R. T. Santoro and J. M. Barnes, *Nuclear Performance Calculations for the UWMAK Tokamak Torus Reactor (EBTR) Reference Design*, ORNL/TM-6085, Oak Ridge, Tennessee (1977).
7. J. M. Barnes, R. T. Santoro, and T. A. Gabriel, *The Sensitivity of the First-Wall Radiation Damage to Fusion Reactor Blanket Composition*, ORNL/TM-6105, Oak Ridge, Tennessee (1977).
8. D. K. Trubey, R. W. Roussin, J. Gurney, and A. B. Gustin, *Bibliography, Subject Index, and Author Index of the Radiation Shielding Information Center (Reactor and Weapons Radiation Shielding)*, ORNL/RSIC-5, Vol. I-V, Oak Ridge, Tennessee (1978).
9. Betty McGill, Betty F. Maskewitz, C. Marie Anthony, Hemma E. Comolander, and Henrietta R. Hendrickson, *Abstracts of Digital Computer Code Packages Assembled by the Radiation Shielding Information Center*, ORNL/RSIC-13, Vol. I-IV, Oak Ridge, Tennessee (1976, updated 1978).
10. Betty F. Maskewitz, *Abstracts of Peripheral Shielding Code Packages Assembled by the Radiation Shielding Information Center*, ORNL/RSIC-31, Vol. I, Oak Ridge, Tennessee (updated 1978).
11. Robert W. Roussin, *Abstracts of the Data Library Packages Assembled by the Radiation Shielding Information Center*, ORNL/RSIC-30, Vol. I, Oak Ridge, Tennessee (1972).

MANAGEMENT SERVICES

R. H. Dilworth, Section Head

S. K. Adkins	R. P. Jernigan	E. T. Rogers*,[1]
D. R. Alford	B. L. Johnson[1]	E. M. Ruckart
A. B. Barnette	M. N. Johnson	W. K. Russell
D. P. Brooks	P. B. Johnston[1]	C. M. Sekula
J. L. Burke	J. A. Kelman[1]	D. G. Sharp
E. L. Cagle[1]	M. G. Kincaid[1]	A. V. Snodgrass
C. J. Chamberlain	J. K. Lovin	S. E. Stockbridge[1]
C. H. Cox	J. B. Martin*,[1]	B. L. Straine
M. V. Dunn	B. J. McClure[1]	C. S. Strickler[1]
R. S. Edwards	J. C. Neeley[1]	C. K. Thomas
J. C. Ezell	B. L. Pope	D. Y. Ware[1]
H. W. Jernigan	P. N. Rader[2]	E. L. Watkin[1]
J. R. Jernigan	M. C. Rhea*	E. E. Webster[1]

E. R. Wells C. Whitmire, Jr.

Abstract. The Management Services Section completed its first full year as a section charged with providing coordinated professional administrative services to the Fusion Energy Division. A permanent section head was employed in June 1977. The addition of two financial assistants in the Finance Office proved valuable in both year-end closing and budget preparation. Subcontract activity with industry continued to grow, with $5 million now in force. The capabilities of the FED Communications Center were increased to keep pace with increased publication activity. The FED Management Information System upgraded the Procurement Module, initiated the Personnel Module, and extended its activities outside the Division. The Engineering Services Group handled major GPP additions during the year. Both the Quality Assurance and the Safety programs initiated formal training for Division staff.

11.1 INTRODUCTION

The Management Services Section was formed just over a year ago to provide coordinated professional administrative services for the Fusion Energy Division, thus enhancing the technical efforts of the Division staff. Included in the work of the section are the finance, general administrative, personnel, engineering services, purchasing coordination, management information, technology commercialization, and communications center functions of the Division.

The section was headed temporarily by the Associate Division Director until June 1977, when a permanent Section Head was employed. During the year, two minor organization changes were made within the section. The purchasing coordination and expediting function was moved into the Engineering Services group to provide better work load leveling, and the emergency planning function of the Division was combined with the safety program. Both of these changes are reflected in the organization chart for FED (Fig. 11.1). The year just concluded was one in which the concept of a centralized section for management services matured into a functional entity. Highlights of these activities follow.

---

*Part-time.

1. Information Division.
2. Finance and Materials Division.

BLANK PAGE

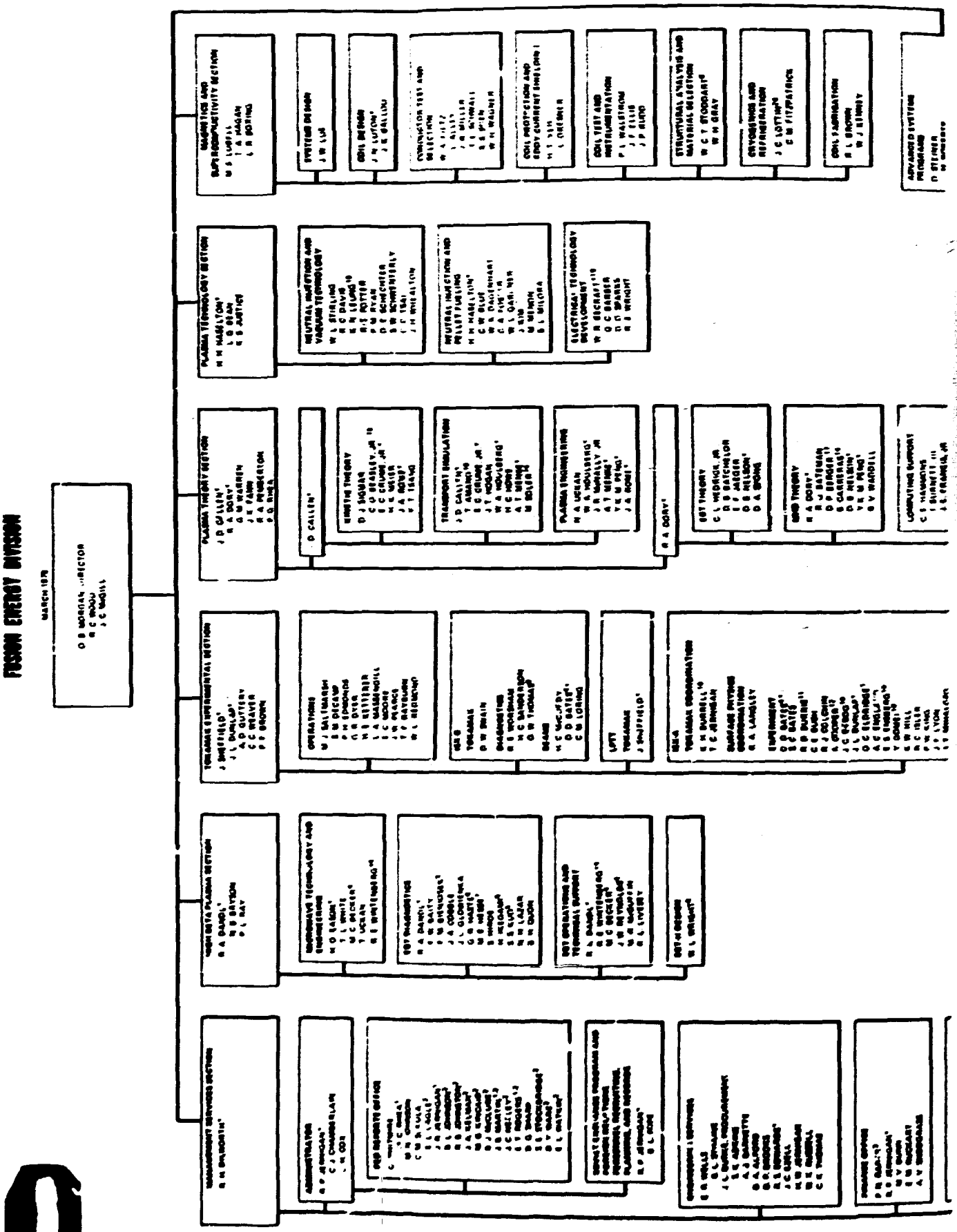

Fig. 11.1. Fusion Energy Division organizational chart.

BLANK PAGE

11.2 FINANCE OFFICE

During this year two Financial Assistants were added to the Finance Office to act as liaison to the technical sections and programs of the Division. Their value was especially noteworthy in the difficult task of closing the budget year and in financial planning for the following year.

The funding trends for the Division have slowed from the rapid growth of prior years, as illustrated in Fig. 11.2 for the entire Division, and in Table 11.1 for the various activities of the Division. Under these changing circumstances, the role of the Finance Office must include scrutiny of accounts and careful cost projections. In addition, important negotiations were supported in which the costs charged the Division by other organizations were determined.

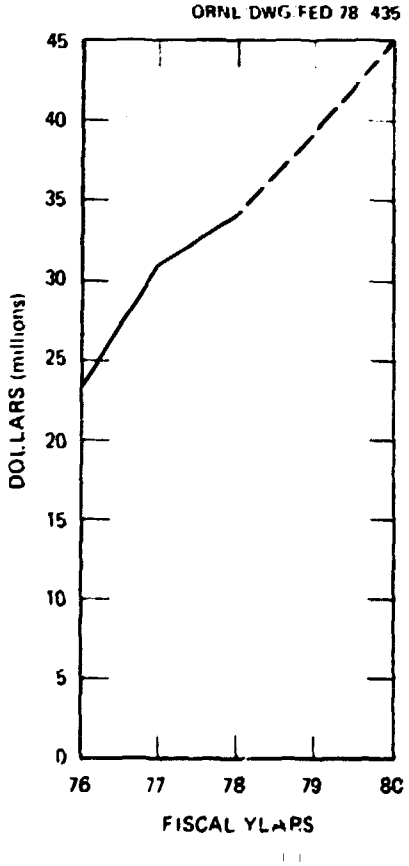

Fig. 11.2. FED funding projection.

The Finance Office continues to provide monthly reports of the status of each funded activity in the Division, working with the section and program heads to properly plan manpower and procurement needs within the budget constraints. It also operates the coordinated work order control system for the Division. This office is also the focal point, through the Financial Assistants, for preparation of Forms 189 for future funding of all Division programs.

11.3 OFFICE OF THE ADMINISTRATOR

Most of the general administrative functions of the Division are handled or coordinated by this office. Some highlights follow.

11.3.1 Personnel Functions

During the past year arrangements were made for interviews with 54 prospective employees, 19 of whom accepted employment. Eleven new employees transferred from other ORNL organizations. Twenty-two guest assignments were processed, by which nonemployees participate in Division programs. The Division personnel files were completely revised to conform with new guidelines.

11.3.2 Visitors

During the past year arrangements were made for 1977 visitors to the Division, including 225 noncitizens.

11.3.3 Subcontracts

The involvement of industry in the work of the Division, first begun in 1976, expanded considerably in 1977, with the total value of contracts to industry exceeding $5 million. In addition to continuing programs in TNS studies and in microwave power tube development, three major contracts were initiated for fabrication of prototype fusion reactor magnet coils as a part of the Large Coil Program. These activities constitute a major technology commercialization effort through which industry becomes involved with the technology of fusion power.

Table 11.1. FED activity funding

Activity	Dollars in thousands					
	FY 76 Actual cost	FY 77 Actual cost	FY 78 Funding as of March 78	FY 78 Total expected funding	FY 79 Presidential budget	FY 80 Projected budget from OFE
Confinement systems — tokamak systems — research operations	3,846	6,811	5,550	5,740	9,000	10,900
Confinement systems — tokamak systems — major device fabrication	2,534	4,574	4,850	4,850	3,000	2,000
Confinement systems — magnetic mirror systems — research operations	1,080	1,969	2,250	2,400	2,250	2,500
Confinement systems — magnetic mirror systems — major device fabrication	0	178	200	200	0	0
Confinement systems — design and engineering	441	721	900	900	1,150	0[a]
Total confinement systems	$ 7,901	$15,253	$13,750	$14,090	$15,400	$15,400
Development and technology — magnetic systems	3,367	5,691	7,200	7,200	11,400	13,400
Development and technology — plasma engineering	4,998	6,063	5,525	5,525	5,600	6,825
Development and technology — fusion reactor materials	1,016	1,645	2,940	2,940	2,205	3,460
Development and technology — fusion systems engineering	789	814	970	1,020	970	2,250[a]
Development and technology — environment and safety	0	0	60	60	60	100
Total development and technology	$10,170	$14,213	$16,695	$16,745	$20,235	$26,035
Applied plasma physics — fusion plasma theory	1,804	2,063	2,200	2,200	2,300	2,400
Applied plasma physics — experimental plasma research	580	643	920	920	920	925
Applied plasma physics — national MFE computer network	0	271	150	150	290	340
Total applied plasma physics	$ 2,384	$ 3,177	$ 3,270	$ 3,270	$ 3,510	$ 3,665
Reactor projects — TFTR	0	321	0	0	0	0
Total reactor projects	0	$ 321	0	0	0	0
Total ORNL funding	$20,455	$32,964	$33,715	$34,105	$39,145	$45,100

[a] TNS is classified under Development and Technology — Fusion Systems Engineering for FY 1980. The TNS projected budget for FY 1980 is $600K.

11.3.4 FED Communications Center

This new name replaces the former "Reports Office" to reflect more accurately the broad range of services provided by this group. The center provides a complete documentation service which includes editorial review, typing, drafting, photographic art, and copying services. During 1977, 59 numbered reports, 47 journal articles, and 199 meeting papers were published; 265 abstracts were processed. The graphics group prepared approximately 2000 drawings, 1000 viewgraphs, and 2000 transparencies by the POS 1 and COLOR POS process. The addition of a 9200 Xerox copier with operator has enabled one-day service for large copying and collating requests.

Growth of this group has continued in order to keep pace with the increasing publication output of the Division; furthermore, while the volume of work has increased, the average processing time has decreased. Our records continue to verify the productivity and cost-effectiveness of this group.

11.3.5 Administrative Guidelines

The FED Administrative Guidelines, initiated in 1976, were updated by the revision of six of the fourteen chapters, reflecting changes in or additions to applicable procedures. These guidelines cover administrative situations unique to the Division and serve as a supplement to the Nuclear Division Office Guide, the ORNL Style Manual, and the Standard Practice Procedures.

11.4 MANAGEMENT INFORMATION SYSTEM

The Management Information System (MIS) activity completed its first full year of operation. The purpose of the system is to provide the Division Director, section heads, and program managers with timely and relevant information needed to maintain control of costs and adherence to schedules.

Most of the effort this year was directed toward improvements in the Procurement Module of the MIS.[1] These improvements provide more accurate data on accounts payable transactions as well as more control by the user on the selection of data. Weekly updates from the financial accounting system revise cost commitment data to reflect recent payments as well as to provide a check on the data. These checks and the resulting corrections are accomplished by a software routine without manual involvement in most cases. Reports from users and computer usage records indicate that the module is in wide use.

The demonstrated usefulness of the FED Procurement Module prompted a request from the Engineering Technology Division to set up a similar system for the procurements related to that division, and this was accomplished.

Work continued to provide a project scheduling capability for the Division and its related engineering organizations. Several PERT (Program Evaluation and Review Techniques) programs were evaluated; one was selected,[2] and it is now being checked out on the FED computer. User classes have been scheduled, and use of the system will begin shortly.

Two new MIS modules were initiated. The Labor Module will provide weekly updated data on nondivisional labor charges to aid program managers in cost control. The Personnel Module provides means for computer-generated personnel reports and information. Both of these new modules are in early stages of development.

11.5 ENGINEERING SERVICES, QUALITY ASSURANCE, SAFETY AND EMERGENCY PLANNING, AND PROCUREMENT EXPEDITING

11.5.1 Engineering Services

The Engineering Services group provides all of the nonprogrammatic engineering work and coordination for the Division. This includes coordination of machine shop work, maintenance craft work, inventory and storage of equipment and materials, and the coordination of Division requests for General Plant Projects, General Plant Equipment, and Line Item facility improvements. It is also responsible for the maintenance of buildings, facilities, and equipment,

and for planning of future facilities. Some of the highlights of this activity in the past year include:

(1) completion of 5 GPP and 17 expense type projects;
(2) initiation of 1 GPP, 17 expense, and 4 equipment projects; and
(3) coordination of 37 man-years of machine shop work in Y-12 shops, and 18 man-years in X-10 shops.

A lump sum subcontract bid package was prepared for a demineralized water system for Building 9204-1. An architect-engineer subcontractor was assigned to provide detailed design for the GPP office and laboratory space addition to Building 9201-2. Coordination was provided for the new telephone system to be installed in 1979.

11.5.2 Safety and Emergency Planning

The Division safety program includes safety and fire inspections plus six formal training sessions per year for all Division personnel. A formal training program was instituted for indoctrination in both plant and Division emergency procedures.

11.5.3 Quality Assurance

The quality assurance program for FED continues to be a model operation for ORNL. The program extends to all shop work, field assembly, and engineering, and continues to be effective in ensuring reliable and cost-effective experimental equipment. A comprehensive training program in quality assurance was instituted for all Division personnel.

11.5.4 Procurement Expediting

The procurement expediting function was placed in the Engineering Services group to obtain advantages of work load leveling among a larger group of people and to provide closer coordination with the material control and inventory function. During 1977 this activity processed 1700 requisitions for materials, equipment, and services, representing a volume of over $10 million. Further improvements were made during the year in the interaction of procurement expediting with the MIS Procurement Module, including a routine computer generated expediting report to the purchasing department on late or critical purchased items.

11.6 TECHNOLOGY UTILIZATION

The Fusion Energy Division is deeply involved in the transfer of fusion technology to industry. Subcontracts with a number of industrial companies now total $5 million. The types of contracts in force include:

(1) studies of fusion technology problems by industry personnel at both ORNL and at the contractor's plant,
(2) fabrication contracts for newly developed equipment,
(3) contracts to obtain industry personnel having unique technical experience for work at ORNL, and
(4) development contracts for advancing the state of industrial art in technical areas essential to Division programs.

Through the Division Technology Utilization and Commercialization Officer, the Division program is closely coordinated with the ORNL program.

11.7 FED LIBRARY

The FED Library maintains a specialized collection of books, technical reports, and scientific journals pertinent to the fields of plasma physics and fusion energy technology. In addition, it functions as a branch of the ORNL Central Research Library, with professional librarian assistance to aid in document location and retrieval problems. Particular goals of the library this year were current awareness of publications in the pertinent fields and suitable additions to the library collection. Activity in the area of automated literature search included the addition of Bibliographic Retrieval

Services (BPS), including Physics Abstracts and Dissertation Abstracts data bases, which will be of particular value to this Division. Other bibliographic services available are DOE Recon, SDC's Orbit, Lockheed's Dialog, New York Times Information Bank, and NASA Recon.

REFERENCES

1. J. K. Lovin and B. A. Clark, *Procurement Module for a MIS: User's Manual*, ORNL/TM-5854, Oak Ridge, Tennessee (March 1977).
2. The New PERT6, Dynamic Solutions Incorporated, Hartsdale, New York (October 1977).

LIST OF ABBREVIATIONS

ADI	alternating direction implicit
AEDC	Arnold Engineering Development Center
AES	Auger electron spectroscopy
appm	atomic parts per million
ARE	aspect ratio enhancement
ATC	Adiabatic Toroidal Compressor
CCW	counterclockwise
CPFF	cost plus fixed fee
CPM	Collisional Plasma Model
CW	clockwise
cw	continuous wave
Demo	Demonstration Reactor
DIIE	Divertor Injector Tokamak Experiment
DMFE	Division of Magnetic Fusion Energy (now Office of Fusion Energy)
DNA	Defense Nuclear Agency
DOE	Department of Energy (formerly ERDA)
dpa	displacement per atom
D-T	deuterium-tritium
EBR-II	Experimental Breeder Reactor II (Idaho)
EBT	ELMO Bumpy Torus
EBTR	ELMO Bumpy Torus Reactor
EBT-S	ELMO Bumpy Torus Scale Experiment
ECH	electron cyclotron heating
ECRH	electron cyclotron resonant heating
EF	equilibrium field
EPR	Experimental Power Reactor
ERDA	Energy Research and Development Administration (now Department of Energy)
FCT	flux conserving tokamak
FED	Fusion Energy Division
FIR	far infrared
FWHM	full width at half maximum
HFIR	High Flux Isotope Reactor
HPTF	High Power Test Facility
HWHM	half width at half maximum
IAEA	International Atomic Energy Agency
IFR	impurity flow reversal
IMP	Injection into Microwave Plasma
ISX	Impurities Study Experiment
JET	Joint European Torus Tokamak
ksi	thousand pounds per square inch
LASL	Los Alamos Scientific Laboratory
LCP	Large Coil Program
LCPTF	Large Coil Program Test Facility
LCS	Large Coil Segment
LCSTF	Large Coil Segment Test Facility
LMFBR	Liquid Metal Fast Breeder Reactor
LPTT	Long Pulse Technology Tokamak
L/R	ratio of inductance to resistance
MCDT	moving coil displacement transducer
METF	Medium Energy Test Facility
MFE	magnetic fusion energy
MFR	magnetic fusion reactor
MHD	magnetohydrodynamic
MIS	Management Information System
MIT	Massachusetts Institute of Technology
MSBR	molten salt breeder reactor
NASA	National Aeronautics and Space Administration
NBS	National Bureau of Standards
NMFECC	National Magnetic Fusion Energy Computing Center
OFE	Office of Fusion Energy (formerly DMFE)
OH	ohmic heating
ORMAK	Oak Ridge Tokamak

BLANK PAGE

ORNL	Oak Ridge National Laboratory
ORR	Oak Ridge Research Reactor
PDX	Poloidal Divertor Experiment
PEPR	Prototype Experimental Power Reactor
PERT	Program Evaluation and Review Techniques
PF	poloidal field
PKA	primary knock-on atom
PLT	Princeton Large Torus
PPPL	Princeton Plasma Physics Laboratory
psi	pounds per square inch
PTP	peripheral target position
rf	radio frequency
RHEL	Rutherford High Energy Laboratory
RSIC	Radiation Shielding Information Center
SCR	silicon controlled rectifier
SIMS	secondary ion mass spectroscopy
SOR	successive overrelaxation
SS	stainless steel
TEA	transversely excited atmospheric pressure
TEXT	Texas Tokamak
TF	toroidal field
TLD	thermoluminescent dosimeter
TFTR	Tokamak Fusion Test Reactor
TNS	The Next Step (Tokamak)
TSTA	Tritium Systems Test Assembly
TTAP	Technology Test Assembly with Plasma
UDB	unified data base
USC	User Service Center
VCD	Vacuum Components Development (Program)
VF	vertical field
vuv	vacuum ultraviolet
0-D	zero-dimensional
1-D	one-dimensional
2-D	two-dimensional
3-D	three-dimensional

PUBLICATIONS, PAPERS, AND REPORTS

BOOKS AND JOURNAL ARTICLES

G. Bateman, Y-K. M. Peng, "Magnetohydrodynamic Stability of Flux-Conserving Tokamak Equilibria," Phys. Rev. Lett. 38, 829 (1977).

C. O. Beasley, Jr., J. E. McCune, H. K. Meier, W. I. van Rij, "Numerical Study of Drift-Kinetic Evolution of Collisional Plasmas in Tori," Plasma Phys. 19, 593 (1977).

D. Berger, R. Gruber, F. Hoffmann, V. K. Nugyen, "Effect of Current Peaking on Non-Circular Uniaxial Tokamak Equilibria," Nucl. Fusion 17, 1095 (1977).

L. A. Berry, C. E. Bush, J. D. Callen, R. J. Colchin, J. L. Dunlap, P. H. Edmonds, A. C. England, C. A. Foster, J. H. Harris, H. C. Howe, R. C. Isler, G. L. Jahns, H. E. Ketterer, P. W. King, J. F. Lyon, J. T. Mihalczo, M. Murakami, R. V. Neidigh, G. H. Neilson, V. K. Paré, D. L. Shaeffer, D. W. Swain, J. B. Wilgen, W. R. Wing, S. J. Zweben, "Confinement and Neutral Beam Injection Studies in ORMAK," *Plasma Physics and Controlled Nuclear Fusion Research*, Vol. I, 49 (IAEA, Vienna, 1977).

D. S. Burch, J. H. Whealton, "Monte Carlo Calculation of Electron Back Diffusion in a Townsend Discharge," J. Appl. Phys. 48, 2213 (1977).

J. D. Callen, "Drift-Wave Turbulence Effects on Magnetic Structure and Plasma Transport in Tokamaks," Phys. Rev. Lett. 39, 1540 (1977).

J. D. Callen, J. F. Clarke, R. A. Dory, J. A. Holmes, F. B. Marcus, D. G. McAlees, J. R. Moore, D. B. Nelson, Y-K. M. Peng, R. O. Sayer, D. J. Sigmar, D. J. Strickler, K. T. Tsang, N. A. Uckan, "Tokamak Plasma Magnetics," *Plasma Physics and Controlled Nuclear Fusion Research*, Vol. II, 369 (IAEA, Vienna, 1977).

J. D. Callen, G. L. Jahns, "Experimental Measurement of Electron Heat Diffusivity in a Tokamak," Phys. Rev. Lett. 38, 491 (1977).

B. Carreras, B. V. Waddell, "Analytic Study of the Interaction of Tearing Modes of Different Helicity," Bull. Am. Phys. Soc. 22, 1171 (1977).

P. J. Catto, K. T. Tsang, "Linearized Gyro-Kinetic Equation with Collisions," Phys. Fluids 20, 396 (1977).

J. F. Clarke, D. J. Sigmar, "High-Pressure Flux-Conserving Tokamak," Phys. Rev. Lett. 38, 70 (1977).

D. Dobrott, D. B. Nelson, J. M. Greene, A. H. Glasser, M. S. Chance, E. A. Frieman, "Theory of Ballooning Modes in Tokamak with Finite Shear," Phys. Rev. Lett. 39, 943 (1977).

R. A. Dory, Y-K. M. Peng, "High Pressure Flux-Conserving Tokamak Equilibria," Nucl. Fusion 17, 21 (1977).

C. A. Foster, R. J. Colchin, S. L. Milora, J. Kim, R. J. Turnbull, "Solid Hydrogen Pellet Injection into the ORMAK Tokamak," Nucl. Fusion 17, 1067 (1977).

W. H. Gray, J. K. Ballou, "Electromechanical Stress Analysis of Transversely Isotropic Solenoids," J. Appl. Phys. 48(7), (July 1977).

L. R. Grisham, C. C. Tsai, J. H. Whealton, W. L. Stirling, "Effect of Emission Aperture Shape upon Ion Optics," Rev. Sci. Instrum. 48, 1037 (1977).

C. L. Hedrick, R. A. Dandl, J. A. Cobble, R. A. Dory, H. O. Eason, E. G. Harris, G. R. Haste, H. Ikegami, E. F. Jaeger, N. H. Lazar, D. H. McNeill, D. G. McAlees, D. B. Nelson, L. W. Owen, D. A. Spong, N. A. Uckan, "Transport and Scaling in the ELMO Bumpy Torus (EBT)," *Plasma Physics and Controlled Nuclear Fusion Research*, Vol. II, 145 (IAEA, Vienna, 1977).

C. L. Hedrick, E. F. Jaeger, D. A. Spong, G. E. Guest, N. A. Krall, J. B. McBride, G. W. Stuart, "A Simple Neoclassical Point Model for Transport and Scaling in EBT," Nucl. Fusion 17, 1237 (1977).

J. T. Hogan, "Tokamak Simulation Models," Nucl. Sci. Eng. 64, 1 (1977).

W. A. Houlberg, R. W. Conn, "Fluid Simulation of Large Tokamak Plasmas Using a Variable Spatial Mesh, Variable Time-Step Implicit Procedure," Nucl. Sci. Eng. 64, 141 (1977).

R. C. Isler, "An Observation of the Reaction $H^0 + O^{8+} \rightarrow H^+ + (O^{7+})^*$ During Neutral Beam Injection Into ORMAK," Phys. Rev. Lett. 38, 1359-1362 (1977).

R. C. Isler, R. V. Neidigh, R. D. Cowan (LASL), "Tungsten Radiation from Tokamak Produced Plasmas," Phys. Lett. 63A, 295-297 (1977).

J. Kim, "Neutron Sources Using D-T Mixed Beams Driven into Solid Target," Nucl. Instrum. Meth. 145, 9-17 (1977).

J. Kim, R. C. Davis, "Enhancement of H^+ Fraction in Hydrogen Ion Sources by Means of Predissociation Method," Appl. Phys. Lett. 30, 130-132 (1977).

J. Kim, J. H. Whealton, "Beam Intensity Distributions in Neutral Beam Injection Systems," Nucl. Instrum. Meth. 141, 187-191 (1977).

H. Knoepfel, D. A. Spong, S. J. Zweben, "Relativistic Runaway Electron Beams in the Oak Ridge Tokamak," Phys. Fluids 20, 511 (1977).

S. L. Lin, L. A. Viehland, E. A. Mason, J. H. Whealton, J. N. Bardsley, "Velocity and Energy Relaxation of Ions in Drift Tubes," J. Phys. B10, 3567 (1977).

J. P. McNally, Jr., "The Ignition Parameter Tn: and the Energy Multiplication Factor k for Fusioning Plasmas," Nucl. Fusion 17, 1273 (1977).

H. K. Meier, W. I. van Rij, C. O. Beasley, Jr., J. E. McCune, "The Collisional Plasma Model: A Velocity-Space Orthogonal-Function Representation for the Distribution Function of a Collisional Plasma," Plasma Phys. 19, 151 (1977).

D. J. Sigmar, S. P. Hirshman, "Neoclassical Transport of A Multispecies Toroidal Plasma in Various Collisionality Regimes," Phys. Fluids 20, 418 (1977).

D. A. Spong, D. C. Eldridge, T. Kammash, "Macroscopic Kink Instabilities in Toroidal Relativistic Beams," Plasma Phys. 19, 817 (1977).

D. Steiner, "Nuclear Fusion: Focus on Tokamak," IEEE Spectrum, 32-38 (July 1977).

W. M. Tang, J. C. Adam, B. I. Cohen, E. A. Frieman, J. A. Krommes, G. Rewoldt, D. W. Ross, M. N. Rosenbluth, P. H. Rutherford, P. J. Catto, K. T. Tsang, J. D. Callen, "Linear and Non-Linear Theory of Trapped-Particle Instabilities," *Plasma Physics and Controlled Nuclear Fusion Research*, Vol. II, 489 (IAEA, Vienna, 1977).

K. T. Tsang, "Banana Drift Diffusion in a Tokamak Magnetic Field with Ripples," Nucl. Fusion 17, 557 (1977).

K. T. Tsang, "Dissipative Trapped-Electron Modes in the Presence of Impurities," Nucl. Fusion 17, 557 (1977).

K. T. Tsang, "Neoclassical Transport in an Elliptic Tokamak," Phys. Fluids 20, 1680 (1977).

K. T. Tsang, J. D. Callen, P. J. Catto, "Collisional Effects on Trapped Electron Instabilities," Phys. Fluids 20, 2113 (1977).

K. T. Tsang, P. J. Catto, "Analytic Solutions of the Two-Dimensional Eigenvalue Problem for the Trapped Electron Instability in Tokamaks," Phys. Rev. Lett. 39, 1664 (1977).

K. T. Tsang, E. C. Crume, "Temperature Screening Effect in Two-Ion-Species Pfirsch-Schlüter Transport," Nucl. Fusion 17, 797 (1977).

W. I. van Rij, H. K. Meier, C. O. Beasley, Jr., J. E. McCune, "Kinetic Equations for the Collisional Plasma Model," Plasma Phys. 19, 135 (1977).

J. H. Whealton, "Ion Speed Distributions in High Field Swarms and Their Relation to Ion-Molecule Rate Constants," Comments At. Mol. Phys. 7, 35 (1977).

J. H. Whealton, "Linear Optics Theory of Ion-Beamlet Steering," Rev. Sci. Instrum. 48, 1428 (1977).

J. H. Whealton, D. S. Burch, A. V. Phelps, "Improved Model for Parallel-Plate Drift-Tube Experiments," Phys. Rev. A15, 1685 (1977).

J. H. Whealton, E. F. Jaeger, D. S. Burch, "Ion Transport Theory for a Slightly Ionized Rarefied Gas in a Strong Electric Field II.," Phys. Rev. A15, 773 (1977).

J. H. Whealton, E. F. Jaeger, J. C. Whitson, "Optics of Single Stage Accelerated Ion Beams Extracted from a Plasma," Rev. Sci. Instrum. 48, 829 (1977).

R. B. White, D. A. Monticello, M. N. Rosenbluth, B. V. Waddell, "Numerical Studies of Resistive Instabilities," *Plasma Physics and Controlled Nuclear Fusion Research*, Vol. I, 596 (IAEA, Vienna, 1977).

R. B. White, D. A. Monticello, M. N. Rosenbluth, B. V. Waddell, "Saturation of the Tearing Mode," Phys. Fluids 20, 800 (1977).

Workshop on High Beta Experiments, DMFE-ERDA, Washington, D.C., January 27, 1977

J. F. Clarke, "Characteristics of an Experimental High Beta Program."

American Physical Society Topical Conference on Atomic Processes in High-Temperature Plasmas. Knoxville, Tennessee, February 16-18, 1977

J. T. Hogan, "Atomic and Molecular Data for Fusion."

R. C. Isler, "An Observation of the Reaction $H^0 + O^{8+} \rightarrow H^+ + (O^{7+})$ During Neutral Beam Injection into ORMAK."

Seminar presented at University of Illinois, Urbana, Illinois, March 7-8, 1977

J. R. McNally, Jr., "Advanced Fusion Fuel Prospects for Magnetic and Inertial Confinement."

Seminar presented at Brookhaven National Laboratory, Upton, New York, March 10, 1977

J. R. McNally, Jr., "Advanced Fusion Fuel Prospects for Magnetic and Inertial Confinement."

In-Service Institute on Resources, Energy and the Environment, Tennessee Technological University, Cookeville, Tennessee, March 24, 1977

A. T. Mense, "Fusion Power."

Topical Meeting on Improved Methods of Numerical Analysis, Tucson, Arizona, March 27-29, 1977

J. T. Hogan, "Tokamak Transport Codes."

Fusion Power Coordinating Committee Meeting, Boston, Massachusetts, March 28, 1977

J. F. Clarke, "TNS and DEMO Studies Show that the Fusion Program Can Embark on a Path To Demonstrate Commercial Feasibility in this Country."

Institute of Electrical and Electronics Engineers Southeastern Conference, Williamsburg, Virginia, April 4-6, 1977

J. M. Bailey, A. Y. Broverman, R. B. Easter, J. F. Harris, R. E. Hill, F. M. Heck, and J. E. Wolf, "Ohmic Heating System for ORMAK Upgrade."

3rd International (Kiev) Conference on Theoretical Plasma Physics, International Center for Theoretical Physics, Trieste, Italy, April 5-9, 1977

Y-K. M. Peng, "Poloidal Field and Free-Boundary Equilibrium in D-Shaped FCT."

Y-K. M. Peng, R. A. Dory, J. Holmes, and D. J. Sigmar, "Properties of High Beta Equilibrium in Flux-Conserving Tokamaks."

B. V. Waddell, M. N. Rosenbluth, D. A. Monticello, R. B. White, and B. Carreras, "Nonlinear Numerical Algorithms for Studying Tearing Modes."

American Physical Society Meeting, Washington, D.C., April 25-28, 1977 (proceedings published in Bull. Am. Phys. Soc. 22, 1977)

J. R. McNally, Jr., "The Ignition Parameter $Tn\tau$ and the Energy Multiplication Factor k for Fusioning Plasmas."

J. R. McNally, Jr., "$Tn\tau$ Criterion for Fusion," p. 581.

Y-K. M. Peng, "MHD Equilibrium and Stability Considerations for High Beta Tokamaks," p. 589.

Annual Controlled Fusion Theory Conference (Project Sherwood) San Diego, California, May 4-6, 1977

T. Amano and E. C. Crume, "Numerical Calculation of Oxygen and Iron Impurity Diffusion in Tokamaks."

D. B. Batchelor, "Recent Results in Microwave Heating Theory for EBT."

D. B. Batchelor and C. L. Hedrick, "A Preliminary Look at Trapped Particle Modes in EBT."

G. Bateman and Y-K. M. Peng, "Large Scale MHD Stability of FCT Tokamaks."

C. O. Beasley, Jr., D. J. Sigmar, W. I. van Rij, and H. K. Meier, "Electrical Conductivity of Tokamak Plasma Calculated by CPM Code."

J. D. Callen, G. G. Kelley, K. T. Tsang, and B. V. Waddell, "Drift Wave Turbulence Effects on Magnetic Structure and Plasma Transport in Tokamaks."

B. Carreras and B. V. Waddell, "Analytic Treatment of the Interaction of Tearing Modes in Tokamaks."

H. C. Chan and D. J. Sigmar, "Anomalous Transport of Alpha-Particles in Toroidal Fusion Plasma Due to Shear Alfvén Wave."

J. F. Clarke, "An Improved Estimate of the Trapped Ion Mode Energy Loss from Tokamak Reactors."

R. A. Dory, D. B. Nelson, Y-K. M. Peng, D. Berger, L. Bernard, R. Gruber, and F. Troyon, "Application of Ideal MHD Stability Code ERATO to High Beta Tokamak Equilibria."

H. R. Hicks, B. V. Waddell, B. Carreras, and J. Holmes, "Nonlinear Evolution of the Reduced Set of Three-Dimensional Resistive MHD Equations for Tokamaks."

J. T. Hogan, "Injection, Compression and Transport Studies."

E. F. Jaeger, "Radial Transport with a Self-Consistent Electric Field in the ELMO Bumpy Torus."

F. B. Marcus and S. E. Attenberger, "Initial Phase of Tokamak Discharges."

A. T. Mense and S. E. Attenberger, "Profile Effects on Plasma Transport in Tokamak Fusion Reactors under the Influence of Trapped Particle Modes."

D. A. Monticello, M. N. Rosenbluth, P. E. White, and B. V. Waddell, "Nonlinear Drift Tearing Modes."

Y-K. M. Peng and J. A. Holmes, "Time Evolution of Flux-Conserving Equilibria with Noncircular Cross Sections in a D-T Tokamak."

J. A. Rome and T. G. Northrop, "Comments on Guiding Center Motion in High Beta Tokamaks."

D. A. Spong, E. G. Harris, and C. L. Hedrick, "Neoclassical Transport Coefficients for the ELMO Bumpy Torus Device."

K. T. Tsang and J. D. Callen, "Anomalous Transport Due to Drift Waves in Tokamaks."

N. A. Uckan and C. L. Hedrick, "Operating Point Considerations for the ELMO Bumpy Torus Reactor (EBTR)."

T. Uckan, E. C. Crume, S. P. Hirshman, and D. K. Lee, "Numerical Evolution of Multi-Impurity Pfirsch-Schlüter Transport."

G. Vahala, L. Vahala, J. H. Harris, G. Bateman, and B. V. Waddell, "Perturbed Magnetic Field Phase Slip for Tokamaks."

B. V. Waddell, J. D. Callen, B. Carreras, H. R. Hicks, J. Holmes, and G. L. Jahns, "Tearing Modes in Tokamaks."

J. H. Whealton, "Reduction in Residual Aberration Effects on Ion Optics in Neutral Beam Generators."

Institute of Electrical and Electronics Engineers 1977 International Conference on Plasma Science, Rensselaer Polytechnic Institute, Troy, New York, May 23-25, 1977 (proceedings published in IEEE Conference Record, Cat. #77CH1205-4 NPS, 1977)

S. E. Attenberger, F. B. Marcus, J. R. McNally, Jr., and A. T. Mense, "A Flux Conserving Tokamak Reactor," p. 94.

F. Bieniosek, P. L. Colestock, K. A. Connor, and R. L. Hickok, "Heavy Ion Beam Probe Measurements on the EBT Device."

J. Kim, W. L. Gardner, M. M. Menon, and G. Schilling, "An Investigation of Ion Beam Optics in a Two-Stage 150 keV Accelerator," p. 132.

J. R. McNally, Jr., "Physics Requirements for Advanced Fuel Fusion."

S. L. Milora, "Revised Neutral Ablation Model for Pellet-Tokamak Plasma Interactions."

N. A. Uckan, "The ELMO Bumpy Torus Reactor (EBTR) Study."

J. H. Whealton, L. R. Grisham, J. Kim, W. L. Stirling, and C. C. Tsai, "Space Charge Ion Optical – Experiment and Theory."

2nd Argonne National Laboratory-Argonne Universities Association Faculty Institute on Fusion Plasma Engineering, Argonne, Illinois, June 6-10, 1977

J. T. Hogan, "Transport Calculations in Tokamaks."

Y-K. M. Peng, "High Beta Tokamak Theory – MHD Equilibrium."

J. A. Rome, "Neutral Beam Injection into Tokamaks – Theory and Experiment."

1977 Annual Meeting of the American Nuclear Society, New York, New York, June 12-17, 1977 (proceedings published in Trans. Am. Nucl. Soc. 26, 1977)

C. A. Foster, "Fueling by High Speed Pellet Injection."

J. T. Hogan, "Impurity Models in Tokamaks."

R. C. Isler, "Measurements of the Concentrations of Impurities in Tokamaks," p. 16.

N. A. Uckan, E. S. Bettis, C. L. Hedrick, R. T. Santoro, H. T. Yeh, and D. G. McAlees, "The ELMO Bumpy Torus Reactor (EBTR) Reference Design Study," p. 57.

Gordon Research Conference on Magnetic Reconnection in Space and Laboratory Plasmas, Brewster Academy, Wolfsboro, New Hampshire, June 20-24, 1977

B. V. Waddell, "Numerical Simulation of Magnetic Reconnection in Tokamaks."

World Electrotechnical Congress, Moscow, U.S.S.R., June 21-25, 1977

M. S. Lubell, "Development of Superconducting Magnet Systems for Fusion Power Generators."

Electric Power Research Institute Review Meeting on Advanced Fuel Fusion, Chicago, Illinois, June 26-28, 1977 (proceedings published as EPRI ER-536-SR, September 1977)

J. R. McNally, Jr., "Autobibliography on Ion-Layer Production, Properties, Needs, and Applications," p. 307.

J. R. McNally, Jr., "General Requirements and Approaches to Advanced Fuel Fusion," p. 197.

3rd International Congress on Wave and Instabilities in Plasmas, Palaiseau, France, June 27-July 1, 1977

K. T. Tsang and J. D. Callen, "Electrostatic Drift Wave Turbulence and its Effects on Anomalous Transport Processes in Tokamaks."

K. T. Tsang, J. D. Callen, G. G. Kelley, and E. V. Waddell, "Drift Wave Turbulence Effects on Magnetic Structure and Plasma Transport in Tokamaks."

Oak Ridge National Laboratory Fusion Energy Division Industrial Information Meeting, Oak Ridge, Tennessee, July 15, 1977

R. A. Dandl, "Microwave Plasma Heating in ELMO Bumpy Torus (EBT)."

H. O. Eason, "Technology of Microwave Plasma Heating in EBT."

Workshop on Stability in Superconducting Magnets, Los Alamos Scientific Laboratory, Los Alamos, New Mexico, July 25-29, 1977

L. Dresner, "Theoretical Research on Stability at ORNL."

American Institute of Aeronautics and Astronautics/Edison Electric Institute Conference on New Options in Energy Technology, San Francisco, California, August 2-4, 1977

J. F. Clarke, "New Prospects for Magnetic Fusion Energy Leading to a Commercial Demonstration."

Cryogenic Engineering Conference, Boulder, Colorado, August 2-5, 1977

R. E. Schwall, S. S. Shen, L. Dresner, J. W. Lue, J. R. Miller, and H. T. Yeh, "Superconductors for Tokamak Poloidal Field Coils."

Oak Ridge Associated Universities Institute on Energy Options for the Future, Oak Ridge, Tennessee, August 4, 1977

J. Rand McNally, Jr., "Fusion."

Legislative Workshop on Energy in Minnesota, Northfield, Minnesota, August 14-16, 1977

J. F. Clarke, "Future Prospects and Challenges of Fusion Energy."

Cryogenic Engineering Conference, Boulder, Colorado, August 17-21, 1977 (proceedings published in Adv. Cryog. Eng. 23, 1977)

J. W. Lue, J. R. Miller, and L. Dresner, "Vapor Locking as a Limitation to the Stability of Composite Conductors Cooled by Boiling Helium," pp. 226-234.

12th Intersociety Energy Conversion Engineering Conference, Washington, D.C., August 28-September 2, 1977

N. A. Uckan, L. M. Lidsky, and D. G. McAlees, "The ELMO Bumpy Torus Reactor."

6th International Conference on Magnet Technology, Bratislava, Czechoslavakia, August 29-September 2, 1977

L. Dresner and J. W. Lue, "Design of Force-Cooled Conductors for Large Fusion Magnets."

J. N. Luton and H. T. Yeh, "Toroidal Magnet System Design for the ELMO Bumpy Torus Reactor."

Course and Workshop on Magnetically Confined Plasmas, Varenna, Italy, September 1-10, 1977

EBT Group (presented by N. A. Uckan), "The ELMO Bumpy Torus – Present and Future."

8th European Conference on Controlled Fusion and Plasma Physics, Prague, Czechoslovakia, September 19-23, 1977

D. Berger, L. Bernard, R. Gruber, F. Troyon, R. A. Dory, D. B. Nelson, and Y-K. M. Peng, "Application of Ideal MHD Stability Code ERATO to High Beta Tokamak Equilibrium."

D. J. Sigmar, "Anomalous Alpha Particle Transport."

D. J. Sigmar, "Progress in FCT Theory."

Atomic International Forum Fusion Committee, ORNL Fusion Energy Division, Oak Ridge, Tennessee, September 21, 1977

J. F. Clarke, L. A. Berry, P. N. Haubenreich, O. B. Morgan, D. Steiner, and J. Steigler, "OPNL Fusion Energy Program."

Symposium on the Production and Neutralization of Negative Hydrogen Ions and Beam, Brookhaven National Laboratory, Upton, New York, September 26-30, 1977

J. H. Whealton, C. C. Tsai, W. L. Stirling, and L. R. Grisham, "Production of Low Energy Positive Ions Suitable for Double Electron Capture Systems."

International Atomic Energy Agency Workshop on Fusion Reactor Design, Madison, Wisconsin, October 10-21, 1977

R. L. Reid and D. Steiner, "An Economic Evaluation of Tokamak Power Plant."

M. Roberts, "TNS Design Space Exploration Has Brought Us a Large Step Closer to Realizable Reactor."

M Roberts, W. R. Becraft, C. A. Flanagan, Y-K. M. Peng, T. E. Shannon, and T. C. Varljen, "Development of the TNS Design Space."

T. E. Shannon and D. Steiner, "ORNL Fusion Power Demonstration Study."

N. A. Uckan, R. A. Dandl, C. L. Hedrick, E. S. Bettis, L. M. Lidsky, D. G. McAlees, R. T. Santoro, H. L. Watts, and H. T. Yeh, "The ELMO Bumpy Torus (EBT) Reactor."

13th Annual Gaseous Electronics Conference, Palo Alto, California, October 18-21, 1977 (proceedings published in Bull. Am. Phys. Soc. 23, 1978)

J. H. Whealton and J. C. Whitson, "Solution of the Collisionless Plasma – SHEATH Equation for Ion Extraction Through an Aperture," p. 151.

7th Symposium on Engineering Problems of Fusion Research, Institute of Electrical and Electronics Engineers, Knoxville, Tennessee, October 25-28, 1977 (proceedings published as IEEE Pub. No. 77CH1267-4-NPS).

G. C. Barber, A. Y. Broverman, R. E. Hill, C. M. [illegible]y, N. S. Ponte, G. Schilling, and R. E. Wright, "The Design Philosophy and Use of High Voltage Power Systems for Multimegawatt Ion Beam Accelerators," Vol. II, p. 1142.

E. S. Bettis, J. K. Ballou, W. R. Becraft, Y-K. M. Peng, and H. L. Watts, "Advantages of Iron Core in a Tokamak," Vol. I, p. 198.

E. S. Bettis, J. M. Barnes, T. J. Huxford, K. C. Liu, R. T. Santoro, and H. L. Watts, "A Practical Blanket Design for a Toroidal Fusion Reactor," Vol. II, p. 1453.

R. L. Brown, "Superconducting Coil Fabrication Development at Oak Ridge National Laboratory," Vol. I, p. 723.

O. Burenko, "Plasma Position Dynamics of ISX Tokamak," Vol. II, p. 1688.

G. L. Campen and R. B. Easter, "Voltage Protection Scheme for MG Sets Used to Drive Inductive Energy Storage Systems," Vol. I, p. 1079.

W. D. Cain, "Magnetic Field Computations for ISX Using GFUN-3D," Vol. II, p. 1362.

W. D. Cain, W. H. Gray, W. R. Hendrick, B. E. Nelson, and W. C. T. Stoddart, "Structural Analysis of the Large Coil Segment Test," Vol. I, p. 751.

L. Dresner, "The Effect of a Continuous Resistive Transition on Self-Field Instability," Vol. I, p. 719.

L. Dresner and J. W. Lue, "Design of Force-Cooled Conductors for Large Fusion Magnets," Vol. I, p. 703.

N. W. Durfee, "Assembly of ISX," Vol. I, p. 126.

W. A. Fietz, "Conductors for Tokamak Toroidal Field Coils," Vol. II, p. 1278.

J. E. Francis, Jr. and C. E. Hammons, "Data Acquisition System for PLT Neutral Beam Test Stand," Vol. II, p. 1217.

W. L. Gardner, J. Kim, M. M. Menon, and G. Schilling, "The ORNL 150 keV Neutral Beam-Test Facility," Vol. II, p. 1545.

R. J. Goldston, D. L. Jassby, H. H. Towner, R. H. Fowler, J. F. Lyon, J. A. Rome, and T. Brown, "Magnetics Design for Ripple-Assisted Beam Injection into the ISX-B and TFTR Tokamaks," Vol. II, p. 1333.

W. H. Gray and J. E. Akin, "Finite Element Stress Analysis of Orthotropic Solenoids," Vol. I, p. 851.

W. H. Gray, W. C. T. Stoddart, and J. E. Akin, "Bending Free Toroidal Shells for Tokamak Fusion Reactors," Vol. I, p. 855.

W. H. Gray, W. C. T. Stoddart, J. K. Ballou, G. F. Churakov, and E. Y. Klimenko, "A Preliminary Structural Analysis of the Toroidal Field Coils for T-10M," Vol. I, p. 756.

W. A. Houlberg, A. T. Mense, and S. E. Attenberger, "Sensitivity of Ignition in TNS to Fueling Profiles and Radial Transport Processes," Vol. II, p. 1693.

J. Kim, R. C. Davis, W. R. Gambill, and H. H. Haselton, "A Heat Transfer Study of Water-Cooled Swirl Tubes for Neutral Beam Targets," Vol. II, p. 1593.

C. G. Lawson and J. P. Kois, "The Helium Liquefier-Refrigerator and Distribution System for the Large Coil Program Test Facility," Vol. II, p. 966.

C. G. Lawson and J. R. May, "The Helium Distribution System for the Large Coil Test Facility (LCTF)," Vol. I, p. 737.

D. C. Lousteau and R. O. Hussung, "Design and Fabrication of the Impurity Study Experiment (ISX) Coils," Vol. I, p. 44.

Y-K. M. Peng, S. E. Attenberger, W. A. Houlberg, A. T. Mense, J. A. Rome, and N. A. Uckan, "Plasma Engineering Innovations for the ORNL TNS Reactor," Vol. II, p. 1697.

Y-K. M. Peng, D. J. Strickler, and R. A. Dory, "Hybrid Equilibrium Field Coils for the ORNL TNS," Vol. I, p. 186.

R. L. Reid and D. Steiner, "Economics of Tokamak Power Systems," Vol. I, p. 575.

M. Roberts, "OAK RIDGE TNS PROGRAM 1976/77: Integration of Engineering Reality Brings Us Closer to Realizable Reactor," Vol. I, p. 580.

R. E. Schwall, W. H. Gray, and C. J. Long, "Mechanical Design of ORPUS-3," Vol. II, p. 1326.

S. W. Schwenterly, "Development of Vacuum Components for Neutral Beam Injection Applications," Vol. II, p. 1793.

S. S. Shen and R. E. Schwall, "Losses and Transient Field Effect in Superconducting Cables for PF and TF Coils," Vol. II, p. 1293.

T. E. Smith, R. L. Dearstone, and P. L. Goranson, "Engineering Features of ISX-B," Vol. I, p. 121.

D. Steiner, "Technological Requirements for Tokamak Power Systems," Vol. I, p. 14.

N. A. Uckan, E. S. Bettis, C. L. Hedrick, R. T. Santoro, H. L. Watts, and H. T. Yeh, "Physics and Engineering Aspects of the EBT Reactor," Vol. I, p. 614.

N. A. Uckan, J. D. Callen, K. T. Tsang, and J. R. Moore, "Toroidal Field Ripple Effects in TNS Design," Vol. I, p. 169.

T. Uckan, "Small Radius Start-Up for a TNS Plasma," Vol. I, p. 81.

M. S. Walker, B. A. Zeitlin, and R. E. Schwall, "Fast Ramp Superconductor for Ohmic Heating Coils," Vol. II, p. 1310.

P. L. Walstrom, P. B. Burn, B. E. Nelson, T. L. Ryan, and R. B. Wysor, "Design of a Three-Meter, 7.5-Tesla Superconducting Segment Test Facility," Vol. I, p. 354.

W. M. We[illegible], "Lithium as a Blanket Coolant," Vol. II, p. 1707.

J. T. Woo, N. A. Uckan, and L. M. Lidsky, "Economic Analysis of EBT Reactor," Vol. I, p. 681.

B. A. Zeitlin, M. S. Walker, J. P. Heinrich, and W. A. Fietz, "An Integrated Composite Conductor for the LCS Program," Vol. II, p. 1273.

Workshop on Fusion Fueling, Princeton, New Jersey, November 1-3, 1977

C. A. Foster and S. L. Milora, "ORNL Pellet Acceleration Program."

W. A. Houlberg, A. T. Mense, S. E. Attenberger, and S. L. Milora, "Effects of Fueling Profiles on Plasma Transport."

S. L. Milora and C. A. Foster, "Pellet Experiments at ORNL."

G. H. Neilson and J. F. Lyon, "Neutral Beam Injection Experiments at ORNL: Fueling Aspects."

J. A. Rome, "Beam Penetration – Theory and Predictions."

American Physical Society, Annual Meeting of the Division of Plasma Physics, Atlanta, Georgia, November 7-11, 1977 [proceedings published in Bull. Am. Phys. Soc. 22(9), 1977]

T. Amano and E. C. Crume, "Numerical Simulation of Multi-Species Impurity Transport in Tokamaks," p. 1095.

C. H. An and R. G. Bateman, "Numerical Study of High Beta Tokamaks with Elongated Cross-Section," p. 1153.

S. E. Attenberger, W. A. Houlberg, and J. T. Mense, "Pellet Fueling Effects in TNS," p. 1135.

F. W. Baity and B. H. Quon, "Ion Temperature Profile Measurements on EBT," p. 1145.

D. B. Batchelor and C. L. Hedrick, "Possible Trapped Particle Modes in EBT," p. 1146.

R. G. Bateman, "Inductive Effects in Flux Conserving Tokamaks," p. 1117.

C. O. Beasley, Jr., H. K. Meier, W. I. van Rij, and J. E. McCune, "CPM Studies of the Current-Driven Drift Instability," p. 1166.

L. A. Berry, J. L. Dunlap, P. H. Edmonds, P. W. King, J. F. Lyon, D. H. McNeill, M. Murakami, and Y-K. M. Peng, "Attainment of a ≈3% Toroidal-Beta at a Low Safety Factor with Neutral Beam Injection in ORMAK," p. 1090.

J. D. Callen, "New Developments in Tokamak Anomalous Transport Theory," p. 1104.

B. Carreras and B. V. Waddell, "Analytic Study of the Interaction of Tearing Modes of Different Helicity," p. 1171.

P. J. Catto, "Drift Instability Eigenvalue Problems in Tokamaks," p. 1105.

P. J. Catto and K. T. Tsang, "Improved Eigenvalue Equations for the Collisionless Drift Wave in Tokamaks," p. 1166.

L. A. Charlton, D. P. Berger, R. A. Dory, and D. B. Nelson, "Wall Action on the MHD Stability of Flux Conservative Tokamak Equilibria," p. 1125.

J. A. Cobble, "Impurity Ion Line Broadening in EBT," p. 1146.

R. J. Colchin, J. L. Anderson, O. Burenko, T. C. Jernigan, A. F. Navarro, and D. H. McNeill, "Equilibrium and Stability Control of ISX."

P. L. Colestock, K. A. Connor, R. L. Hickok, and R. A. Dandl, "Ambipolar Field Measurements on EBT," p. 1145.

E. C. Crume, M. A. Zuniga, and D. J. Sigmar, "Kinetic Effects of Impurity Atomic Physics," p. 1096.

J. N. Davidson and A. T. Mense, "The Electrostatic Sheath Potential for a Hot, Multispecies Plasma," p. 1208.

R. A. Dory, D. P. Berger, L. A. Charlton, D. B. Nelson, and Y-K. M. Peng, "Ideal MHD Instability Limitations and Beta for Tokamak Systems," p. 1125.

J. L. Dunlap, V. K. Paré, and R. D. Burris, "Internal Mode Structures in ORMAK."

C. A. Foster, S. L. Milora, J. A. Mayhall, and T. L. Phillips, "ORNL Pellet Injection Programs."

W. L. Gardner, J. Kim, M. M. Menon, and J. H. Whealton, "Beamlet Steering for Multi-Aperture, Two Stage Ion Accelerators," p. 1082.

R. C. Goldfinger, D. B. Nelson, and C. L. Hedrick, "Marginal Equilibrium and Stability Calculations for the Axisymmetric EBT," p. 1146.

C. L. Hedrick, "A Two-Region Model for Transport in EBT," p. 1146.

H. R. Hicks, J. A. Holmes, B. Carreras, and B. V. Waddell, "Numerical Study of the Interaction of Tearing Modes of Different Helicity," p. 1171.

S. P. Hirshman and D. J. Sigmar, "Moment Equation Approach to Neoclassical Transport Theory," p. 1105.

J. T. Hogan, "Calculations of High(er) Beta Transport in Tokamaks," p. 1179.

J. A. Holmes and Y-K. M. Peng, "Time Dependent Equilibrium Evolution in a Flux-Conserving D-T Tokamak Reactor," p. 1135.

H. C. Howe and D. J. Sigmar, "Effects of Wall Reflection on Neutral Transport in a Plasma Slab," p. 1178.

M. A. Iskra, S. E. Attenberger, and A. T. Mense, "Feedback Control of Tokamak Reactors by Controlled Cold Fueling Rates," p. 1135.

R. C. Isler, E. C. Crume, and H. C. Howe, "Impurity Behavior during Injection and Gas Puffing into ORMAK," p. 1091.

E. F. Jaeger and C. L. Hedrick, "Radial Transport in the ELMO Bumpy Torus," p. 1145.

G. L. Jahns, B. V. Waddell, and J. D. Callen, "Tearing Modes and Sawtooth Oscillations Revisited," p. 1152.

J. Kim and R. C. Davis, "A Surface-Ionization Negative Ion Source," p. 1083.

D. Meade, D. P. Berger, L. A. Berry, M. Chance, R. A. Dory, S. Jardin, J. Manickam, D. B. Nelson, M. Okabayashi, and Y-K. M. Peng, "Study of PDX High-Beta MHD Limits," p. 1141.

H. K. Meier, C. O. Beasley, Jr., W. I. van Rij, and J. E. McCune, "Extension of Hazeltine's Drift Kinetic Equation," p. 1166.

J. R. McNally, Jr., "Fusion-Fission Analogy," p. 1132.

D. H. McNeill, M. Murakami, C. E. Bush, G. R. Dyer, P. H. Edmonds, H. E. Ketterer, P. W. King, and J. F. Lyon, "Electron Confinement of Injection-Heated Plasmas in ORMAK," p. 1148.

M. M. Menon, W. L. Gardner, and J. Kim, "Beam Optics in a Two-Stage High Energy Ion Beam Accelerator," p. 1082.

A. T. Mense, L. A. Berry, J. T. Hogan, D. Mikkelsen, J. A. Schmidt, "Transport Calculations for the 12-MW Oak Ridge-Princeton Injection Experiment," p. 1141.

A. P. Navarro, R. J. Colchin, T. C. Jernigan, D. H. McNeill, T. C. Tucker, and W. R. Wing, "Magnetic Field Measurements and Calculations for ISX."

G. H. Neilson, "Measurement of Mass-Resolved Neutral Particle Energy Distribution in ISX."

D. B. Nelson, J. K. Munro, D. P. Berger, R. A. Dory, and Y-K. M. Peng, "Stability Limits for Internal MHD Modes in High Beta Tokamaks," p. 1125.

L. W. Owen and C. L. Hedrick, "Calculated Effects on EBT Particle Confinement Using Experimentally Determined Electric Field Profiles," p. 1146.

Y-K. M. Peng, D. P. Berger, R. A. Dory, D. K. Lee, and D. B. Nelson, "Ideal MHD Stability Beta Optimization with Noncircular Plasmas in ISX-B," p. 1125.

M. Roberts, "Realizable Reactor Designs Require Even Closer Coupling Between Plasma Engineering and Engineering Design."

J. A. Rome, R. H. Fowler, R. J. Goldston, H. L. Hassby, and J. F. Lyon, "Ripple Injection Calculations for ISX-B," p. 1116.

M. Soler and J. D. Callen, "Resolutions of the Heat Pulse Propagation Paradox," p. 1178.

D. A. Spong, "EBT Neoclassical Transport Coefficients Using Model Collision Operators," p. 1145.

D. J. Strickler, Y-K. M. Peng, and D. W. Swain, "Poloidal Field System and Noncircular MHD Equilibria in ISX-B," p. 1158.

D. W. Swain, Y-K. M. Peng, M. Murakami, and L. A. Berry, "High Beta Experiments for ISX-B," p. 1158.

K. T. Tsang and P. J. Catto, "Analytic Solutions of the Two-Dimensional Eigenvalue Problem for the Trapped Electron Instability in Tokamaks," p. 1166.

T. C. Tucker, W. D. Cain, D. H. McNeill, and Y-K. M. Peng, "Poloidal Field Modeling in ISX," p. 1157.

J. M. Tyson, R. K. Richards, E. S. Warden, H. W. Moos, and N. H. Lazar, "Spectrophotometric Studies of Impurity Distribution in EBT."

N. A. Uckan and C. L. Hedrick, "Reactor Applications for EBT's," p. 1147.

T. Uckan, "Possible Separable Solutions for Plasma Transport in Tokamaks," p. 1179.

G. Vahala and D. J. Sigmar, "Analytic, High Beta Flux Conserving Equilibria for Cylindrical Tokamaks," p. 1126.

B. V. Waddell, "Disruptions in Tokamaks," p. 1104.

J. H. Whealton and J. Kim, "Space Charge Ion Optics of Two Stage Accelerators," p. 1114.

S. J. Zweben, D. W. Swain, J. B. Wilgen, and B. V. Waddell, "Effects of Instabilities on Runaway Confinement in ORMAK," p. 1149.

Electric Power Research Institute Fusion Committee, ORNL Fusion Energy Division, Oak Ridge, Tennessee, November 17, 1977

O. B. Morgan, L. A. Berry, D. Steiner, R. A. Dandl, N. A. Uckan, H. H. Haselton, P. N. Haubenreich, and J. O. Stiegler, "ORNL Fusion Energy Program" (slide presentation).

American Nuclear Society Winter Meeting, 25th Conference on Remote Systems Technology, San Francisco, California, November 27-December 2, 1977 (proceedings published in Trans. Am. Nucl. Soc. 27, 1977)

R. A. Dandl, R. A. Dory, and N. A. Uckan, "The ELMO Bumpy Torus," p. 41.

A. T. Mense, S. E. Attenberger, and W. A. Houlberg, "Fueling Profile Sensitivities of Trapped Particle Mode Transport for TNS," p. 30.

Y-K. M. Peng, S. E. Attenberger, J. D. Callen, J. A. Holmes, W. A. Houlberg, F. B. Marcus, J. R. McNally, Jr., A. T. Mense, J. A. Rome, and N. A. Uckan, "Plasma Engineering Considerations for a Medium-Field Ignition Test Reactor – The Next Step (TNS) Beyond TFTR," p. 27.

Y-K. M. Peng and D. J. Strickler, "Equilibrium Field Coils and Free-Boundary Equilibrium Considerations for TNS," p. 29.

R. L. Reid, W. B. Wood, and D. Steiner, "The Commercial Feasibility of Fusion Power Based on the Tokamak Concept," p. 10.

J. A. Rome, Y-K. M. Peng, and J. N. Davidson, "Injection Scenarios for TNS," p. 89.

S. W. Schwenterly, W. K. Dagenhart, H. H. Haselton, W. L. Stirling, and C. C. Tsai, "Performance of 4.2 K Cryopumps in Neutral Beam Injectors," pp. 56-57.

T. E. Shannon, P. T. Spampinato, and R. W. Werner, "Remote Servicing Considerations for Near-Term Tokamak Power Reactors (TNS and DEMO)."

T. E. Shannon and D. Steiner, "Design Approaches for Enhancing the Engineering Feasibility of Tokamak Power Reactors."

P. T. Spampinato, "Remote Servicing Considerations for Near-Term Power Reactors (TNS)."

N. A. Uckan, E. S. Bettis, C. L. Hedrick, R. T. Santoro, H. T. Yeh, and H. L. Watts, "Design Features of the ELMO Bumpy Torus Reactor (EBTR)."

Miami International Conference on Alternative Energy Sources, Miami, Florida, December 5-7, 1977

A. T. Mense, "Fusion Power Demonstration Study at ORNL."

R. L. Reid and D. Steiner, "Systems Studies for a Tokamak Fusion Power Plant."

N. A. Uckan, "The ELMO Bumpy Torus – An Alternative Fusion Reactor Concept."

REPORTS

ORNL Reports

Author(s)	Title	Number
J. Wooten, H. R. Hicks, R. G. Bateman, R. A. Dory	Preliminary Results of the 3-D Nonlinear Ideal MHD Code	ORNL/TM-4784
M. Roberts	Oak Ridge Tokamak Experimental Power Reactor Study Scoping Report	ORNL/TM-5038
K. T. Tsang, J. D. Callen, P. J. Catto	Collisional Effects on Trapped Electron Instabilities	ORNL/TM-5236
J. K. Munro, J. T. Hogan, H. C. Howe, D. E. Arnurius	A User's Manual for the Oak Ridge Tokamak Transport Code	ORNL/TM-5262
C. L. Hedrick, E. F. Jaeger, D. A. Spong, G. E. Guest, N. A. Krall, J. B. McBride, G. W. Stuart	A Simple Neoclassical Point Model for Transport and Scaling in EBT	ORNL/TM-5490
W. H. Gray, J. K. Ballou	Electromechanical Stress Analysis of Transversely Isotropic Solenoids	ORNL/TM-5528
M. Roberts, D. G. McAlees, C. A. Flanagan, T. E. Shannon, J. W. Lee	Oak Ridge Tokamak Experimental Power Reactor Study – 1976 Part 1 – EPR Summary	ORNL/TM-5572
T. E. Shannon, R. L. Reid	Oak Ridge Tokamak Experimental Power Reactor Study – 1976 Part 5 – Engineering	ORNL/TM-5576

M. Roberts, D. G. McAlees, J. W. Lue, C. A. Flanagan, T. E. Shannon	Oak Ridge Tokamak Experimental Power Reactor Study — 1976 Part 6 — Research, Development, and Demonstration Needs	ORNL/TM-5577
K. T. Tsang	Neoclassical Transport in an Elliptic Tokamak	ORNL/TM-5631
Y-K. M. Peng, R. A. Dory, D J. Strickler	Poloidal Field Considerations for Tokamaks	ORNL/TM-5648
R. J. Colchin, R. E. Clausing, L. C. Emerson, L. Heatherly, R. C. Isler	Surface and Impurity Studies in ORMAK and ISX	ORNL/TM-5671
H. Pih	Photoelastic Analyses of Stresses in Toroidal Magnetic Field Coils	ORNL/TM-5724
D. L. Shaeffer	Impurity Electron Core Effect in ORMAK	ORNL/TM-5745
T. Uckan, C. O. Beasley, Jr.	Comparison of Model Distribution Functions with Collisional Plasma Model (CPM) Results in Various Collisionality Regimes	ORNL/TM-5761
J. R. McNally, Jr.	The Ignition Parameter $T n\tau$ and the Energy Multiplication Factor k for Fusioning Plasmas	ORNL/TM-5766
S. L. Milora, C. A. Foster	ORNL Neutral Gas Shielding Model for Pellet-Plasma Interactions	ORNL/TM-5776
C. O. Beasley, H. K. Meier, W. I. van Rij, J. E. McCune	Calculation of a Self-Consistent, Low Frequency Electrostatic Field in Toroidal Geometry	ORNL/TM-5784
R. G. Bateman, H. R. Hicks, J. Wooten	3-D Nonlinear Evolution of MHD Instabilities	ORNL/TM-5796
J. R. McNally, Jr.	Energy Transfer From Ions to Electrons and the Coulomb Logarithm	ORNL/TM-5803
D. Steiner, E. S. Bettis, T. J. Huxford, W. J. McAfee, H. E. McCoy, A. T. Mense, R. L. Reid, J. L. Scott, T. E. Shannon, W. C. T. Stoddart, H. L. Watts, W. M. Wells, R. W. Werner, F. W. Wiffen	ORNL Fusion Power Demonstration Study: Interim Report	ORNL/TM-5813
M. S. Lubell, L. Dresner	Letter Report for the Superconducting Magnet Development Program, June 1, 1976-October 1, 1976	ORNL/TM-5820
B. V. Waddell, G. L. Jahns, J. D. Callen, W. R. Hicks	Internal Disruption in Tokamaks	ORNL/TM-5840
J. F. Clarke	An Improved Estimate of Trapped Ion Mode Energy Loss from Tokamak Reactors	ORNL/TM-5860
M. J. Mohan	Design and Construction of a Resistive Energy Dump Device for Bipolar Superconducting Magnet Systems	ORNL/TM-5892
C. A. Foster, R. J. Colchin, S. L. Milora, K. Kim, R. J. Turnbull	Solid Hydrogen Pellet Injection into the ORMAK Tokamak	ORNL/TM-5897
E. H. Warden, H. W. Moos, N. H. Lazar	Observations of Low Charge State Impurities in EBT	ORNL/TM-5899
M. S. Lubell, L. Dresner	Letter Report for the Superconducting Magnet Development Program, January 1, 1977-April 1, 1977	ORNL/TM-5904
A. Cooper, D. W. Swain, F. B. Marcus, T. Kammash	Runaway Modeling in ORMAK and TNS	ORNL/TM-5905
M. S. Lubell	Magnetics and Superconductivity Section Annual Progress Report for Period Ending December 31, 1976	ORNL/TM-5922

J. A. Rome, Y-K. M. Peng, J. A. Holmes	Injection Heating Scenarios for TNS	ORNL/TM-5931
H. M. Long	Cryogenic Power Transmission Technology — Cryogenic Dielectrics	ORNL/TM-5941
K. T. Tsang, J. D. Callen, G. Vahala	Turbulence Theory for the Dissipative Trapped Electron Instability	ORNL/TM-5942
T. G. Northrop, J. A. Rome	Extensions of Guiding Center Motion to Higher Order	ORNL/TM-5952
R. Werner	ORNL Fusion Power Demonstration Study: The Concept of the Cassette Blanket	ORNL/TM-5964
D. B. Nelson. C. L. Hedrick	Macroscopic Stability and β Limits in the ELMO Bumpy Torus	ORNL/TM-5967
B. V. Waddell, G. Laval, M. N. Rosenbluth	Reduction of the Growth Rate of the m = 1 Resistive Magnetohydrodynamic Mode by Finite Gyroradius Effects	ORNL/TM-5968
K. T. Tsang, P. J. Catto	The Trapped Electron Instability in Tokamaks: Analytic Solutions of the Two-Dimensional Eigenvalue Problem	ORNL/TM-5970
J. D. Callen	Drift Wave Turbulence Effects on Magnetic Structure and Plasma Transport in Tokamaks	ORNL/TM-5974
M. Roberts, ed.	Draft Program Plan for TNS — The Next Step After the Tokamak Fusion Test Reactor Part I — Summary	ORNL/TM-5982
Oak Ridge TNS Program Staff	Draft Program Plan for TNS — The Next Step After the Tokamak Fusion Test Reactor Part II — R&D Needs Assessment	ORNL/TM-5983
D. W. Swain, T. E. Smith, D. J. Sigmar, M. Murakami	Proposal for a Major Modification to the ISX Tokamak to Study Equilibrium and Stability of Externally Heated High Beta Plasmas in Noncircular Geometry	ORNL/TM-5985
L. Dresner	The Effect of Flux Flow on Self-Field Instability	ORNL/TM-5986
A. C. England, C. M. Loring, O. C. Eldridge, W. Namkung, H. C. Howe, G. L. Campen, H. L. Mitchell, D. B. Batchelor	Program Plan for Electron Cyclotron Heating Experiments on the ISX Tokamak	ORNL/TM-6011
E. F. Jaeger, C. L. Hedrick	A Numerical Model for Radial Transport in the ELMO Bumpy Torus	ORNL/TM-6013
N. A. Uckan, C. L. Hedrick	Plasma Simulation and Modeling for ELMO Bumpy Torus Reactor	ORNL/TM-6019
A. C. England, H. C. Howe, J. T. Mihalczo, R. H. Fowler	Neutron Time Behavior for Deuterium Neutral Beam Injection into a Hydrogen Plasma in ORMAK	ORNL/TM-6035
P. J. Catto, K. T. Tsang	Improved Eigenvalue Equations for the Collisionless Drift Instability in Tokamaks	ORNL/TM-6045
E. C. Crume, D. E. Arnurius	Numerical Calculation of Impurity Charge State Distributions	ORNL/TM-6050
W. A. Fietz, M. S. Lubell	Letter Report for the Superconducting Magnet Development Program, April 1, 1977-June 30, 1977	ORNL/TM-6059
T. Uckan	A Study of Possible Separable Solutions for Plasma Transport in Ohmically Heated Tokamaks	ORNL/TM-6065

R. T. Santoro, J. M. Barnes	Nuclear Performance Calculations for the ELMO Bumpy Torus Reactor (EBTR) Reference Design	ORNL/TM-6085
H. R. Hicks, B. Carreras, J. A. Holmes, B. V. Waddell	Interaction of Tearing Modes of Different Pitch in Cylindrical Geometry	ORNL/TM-6096
T. Uckan	Small Radius Start-up of Tokamak Plasmas with a Moving Limiter	ORNL/TM-6111
Y-K. M. Peng, S. K. Borowski	ORNL TNS Program: Microwave Start-up of Tokamak Plasmas Near Electron Cyclotron and Upper Hybrid Resonances	ORNL/TM-6112
Y-K. M. Peng, S. E. Attenberger, W. A. Houlberg, A. T. Mense, J. A. Rome, N. A. Uckan	ORNL TNS Program: Plasma Engineering Considerations and Innovations for a Medium Field Tokamak Fusion Reactor	ORNL/TM-6150
Fusion Energy Division Staff	Fusion Energy Division Annual Progress Report for Period Ending December 31, 1976	ORNL-5275
M. Roberts	Conclusions from the Oak Ridge EPR Studies and Initiation of the TNS Program — A Brief Summary	ORNL-5278
J. E. Roberts, N. A. Uckan	EBT Time-Dependent Point Model Code: Description and User's Guide	ORNL/CSD/TM-27
O. P. Pogutse, E. I. Yurchenko	Energy Principle and the Kink Instability in a Toroidal Plasma with a Strong Magnetic Field (translated by Linda Kobylenski, edited by D. J. Sigmar and B. V. Waddell)	ORNL/tr 4410 December 1977

Other Reports

J. T. Hogan, L. R. Grisham, K. Bol	Free Expansion Experiment on ATC	PPPL-1330 March 1977